

DISSERTATION

ELECTRONIC SCAN WEATHER RADAR: SCAN STRATEGY AND SIGNAL
PROCESSING FOR VOLUME TARGETS

Submitted by

Cuong Manh Nguyen

Department of Electrical and Computer Engineering

In partial fulfillment of the requirements

For the Degree of Doctor of Philosophy

Colorado State University

Fort Collins, Colorado

Fall 2013

Doctoral Committee:

Advisor: Chandrasekar V. Chandra

Anura P. Jayasumana

Paul W. Mielke Jr.

Branislav Notaros

Copyright by Cuong Manh Nguyen 2013

All Rights Reserved

ABSTRACT

ELECTRONIC SCAN WEATHER RADAR: SCAN STRATEGY AND SIGNAL PROCESSING FOR VOLUME TARGETS

Following the success of the WSR-88D network, considerable effort has been directed toward searching for options for the next generation of weather radar technology. With its superior capability for rapidly scanning the atmosphere, electronically scanned phased array radar (PAR) is a potential candidate. A network of such radars has been recommended for consideration by the National Academies Committee on Weather Radar Technology beyond NEXRAD. While conventional weather radar uses a rotating parabolic antenna to form and direct the beam, a phased array radar superimposes outputs from an array of many similar radiating elements to yield a beam that is scanned electronically. An adaptive scan strategy and advanced signal designs and processing concepts are developed in this work to use PAR effectively for weather observation.

An adaptive scan strategy for weather targets is developed based on the space-time variability of the storm under observation. Quickly evolving regions are scanned more often and spatial sampling resolution is matched to spatial scale. A model that includes the interaction between space and time is used to extract spatial and temporal scales of the medium and to define scanning regions. The temporal scale constrains the radar revisit time while the measurement accuracy controls the dwell time. These conditions are employed in a task scheduler that works on a ray-by-ray basis and is designed to balance task priority and radar resources. The scheduler algorithm also includes an optimization procedure for minimizing radar scan time.

In this research, a signal model for polarimetric phased array weather radar (PAWR) is presented and analyzed. The electronic scan mechanism creates a complex coupling of horizontal and vertical polarizations that produce the bias in the polarimetric variables retrieval. Methods for bias correction for simultaneous and alternating transmission modes are proposed. It is shown that the bias can be effectively removed; however, data quality degradation occurs at far off boresight directions. The effective range for the bias correction methods is suggested by using radar simulation.

The pulsing scheme used in PAWR requires a new ground clutter filtering method. The filter is designed to work with a signal covariance matrix in the time domain. The matrix size is set to match the data block size. The filter's design helps overcome limitations of spectral filtering methods and make efficient use of reducing ground clutter width in PAWR. Therefore, it works on modes with few samples. Additionally, the filter can be directly extended for staggered PRT waveforms. Filter implementation for polarimetric retrieval is also successfully developed and tested for simultaneous and alternating staggered PRT. The performance of these methods is discussed in detail.

It is important to achieve high sensitivity for PAWR. The use of low-power solid state transmitters to keep costs down requires pulse compression technique. Wide-band pulse compression filters will partly reduce the system sensitivity performance. A system for sensitivity enhancement (SES) for pulse compression weather radar is developed to mitigate this issue. SES uses a dual-waveform transmission scheme and an adaptive pulse compression filter that is based on the self-consistency between signals of the two waveforms. Using SES, the system sensitivity can be improved by 8 to 10 dB.

ACKNOWLEDGEMENTS

I would like to express my profound gratitude to my advisor Dr. V. Chandrasekar for introducing me to radar meteorology, for challenging me with new ideas and for supporting me during my Ph.D studies. I am thankful to Dr. Paul W. Mielke, Dr. Anura P. Jayasumana, Dr. Branislav Notaros for serving as my committee members, for their support and guidance.

I wish to thank Patrick Kennedy and David Brunkow of CSU-CHILL National Weather Radar Facility for their kind help during my graduate program. I also greatly appreciate the support I received from my colleagues at the Radar and Communication Group. Here, I would like to express my sincere thanks to Dmitri Moisseev, Nitin Bharadwaj, Jim George, Evan Ruzanski, Minda Le, Haonan Chen and Joseph Hardin for their friendship and for many interesting discussions on my research work.

I would like to thank my mother, sister and family for their love, support and encouragement while I was far away from home. I thank to my beautiful daughter Anh born during this pursuit who added further inspiration to finish it. Lastly, I am grateful to my wife Hanh for the unconditional love, support, understanding and encouragement during this work.

The results presented in this dissertation were obtained from research supported by the National Science Foundation (CASA ERC and CSU-CHILL program) and NASA (D3R Radar program and PMM program).

DEDICATION

This work is dedicated to my father.

TABLE OF CONTENTS

Abstract	ii
Acknowledgements	iv
Dedication	v
Table of contents.....	vi
List of tables.....	xi
List of figures	xii
1. INTRODUCTION.....	1
1.1 Introduction	1
1.2 Literature review	3
1.2.1 Phased array weather radar	3
1.2.2 Transmission scheme and signal processing.....	3
1.2.3 Scan strategy	4
1.3 Problem statement.....	4
1.4 Objectives of the research.....	4
1.5 Dissertation outline	6
2. BACKGROUND.....	9
2.1 Doppler weather radar	9
2.2 Signal covariance matrix and radar observables.....	11
2.2.1 Doppler spectral moments.....	13
2.2.1.1 Reflectivity factor.....	13
2.2.1.2 Mean Doppler velocity.....	14
2.2.1.3 Doppler spectrum width.....	15
2.2.2 Dual-polarized variables.....	15

2.2.2.1	Differential reflectivity	16
2.2.2.2	Co-polar correlation coefficient	16
2.3	Phased array radar	16
3.	ELECTRONIC SCAN PRINCIPLE FOR PHASED ARRAY WEATHER RADAR	21
3.1	Introduction	21
3.2	Space-time characterization model for precipitation	22
3.2.1	Spatial scales in precipitation systems	22
3.2.1.1	An algorithm for spatial scale estimation	22
3.2.1.2	Performance evaluation.....	26
3.2.2	Data model	30
3.2.3	Model illustration using simulation	36
3.2.4	Model illustration using observed radar data	38
3.3	Radar scanning regions.....	42
3.4	Measurement error model.....	45
3.5	Design of scan strategy for PAWR	50
3.5.1	Adaptive scanning strategy	50
3.5.1.1	Revisit time constraints.....	51
3.5.1.2	Improved adaptive scanning with nowcasting.....	52
3.5.1.3	Azimuthal sampling resolution.....	52
3.5.1.4	Waveform selection.....	53
3.5.2	Scheduler requirements	54
3.5.3	An algorithm for task scheduling in PAWR	55
3.5.4	The scheduler performance evaluation using simulation	58

3.6	Summary.....	62
4.	PARAMETER ESTIMATION FOR POLARIMETRIC PHASED ARRAY WEATHER RADAR.....	65
4.1	Introduction	65
4.2	Problem formulation	66
4.2.1	Element pattern model.....	66
4.2.2	Scattering matrix.....	69
4.2.3	Voltage equation.....	70
4.3	Example of polarimetric PAWR inherent bias.....	72
4.4	Methods for parameter estimation and bias correction.....	74
4.4.1	Simultaneous mode.....	74
4.4.2	Alternating mode	77
4.5	Effect of noise	82
4.6	Evaluation of bias correction method using simulation	87
4.6.1	Signal simulation for polarimetric PAWR	87
4.6.2	Results for simultaneous mode.....	88
4.6.3	Results for alternating mode	91
4.7	Summary.....	94
5.	CLUTTER FILTERING FOR BLOCK PULSING SCHEME	96
5.1	Introduction	96
5.2	Gaussian model adaptive processing – Time domain system.....	98
5.2.1	Signal model	98
5.2.2	Clutter transformation matrix.....	101

5.2.3	Signal interpolation procedure	104
5.3	GMAP-TD filter for staggered PRT	106
5.4	Performance of GMAP-TD using signal simulation	110
5.4.1	Uniform sampling case.....	111
5.4.2	Staggered PRT 2/3 sampling case	115
5.4.3	Application to block sampled data	118
5.5	Test on CSU-CHILL radar data	123
5.6	Summary.....	125
6.	POLARIMETRIC VARIABLES RETRIEVAL WITH CLUTTER SUPPRESSION FOR STAGGERED PRT SEQUENCES	129
6.1	Introduction	129
6.2	Dual-polarized staggered PRT scheme in simultaneous mode	131
6.3	Dual-polarized staggered PRT scheme in alternating mode	132
6.4	GMAP-TD implementation.....	134
6.4.1	Simultaneous mode.....	135
6.4.2	Alternating mode	136
6.5	Method evaluation using signal simulation.....	142
6.5.1	Results for simultaneous mode	143
6.5.2	Results for alternating mode	146
6.6	Test on CSU-CHILL radar data	149
6.7	Summary.....	150
7.	SENSITIVITY ENHANCEMENT SYSTEM FOR PULSE COMPRESSION WEATHER RADAR.....	153

7.1	Introduction	153
7.2	Signal model.....	155
7.3	Sensitivity enhancement system (SES)	157
7.4.1	Sensitivity of pulse compression weather radar	157
7.4.2	Signal covariance matrix.....	160
7.4.3	SES processing.....	161
7.4.4	Doppler compensation.....	162
7.4	SES dual-waveform scheme.....	163
7.4.1	Waveform design procedure	164
7.4.2	Result combination	166
7.5	Method evaluation using simulation	166
7.5.1	Pulse compression weather radar data simulation	166
7.5.2	Minimum ISL filter	167
7.5.3	SES range-sidelobe performance.....	168
7.5.4	SES power measurement accuracy	170
7.5.5	SES Doppler velocity measurement accuracy	171
7.5.6	SES sensitivity gain	172
7.6	Illustration with D3R Ku-Ka system observations	176
7.7	Summary.....	180
8.	SUMMARY AND FUTURE WORK.....	182
8.1	Introduction	182
8.2	Future work	186
	Bibliography.....	187

LIST OF TABLES

Table 3.1: Space-time parameters of scanning regions.....	58
Table 3.2: Radar parameters.	58
Table 4.1: Input for polarimetric PAWR signal simulation.....	88
Table 5.1: Simulation input parameters.	111
Table 6.1: Simulation input parameters.	143
Table 7.1: Pulse compression simulation input parameters.....	167

LIST OF FIGURES

Figure 2.1: (a) The incremental voltage $\delta V(t)$ due to scattering from particles located within a shell extending from $(r, r + \Delta r)$. (b) Range-time diagram for a shell of particles between r and $r + \Delta r$ (Bringi and Chandrasekar 2001)..... 10

Figure 2.2: Illustrating the (continuous) range-time axis (τ) and the (discrete) sample-time axis (t_s). The pulse-repetition time (PRT) is T_s (Bringi and Chandrasekar 2001)..... 11

Figure 2.3: Linear array with N elements uniformly spaced by s (Skolnik 2008). 17

Figure 2.4: Array factor with 10 elements (Skolnik 2008). 18

Figure 2.5: Example of a 10 element linear array steered to 60 deg; element spacing $s = \lambda / 2$ (Skolnik 2008). 19

Figure 2.6: Diagram model of a planar phase array. 20

Figure 3.1: Example of regions with different spatial scales within a storm..... 23

Figure 3.2: Time and space scales associated with “high-impact” weather phenomena. (Courtesy: “Observing Weather and Climate from the Ground Up: A Nationwide Network of Networks”, the National Academies Press.) 24

Figure 3.3: The checkerboard image. 27

Figure 3.4: Output of the scale estimation algorithm for image in fig. 3.3: (a) The derivative of the correlation coefficients at the first iteration shows a local maximum at scale 10 (pixels); (b) 2D Gaussian filter with scale 10. 28

Figure 3.5: Output of the scale estimation algorithm for image in fig. 3.3: (a) The derivative of the correlation coefficients at the second iteration shows a local maximum at scale 21 (pixels); (b) 2D Gaussian filter with scale 21. 29

Figure 3.6: A synthesized radar reflectivity field for scale estimation study. 31

Figure 3.7: Output of the scale estimation algorithm for the image in fig. 3.6: (a) The derivative of the correlation coefficients at the first iteration shows a local maximum at scale 1.25 (km); (b) 2D Gaussian filter with scale 1.25.	32
Figure 3.8: Output of the scale estimation algorithm for the image in fig. 3.6: (a) The derivative of the correlation coefficients at the second iteration shows a local maximum at scale 2.5 (km); (b) 2D Gaussian filter with scale 2.5.	33
Figure 3.9: Simulated reflectivity factor fields of a tornado.	36
Figure 3.10: Segmentation of the tornado based on its spatial scales: (a) region 1 with major spatial scale of 1.8 km and (b) region 2 with major spatial scale of 0.48 km.	37
Figure 3.11: Correlation functions of regions in the tornado simulated data.	38
Figure 3.12: Storm reflectivity sequences from CASA IP1 radar network on April 26, 2009.	39
Figure 3.13: Estimated motion field from observations in figure 3.12.	40
Figure 3.14: Motion aligned data obtained from the observations in Fig 3.12. All images are aligned with reference to the last one.	40
Figure 3.15: Spatial decomposition for the motion aligned sequence in fig 3.14.	41
Figure 3.16: Correlation functions of the regions in fig. 3.15.	42
Figure 3.17: Radar scanning region scheme.	44
Figure 3.18: Space-time diagram of radar scanning regions.	45
Figure 3.19: Standard deviation of mean power estimate for S-band ($\lambda = 10\text{ cm}$) at PRT=1 ms with various spectrum widths.	46
Figure 3.20: Signal auto-correlation function with various spectrum widths.	47
Figure 3.21: Block pulsing scheme.	47

Figure 3.22: The standard deviation of power estimates as a function of block size and number of independent blocks for S-band radar with spectrum width of 2 ms^{-1} (a) and 4 ms^{-1} (b).....	49
Figure 3.23: Example demonstrating the importance of incorporating nowcasting with scan strategy. Images from the CASA MC&C display on May 17, 2009, comparing coverage obtained by radar nodes steering using previous observations (left) vs adaptive scanning using five-minute nowcasts (right) (Ruzanski et al. 2010).....	53
Figure 3.24: Flowchart of PAWR adaptive scan strategy.....	54
Figure 3.25: Flowchart of the scheduler algorithm.	57
Figure 3.26: Schedule beam positions for the case of block size 1.....	60
Figure 4.1: Sketch of diagram for signal radiating by a pair of cross-dipoles with moments \vec{M}_1 and \vec{M}_2	67
Figure 4.2: Example of inherent bias in Z_{dr} estimates in simultaneous mode.	73
Figure 4.3: Alternating transmission mode for PAWR.....	78
Figure 4.4: SNR loss in simultaneous mode after bias correction at the horizontal channel (a) and at the vertical channel (b).	85
Figure 4.5: SNR loss in even sequence for alternating mode after bias correction at the horizontal channel (a) and at the vertical channel (b).	86
Figure 4.6: Bias and standard deviation of spectral moments estimates for polarimetric PAWR in simultaneous mode. The top row is for reflectivity, the middle row is for Doppler velocity, and the bottom one is for spectrum width.....	89
Figure 4.7: Bias and standard deviation of dual-polarization variables estimates for polarimetric PAWR in simultaneous mode. The top row is for differential reflectivity Z_{dr} , the middle row is for copolar correlation coefficient $ \rho_{co} $, and the bottom one is for differential phase Φ_{dp}	90

Figure 4.8: Bias and standard deviation of spectral moments estimates for polarimetric PAWR in alternating mode. The top row is for reflectivity, the middle row is for Doppler velocity, and the bottom one is for spectrum width. 92

Figure 4.9: Bias and standard deviation of dual-polarization variables estimates for polarimetric PAWR in simultaneous mode. The first row is for differential reflectivity Z_{dr} , the middle row is for copolar correlation coefficient $|\rho_{co}|$, and the bottom one is for differential phase Φ_{dp} 93

Figure 5.1: Power response of filter matrix \mathbf{A} for the uniform sampling case with clutter-to-noise ratio $CNR = 50dB$, clutter spectrum width $\sigma_c = 0.3ms^{-1}$ 103

Figure 5.2: Example of signal spectrum before and after applying the filter matrix \mathbf{A} 104

Figure 5.3: The architecture of the GMAP-TD system. 106

Figure 5.4: The staggered PRT transmission scheme. 107

Figure 5.5: (a) The power response of filter matrix \mathbf{A} for staggered PRT 2/3 waveform with $CNR = 60dB$, $\sigma_c = 0.3ms^{-1}$. (b) The power response of modified filter matrix \mathbf{A}_{mod} for the velocity de-aliasing solution. 110

Figure 5.6: Error analysis for GMAP-TD filter and the GMAP filter in case of uniform sampling. Simulated data with $SNR = 10dB$, $CSR = 40dB$, signal spectrum width σ_p of 2 and 4 m/s and number of samples of 64. The left column is for bias and the right column is for standard deviation. Solid lines are for GMAP-TD results and dashed lines for GMAP. 114

Figure 5.7: Same as in fig. 5 but $CSR = 55dB$. In this case, GMAP breaks in velocity and spectrum width estimates. 115

Figure 5.8: A scatter plot for velocity estimates for staggered PRT 2/3 with $CSR = 50dB$, $SNR = 20dB$ and $\sigma_p = 4ms^{-1}$ using GMAP-TD. The maximum unambiguous velocity in this case is $55ms^{-1}$ 117

Figure 5.9: Bias and standard deviation of power, mean velocity and spectrum width estimates for staggered PRT 2/3 using GMAP-TD (solid lines) with $CSR = 50dB$, $SNR = 20dB$, $\sigma = 4ms^{-1}$ and 64 samples. For comparison, pulse pair (PP) estimator's results with the same parameters but without clutter are plotted (dashed lines). 118

Figure 5.10: Standard deviation of power estimate as a function of data block size and number of blocks. CSR is 20 dB and (a) spectrum width $\sigma_p = 2ms^{-1}$; (b) spectrum width $\sigma_p = 4ms^{-1}$...120

Figure 5.11: Same as figure 5.10 but for CSR=40 dB. 121

Figure 5.12: Standard deviation of power estimate at different values of CSR and number of blocks. Block size is 8 and (a) spectrum width $\sigma_p = 2ms^{-1}$; (b) spectrum width $\sigma_p = 4ms^{-1}$. 122

Figure 5.10: PPI plots show performance of GMAP-TD filter and GMAP filter on CSU-CHILL measurements. The first column is for reflectivity, the middle column is for velocity and the third column is for spectrum width. First row is for PP method (no clutter filtering) applied to uniform data set collected at 23:59:20 UTC. The second and third rows are for GMAP and GMAP-TD applied to the same uniform data set. Figures in the last row are GMAP-TD results on staggered PRT 2/3 data collected at 23:58:19 UTC. The unambiguity velocity is $27.5 ms^{-1}$ for uniform case and $55ms^{-1}$ for staggered PRT 2/3. Except for the unfiltered data, others are threshold using $SNR > 3dB$ 127

Figure 5.14: Comparison of reflectivity and radial velocity profiles at azimuths of 120° ((b) and (d)) and 280° ((a) and (c)). Top panels are reflectivity profiles and bottom panels are corresponding velocity profiles. 128

Figure 6.1: Dual-polarized staggered PRT pulsing scheme in simultaneous mode. 131

Figure 6.2: Dual-polarized staggered PRT pulsing scheme in alternating mode. 132

Figure 6.3: The power frequency response of GMAP-TD filter for H channel (a) and V channel (b). 138

Figure 6.4: The power frequency response of GMAP-TD filter with respect to Doppler range $v_a = 55ms^{-1}$ for the case presented in figure 6.3 for H channel (a) and V channel (b). 139

Figure 6.5: The power frequency response of the modified GMAP-TD filter for polarimetric variables retrievals for H channel (a) and for V channel (b). 141

Figure 6.6: The power frequency responses of the modified GMAP-TD filters with respect to the Doppler range $v_a = 55ms^{-1}$ are identical for both channels. 141

Figure 6.7: Biases and standard deviations in the dual-polarization parameters estimates using the GMAP-TD method for staggered PRT sequences in simultaneous mode. Inputs parameters for the simulation program are $CSR = 40 dB, \sigma_p = 1 m s^{-1}$ 145

Figure 6.8: Same as figure 6.7, but for $\sigma_p = 4 m s^{-1}$ 146

Figure 6.9: Biases and standard deviations in the dual-polarization parameter estimates using the GMAP-TD method for staggered PRT sequences in alternating mode. Inputs parameters for the simulation program are $CSR = 40 dB, \sigma_p = 1 m s^{-1}$ 148

Figure 6.10: Same as figure 6.9, but for $\sigma_p = 4 m s^{-1}$ 149

Figure 6.11: PPI plots show performance of GMAP-TD for dual-polarized variable retrieval on CSU-CHILL measurements. Panels in the top row (a) are differential reflectivity (Z_{dr}), co-polar correlation coefficient ($|\rho_{co}|$) and differential phased (Φ_{dp}) before clutter filtering. Panels in the bottom row (b) are the corresponding estimates with GMAP-TD. 152

Figure 7.1: Discrete signal model.....	156
Figure 7.2: Illustrating the shifted reference plane for reflectivity calculation (Bringi and Chandrasekar, 2001).....	158
Figure 7.3: The SES transmission waveform scheme.....	163
Figure 7.4: Simulated input profile (solid black line) and results from different pulse compression filters.....	169
Figure 7.5: A trapezoid-shaped profile with a specific gradient of 40 dB/km. (a) Range profiles of input powers and estimated powers; (b) bias and standard deviation of the power estimates.	171
Figure 7.6: Step-function Doppler velocity profile with a 26 ms^{-1} step. Range profiles of signal power (a) and Doppler velocity (b).	172
Figure 7.7: Cyril radar reflectivity profile at azimuth 330° (lowered by 20 dB for sensitivity analysis). (a) Estimated reflectivity profiles for MF and SES; (b) bias and standard deviation of reflectivity estimates.....	175
Figure 7.8: Same as in fig. 7 but the input reflectivity profile was lowered by 30 dB.	176
Figure 7.9: Waveform scheme for SES experiment on D3R system.	178
Figure 7.10: Sector PPI images of reflectivity (H-polarization) (left column), velocity (middle column), and spectrum width (right column) during a light rain event observed by the D3R system. Data are masked using a threshold of $\text{SNR} > 0 \text{ dB}$. (a) Top row: 3.6 MHz bandwidth medium pulse output processed with a matched filter. (b) Bottom row: Output of the SES system - a 3.6 MHz bandwidth medium pulse processed with an ISL filter as the reference signal for 1 MHz bandwidth long pulse, coded and processed using SES algorithm.....	179

Figure 7.11: Sample profile at azimuth of 279° to show the reflectivity and velocity measurements from SES (red lines) and from second waveform of D3R (blue lines).180

CHAPTER 1

INTRODUCTION

1.1 Introduction

Weather radars, especially Doppler and dual polarization weather radars, have proven to be indispensable tools for many meteorological and hydrological applications. The applications can range from detection and warning of hazards such as severe storms, tornadoes, hail, winds, and flash floods to aviation safety surveillance. To obtain better measurements, weather radars have been developed and upgraded over time. For instance, the upgrade to dual polarization allows weather radars to estimate rainfall more accurately, classifying different types of hydrometeors and efficiently retrieving microphysics parameters of the medium or media. Advanced signal processing techniques such as pulse compression allow building more sensitive weather radar systems. Ongoing research at many laboratories, industries, and in academia are continually searching various innovative options for replacing/upgrading the current systems/technologies. One attractive choice is developing electronically scanned phased array weather radar.

Phased array radars (PAR) have been widely used in the defense sector and recently they have been considered for meteorological application. The advantage of PAR compared to conventional weather radar systems is the capability of electronically steering the beam. Conventional weather radars scan the 3D-volume by rotating the antenna at some pre-defined elevation angles known as volume coverage patterns (VCP) and need an update time of 4 to 6 minutes for a scan in order to provide estimated parameters within the required accuracy. However, fast updates are not always possible with those radar systems due to the inertia of

mechanically rotated antennas. In contrast, PAR can instantly steer the beam to a region of interest. This property of PAR provides faster update time without compromising data quality. Firstly, only precipitation regions will be scanned; regions with no echo will be skipped. Secondly, the electronic beam steering capability of PAR allows scanning and revisiting many regions in a sequence. This increases the number of independent samples within an integration cycle and, therefore, fewer samples are needed to maintain adequate data quality. Short update times are critical for better understanding storm structures as well as forecasting them, especially for fast-evolving systems. For example, Rasmussen et al. (2000) suggested that update times of 20 to 30 seconds are necessary to resolve the evolutionary processes in tornado genesis. Also, it is shown that the lead time for microburst warning can increase from 2.2 to 5.2 minutes by reducing the update time from 3 to 1 minutes (Wolfson and Meuse, 1993).

In addition, with PAR, the regions that evolve faster can be scanned more often. This feature is limited on mechanically scanning radar. Thus, PAR is a better platform for precisely capturing the features of storms system when compared to conventional weather radars.

The benefit of PAR for weather observation is clear. Its capability opens a new era in scan strategy for weather radars while bringing more challenges to both hardware and software. For instance, scan strategies and signal processing techniques for phased array weather radars differ from those of hard-target radars in many aspects. Fundamentally, weather is a volume target consisting of a large number of precipitation particles spreading over a large space and evolving in both spatial and temporal dimensions. Moreover, weather radars do not only detect but also measure the volume target accurately. Each of the above aspects has specific requirements and needs a specific algorithm; they are the foci of this research.

1.2 Literature review

1.2.1 Phased array weather radar

The National Weather Radar Testbed (NWRT) is a phased array weather radar (PAWR) operating in S-band and has been available to research communities since September 2003. The NWRT uses a converted phased array antenna from a U.S. Navy AN/SPY-1A radar and a modified transmitter from a WSR-88D weather radar. The single-aperture antenna is mounted on a pedestal capable of rotating at a maximum rate of 18° per second. Azimuth scans are performed by combining electronic steering beam (within a 90° sector) and moving the pedestal. Elevation scans are achieved using electronic scanning. The radar is designed for use in studying and developing a multimission radar with the capability of performing aircraft tracking, wind profiling, and weather detection at the same time (Zrnic et al. 2007).

1.2.2 Transmission scheme and signal processing

Beam multiplexing (BMX) is proposed to maximize the use of radar resources. First, the radar transmits two consecutive pulses at the same beam location and estimates spectral moments from that pair of samples. Then, while waiting for the scatterers in the resolution volume to reshuffle into an independent state, the radar switches its beam to scan other directions and returns to the original direction after the signal is no longer correlated. Independent samples allow the NWRT to reduce scan time and achieve performance similar to that of WSD-88D radars. Both traditional and advanced signal processing techniques are being implemented and tested for the NWRT. However, ground clutter mitigation in BMX or any other mode with few sample returns cannot be done with current filter solutions.

1.2.3 Scan strategy

The beam agility of phased array radar enables an adaptive scanning plan in which only precipitation regions are observed. A scheduling algorithm is developed to arrange scanning and surveillance tasks without significant delays (Rondinel et al. 2010). Targets are individual storm cells and update times are chosen based on the user's experience. Dynamic evolution parameters of a storm are not automatically extracted and integrated into the scan strategy and therefore, update times are not optimized for fast update.

1.3 Problem statement

The primary objective of a phased array weather radar is to provide the ability to capture more features accurately from the weather system while minimizing the scan time. This research aims to address the unique and specific problems associated with phased array weather radar. In particular, it focuses on the adaptive scan strategy, advanced signal design, and processing algorithms. The question of how to steer the beam of phased array weather radar to the regions of interest to obtain the best measurements must be addressed. A scheme that allows the radar to transmit a few samples at each beam position and revisit as needed will reduce scan time significantly but also creates many challenges in signal design and filtering algorithm.

1.4 Objectives of the research

The following items summarize the objects of this dissertation:

Adaptive scan strategy

- Study governing factors for scanning precipitation
- Develop a method for extracting spatial scale information from radar observations

- Develop a space-time characterization model for the precipitation system
- Study the space-time variability feature of the precipitation system
- Develop a measurement error model for a block pulsing transmission scheme
- Establish requirements for a scheduler for phased array weather radar
- Develop an adaptive scan strategy based on the space-time variability features of the precipitation system
- Develop an algorithm for task scheduling

Signal processing

- Study a signal model for polarimetric phased array weather radar
- Develop a signal simulation for polarimetric phased array weather radar
- Investigate the inherent biases associated with polarimetric phased array weather radar and propose a bias correction method
- Evaluate degradation of polarimetric measurement at off-axis directions
- Develop a new ground clutter filtering algorithm for block sampled data with fewer samples
- Extend the clutter filtering algorithm to non-uniform waveforms
- Extend the clutter filtering algorithm for polarimetric variables retrieval for both uniform and non-uniform waveforms
- Design an adaptive system to improve the system sensitivity for pulse compression weather radar

1.5 Dissertation outline

This dissertation is organized as follows:

In Chapter 2, a short description of the observed signals in dual-polarization weather radar, the transmission modes, and the method of parameter estimation is presented. An overview of phased array weather radar is also provided.

In Chapter 3, the principle of adaptive scan strategy for beam agile phased array weather radar is presented. Important governing factors for scanning precipitation are studied and discussion of their effects on scan strategy is provided. The scan strategy is based on the space-time variability features of the storm. The most challenging task is to characterize the space-time variability feature of a precipitation system. First, a method for extracting spatial scale information from weather observations is developed. Then we propose a space-time model that explicitly involves the interactions between space and time. Using the model, radar observation can be segmented into different scanning regions based on their spatial scale feature. Then, temporal scales associated with these regions are computed. The center of the proposed scan strategy, a task scheduler, is developed based on a time balance concept. The scheduler's constraints and requirements are addressed and an optimization procedure is used to minimize the scan time. To make the scan strategy effective, advanced signal designs such as block pulsing scheme, adaptive waveforms, and other considerations are also introduced. The chapter ends with an example to demonstrate the advantages of beam agile phased array weather radar over conventional weather radar.

In Chapter 4 we analyze a signal model for planar polarimetric phased array weather radar (polarimetric PAWR). The fundamental differences in the measured scattering matrix between electronically scanned polarimetric PAWR and the mechanically scanned weather radar are

presented. It is shown that the coupling effect of horizontal and vertical polarizations, if not removed properly, could result in large biases in the estimates. Based on the model, methods to mitigate these inherent biases and a radar signal simulation for polarimetric PAWR are developed. A study of the effect of noise on polarimetric products quality is also conducted. This is very helpful in the designing of PAWR.

Chapter 5 introduces a new clutter filtering algorithm for the block pulsing scheme employed in PAWR. The new filtering method works with a signal covariance matrix in the time domain. The size of the covariance matrix can be varied; therefore, it can adapt to the block sampled data. In addition, the filter can be directly extended to work with the non-uniform waveforms (e.g., staggered PRT) used in range-velocity ambiguity mitigation problem.

In Chapter 6 we extend the clutter filter algorithm for polarimetric variables retrieval. Algorithm modifications for simultaneous and alternating modes with staggered PRT waveform are made. In simultaneous mode, even with strong ground clutter contamination, results with the filter are as good as in the case of data without clutter. In the alternating mode the complexity of the waveform slightly degrades the estimate's quality in extreme scenarios where the signal width is narrow and overlaps clutter. However, in most cases, statistical errors are acceptable for meteorological applications.

In Chapter 7 we introduce a system for enhancing sensitivity (SES) of pulse compression weather radar. Better sensitivity increases working distance and provides a larger signal-to-noise ratio that helps reduce the errors of estimates. SES overcomes this issue by utilizing a dual-waveform scheme and adaptive pulse compression filter. Waveforms transmission can be made in the frequency domain or the time domain. The adaptive filter is designed based on the self-

consistency between signals of the two waveforms. Analysis shows that, with SES, the system sensitivity can be improved by 8 to 10 dB.

In Chapter 8 the main results of this research are summarized and the major contributions of the dissertation are reviewed. Recommendations for future studies are also given.

CHAPTER 2

BACKGROUND

2.1 Doppler weather radar

In a Doppler radar system, a returned signal from a point target moving at a constant velocity is a scaled replica of the transmitted waveform with time shifted by range-time delay and frequency shifted by the Doppler shift. Volume scatterers such as precipitation are composed of a large number of point targets that have widely different scattering amplitudes and are moving with different velocities relative to the radar. For meteorological targets, the returned signal is the sum of the backscatter from individual hydrometeors extending over a large range. A pulse Doppler radar transmits a pulse train with pulse width T_o and a pulse repetition time (PRT) T_s . All the backscatters between the leading edge and the trailing edge of the transmit pulse return a single-voltage sample at the receiver as seen in fig. 2.1 (Bringi and Chandrasekar 2001). For pulse width T_o , the range resolution is given by

$$\Delta r = \frac{cT_o}{2} \quad (2.1)$$

For a single transmitted pulse the range time is defined as $\tau = 2r/c$, and the received voltage $V_r(t)$ at $t = \tau$ is due to signal scattered back from particles located in the resolution volume at range $c\tau/2$. For a periodic pulse train, the received voltages at the same range-time (τ) are given as $V_r(t = \tau), V_r(t = \tau + T_s), \dots, V_r(t = \tau + nT_s)$ which form a sequence of temporal samples from the same resolution volume. At a given range-time τ , the voltage samples $V_r(t = \tau + mT_s) = V_r(\tau, t_s = mT_s)$ can be observed as regularly spaced samples along a

continuous sample-time axis (t_s) (fig 2.2). Each observation of the received signal is one realization of the underlying complex stochastic process. The fluctuations of the received voltage in sample-time are determined by the time-varying properties of the particles located in the resolution volume.

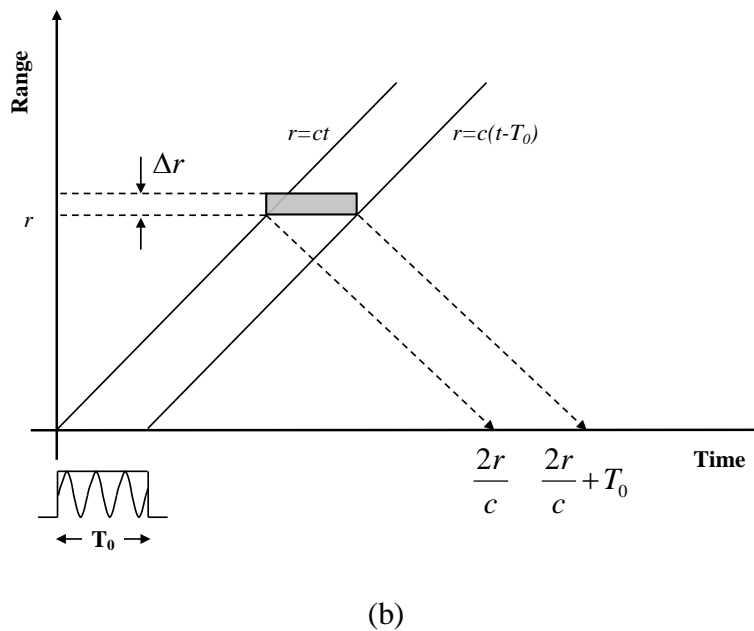
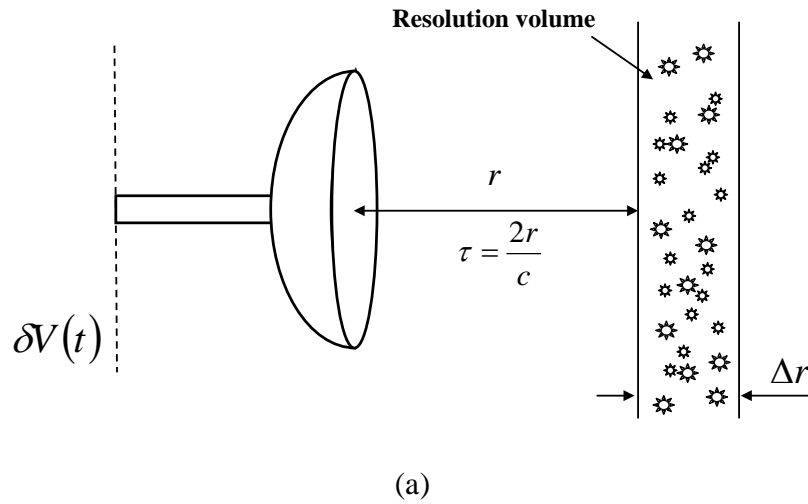


Figure 2.1: (a) The incremental voltage $\delta V(t)$ due to scattering from particles located within a shell extending from $(r, r + \Delta r)$. (b) Range-time diagram for a shell of particles between r and $r + \Delta r$ (Bringi and Chandrasekar 2001).

intrinsic backscattering properties of the hydrometeors relative to the two polarization states enable the measurement of characteristics such as size, shape, and spatial orientation of the precipitation particles in the radar resolution volume. These characteristics are described in terms of the backscattering matrix \mathbf{S}_{BSA} . When a uniform precipitation medium exists between the radar and the particle, the radar equation is given (Bringi and Chandrasekar, 2001)

$$\begin{bmatrix} E_h^r \\ E_v^r \end{bmatrix} = \sqrt{\frac{Z_0 P_t G}{2\pi}} \frac{1}{r^2} [\mathbf{T}] [\mathbf{S}_{\text{BSA}}] [\mathbf{T}] \begin{bmatrix} M_h \\ M_v \end{bmatrix} \quad (2.2)$$

where \mathbf{T} is the transmission matrix of the uniform precipitation medium

$$\mathbf{T} = \begin{bmatrix} T_{hh} & T_{hv} \\ T_{vh} & T_{vv} \end{bmatrix} \quad (2.3)$$

and \mathbf{S}_{BSA} is the back scattering matrix on the back scatter alignment convention

$$\mathbf{S}_{\text{BSA}} = \begin{bmatrix} S_{hh} & S_{hv} \\ S_{vh} & S_{vv} \end{bmatrix} \quad (2.4)$$

M_h and M_v are the transmitter excitation states in the horizontal and vertical ports of a dual-polarized antenna with an antenna gain G , and transmit power P_t . Z_0 is the intrinsic impedance in the empty space. From (2.2) the voltages at the ports of the antenna are derived as

$$\begin{bmatrix} V_h \\ V_v \end{bmatrix} = \frac{\lambda \sqrt{P_t} G}{4\pi r^2} [\mathbf{T}] [\mathbf{S}_{\text{BSA}}] [\mathbf{T}] \begin{bmatrix} M_h \\ M_v \end{bmatrix} \quad (2.5)$$

The transmission matrix is assumed to be diagonal because the cross-coupling of the H and V fields is often negligible,

$$\mathbf{T} = \begin{bmatrix} T_{hh} & 0 \\ 0 & T_{vv} \end{bmatrix} \quad (2.6)$$

Therefore, the combined backscattering and transmission matrix is given by

$$\mathbf{S}'_{\text{BSA}} = [\mathbf{T}][\mathbf{S}_{\text{BSA}}][\mathbf{T}] = \begin{bmatrix} T_{hh}^2 S_{hh} & T_{hh} T_{vv} S_{hv} \\ T_{hh} T_{vv} S_{vh} & T_{vv}^2 S_{vv} \end{bmatrix} = \begin{bmatrix} S'_{hh} & S'_{hv} \\ S'_{vh} & S'_{vv} \end{bmatrix} \quad (2.7)$$

The radar equation in (2.2) now can be written as

$$\begin{bmatrix} V_h \\ V_v \end{bmatrix} = \frac{\lambda \sqrt{P_t G}}{4\pi r^2} \begin{bmatrix} S'_{hh} & S'_{hv} \\ S'_{vh} & S'_{vv} \end{bmatrix} \begin{bmatrix} M_h \\ M_v \end{bmatrix} \quad (2.8)$$

2.2.1 Doppler spectral moments

Let $S(v)$ be the probability density function (pdf) of the radial velocity. If $S(v)$ is a Gaussian pdf with mean \bar{v} and standard deviation σ_p , the sample autocorrelation coefficient (as given by Bringi and Chandrasekar, 2001) is

$$\rho(nT_s) = e^{-j\frac{4\pi}{\lambda}\bar{v}nT_s} \exp\left(-\frac{8\pi^2}{\lambda^2}\sigma_p^2 n^2 T_s^2\right) \quad (2.9)$$

and the corresponding Doppler velocity spectrum is

$$S(v) = \frac{P}{\sigma_p \sqrt{2\pi}} \exp\left(-\frac{(v - \bar{v})^2}{2\sigma_p^2}\right) + \frac{2T_s}{\lambda} \sigma_N^2 \quad (2.10)$$

where P is the power of the received signal and σ_N^2 is the noise power. T_s and λ are the pulse repetition and wavelength, respectively. The first three spectral moments, power, mean velocity, and spectrum width, are very important and have been widely used in meteorological applications.

2.2.1.1 Reflectivity factor

The back scattering cross-section per unit volume (η) (Bringi and Chandrasekar, 2001) is normally referred to as radar reflectivity. It is conventional in radar meteorology to express

$\eta_{hh} = \langle 4\pi |S_{hh}|^2 \rangle$ in terms of the equivalent reflectivity factor which is expressed in mm^6m^{-1} or dBZ in decibel scale,

$$Z_e = \frac{\lambda^4}{\pi^5 |K_w|^2} \eta_{hh} \quad (2.11)$$

where K_w is the dielectric factor of water. The mean received power from a resolution volume at range r_0 is related to the radar reflectivity at range r_0 (Bringi and Chandrasekar, 2001) as

$$\bar{P}(r_0) = \left(\frac{cT_0}{2} \right) \left[\frac{\lambda^2 P_t G_0^2}{(4\pi)^3} \right] \left[\frac{\pi \theta_B \phi_B}{8 \ln 2} \right] \frac{\eta_{hh}(r_0)}{r_0^2} \quad (2.12)$$

From equations (2.8) and (2.9), a relationship between the equivalent reflectivity Z_e at range r_0 and the mean received power is derived

$$Z_e = C + \bar{P}(r_0) + 20 \log(r_0) \quad (2.13)$$

where C is the radar constant expressed in dB , r_0 is the range in km , and \bar{P} is expressed in dBm .

$$C = 10 \log_{10} \left[\frac{10^{21}}{\pi^5 |K_w|^2} \left(\frac{2}{cT_0} \right) \left[\frac{(4\pi)^3}{\lambda^2 P_t G_0^2} \right] \left[\frac{8 \ln 2}{\pi \theta_B \phi_B} \right] \lambda^2 \right] \quad (2.14)$$

All the parameters in eq. (2.11) are expressed in SI units.

2.2.1.2 Mean Doppler velocity

In addition to the received power, Doppler weather radars have the ability to measure the relative phase shift between the signal from the scatterers in the resolution volume and the transmitted signal. This phase shift is used to estimate the mean radial velocity of the particles in the resolution volume. The mean Doppler velocity \bar{v} within the resolution volume can be obtained from lag-1 of the auto-correlation function estimate,

$$\hat{R}[n] = \frac{1}{N} \sum_{k=1}^{N-n} V_{hh}(k+n) V_{hh}^*(k) \quad (2.15)$$

$$\hat{v} = \frac{\lambda}{4\pi T_s} \arg(\hat{R}[1]) \quad (2.16)$$

2.2.1.3 Doppler spectrum width

The radar resolution volume consists of a large number of hydrometeors with widely varying velocities. Consequently, the received signal spectrum has Doppler spectral components spreading around the mean Doppler velocity. The spectrum width σ_v indicates the turbulence of the medium within the resolution volume; also, it presents the reflectivity-weighted velocity dispersion. If the signal spectrum is approximated Gaussian, the Doppler spectrum width can be estimated from multiple lags of lag 1 of the auto-correlation function. For example, if lag-0 and lag-1 are used,

$$\hat{\sigma}_v = \frac{\lambda}{2\pi T_s \sqrt{2}} \left[\ln \left| \frac{R(0)}{R(1)} \right| \right]^{1/2} \quad (2.17)$$

2.2.2 Dual-polarized variables

The back scattering properties of the hydrometeors change with the incident polarization state due to the shape and orientation of these particles. Polarimetric Doppler weather radar offers dual-polarization variables in addition to the spectral moments. Polarimetric variables provide additional information about the hydrometeors and are used to improve measurements of precipitation.

2.2.2.1 Differential reflectivity

Differential reflectivity, or the reflectivity depolarization ratio in dB unit (Z_{dr}), is defined as

$$Z_{dr} = 10 \log_{10} \left[\frac{\langle S_{hh} \rangle^2}{\langle S_{vv} \rangle^2} \right] \quad (2.18)$$

It is estimated from the co-polar mean power estimates,

$$\hat{Z}_{dr} = 10 \log_{10} \left[\frac{\hat{P}_h}{\hat{P}_v} \right] \quad (2.19)$$

Z_{dr} measures the mean particles shape. For example, large rain drops are ablate in shape and result in positive Z_{dr} , while for light rain or hail, Z_{dr} is close to zero.

2.2.2.2 Co-polar correlation coefficient

The estimate of the co-polar correlation coefficient is given in (2.12) with $n = 0$.

$$\hat{R}_{vvhh}[0] = \frac{1}{N} \sum_{k=1}^N V_{hh}(k) V_{hh}^*(k) \quad (2.20)$$

Estimates of the magnitude and phase of the co-polar correlation coefficient are given by

$$|\rho_{co}| = \frac{|\hat{R}_{vvhh}[0]|}{\sqrt{\hat{P}_h} \sqrt{\hat{P}_v}} \quad (2.21)$$

$$\Psi_{dp} = \Phi_{dp} + \delta = \arg(\hat{R}_{vvhh}[0]) \quad (2.22)$$

2.3 Phased array radar

For a phased array antenna the complete radiation pattern of the antenna is the product of element pattern G_e and array pattern (or array factor) G_a

$$G(\theta, \phi) = G_e(\theta, \phi) G_a(\theta, \phi) \quad (2.23)$$

where (θ, ϕ) defines angular direction in spherical coordinate.

The array factor G_a depends on the array geometry of the array (i.e., distances between elements) and the relative phase between the antenna elements and is independent of the element pattern G_e .

To illustrate how an antenna pattern is formed and steered, we analyze the case of a linear array including N elements (fig. 2.3) that are assumed to be isotropic radiators. If each element is separated by distance s , summing the phase vector contributions from all elements, with element 0 as phase reference, gives the field-intensity pattern (Skolnik 2001) as a function of incident angle (ϕ),

$$|E_a(\phi)| = \left| \sum_{n=0}^{N-1} e^{j(2\pi/\lambda)ns \sin \phi} \right| = \left| \frac{\sin[N\pi(s/\lambda) \sin \phi]}{\sin[\pi(s/\lambda) \sin \phi]} \right| \quad (2.24)$$

An example of an array factor with $N = 10$ elements is given in fig. 2.4.

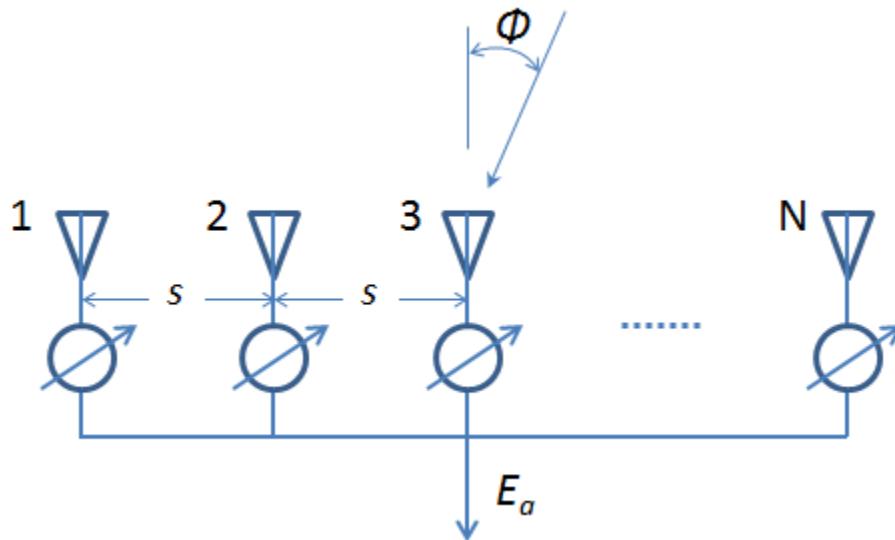


Figure 2.3: Linear array with N elements uniformly spaced by s .

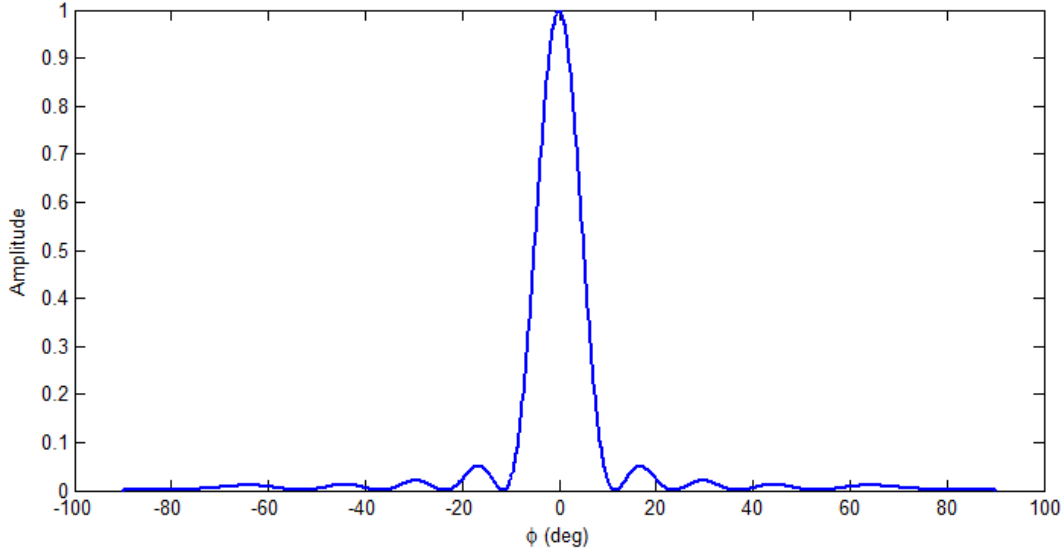


Figure 2.4: Array factor with 10 elements and $s = \lambda / 2$.

The normalized radiation pattern of an array of isotropic elements is

$$G_a(\phi) = \frac{|E_a(\phi)|^2}{N^2} = \frac{\sin^2[N\pi(s/\lambda)\sin\phi]}{N^2 \sin^2[\pi(s/\lambda)\sin\phi]} \quad (2.25)$$

When the radiating elements are not isotropic, the antenna radiation pattern has to be modified by the element pattern $G_e(\phi)$ so that

$$G(\phi) = G_e(\phi)G_a(\phi) = G_e(\phi) \frac{\sin^2[N\pi(s/\lambda)\sin\phi]}{N^2 \sin^2[\pi(s/\lambda)\sin\phi]} \quad (2.26)$$

The pattern of the phased array can be steered to an angle ϕ_0 by changing the phases of elements so that the differential phase between adjacent elements is $2\pi(s/\lambda)\sin\phi_0$. Then the pattern is

$$G(\phi) = G_e(\phi) \frac{\sin^2[N\pi(s/\lambda)(\sin\phi - \sin\phi_0)]}{N^2 \sin^2[\pi(s/\lambda)(\sin\phi - \sin\phi_0)]} \quad (2.27)$$

This pattern has a peak at angle ϕ_0 . Note that the element pattern ($G_e(\phi)$) is not steered. An example of a complete antenna pattern is shown in fig. 2.5.

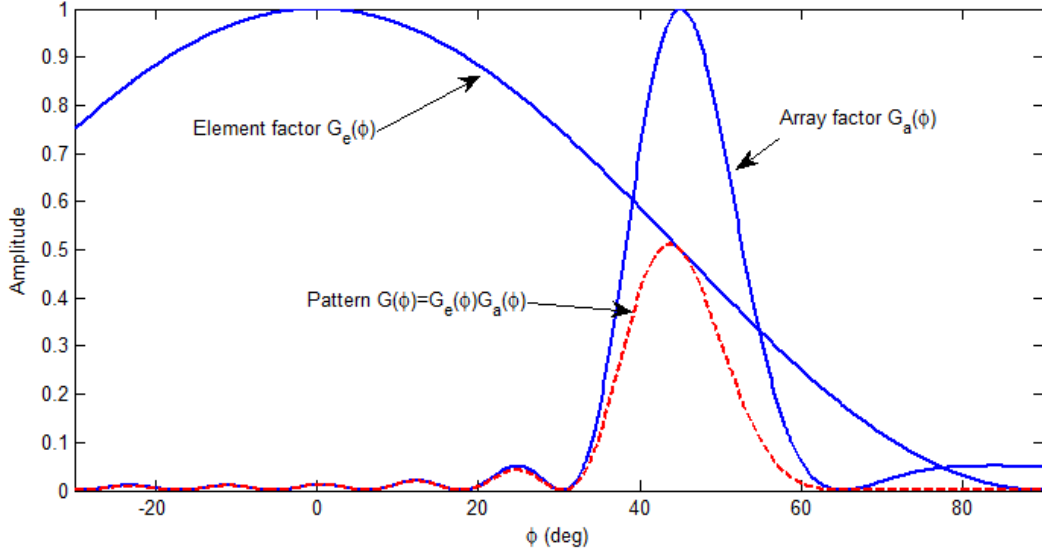


Figure 2.5: Example of a 10 element linear array steered to 45 deg; element spacing $s = \lambda/2$.

In addition, at azimuth angle ϕ_0 , the beamwidth increase by a factor of $1/\cos\phi_0$ and the antenna gain changes as

$$G_{ant}(\phi_0) = G_0 \cos\phi_0 \quad (2.28)$$

where G_0 is the antenna gain at broadside ($\phi_0 = 0$).

Generally, for a planar array ($M \times N$) (fig. 2.6) where the beam can be steered in two dimensions (θ, ϕ) , a radiation pattern is expressed by,

$$G(\theta, \phi) = G_e(\theta, \phi)G_a(\theta, \phi) = G_e(\theta, \phi) \frac{\sin^2[N\pi(s/\lambda)\sin\theta]}{N^2 \sin^2[\pi(s/\lambda)\sin\theta]} \frac{\sin^2[M\pi(s/\lambda)\sin\phi]}{M^2 \sin^2[\pi(s/\lambda)\sin\phi]} \quad (2.29)$$

At angle (θ_0, ϕ_0)

$$G(\theta, \phi) = G_e(\theta, \phi) \frac{\sin^2[N\pi(s/\lambda)(\sin\theta - \sin\theta_0)]}{N^2 \sin^2[\pi(s/\lambda)(\sin\theta - \sin\theta_0)]} \frac{\sin^2[M\pi(s/\lambda)(\sin\phi - \sin\phi_0)]}{N^2 \sin^2[\pi(s/\lambda)(\sin\phi - \sin\phi_0)]} \quad (2.30)$$

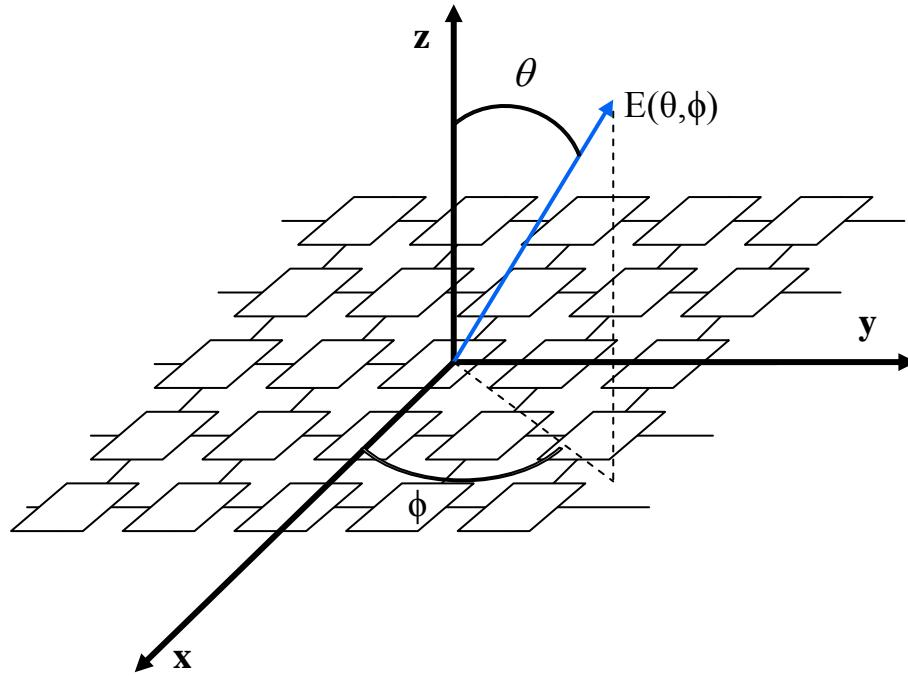


Figure 2.6: Diagram model of a planar phase array.

CHAPTER 3

ELECTRONIC SCAN PRINCIPLE FOR PHASED ARRAY WEATHER RADAR

3.1 Introduction

For observing precipitation, three governing factors must be taken into account: spatial sampling, temporal updates, and accuracy of measurement. It is well known that storms exhibit a wide range of variability in both spatial distribution of intensity and in temporal evolution. For example, a tornado can touch down a highly localized swath at a few hundred meter width over a few minutes, while a hurricane can span a few hundred kilometer range and evolve over multiple days. To characterize the space-time variability features of a storm system, an integrated space-time model is studied that explicitly includes the interaction between space and time. Then, regions within a storm with different spatial and evolution time scales can be determined from the model. The accuracy of precipitation measurements at each spatial location is a function of signal parameters at that position (Bringi and Chandrasekar, 2001). For a given level of accuracy, that relationship provides a constraint on the scanning time of PAWR at each beam location.

In this work, a sequence of tasks including characterizing the space-time model for the precipitation system, estimating the model parameters, and optimizing the scheduler will be described in the context of phased array weather radar. The data model and the estimation of spatial scales present in the weather system are described in section 3.2. Section 3.3 will describe a proposed scheme of radar scanning regions for PAWR. A measurement error model for a block pulsing scheme is introduced in section 3.4. Next, in section 3.5, requirements and considerations

for adaptive scan strategy are addressed and discussed. This section also contains a scheduling algorithm for the PAWR, and an example of its implementation with comparison of results to mechanically steered beam weather radar is introduced. Lastly, a summary is provided in section 3.5.

3.2 Space-time characterization model for precipitation

3.2.1 Spatial scales in precipitation systems

It has been observed that a storm system includes regions exhibiting different spatial scales. Figure 3.1 is an example of an RHI measurement collected by CSU-CHILL radar during a thunderstorm event in summer 2008. In the convective region composed of a cluster of convective cells, small scales dominate over large scales. Those cells may evolve through various stages of their lifecycle during a few hours. In contrast, in the stratiform portion (top right corner), which involves weaker upward motion and less intense precipitation, large scales seem to dominate. Stratiform precipitation growth is slow and may last up to a few days. Figure 3.2 presents a relative scale map for different high-impact weather phenomena. It reveals the relation between space scales and time scales. The figure shows that for precipitation, the temporal scale of a specific region generally increases with its spatial scale.

3.2.1.1 An algorithm for spatial scale estimation

Figure 3.2 suggests that knowing the spatial scales present in the storm system will provide information about its temporal scales. In general, a radar observation includes features over a wide range of spatial scales. According to the Nyquist theorem, the smallest resolvable scale in the observation is equal to twice the grid spacing while the largest scale can be as large as the

size of the storm. An intuitive way of tackling this problem is to consider all possible scales. However, it requires considerable extra time in processing and makes the algorithm complex. For the purpose of designing radar scanning regions, we focus on identifying a small set of significant scales that contains most of the spatial information of the storm.

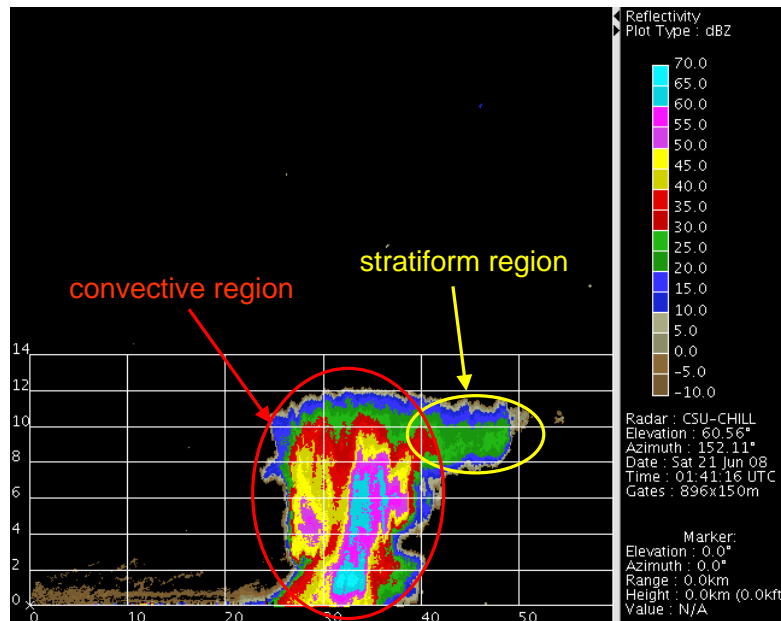


Figure 3.1: Example of regions with different spatial scales within a storm.

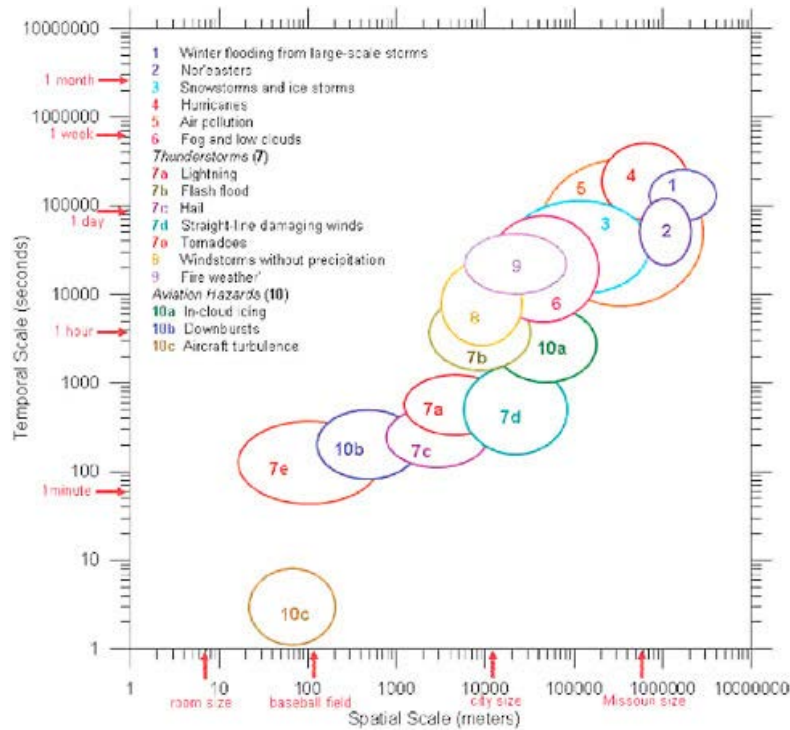


Figure 3.2: Time and space scales associated with “high-impact” weather phenomena. (Courtesy: “Observing Weather and Climate from the Ground Up: A Nationwide Network of Networks”, the National Academies Press.)

When applying a 2D averaging filter to a radar observation, filter size has effects on the scales present in the output field. A filter with a larger area removes more smaller spatial scale features while a filter with a smaller area retains the most scales. Thus, information about the scales can be extracted from filtered fields corresponding to different filter sizes. One way to do that is to compare the similarity measurement between the original field and the filtered fields. The similarity measurement essentially determines the similarity between the features of the original field and the features of the field after filtering. There are several ways to define the similarity measurement such as correlation coefficient, cosine distance, Chord distance, etc. Results from an initial study show that the correlation measurement yielded the best results in terms of accuracy and robustness for radar reflectivity observations. Thus, results presented in

this work will be based on this method. The 2D correlation coefficient between two sampled fields Z_i and Z_j (size of $N_1 \times N_2$) is defined as

$$R(Z_i, Z_j) = \frac{1}{N_1} \frac{1}{N_2} \sum_{l=1}^{N_1} \sum_{k=1}^{N_2} \frac{(Z_i(l, k) - \mu_i)(Z_j(l, k) - \mu_j)}{\sqrt{\sum_{l=1}^{N_1} \sum_{k=1}^{N_2} (Z_i(l, k) - \mu_i)^2 \sum_{l=1}^{N_1} \sum_{k=1}^{N_2} (Z_j(l, k) - \mu_j)^2}} \quad (3.1)$$

$$\mu_{i,j} = \frac{1}{N_1} \frac{1}{N_2} \sum_{l=1}^{N_1} \sum_{k=1}^{N_2} Z_{i,j}(l, k)$$

And the similarity measurement based on correlation is given by

$$\delta(Z_i, Z_j) = 1 - R(Z_i, Z_j) \quad (3.2)$$

The correlation coefficient is inversely proportional to the size of the filter because when increasing the filter size, more scales will be removed. In order to detect and estimate significant scales, we generate the correlation coefficient between the original field and filtered fields as a function of filter sizes. It is noted that the difference between the two correlation coefficients will be at its local maximum when a significant scale is removed from either filtered field. More importantly, the value of the significant scale is located between the sizes of the two filters. If the spacing of the filter sizes is sufficiently small, the significant scale can be estimated. That means the derivative of the correlation coefficient function takes a local maximum at the location of a significant scale. This idea can be expanded to find all the significant spatial scales within a radar observation.

The spatial scale estimation algorithm based on the 2D correlation coefficient is described by the following steps:

1. A vector of spatial scale candidates is pre-set for each radar observation. Normally, we choose the minimum scale in the vector is to be equal to twice the data grid spacing and

the maximum scale is to be equal to the size of the minor axis of the storm. In addition, the scale's step is equal to half of the grid spacing.

2. An averaging filter with filter size equal to the first scale in the vector (step 1) is applied to the original observation and yields the first filtered image. This process is repeated to the other scales in the vector.
3. Compute a sequence of the correlation coefficients between the original field and the filtered fields (correlation coefficient as a function of scale)
4. Compute the derivative of the correlation coefficient function (from step 3).
5. Find the first local maximum and its corresponding spatial scale. This scale is considered as a estimated significant spatial scale of the radar observation.
6. Filter the original observation by a filter with the filter size equal to the significant spatial scale found in step 5 and replace the original observation with this filtered field.
7. Step 2-6 are repeated until no significant scale is found.

3.2.1.2 Performance evaluation

We validate the performance of the scale estimation algorithm developed in the previous section by applying it to several synthesized images. The first image (fig. 3.3) is a tiled checkerboard. This image shows two major scales, the size of the smaller checkerboard squares at 25 pixels and the size of the larger checkerboard squares at 50 pixels. The initial scale vector is chosen as [2:1:50] pixels for this particular image. In this study, Gaussian averaging filters are used for scale estimation procedure. A 2D isotropic Gaussian filter has the form,

$$G_{(x,y)}(u, v; s) = \frac{1}{2\pi s^2} e^{-\left[\frac{(u-x)^2 + (v-y)^2}{2s^2}\right]} \quad (3.3)$$

The width of a 2D Gaussian filter is specified by its standard deviation of the distribution s ; for that reason, s is also considered as the “*scale*” of the filter. Figure 3.4a shows the derivative of the correlation coefficients as a function of spatial scale for the first iteration of the algorithm. We find a local maximum at scale 10. The Gaussian filter with scale $s = 10$ is shown in fig. 3.4b and it corresponds very well with the smaller checkerboard tile.

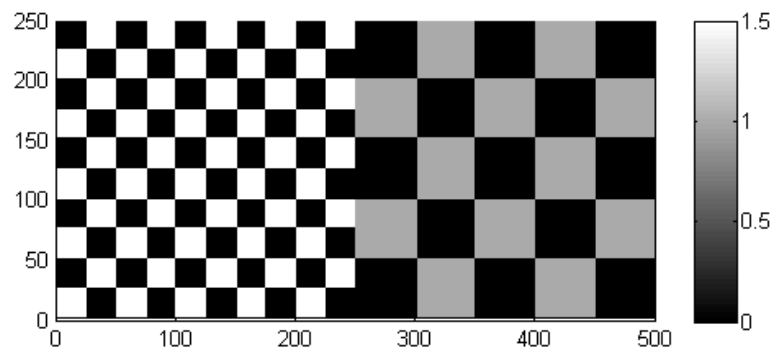


Figure 3.3: The checkerboard image.

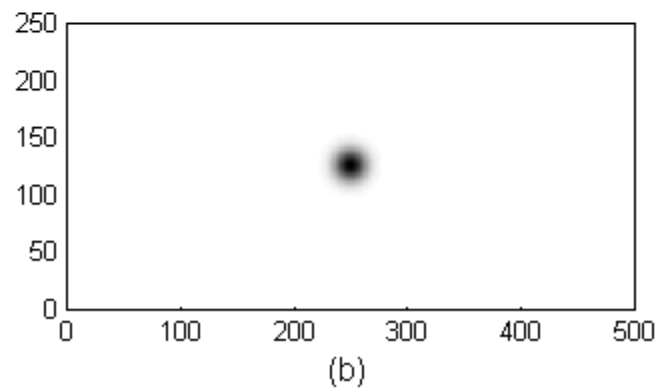
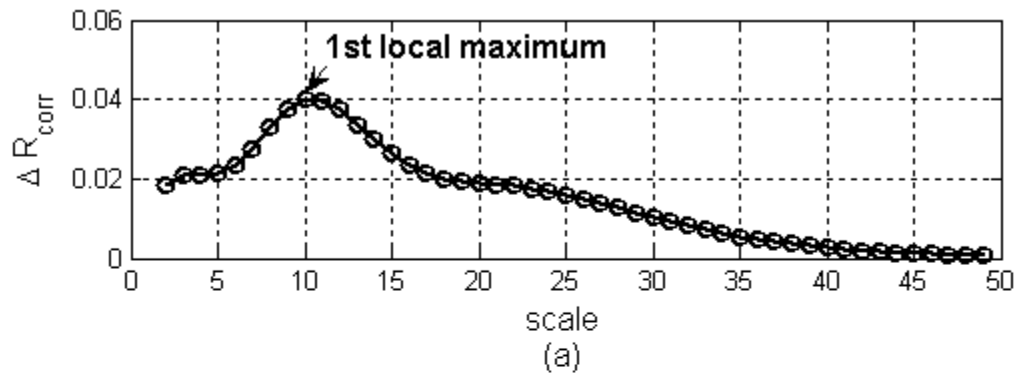


Figure 3.4: Output of the scale estimation algorithm for image in fig. 3.3: (a) The derivative of the correlation coefficients at the first iteration shows a local maximum at scale 10 (pixels); (b) 2D Gaussian filter with scale 10.

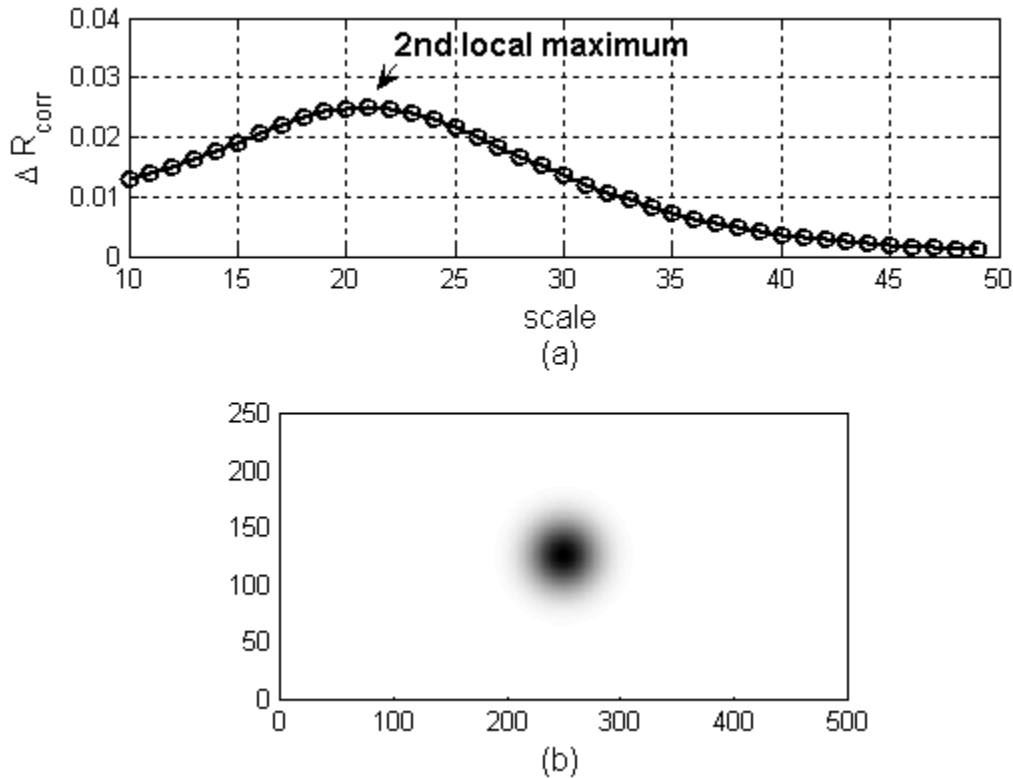


Figure 3.5: Output of the scale estimation algorithm for image in fig. 3.3: (a) The derivative of the correlation coefficients at the second iteration shows a local maximum at scale 21 (pixels); (b) 2D Gaussian filter with scale 21.

The algorithm is continuously processed and one more scale is detected at 19 (fig. 3.5a) in the second iteration. The associated Gaussian filter is shown in fig. 3.5b. This estimated scale agrees with the larger checkerboard square. After this step, no further scale is found.

The second image is a simulated radar reflectivity field of a storm in a region of 50×50 km (fig. 3.6) and the sampling interval is 0.5 km on both the x-axis and y-axis. This is a single simulated field that is used to study the scale estimation algorithm only; therefore, no motion or evolutionary process is associated with it. To generate the data, we start with a $1/f$ spatial noise with a normal error distribution. The noise data are passed through a bank of band pass filters. By varying the bandwidth of the filter we can control the range of the output image's spatial

scales. Filtered images then are spatially weighted and added to produce the synthesized radar reflectivity. In this simulation, we used two scales of 0.75 km and 2.2 km for the band pass filters. In fig. 3.6, the ellipses indicate two regions representing larger and smaller scales. Similar to the previous example, we use the Gaussian averaging filter in the scale estimation algorithm. The algorithm starts with an initial scale vector [0.25:0.25:5] km. In the first iteration, the derivative of the correlation coefficients (fig. 3.7a) shows a local maximum at scale of 1.25 km. Correspondingly, it is the first estimated significant scale. The second scale is found at 2.5 km (fig. 3.8a) and in the following step no further scale is detected. Note that the second estimated scale is very close to its corresponding input whereas the first one is not. This is because even though the centers of band pass filters used to generate the field are set at two pre-defined scales, the resulting image contains a much wider range of scales. In this type of application, the goal is not to find absolutely accurate estimates but to specify the scales that represent important structures of the image. Figure 3.7b and figure 3.8b depict the size of the Gaussian averaging filters corresponding to the estimated scales. Visually, they match well to the structure of the two regions within the ellipses in fig. 3.6.

3.2.2 Data model

Storms generally consist of many features at different spatial scales that are moving and evolving over time. Distinguishing between separating areas of convective and stratiform precipitations or, in general, between quickly and slowly evolving regions within a storm and estimating temporal scales of these regions are very important challenges in designing an efficient scan strategy. To overcome these challenges, a space-time characterization model that includes the interaction between space and time for precipitation system is proposed.

The weather radar observations $Z(x_1, y_1, t_1), Z(x_2, y_2, t_2), \dots$ are sampled from the underlying field $Z(x, y, t)$

$$Z(x, y, t) = X(x, y, t) + e(x, y, t) \quad (3.4)$$

where (x, y) is the location, t is the sampling time, $X(x, y, t)$ is the reflectivity field and $e(x, y, t)$ is the measurement uncertainty.

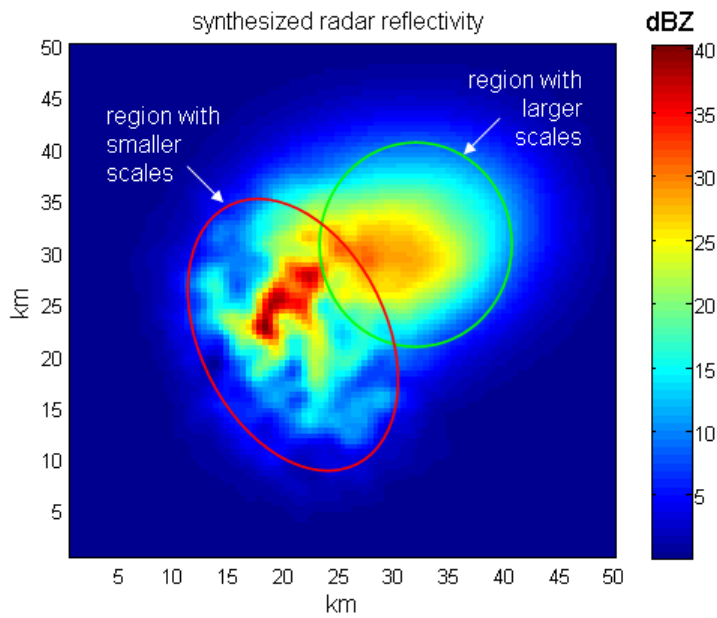


Figure 3.6: A synthesized radar reflectivity field for scale estimation study.

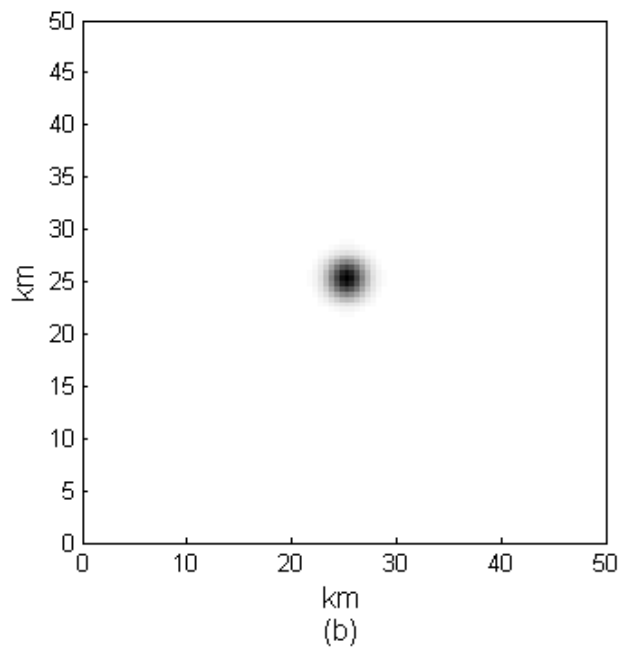
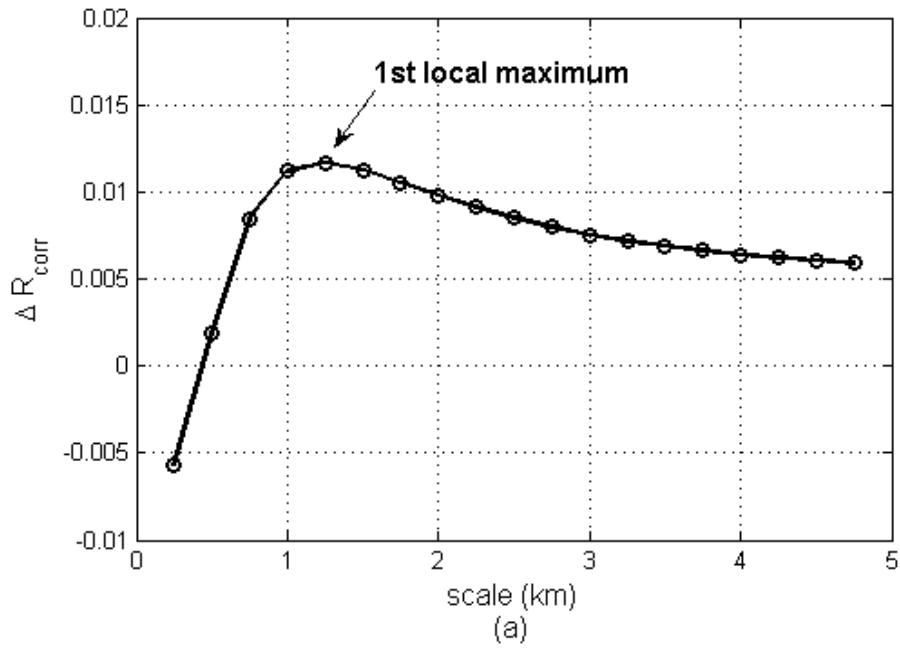


Figure 3.7: Output of the scale estimation algorithm for the image in fig. 3.6: (a) The derivative of the correlation coefficients at the first iteration shows a local maximum at scale 1.25 (km); (b) 2D Gaussian filter with scale 1.25.

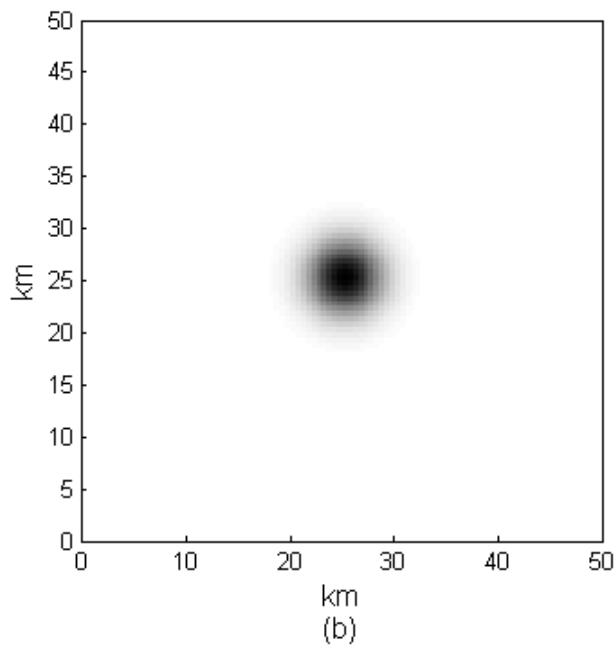
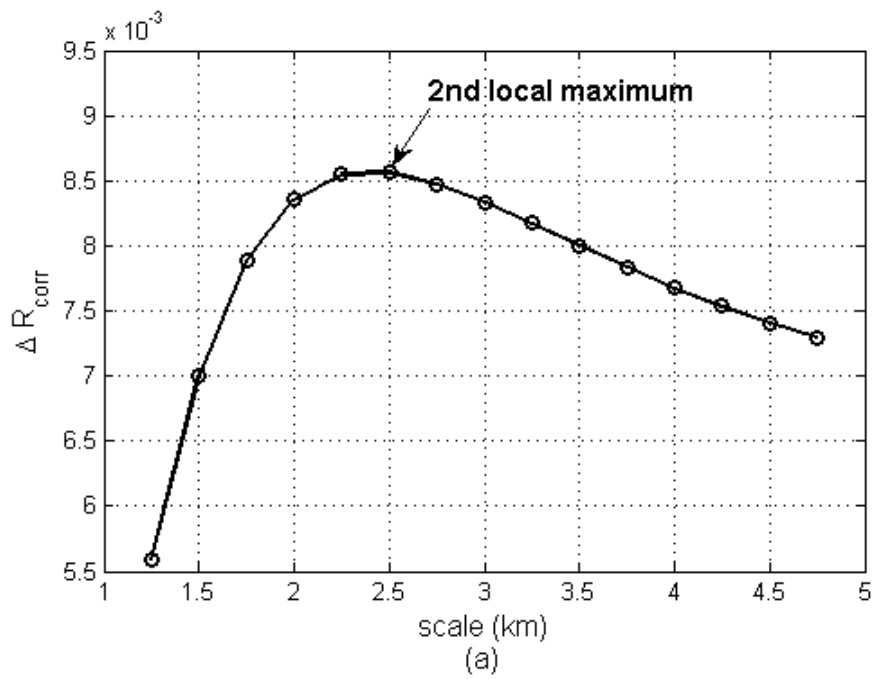


Figure 3.8: Output of the scale estimation algorithm for the image in fig. 3.6: (a) The derivative of the correlation coefficients at the second iteration shows a local maximum at scale 2.5 (km); (b) 2D Gaussian filter with scale 2.5.

A storm system is a complex physical process but it can be assumed to consist of two separate processes: *motion process* and *evolution process*. The motion process can be presented by a general flow system equation,

$$\begin{aligned} \frac{\partial}{\partial t} X(x, y, t) = & -U(x, y) \frac{\partial}{\partial x} X(x, y, t) - V(x, y) \frac{\partial}{\partial y} X(x, y, t) \\ & + S(x, y, t) \end{aligned} \quad (3.5)$$

where $U(x, y)$ is the x-axis motion velocity and $V(x, y)$ is the y-axis motion velocity over the spatial domain. $S(x, y, t)$ presents the growth-decay term.

The motion field (U, V) of the storm system can be estimated by solving the system of equations (3.5) (Xu et al. 2005). Once the motion fields are obtained, they can be removed from the radar observations $X(x, y, t)$ by using an advection algorithm (Rood, 1987) to yield the motion-aligned fields denoted by $Y(x, y, t)$.

In this work, the evolution process is characterized by a Kernel dilation model (Wikle, 2002),

$$Y(x, y; t) = \gamma \int_D k_{(x,y)}(u, v) Y(u, v; t-1) du dv + \eta(x, y; t) \quad (3.6)$$

where D denotes the spatial domain, $k_{(x,y)}(u, v)$ is the Kernel function at spatial location (x, y) ; γ is the evolution control factor, and $\eta(x, y, t)$ is the spatially independent colored/white noise.

The dilation kernel can be approximated by summation of many isotropic Gaussian kernels at different scales s_i ,

$$k_{(x,y)}(u, v) = \sum_i \beta_i G_{(x,y)}(u, v; s_i) \quad (3.7)$$

where β_i is the weight corresponding to isotropic Gaussian kernel $G_{(x,y)}(u, v; s_i)$ (eq. (3.3)).

Assuming there are M spatial scales present in the observations, then equation (3.6) can be expressed as a linear model,

$$\begin{cases} \alpha_1 Y_{1,1} + \alpha_2 Y_{1,2} + \dots + \alpha_M Y_{1,M} = Y_2 \\ \alpha_1 Y_{2,1} + \alpha_2 Y_{2,2} + \dots + \alpha_M Y_{2,M} = Y_3 \\ \vdots \\ \alpha_1 Y_{N,1} + \alpha_2 Y_{N,2} + \dots + \alpha_M Y_{N,M} = Y_N \end{cases} \quad (3.8)$$

$$Y_{n,i} = \int_D G_{(x,y)}(u, v; s_i) Y(u, v; n) du dv$$

$$Y_n = Y(x, y; n)$$

where N is the number of observations, n is the discrete sampling time stamp and $\alpha_i = \gamma\beta_i$.

When the number of observations is no smaller than the number of spatial scales, i.e. $N \geq M$, the equation (3.8) forms an over-determined linear system and can be solved by standard methods such as linear least-squares estimator (Lawson et al. 1987).

It is noticed that the term $Y_{n,i}$ (eq. 3.8) is the convolution between a Gaussian kernel of scale s_i with the observation $Y(u, v; n)$ and for that reason, it only contains features with spatial scales equal to or larger than s_i . From equation (3.8) one can interpret the weight α_i as an evolution indicator of the feature related to scale s_i (hereafter called feature s_i). $\alpha_i > 1$ indicates that the feature s_i grows and $\alpha_i < 1$ indicates that the feature s_i decays. Consequently, segmentation of the radar observations $Y(u, v; n)$ ($n = 1 \dots N$) based on the distribution of α_i will define the quickly and slowly evolving regions and these regions are related to the spatial scale s_i of the observations. The temporal scale of a region is simply calculated as the time when its auto-correlation function (eq. 3.1) drops below 0.9.

3.2.3 Model illustration using simulation

To illustrate the space-time characterization model described in the section above, we apply it to both simulated radar reflectivity sequences and actual radar observations. In this section, radar data from a simulation (Tripoli et al. 2012) demonstrating a tornado development is used. Figure 3.9 shows four consecutive radar reflectivity factor fields at height 1 km above the ground. The spatial sampling resolution is 120 m on both the x and y axes and the temporal spacing between each observation is 30 seconds. The images show that there is a fast development of the small features around the vortex of the tornado while the structures of the near by regions seem to change more slowly.

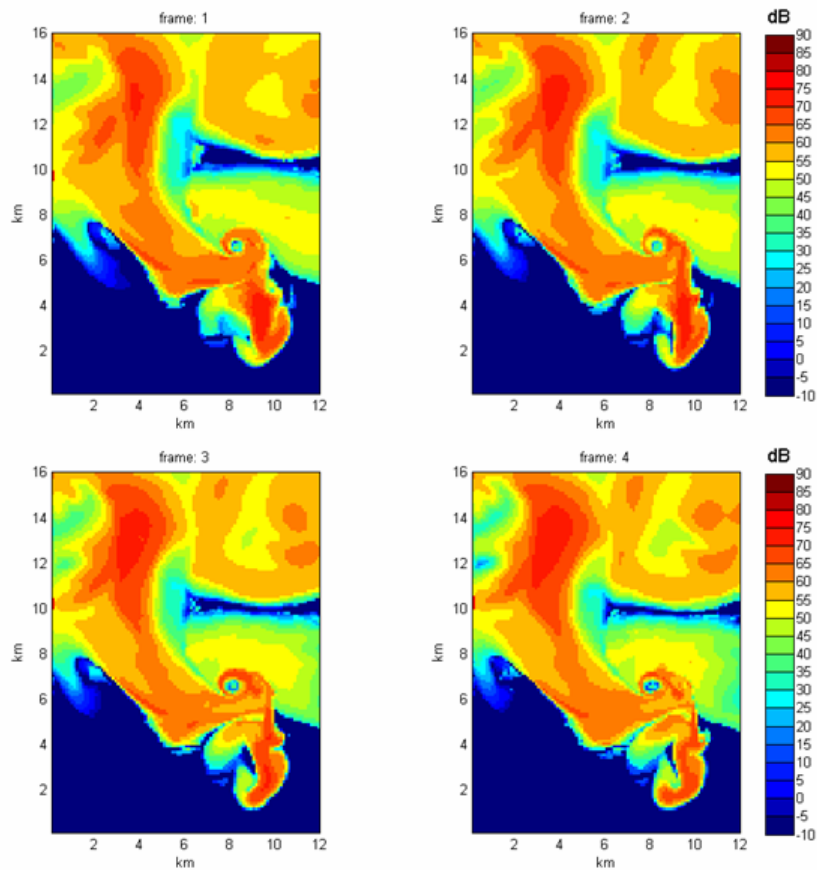


Figure 3.9: Simulated reflectivity factor fields of a tornado.

The scale estimation algorithm (section 3.2.1.1) is applied to the sequence and two significant spatial scales, 0.48 km and 1.8 km, are found. Substituting these scales into equation 3.8 we obtain a system of three linear equations and two unknowns that can be solved by the linear least-squares method. Regions corresponding to the two estimated spatial scales are separated by contours (fig. 3.10). It can be seen that the region of the main updraft and forward flank downdraft near the tornado vortex circulation and the region of rear flank downdraft where the smaller scale features are prominent are successfully localized (fig 3.10b). The evolution times of the two regions are shown in fig. 3.11. It is shown that the region near the tornado vortex (corresponding to the smaller scale, 0.48 km) evolves faster, with a decorrelation time of 0.145 minutes, while the other region develops more slowly with a decorrelation time of 0.269 minutes.

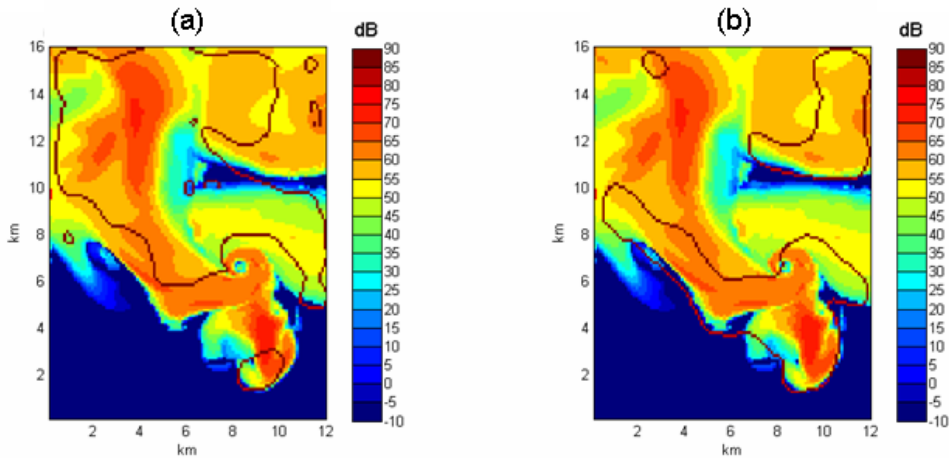


Figure 3.10: Segmentation of the tornado based on its spatial scales: (a) region 1 with major spatial scale of 1.8 km and (b) region 2 with major spatial scale of 0.48 km.

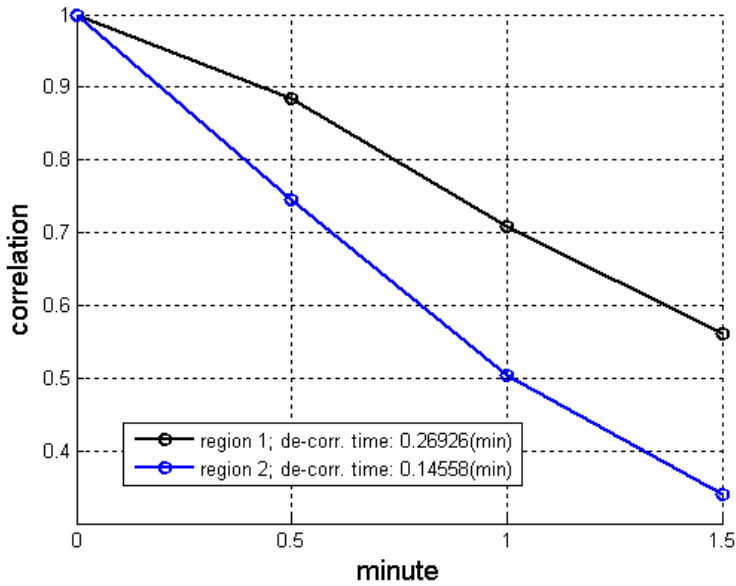


Figure 3.11: Correlation functions of regions in the tornado simulated data.

3.2.4 Model illustration using observed radar data

To further illustrate the space-time characterization model, we have applied it to a set of observed radar reflectivities. The reflectivity data were collected and merged from four radars in the CASA IP1 network. The four radars of CASA IP1 are located at Chickasha (KSAO), Cyril (KCYR), Lawton (KLEWE) and Rush Springs (KRSP), Oklahoma. These are X-band radars, each with a beamwidth of 1.8° and a scanning range of 30 km, so they are able to provide high spatial and temporal resolution data. The composite data at the height of 1 km above the ground are used for this study. The data were re-sampled in a 2D region of 140 x 140 km with a spatial resolution of 0.5 km on both the x-axis and the y-axis. The storm occurred on April 26, 2009, and spanned approximately 70 minutes. The temporal resolution is 1 minute; therefore, we have about 70 successive observations in total. The model is applied to each of nine consecutive observations that span 9 minutes. An example of the experimental data set is shown in fig. 3.12.

The reflectivity sequences indicate a storm motion in a north east direction. To apply the characterization model to the data, we need to remove the motion trend (section 3.2.2). A method similar to the DART algorithm (Gang, 2005) is implemented to estimate the motion field from this temporal sequence. The result is shown in fig 3.13. It is assumed that within a short time period, the motion at each observation time is the same. Using the estimated motion field, the image at time “ t ” is extrapolated to time “ $t+I$ ” and the result is spatially aligned with the measurement at time “ $t+I$ ”. In general, we can align all the radar precipitation fields with reference to a certain temporal point. Figure 3.14 show an example of a sequence of nine radar reflectivity images where all images are aligned with reference to the last image.

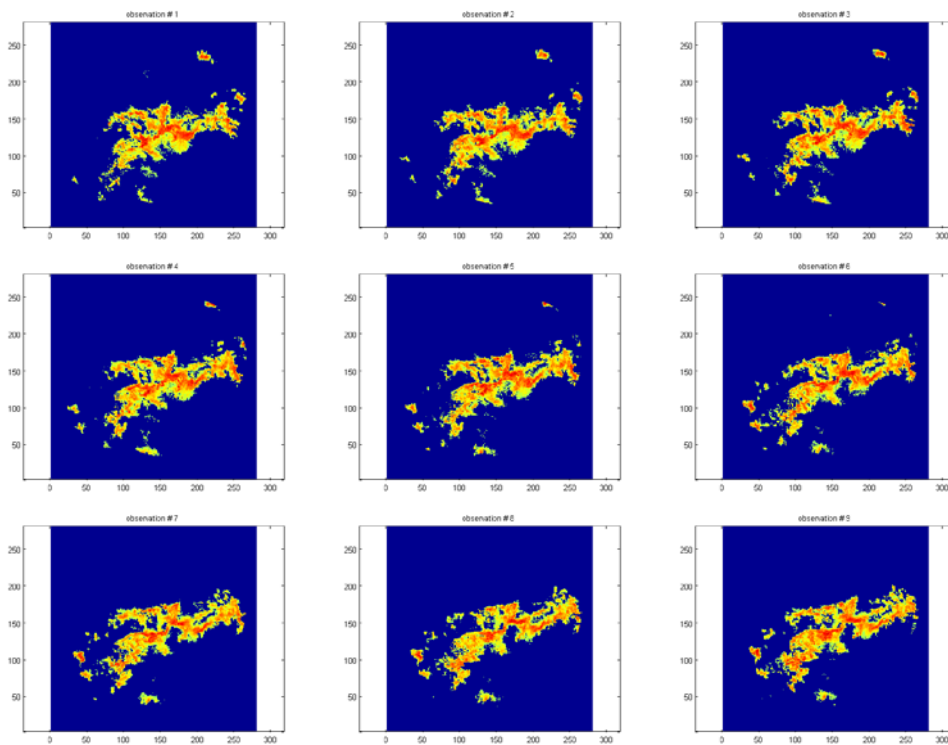


Figure 3.12: Storm reflectivity sequences from CASA IP1 radar network on April 26, 2009.

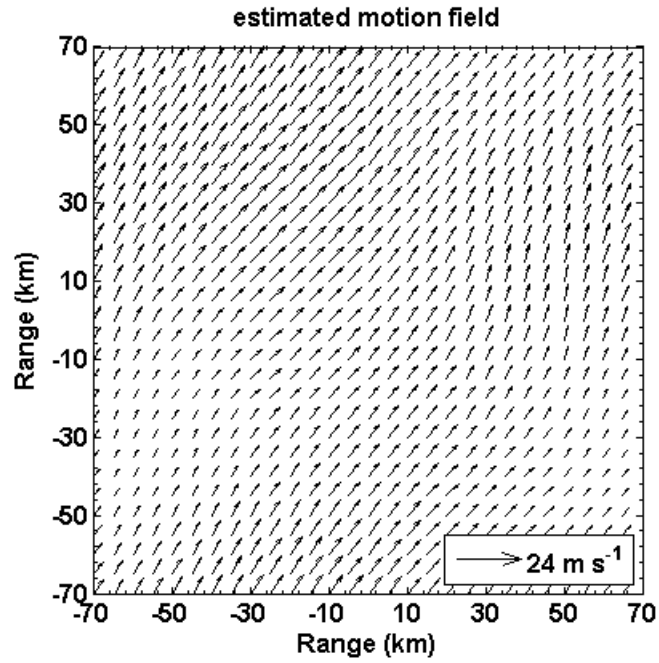


Figure 3.13: Estimated motion field from observations in figure 3.12.

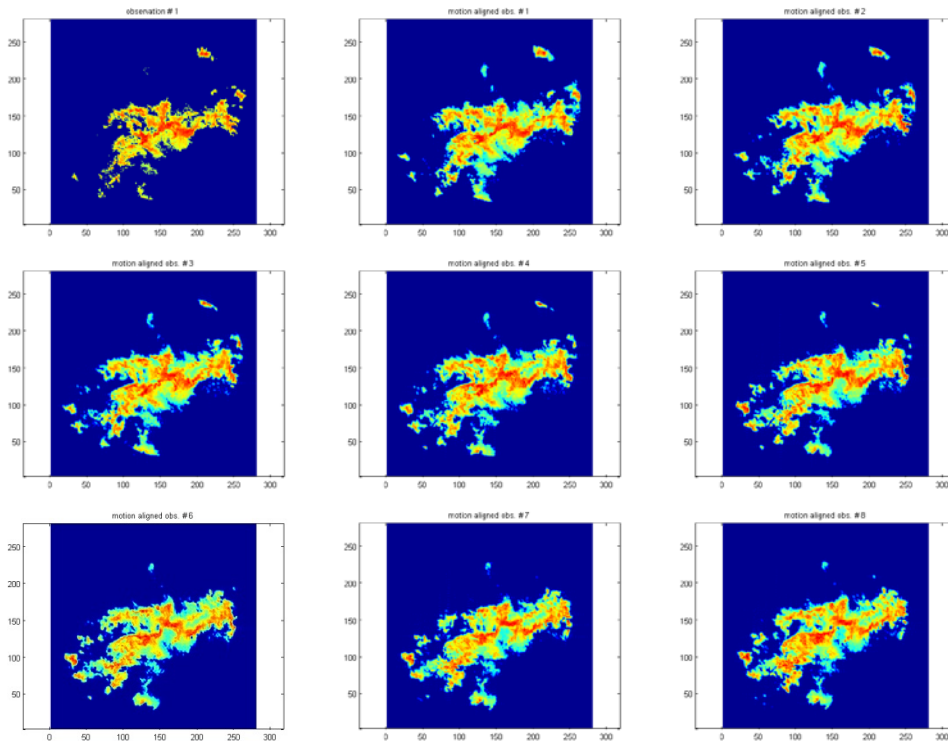


Figure 3.14: Motion aligned data obtained from the observations in fig. 3.12. All images are aligned with reference to the last one.

Applying the scale estimation algorithm to the aligned sequence, we estimate two significant spatial scales, 1.27 km and 2.52 km, and feed them into the space-time characterization model. Then the storm is segmented into different regions as shown in fig. 3.15. It can be seen that the regions corresponding to the smaller scale are mostly located at the front edge of the storm. The evolution time associated with each region in fig. 3.15 is depicted in fig. 3.16. De-correlation time for the smaller-scale region is 0.23 minutes and for the larger-scale region is 0.45 minutes. This result is consistent with our hypothesis of the space-time variability of weather systems where small-scale features evolve more quickly than large-scale features.

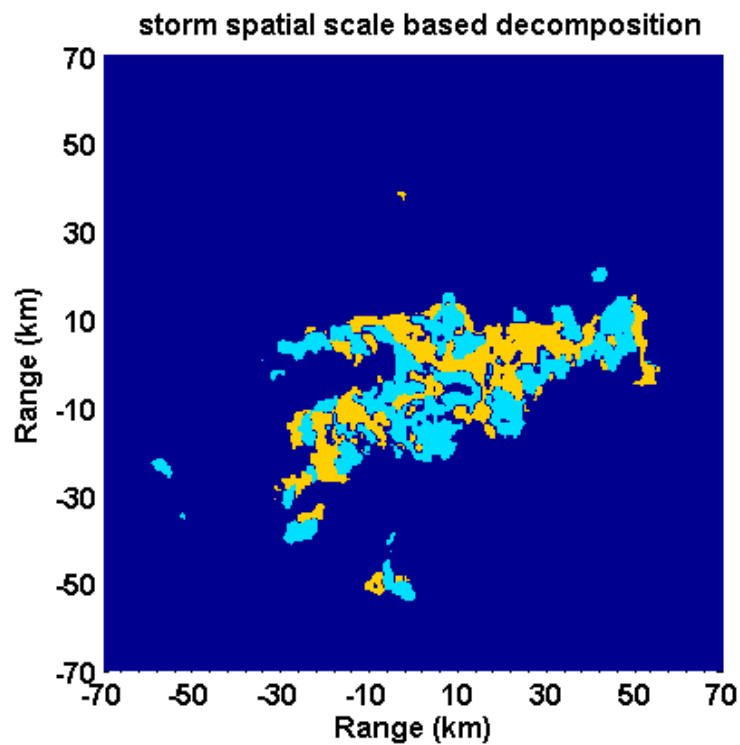


Figure 3.15: Spatial decomposition for the motion aligned sequence in fig. 3.14.

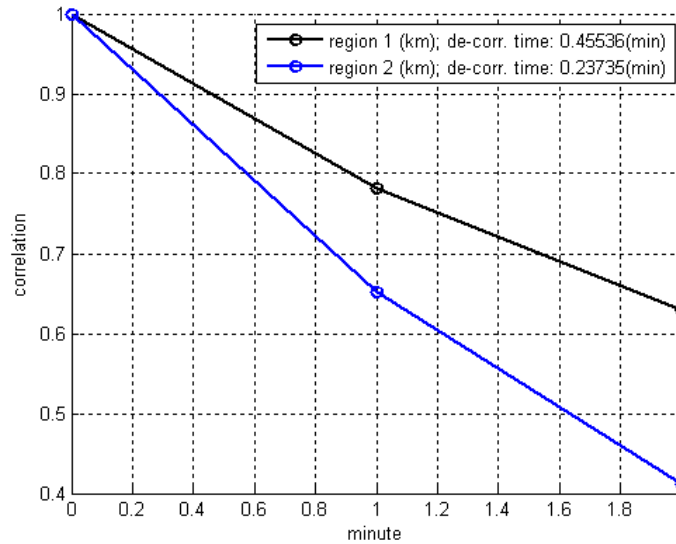


Figure 3.16: Correlation functions of the regions in fig. 3.15.

3.3 Radar scanning regions

The space-time characterization model provides a framework for segmenting a storm into different areas based on its space-time variability features. Each area is represented by a unique spatial and temporal scale. At this point, the model is only developed for 2D data. In practice, PAWR is designed to scan the precipitation volume in both azimuth and elevation dimensions. An adaptive scan strategy should be optimized for both dimensions. It requires the model be modified to work with 3D data, and that is beyond the scope of the present work. We therefore simplify the task by optimizing the scan strategy for each elevation angle. The outputs of the adaptive scheduler will be a sequence of azimuth angles where the radar beam will be located to obtain optimal measurements.

Without the loss of generality, only a single-aperture PAWR is considered and we assume that the radar observation is limited to a 120° sector. The radar scanning region scheme within a storm varies constantly due to a storm's evolution over time and it can be also very different

between storms but in general, it can be grouped into three categories: separated, partially overlapped and completely overlapped. In the first case, where scanning regions are separated (fig. 3.17a), no further processing is required before information is fed to the scheduler. A case of partial overlapping is shown in fig. 3.17b. The azimuthal boundaries of the overlapping region are indicated by dashed lines. The spatial scale and temporal scale of the overlapping region is defined as $\min(s_1, s_2)$ and $\min(\tau_1, \tau_2)$ where (s_i, τ_i) are denoted for spatial and temporal scales of region i^{th} , respectively. If the spatial and temporal scales of the overlapping region are different from that of either existing region, then it is treated as a new scanning region. A similar approach is used for the case of the completely overlapped category (fig. 3.17c). If the space-time scales of the smaller region are equal to or larger than that of the larger region (region 1), then we do not care about the smaller region and it can be removed from the scheme. Otherwise, it creates a new scanning region and the larger region is split into two separate regions (region 1a and region 1b) with the same space-time parameters.

Once all the scanning regions are specified, their space-time diagram can be generated. In general, scanning regions may begin at different time stamps and have different evolution times. Figure 3.18 depicts this idea. Knowing the space-time diagram helps the radar scheduler optimize the scan with the goal of accurately capturing more features from the storm.

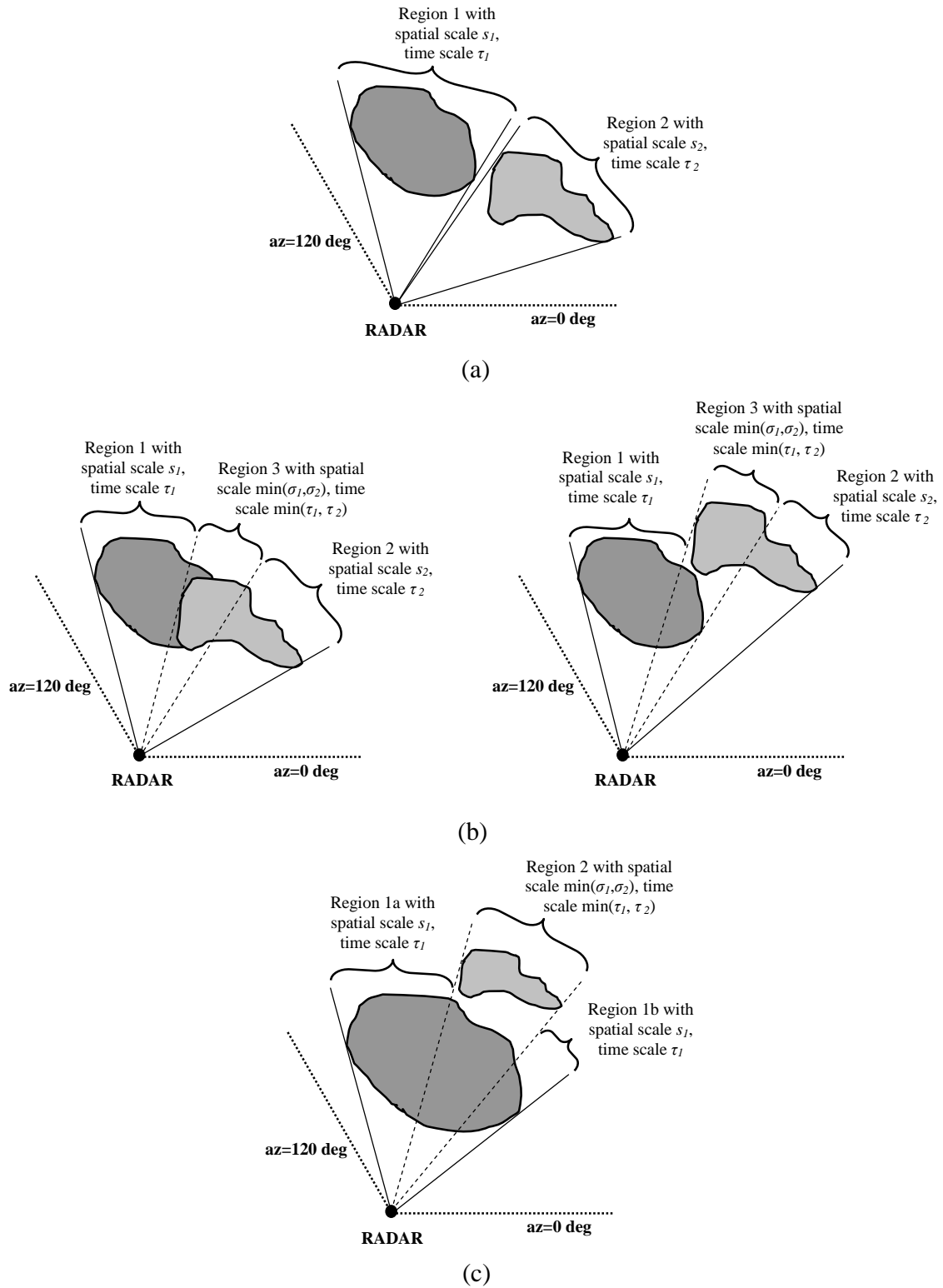


Figure 3.17: Radar scanning region scheme.

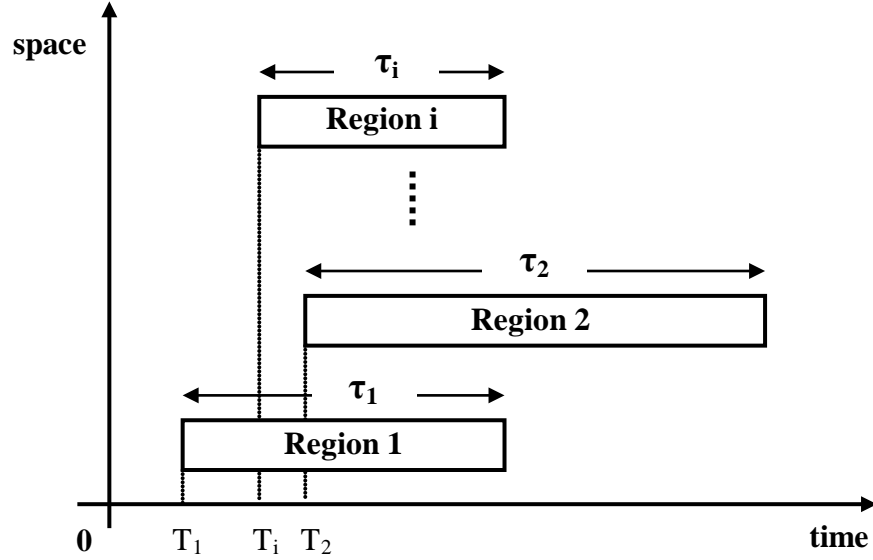


Figure 3.18: Space-time diagram of radar scanning regions.

3.4 Measurement error model

In a conventional weather radar system, a number of pulses is transmitted every pulse repetition time (PRT) and signal parameters are estimated from a sequence of uniformly spaced samples. For the autocovariance method (Bringi and Chandrasekar, 2001), signal power is estimated as the mean of instantaneous power samples. The number of samples determines the accuracy of measurement. In the ideal case where the samples are independent, the standard deviation of power estimate is computed as

$$std[\hat{P}] = 10 \log_{10} \left(1 + \frac{1}{\sqrt{m}} \right) \quad (3.9)$$

where m is the number of samples. For example, we only need $m = 15$ independent samples to achieve $std[\hat{P}] = 0.99$ dB. However, if the precipitation signals are correlated, a larger number of samples is required to obtain the same statistical variance. Figure 3.19 shows the standard

deviation of signal power estimates as a function of number of samples with various spectrum widths. For a given number of samples, the variance of power estimates increases with decreasing spectrum width. This is because the signal de-correlation time is larger at smaller spectrum widths (fig. 3.20) and, therefore, the equivalent number of independent samples is smaller. In this work, the decorrelation time of the medium is defined as the time for the signal autocorrelation function to fall to 0.01:

$$T_d = \frac{2.146\lambda}{2\sqrt{2\pi}\sigma_p} \quad (3.10)$$

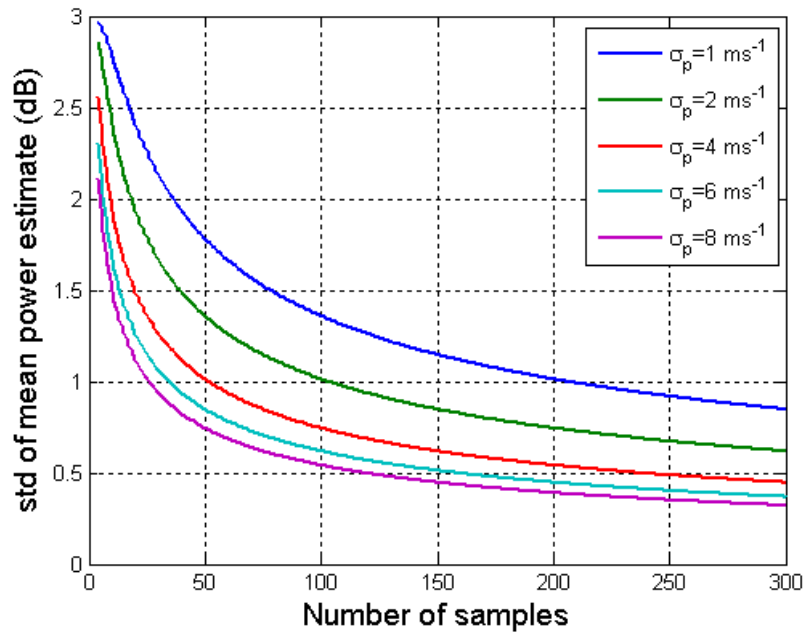


Figure 3.19: Standard deviation of mean power estimate for S-band ($\lambda = 10 \text{ cm}$) at PRT=1 ms with various spectrum widths.

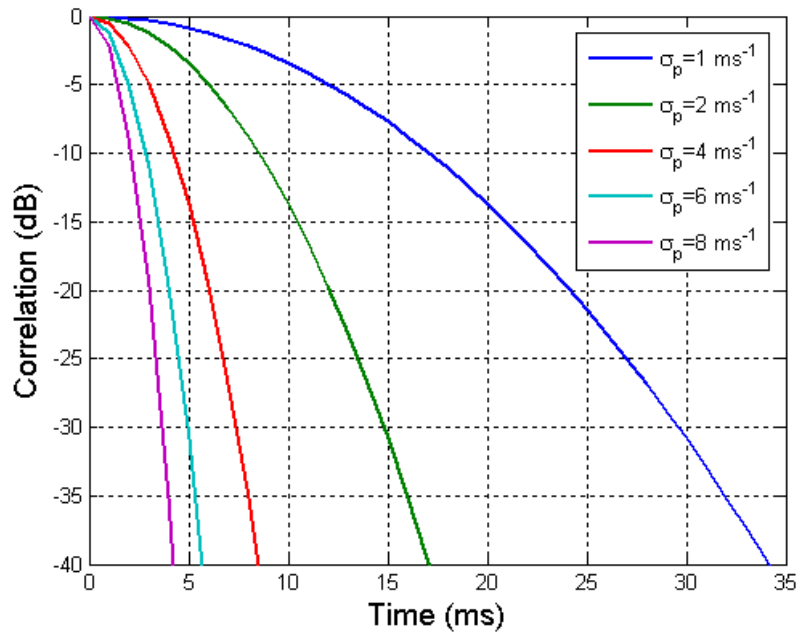


Figure 3.20: Signal auto-correlation function with various spectrum widths.

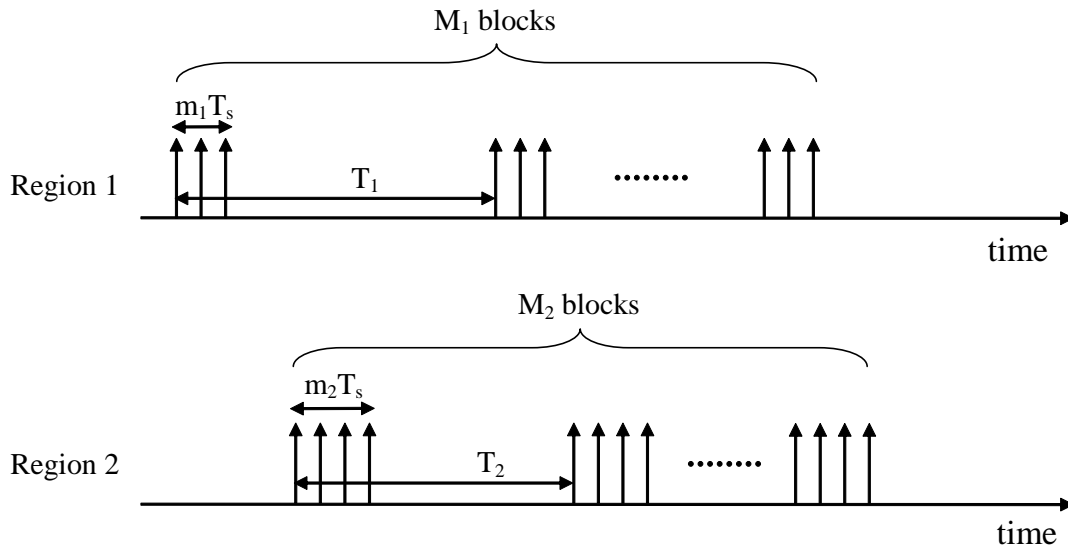


Figure 3.21: Block pulsing scheme.

As mentioned above, PAWR can instantly steer the beam to scan and revisit a region. This capability of PAWR enables a new pulsing scheme in order to reduce the scan time without

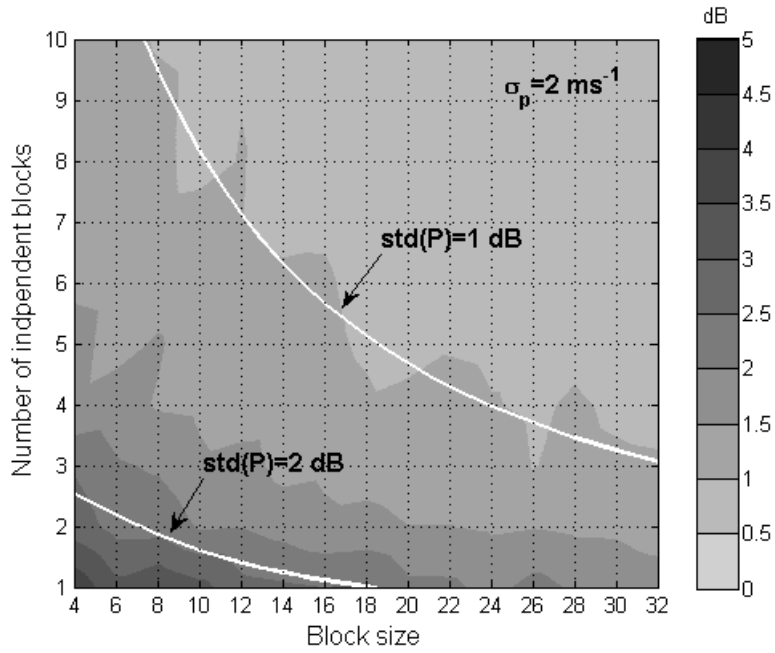
compromising the accuracy of the radar measurements. The pulsing scheme for PAWR is shown in fig. 3.21. In this scheme, PAWR transmits and receives a block of a small number of pulses, denoted by m_i for regions i^{th} , and revisits that region after time T_i . The revisit time (or update time) T_i is sufficiently large such that the signals from adjacent blocks are uncorrelated. During the revisit time, the radar beam of PAWR is steered within the other regions of interest to collect samples at many beam locations. Block size $m_i \geq 2$ is required for the estimation of mean Doppler velocity and spectrum width. It is favorable to choose a block size (m_i) as small as possible to reduce the scan time. However, it needs to be sufficiently large to allow implementing a clutter filtering algorithm (Chapter 5). Next, we will examine the statistical errors of the power estimates for the block pulsing scheme. The variance of the mean power estimate from a block is given as

$$\text{var}\left[\hat{\bar{P}}\right] = \frac{(\bar{P})^2}{m_i} \sum_{l=-(m_i-1)}^{(m_i-1)} \left(1 - \frac{|l|}{m_i}\right) \rho_p[l] \quad (3.11)$$

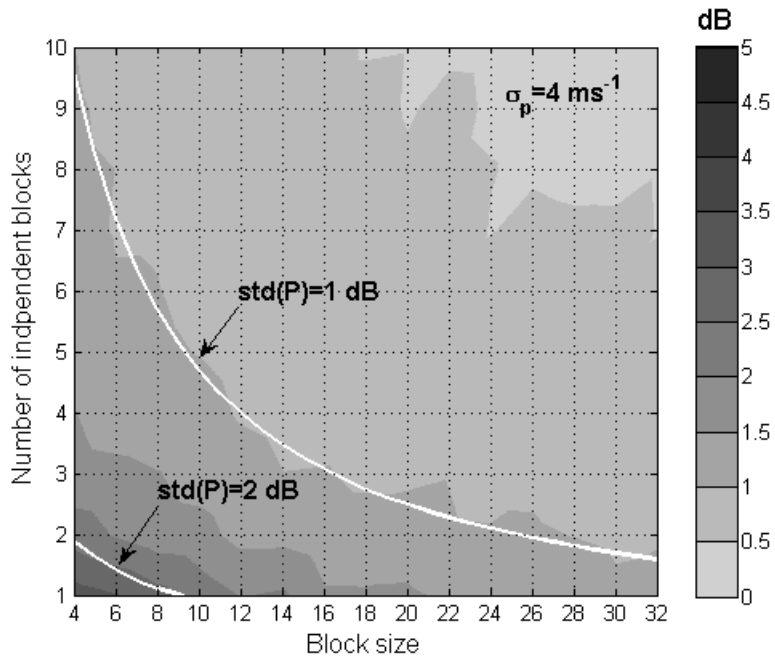
where $\rho_p[l]$ is the correlation coefficient of weather signal at lag l (Bringi and Chandrasekar, 2001).

When M_i blocks are independent, then the variance of the mean power estimate is

$$\text{var}\left[\hat{\bar{P}}\right] = \frac{(\bar{P})^2}{M_i m_i} \sum_{l=-(m_i-1)}^{(m_i-1)} \left(1 - \frac{|l|}{m_i}\right) \rho_p[l] \quad (3.12)$$



(a)



(b)

Figure 3.22: The standard deviation of power estimates as a function of block size and number of independent blocks for S-band radar with spectrum width of 2 ms^{-1} (a) and 4 ms^{-1} (b).

Figure 3.22 shows the standard deviation in estimated powers using simulation for an S-band radar. In this example, block size varies from 4 to 32 and spectrum widths of $2ms^{-1}$ and $4ms^{-1}$ are used. The parameters are estimated using the autocovariance method. White lines are theoretical curves derived from equation (3.12) for the standard deviation of power estimates 1 and 2 dB. The analysis aids the design stage of selecting a combination of block size and number of independent blocks to achieve a desired measurement accuracy. For example, at spectrum width of $4ms^{-1}$ and a block size of 4, we need 10 blocks (i.e., 40 samples) to achieve a standard deviation of estimated mean power less than 1 dB, while for conventional weather radar, at least 64 samples are needed to obtain a similar performance.

3.5 Design of scan strategy for PAWR

3.5.1 Adaptive scanning strategy

In designing the scan strategy for PAWR, the space-time characterization model plays a key role. It handles the storm motion and provides position information for radar scanning regions as well as their space-time variability parameters. Quickly evolving regions need to be scanned more often than slowly evolving regions and the scan needs to be complete within the evolution time. In addition, regions with larger spatial scale can be sampled at coarse resolution while regions with smaller scales need to be scanned in finer resolution. Moreover, the measurement error model provides information about the number of independent samples that must be collected at each beam location to achieve good data. As a result, data quality and acquisition time can be optimized. This is a fundamental principle of an adaptive scan strategy as proposed in this work. However, the scan strategy will not be complete without addressing the following considerations.

3.5.1.1 Revisit time constraints

First of all, the revisit time or update time is defined in fig. 3.21 to be specified for each scanning region during scheduling in order to minimize scan time. The requirements of independent samples and fast scan put constraints on the revisit time. While it is desirable to have a large revisit time to obtain independent samples, the scan has to be completed within the evolution time of the event. The revisit time may or may not satisfy both conditions. To examine this question, let us consider an extreme scenario where an S-band PAWR is scanning a fast-evolving region such that the area around the tornado vortex (fig. 3.9) with an evolution time of 0.145 minutes, or 8.7 seconds. Assuming the signal spectrum width is as small as 1 ms^{-1} at that region, the revisit time should be equal to or larger than 24.2 ms (eq. 3.10) to get independent samples. Thus, in this case, we are able to collect 270 independent blocks of 8 samples that provide an estimated power with standard deviation less than 1 dB (fig. 3.22). For most meteorological applications, this level of accuracy is adequate (ROC 2007). Therefore, it is assured that when we constrain the total scan time to be equal to the estimated evolution time, the average revisit time will be equal to or larger than the signal decorrelation time. Having said that, for each scanning region, we define the lower boundary of the revisit time as the signal decorrelation time, and the following procedure provides the upper boundary: 1) given the block size and level of data accuracy, specify a number of independent blocks (M_i) based on the measurement error model (section 3.4); 2) divide the evolution time by M_i to obtain the upper boundary of the revisit time. The revisit time will then be selected in this interval to produce an optimal scan.

3.5.1.2 Improved adaptive scanning with nowcasting

Adaptive scanning strategies mean the radar is able to adjust the beam location to regions of weather phenomena as they are predicted to develop. Hence, short-term prediction (nowcasting) needs to be integrated into the scan strategy to improve radar observations. The predicted reflectivity field provides better information on the future position of a moving storm and then this information is used to adjust the scan strategy to observe the entire storm. This is very important, especially when tracking or scanning a fast-moving storm. The capability of this strategy is demonstrated in fig. 3.23. Figure 3.23 depicts an image of a CASA MC&C display on May 17, 2009, comparing coverage afforded by radar node steering using previous observation versus steering using a five-minute prediction. In this case, the storm was moving toward the northeast. It can be seen that the leading edge is observed when prediction information is used in scan strategy and is missed when it is not used.

3.5.1.3 Azimuthal sampling resolution

The third consideration is the question of how PAWR adjusts azimuthal resolution to adapt to regions with different spatial scales. To address this issue, we suggest an approach of adaptively changing the antenna pattern of PAWR. At a location where smaller spatial scales are present, the antenna pattern is formed to have a narrow beamwidth. At a region with a large spatial scale the antenna pattern is synthesized with a wider beamwidth. Because the radar beamwidth is wider at off boresight, to improve the angle resolution at these locations, oversampling (i.e., overlapped beams) can be used such as with super-resolution on the NEXRAD network (Brown et al. 2002, Torres et al. 2003). The number of beam positions in azimuth is determined by the

extent of coverage and the spatial scales present in the scanning regions. A detailed discussion of this topic is beyond the scope of this work and is not presented here.

3.5.1.4 Waveform selection

The waveform selection process is responsible for selecting adequate waveforms from a waveform database for each radar scanning region. Primarily, this ensures selecting the correct waveform and signal processing to match the requirements of maximum unambiguity range, maximum unambiguity velocity, range resolution, and measurement sensitivity. For surveillance tasks the radar may use a set of two pre-defined waveforms: one for longer range measurement and one for high Doppler velocity measurement. For the main tasks, the choice of waveform depends on the storm's parameters at beam position as well as the goal of the measurement. Available waveforms are uniform PRT, batch PRT, and staggered PRT.

In summary, the flow diagram of the adaptive scan strategy for PAWR is shown in fig. 3.24.

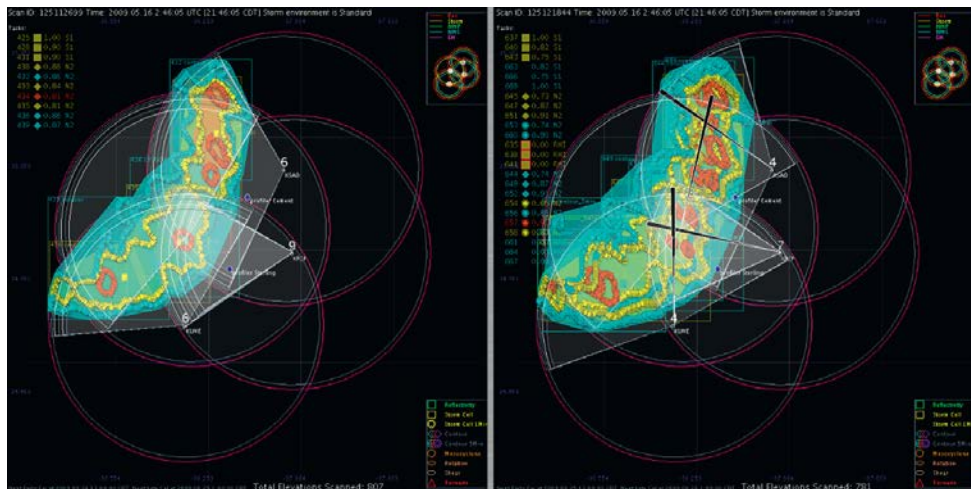


Figure 3.23: Example demonstrating the importance of incorporating nowcasting with scan strategy. Images from the CASA MC&C display on May 17, 2009, comparing coverage obtained by radar nodes steering using previous observations (left) vs adaptive scanning using five-minute nowcasts (right) (Ruzanski et al. 2010).

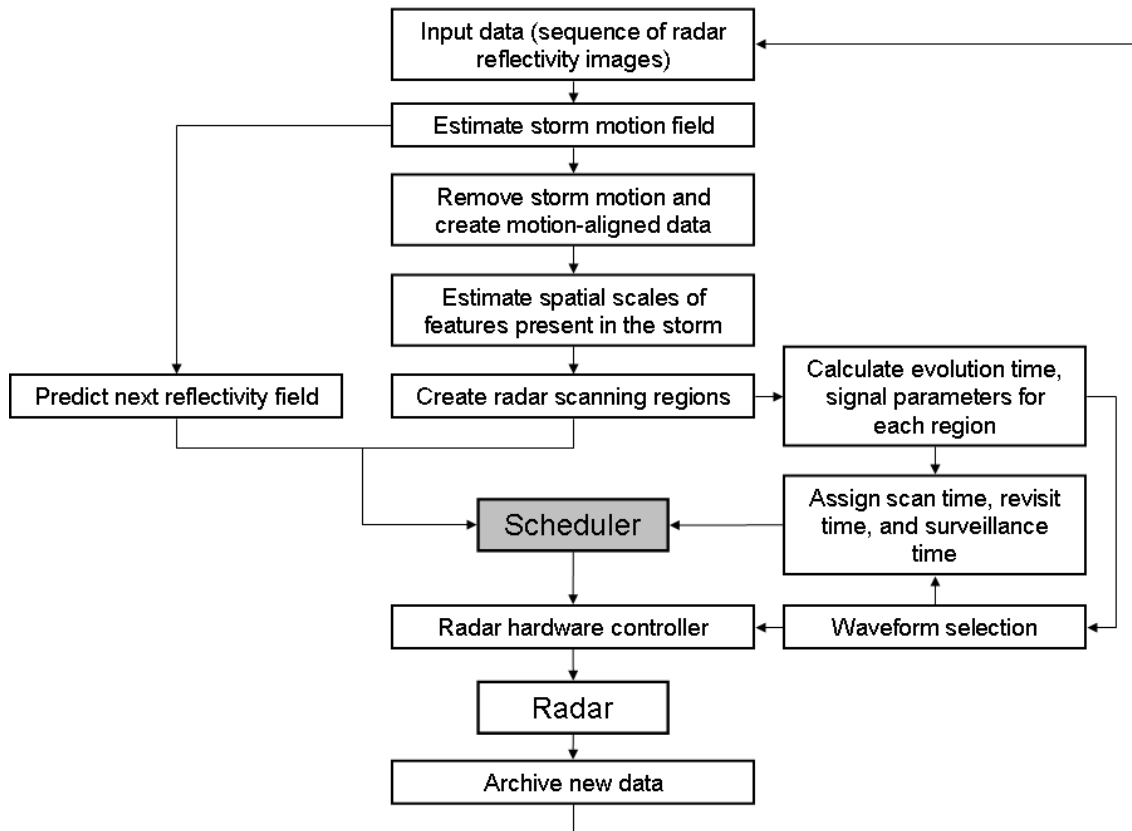


Figure 3.24: Flowchart of PAWR adaptive scan strategy.

3.5.2 Scheduler requirements

In this study, the scan strategy algorithm for PAWR works on a ray-to-ray basis. Each ray is considered as a task and the dwell time of the task (or task time) is equal to the length of the block of pulses at that ray. All tasks are competing for radar resources (time and hardware) and therefore, effective resource management is required for a successful operation. The central part of resource management is a scheduler that arranges the tasks in a sequence without significant delays. The requirements for a real-time scheduler for PAWR can be summarized as follows:

- Determine in real time a sequence of beam position in which the sampling time at each position is conditioned by the accuracy of measurement.

- Follow a priority structure for the revisit times according to the evolution of different storm regions.
- Minimize the scan time to obtain high temporal resolution observation of the storm.
- Allow implementation of adaptive waveform control according to different types of storms.
- Maintain the angular separation between two consecutive beam positions to suppress high order (e.g., second) trip echo from the previous beam position.
- Balance scan time and surveillance time.
- Fully use the antenna/radar resource.

3.5.3 An algorithm for task scheduling in PAWR

In this section, we propose an algorithm that arranges a sequence of the tasks based on tasks' priority and an approach to optimize the radar scan time. The algorithm works similar to the time balance scheme to control the scheduling of tasks as in the work of Stafford (1990). The time balance concept was first introduced for military applications and recently was extended for use in the application of phase array radar for tracking multiple storms (Reinoso-Rodinel et al. 2010).

A scheduling algorithm using time balance scheme is summarized as following:

1. Each task is associated with a time balance variable.
2. A positive time balance means the task is late for execution. The task with the highest time balance value has the highest priority.
3. When a task is finished, the time balance of all the tasks is increased by the task time. Then, the time balance variable associated to this task will be decreased by its revisit time.

4. Steps 1-3 are repeated.

In addition to the main tasks, a surveillance task is included in the scan strategy. When a surveillance task is triggered, the radar will scan the non-precipitation regions at a rate that depends on the requirement of data quality. The number of non-precipitation regions defines the number of surveillance tasks. Surveillance task time is defined as the time needed by the radar to scan the entire surveillance area continuously. The update time of a surveillance task is provided by the user. For example, the user can assign a high surveillance update time to important and potentially hazardous storms and a low update time to other storms. Usually, surveillance task time and update time is much longer than the task time of scanning a ray. A surveillance task is executed when it is in the highest priority level or when the time balance of all the main tasks are negative. In other words, surveillance runs when it is requested or when radar resources are available.

A flowchart of the scheduler algorithm proposed is shown in fig. 3.25. A description is given below.

Starting from the highest priority level task:

1. If there is any task with a positive time balance, then choose the task with highest time balance. Otherwise, schedule a surveillance task.
2. Schedule the chosen task.
3. Increase all the time balances by the task time of the chosen task.
4. Decrease the executed task's time balance by its update time.
5. Steps 1-4 are repeated until the radar finishes scanning all regions (i.e., when a new reflectivity image is generated).

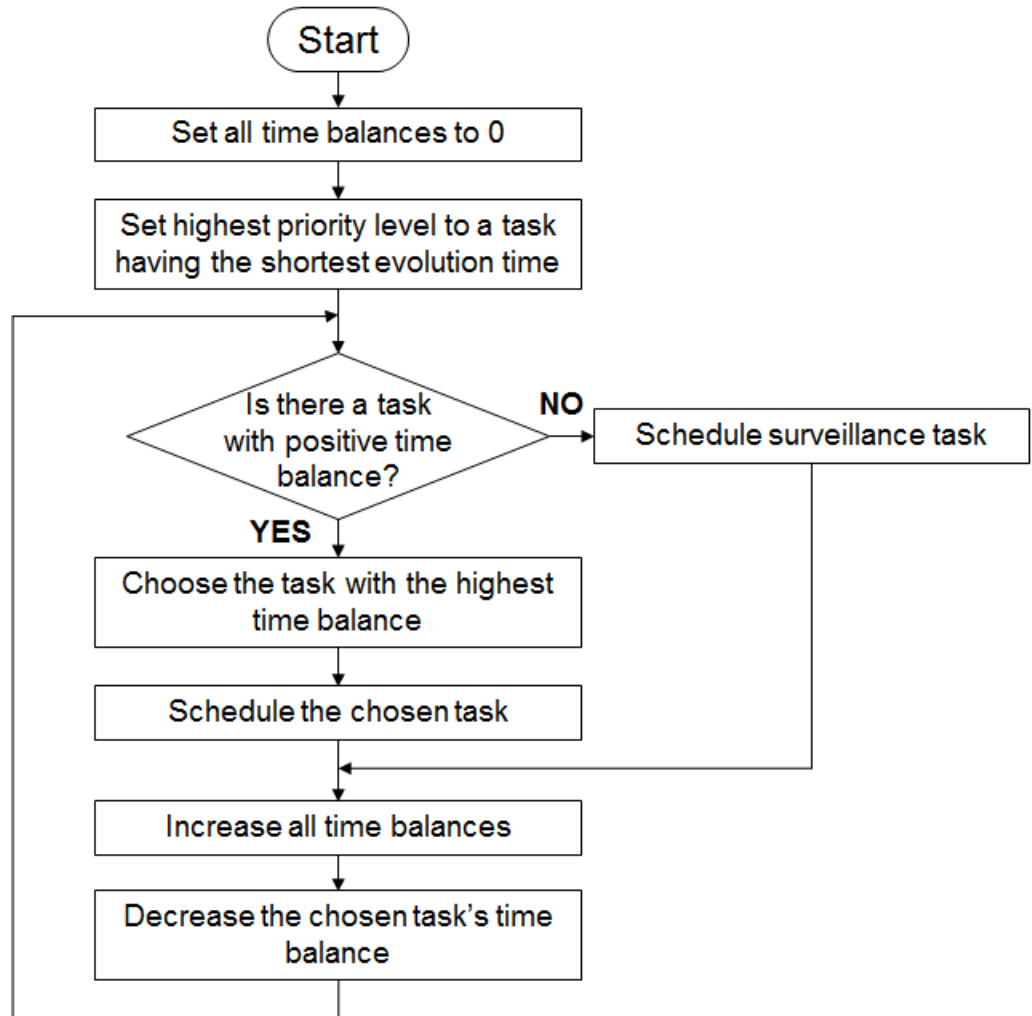


Figure 3.25: Flowchart of the scheduler algorithm.

As can be seen from the scheduler algorithm, changing the update times of tasks will produce different results. The question is how to choose the revisit times to obtain optimal results and to avoid an overloading problem for PAWR. In section 3.5.1.a, we have proposed a method for finding the constraints for revisit time at every scanning region. Each visit time is constrained in an specific interval. Apparently, there is no closed-form expression for this optimization problem since the conditions vary from case to case. Also, trying to change the update times while scheduling tasks will make the algorithm very complex. We approach this problem in a

traditional way: by considering all possible input combinations. To do this, each revisit time is scanned within its interval with the increment of radar PRT (normally in order of ms) and then the combination that provides the smallest scan time result will be chosen. Because the scheduler algorithm is fairly simple, this solution works quite well as demonstrated in the next section.

3.5.4 The scheduler performance evaluation using simulation

An example of scheduling scanning tasks for a storm consisting of two separate radar scanning regions is presented in this section. One region represents the fast-evolving (e.g., convective) part of the storm. The other represents the slower-developing region (e.g., stratiform) part of the storm. The regions' locations are shown in fig. 3.17a. The space-time parameters of the two regions generated by the characterization model are given in table 3.1. The radar parameters are given in table 3.2.

Table 3.1: Space-time parameters of scanning regions.

	<i>azimuthal range (deg)</i>	<i>azimuthal resolution (deg)</i>	<i>evolution time (min)</i>	<i>spectrum width (m/s)</i>
region 1	31-65	1	0.15	4
region 2	70-100	2	0.30	2

Table 3.2: Radar parameters.

λ (m)	<i>min. antenna beamwidth</i>	<i>pri (ms)</i>
0.10	1°	1

In addition, the requirement of minimum angular separation between two consecutive PAWR beam positions is 6°. The scan will complete when it achieves $std(P)=1$ dB or better at all

azimuth locations. In order to compare PAWR with mechanically scanned radar on scanning speed, no surveillance task is scheduled in this example.

Two pulsing schemes are studied:

- *Case 1*: Block size of 1 for both regions

Clearly, this pulsing scheme will provide the fastest scan speed but no Doppler velocity or spectrum width. Using the method proposed in section 3.5.1.a, we compute the revisit time intervals for regions 1 and 2, they are $[6, 600]$ ms and $[12, 1200]$ ms, respectively. We try all the combinations for the two revisit times (in this case the increment is 1 ms); the pair (10, 12) ms provides the smallest scan time. The final scheduled tasks (beam positions) are shown in fig. 3.26 for the first 200 ms (just for visualization). As a result, PAWR is able to finish scanning the storm in only 0.835 seconds. In contrast, a conventional radar with a 1° beamwidth antenna requires 105 samples (fig. 3.19) at each azimuth location to obtain $std(\hat{P}) \leq 1$ and therefore, takes 7.35 seconds ($105ms \times 70rays$) to finish this sector (from azimuth 31° to 100°).

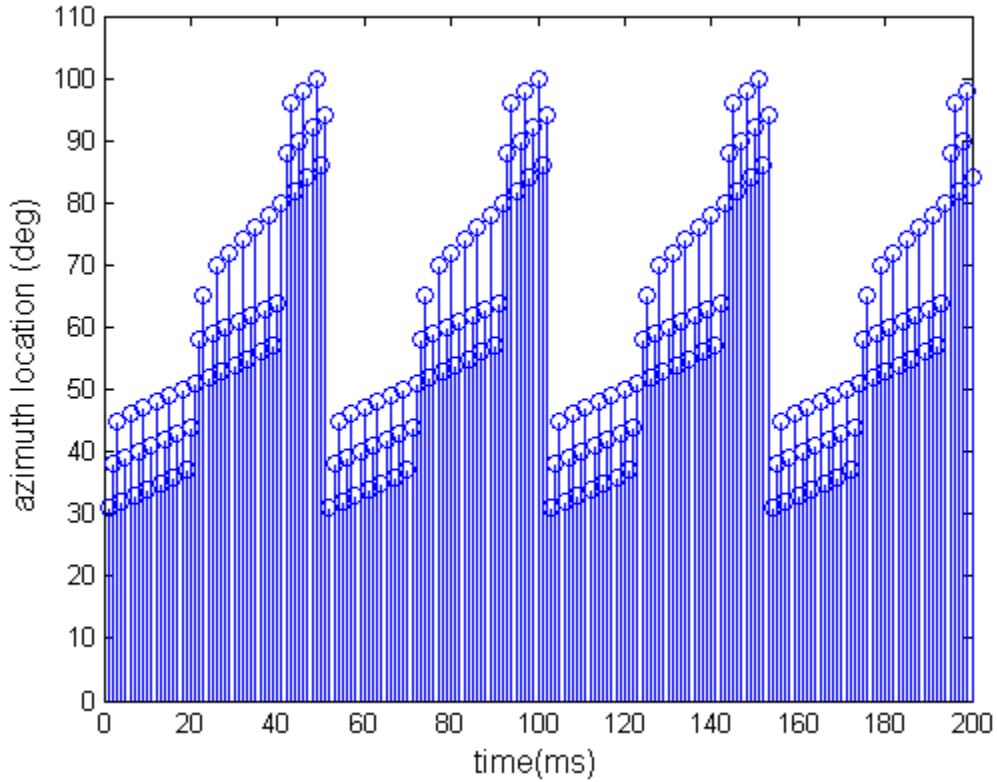


Figure 3.26: Schedule beam positions for the case of block size 1.

- *Case 2: Block size of 8 for both regions*

Increasing the block size will reduce the scan speed but it provides Doppler velocity and spectrum width estimates and more importantly, it allows the implementation of a ground clutter filtering algorithm (Chapter 5). Hence, this scheme is more practical for normal radar operation. From the measurement error model, we need to collect at least six independent blocks at each beam position for region 1 (spectrum width $4ms^{-1}$) and 10 independent blocks at each beam position for region 2 (spectrum width $2ms^{-1}$). In this case, the upper boundary for revisit times (in order to meet the requirement of evolution time) for the two regions are 1285 ms and 1800 ms. The revisit time intervals for regions 1 and 2 are $[6, 1285]$ ms and $[12, 1800]$ ms,

respectively. Again, by scanning all the possible combinations for the revisit times, we come up with values of 20 ms and 12 ms that provide a minimum scan time of 2.96 seconds. Scheduled beam positions for the first 1000 ms are shown in fig. 3.27.

In both simulation cases, besides the total scan time, scheduling parameters such as number of schedule tasks at each beam location, and total task time are included to assess the proposed scheduler algorithm. Simulation results are summarized in table 3.3.

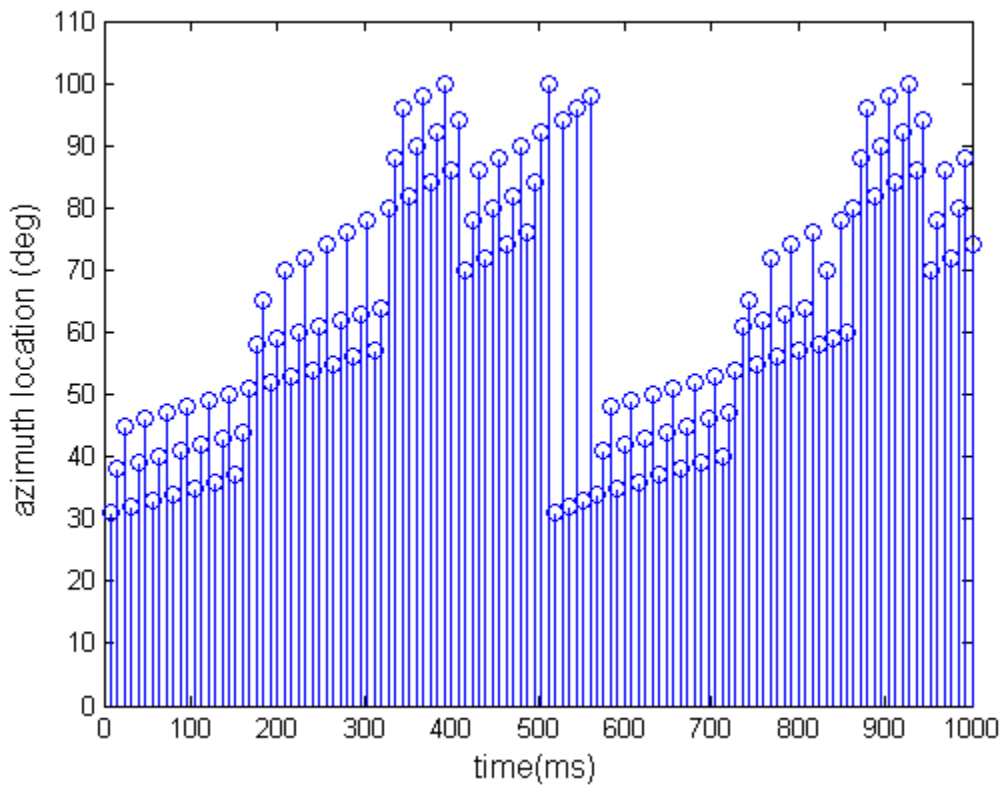


Fig 3.27: Schedule beam positions for the case of block size 8.

Table 3.3: Comparing simulation results

	Block size of 1		Block size of 8	
	CWR	PAWR	CWR	PAWR
average number of schedule tasks region 1	1 @ 105 samples	15 @ 1 sample	1 @ 105 samples	6 @ 8 samples
average number of schedule tasks region 2	1 @ 105 samples	15 @ 1 sample	1 @ 105 samples	10 @ 8 samples
total task time (s)	5.35	0.765	5.35	2.96
total scan time (s)	7.35	0.765	7.35	2.96
std(P) region 1 (dB)	0.99	0.99	0.99	1.00
std(P) region 2 (dB)	0.73	0.99	0.73	0.95

* CWR: Conventional Weather Radar

3.6 Summary

There is no doubt that PAWR has the potential to provide fast updates and high data quality that help increase warning lead times and better understanding of quickly evolving weather phenomena. To make full use of radar resources and to achieve optimal observations, a scan strategy must be addressed. In this chapter, the principle of adaptive scan strategy for PAWR has been introduced for this purpose. The adaptive sensing framework is based on the space-time variability feature of the storm. It is suggested that regions with smaller spatial scales tend to evolve more quickly than regions with larger scales and therefore, need to be updated more often. To validate this hypothesis and to obtain qualitative measurements, a new space-time characterization system for precipitation system is developed. The space-time system includes an algorithm for scale detection and estimation, a characterization model, and a scheme for mapping space-time parameters into radar scanning regions. The scale estimation algorithm detects the significant changes in similarity measurements of the observation and its filtered outputs. Using simulation, it is demonstrated that the algorithm performs well even with images containing a

wide range of spatial scales. A space-time characterization model that explicitly includes the interaction between space and time has also been presented and assessed. The storm evolution process over time is characterized by a kernel dilation model after the storm motion pattern is removed. To preserve the signal spatial characteristic, each kernel is approximated by summation of many isotropic Gaussian kernels whose scales are extracted from all images in the sequence. The weight factors of the kernels then are thresholded and mapped into regions termed radar scanning regions. The model has been extensively tested on both simulated radar data and observed radar measurements from CASA IP1 network. Results are consistent with the space-time variability hypothesis.

Next, a new pulsing scheme solely developed for PAWR and an associated measurement error model are introduced. In this scheme, a radar beam will be rapidly steered within the scanning regions to collect blocks of a small number of samples and revisit after certain intervals. A block size from 2 to 8 is chosen depending on the clutter level at beam position. The measurement error model is used to determine if the data quality requirement is satisfied.

The last, but one of the most important, tasks proposed in this chapter is an adaptive scan strategy for PAWR. Within the strategy, many aspects have been considered and discussed such as calculation of revisit time constraints, incorporation with nowcasting to improve observation, spatial sampling adaptation, and waveform selection. All these considerations provide critical inputs for the scheduler that is responsible for scheduling all radar tasks. A scheduling algorithm based on the time balance concept is used in this work. Additionally, a procedure to optimize the selection of revisit times for scanning regions is also presented. The scheduler algorithm is demonstrated to be stable while the computation is very efficient. The occupancy is very high owing to the small task time (equal to block size). As a result, PAWR can significantly reduce

scan time while maintaining the data quality required by conventional weather radar. Moreover, the designed scan strategy allows PAWR to accurately capture storm features within their evolution times.

CHAPTER 4

PARAMETER ESTIMATION FOR POLARIMETRIC PHASED ARRAY WEATHER RADAR

4.1 Introduction

In the previous chapter, features of phased-array weather radar that are important for sensing precipitation are described. It is shown that phased-array weather radar is a superior platform for observing weather compared to conventional weather radar. In particular, phased-array weather radar with polarimetric capability (polarimetric PAWR) should become a very powerful tool for meteorological applications. Since bias in dual-polarization parameters affects quantitative estimation, maintaining accurate polarimetric PAWR measurements is critical. Removing biases in polarimetric PAWR is more challenging than in the conventional polarimetric weather radar because of its electronic steering mechanism. To address this issue, a preliminary study of signals using this type of weather radar is done via modeling and simulating.

In this chapter, a signal model for electronically scanned polarimetric PAWR is presented. The array element is modeled using the same method described in Zrnic et al. (2011). Due to the projection effect, received signals include cross-coupling between the horizontal and vertical polarizations. If the coupling effect is not removed, it can introduce biases into the estimates of fundamental spectral moments as well as dual-polarization variables. The biases are functions of the antenna's beam position. The farther off the antenna axis the beam is steered, the larger the biases will be. It is shown that those biases can be larger than the intrinsic values of the

polarimetric parameters. Therefore, developing efficient methods for bias correction is critical for maintaining the accuracy of the estimates for quantitative meteorological applications.

Bias correction methods are proposed for both simultaneous and alternating polarization transmission modes for polarimetric PAWR. The correction can be implemented on a pulse-by-pulse basis or from the powers and correlations of the measured signals. They can be done at the receiver side without any adjustments to the transmitted fields, as shown in Zrnic et al. (2011). In addition to the bias correction, the effect of noise on the polarimetric PAWR data quality is also studied. Lastly, a signal simulation for polarimetric PAWR is developed to verify the performance of the proposed bias-correction methods. This turns out to be an excellent additional tool for designing polarimetric PAWR.

4.2 Problem formulation

An aperture of a planar phased-array antenna consists of many similar radiating elements and each element can be individually controlled in phase and amplitude. Similar to Peebles (1998), we assume that there is no coupling effect between the elements' transmit fields. The complete radiation pattern of the phased array is a product of two independent components: the array pattern and the element pattern (eq. 2.23). The array pattern solely depends on the array's physical layout and phase differences between the array elements. Therefore, the characterization of the transmit and receive signals of a polarimetric PAWR can be represented by the array element.

4.2.1 Element pattern model

It is assumed that an aperture of a planar phased-array antenna consists of $N \times M$ elements where each element is modeled by a pair of crossed Hertzian dipoles (fig. 4.1). A Cartesian

coordinate with unit vectors $(\vec{a}_x, \vec{a}_y, \vec{a}_z)$ is chosen so that the horizontal dipole is aligned with the y-axis and the vertical dipole is aligned with the z-axis. With this setup, the y-z plane is the antenna plane and x-axis is the antenna's normal axis, or boresight.

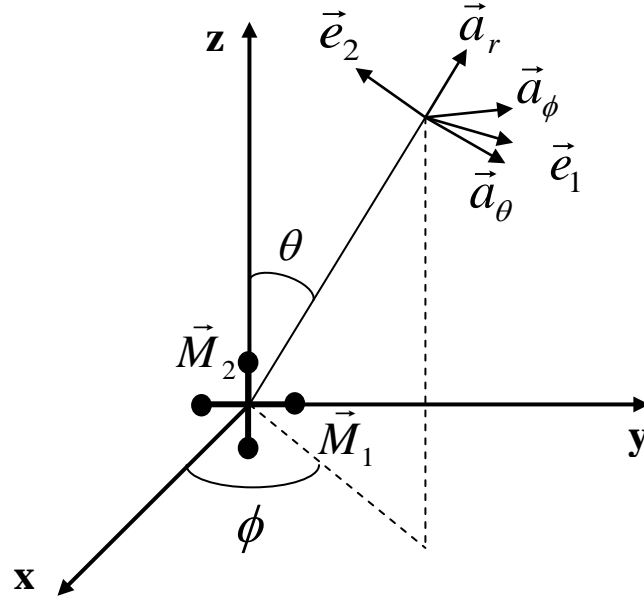


Figure 4.1: Sketch of diagram for signal radiating by a pair of cross-dipoles with moments \vec{M}_1 and \vec{M}_2 .

Let \vec{M}_1 and \vec{M}_2 be the moments of horizontal and vertical dipoles, respectively,

$$\vec{M}_1 = \vec{a}_y A_1 \exp(j\phi_1) \quad (4.1a)$$

$$\vec{M}_2 = \vec{a}_z A_2 \exp(j\phi_2) \quad (4.1b)$$

where A_i is the dipole moment amplitude and ϕ_i is the phase ($i=1,2$). Given a resolution volume filled with precipitation particles at range r (fig. 2.1) and angular direction (θ, ϕ) , we form a local orthogonal coordinate at the volume with a set of unit vectors $(\vec{a}_r, \vec{a}_\theta, \vec{a}_\phi)$, where

\vec{a}_r is along \vec{r} direction, \vec{a}_θ is on θ plane, and \vec{a}_ϕ is parallel to x-y plane (fig. 4.1). Thus, the local horizontal and vertical directions are $\vec{a}_H \equiv \vec{a}_\phi$ and $\vec{a}_V \equiv -\vec{a}_\theta$, respectively. The local base can be expressed in terms of the Cartesian unit vectors as

$$\begin{aligned}\vec{a}_r &= \vec{a}_x \sin \theta \cos \phi + \vec{a}_y \sin \theta \sin \phi + \vec{a}_z \cos \theta \\ \vec{a}_\theta &= \vec{a}_x \cos \theta \cos \phi + \vec{a}_y \cos \theta \sin \phi - \vec{a}_z \sin \theta \\ \vec{a}_\phi &= -\vec{a}_x \sin \phi + \vec{a}_y \cos \phi\end{aligned}\quad (4.2)$$

If r is large enough, the electric far field radiated by a dipole at range r (Cheng, 1989) in vector notation is

$$\vec{E}_n(\vec{r}) = -\frac{k^2 e^{-jkr}}{4\pi\epsilon r} \left\{ \vec{a}_r \times \left[\vec{a}_r \times \vec{M}_n \right] \right\}; \quad n = 1, 2 \quad (4.3)$$

Substituting (4.2) into (4.3), we have

$$\vec{E}_1 = E_1^t \left[\vec{a}_y - \left(\vec{a}_x \sin \theta \cos \phi + \vec{a}_y \sin \theta \sin \phi + \vec{a}_z \cos \theta \right) \sin \theta \sin \phi \right] = E_1^t \vec{e}_1 \quad (4.4a)$$

$$\vec{E}_2 = E_2^t \left[\vec{a}_z \sin^2 \theta - \left(\vec{a}_x \cos \phi + \vec{a}_y \sin \phi \right) \sin \theta \cos \theta \right] = E_2^t \vec{e}_2 \quad (4.4b)$$

where

$$E_1^t = \frac{k^2 e^{-jkr}}{4\pi\epsilon r} M_1 \quad (4.5a)$$

$$E_2^t = \frac{k^2 e^{-jkr}}{4\pi\epsilon r} M_2 \quad (4.5b)$$

are the magnitude of electric fields radiated by moments \vec{M}_1 and \vec{M}_2 along the array boresight at range r , respectively.

Projecting the electric fields in (4.4) onto the local horizontal (\vec{a}_H) and vertical (\vec{a}_V) axes and using the relation in (4.2), we obtain the incident fields at the resolution volume

$$E_h^i = \cos \phi E_1^t \quad (4.6a)$$

$$E_v^i = -\cos\theta \sin\phi E_{h1}^i + \sin\theta E_2^i \quad (4.6b)$$

where the subscript h (v) is for horizontal (vertical) polarization and the superscript i denotes incident field. Using vector notation, (4.6) can be written as

$$\vec{E}^i = \begin{bmatrix} E_h^i \\ E_v^i \end{bmatrix} = \begin{bmatrix} \cos\phi & 0 \\ -\cos\theta \sin\phi & \sin\theta \end{bmatrix} \begin{bmatrix} E_1^i \\ E_2^i \end{bmatrix} \quad (4.7)$$

Denote $\mathbf{P} = \begin{bmatrix} \cos\phi & 0 \\ -\cos\theta \sin\phi & \sin\theta \end{bmatrix}$ to be the projection matrix and $\vec{E}^t = \begin{bmatrix} E_1^t \\ E_2^t \end{bmatrix}$ to be the electric

vector when measured at boresight; then (4.7) can be expressed in matrix notation

$$\vec{E}^i = \mathbf{P}\vec{E}^t \quad (4.8)$$

In summary, for an agile-beam polarimetric PAWR, the incident electric fields at angular direction (θ, ϕ) are the product of a projection matrix and the electric fields at boresight. This is the main difference between an electronically scanned polarimetric PAWR and a mechanically scanned weather radar.

4.2.2 Scattering matrix

The scattered electric fields from resolution volume at (r, θ, ϕ) are given by Bringi and Chandrasekar, 2001,

$$\vec{E}^s = \begin{bmatrix} E_h^s \\ E_v^s \end{bmatrix} = \frac{\exp(-jkr)}{r} \begin{bmatrix} S_{hh} & S_{hv} \\ S_{hv} & S_{vv} \end{bmatrix}_{FSA} \begin{bmatrix} E_h^i \\ E_v^i \end{bmatrix} = \mathbf{S}_{SFA} \vec{E}^i \quad (4.9)$$

where \mathbf{S}_{SFA} is the intrinsic scattering matrix of hydrometeors in the FSA convention. To obtain the received fields at the array element (assumed to be the same as the transmit array element), we project the scattered fields onto the corresponding dipole axes. A similar method as that used to achieve (4.7) is carried out and final results are

$$\vec{E}^r = \begin{bmatrix} E_h^r \\ E_v^r \end{bmatrix} = \begin{bmatrix} \cos \phi & -\cos \theta \sin \phi \\ 0 & \sin \theta \end{bmatrix} \begin{bmatrix} -1 & 0 \\ 0 & 1 \end{bmatrix} \begin{bmatrix} E_h^s \\ E_v^s \end{bmatrix} = \mathbf{P}^T \vec{E}^s \quad (4.10)$$

From equations (4.7), (4.9), and (4.10), the received fields at array element can be expressed as

$$\vec{E}^r = \frac{\exp(-jkr)}{r} \mathbf{P}^T \mathbf{S}_{BSA} \mathbf{P} \vec{E}^t \quad (4.11)$$

If the differential phase shift and attenuation along the path are significant, the transmission matrix needs to be accounted for (Bringi and Chandrasekar, 2001)

$$\vec{E}^r = \frac{\exp(-jkr)}{r} \mathbf{P}^T \mathbf{T} \mathbf{S}_{BSA} \mathbf{T} \mathbf{P} \vec{E}^t = \frac{\exp(-jkr)}{r} \mathbf{P}^T \mathbf{S}'_{BSA} \mathbf{P} \vec{E}^t \quad (4.12)$$

where the transmission matrix \mathbf{T} and scattering matrix \mathbf{S}'_{BSA} are defined in (2.3) and (2.7).

4.2.3 Voltage equation

When the array element is used as a receiver, there will be open circuit voltages at its terminals due to the scatter fields \vec{E}^r . Let $\mathbf{G}_e = [G_h^e \ G_v^e]^T$ be the element gains. The voltage received at each array element can be written (Bringi and Chandrasekar, 2001) as

$$\begin{bmatrix} V_h^e \\ V_v^e \end{bmatrix} = \frac{\lambda}{\sqrt{8\pi Z_0}} \begin{bmatrix} \sqrt{G_h^e} & 0 \\ 0 & \sqrt{G_v^e} \end{bmatrix} \begin{bmatrix} E_h^r \\ E_v^r \end{bmatrix} \quad (4.13)$$

If the array is made up of $N \times M$ equal elements and is matched to accept the return power, then the overall gain from all elements is

$$\mathbf{G} = \begin{bmatrix} G_h \\ G_v \end{bmatrix} = NM\eta \begin{bmatrix} G_h^e \\ G_v^e \end{bmatrix} \quad (4.14)$$

where η is the efficiency factor.

The received voltages at the ports of the array are expressed as

$$\begin{bmatrix} V_h \\ V_v \end{bmatrix} = \frac{\lambda}{\sqrt{8\pi Z_0}} \begin{bmatrix} \sqrt{G_h} & 0 \\ 0 & \sqrt{G_v} \end{bmatrix} \begin{bmatrix} E_h^r \\ E_v^r \end{bmatrix} \quad (4.15)$$

Substituting (4.5) into (4.12), the received fields can be written as

$$\bar{E}^r = \begin{bmatrix} E_h^r \\ E_v^r \end{bmatrix} = \frac{k^2}{4\pi\epsilon_0} \frac{e^{-jkr}}{r} \mathbf{P}^T \mathbf{S}'_{BSA} \mathbf{P} \begin{bmatrix} M_1 \\ M_2 \end{bmatrix} \frac{e^{-jkr}}{r} \quad (4.16)$$

From eqs. (4.15) and (4.16), we obtain the voltage equation for the phased array antenna

$$\begin{bmatrix} V_h \\ V_v \end{bmatrix} = \frac{\lambda}{\sqrt{8\pi Z_0}} \frac{k^2}{4\pi\epsilon_0} \left(\frac{e^{-jkr}}{r} \right)^2 \begin{bmatrix} \sqrt{G_h} & 0 \\ 0 & \sqrt{G_v} \end{bmatrix} \mathbf{P}^T \mathbf{S}'_{BSA} \mathbf{P} \begin{bmatrix} M_1 \\ M_2 \end{bmatrix} \quad (4.17)$$

For an ideal antenna, $G_h = G_v = G$, (4.17) is simplified to

$$\begin{bmatrix} V_h \\ V_v \end{bmatrix} = \frac{\lambda\sqrt{G}}{\sqrt{8\pi Z_0}} \frac{k^2}{4\pi\epsilon_0} \left(\frac{e^{-jkr}}{r} \right)^2 \mathbf{P}^T \mathbf{S}'_{BSA} \mathbf{P} \begin{bmatrix} M_1 \\ M_2 \end{bmatrix} \quad (4.18)$$

The transmit powers are implicit in the input dipole moments. For agile-beam polarimetric PAWR, the scattering matrix is given by

$$\mathbf{P}^T \mathbf{S}'_{BSA} \mathbf{P} = \begin{bmatrix} S'_{hh} \cos^2 \phi - 2S'_{hv} \cos \theta \sin \phi \cos \phi + S'_{vv} \cos^2 \theta \sin^2 \phi & S'_{hv} \sin \theta \cos \phi - S'_{vv} \sin \theta \cos \theta \sin \phi \\ S'_{hv} \sin \theta \cos \phi - S'_{vv} \sin \theta \cos \theta \sin \phi & S'_{vv} \sin \theta \end{bmatrix} \quad (4.19)$$

Compared to a mechanically scanned weather radar, the received scattering matrix by a polarimetric PAWR includes the effect of projection when the antenna is directed at off-boresight. Note that when a single polarization is transmitted (say horizontal polarization, i.e., $M_1 \neq 0, M_2 = 0$), the received wave amplitudes are not proportional to the first column of the intrinsic scattering matrix (\mathbf{S}'_{BSA}) as in the case of conventional weather radar. Hereafter,

assuming the receiver gains and another constant parameters are accounted for and removed from the voltage equation, (4.18) is simplified to

$$\begin{aligned} \begin{bmatrix} V_h \\ V_v \end{bmatrix} &= \mathbf{P}^T \mathbf{S}'_{BSA} \mathbf{P} \begin{bmatrix} M_1 \\ M_2 \end{bmatrix} \\ &= \begin{bmatrix} S'_{hh} \cos^2 \phi - 2S'_{hv} \cos \theta \sin \phi \cos \phi + S'_{vv} \cos^2 \theta \sin^2 \phi & S'_{hv} \sin \theta \cos \phi - S'_{vv} \sin \theta \cos \theta \sin \phi \\ S'_{hv} \sin \theta \cos \phi - S'_{vv} \sin \theta \cos \theta \sin \phi & S'_{vv} \sin \theta \end{bmatrix} \begin{bmatrix} M_1 \\ M_2 \end{bmatrix} \end{aligned} \quad (4.20)$$

4.3 Example of polarimetric PAWR inherent bias

In this section, an example of the bias problem associated with agile-beam polarimetric PAWR is illustrated. In the alternating mode, we can measure a full polarimetric scattering matrix (4.19). If the standard processing method (Bringi and Chandrasekar, 2001) is applied to the received signals, the differential reflectivity from polarimetric PAWR is

$$Z_{dr}^{PPAWR} = 10 \log_{10} \left(\frac{\left\langle \left| S'_{hh} \cos^2 \phi - 2S'_{hv} \cos \theta \sin \phi \cos \phi + S'_{vv} \cos^2 \theta \sin^2 \phi \right|^2 \right\rangle}{\left\langle \left| S'_{vv} \sin \theta \right|^2 \right\rangle} \right) \quad (4.21)$$

where the superscript *PPAWR* indicates estimates obtained directly from the measured signals from polarimetric PAWR without bias removal. On the other hand, the differential reflectivity by definition is

$$Z_{dr} = 10 \log_{10} \left(\frac{\left\langle \left| S'_{hh} \right|^2 \right\rangle}{\left\langle \left| S'_{vv} \right|^2 \right\rangle} \right) \quad (4.22)$$

Here, the propagation effects are not considered as polarimetric PAWR inherent biases.

It can be shown that Z_{dr}^{PPAWR} is related to Z_{dr} via the following equation

$$Z_{dr}^{PPAWR} = Z_{dr} + 10 \log_{10} \left(\frac{\cos^4 \phi + 2\sqrt{Z_{dr}} \operatorname{Re}\{\rho_{co}\} \cos^2 \theta \cos^2 \phi \sin^2 \phi + \cos^4 \theta \sin^4 \phi / Z_{dr}}{\sin^2 \theta} \right) \quad (4.23)$$

where ρ_{co} is the signal co-polar correlation coefficient (eq. 2.16). The second term in (4.23) is the Z_{dr} bias associated with polarimetric PAWR. Note that this bias depends on the measurement direction (θ, ϕ) . Figure 4.2 depicts the Z_{dr} bias as a function of measurement direction angles in the case of $Z_{dr} = 2$ dB, $|\rho_{co}| = 0.99$ and $\Phi_{dp} = 45^\circ$.

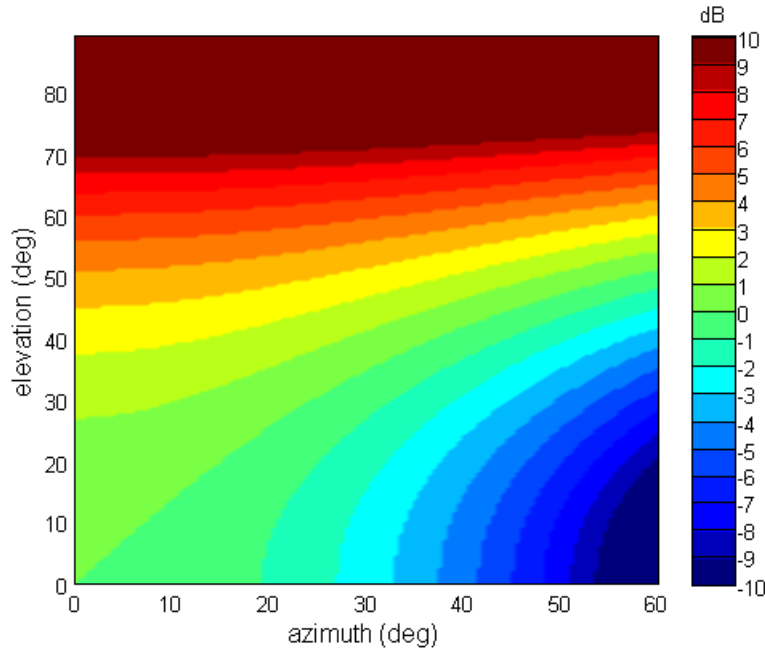


Figure 4.2: Example of inherent bias in Z_{dr} estimates in simultaneous mode.

From fig. 4.2, it can be observed that the Z_{dr} bias in polarimetric PAWR can be as high as 10 dB. Because the dynamic range of Z_{dr} is within a few dBs, the bias is intolerable. Therefore, the estimates cannot be obtained directly from the measured fields.

4.4 Methods for parameter estimation and bias correction

The received voltages with polarimetric PAWR are related to the elements of the intrinsic scattering matrix via linear equations (4.20). The method of parameter estimation depends on the transmission mode. In the simultaneous mode ($[M_1 \ M_2] \propto [1 \ 1]$) all the elements of the scattering matrix can be obtained at the same time, while in the alternating mode ($[M_1 \ M_2] \propto [1 \ 0]$ and $[M_1 \ M_2] \propto [0 \ 1]$), with no special coding (Bharadwaj et al. 2007), the matrix columns are available at alternating times.

4.4.1 Simultaneous mode

In this mode, it can be assumed that the intrinsic scattering matrix has a diagonal form (Bringi and Chandrasekar, 2001)

$$\mathbf{S}'_{BSA} = \begin{bmatrix} S'_{hh} & 0 \\ 0 & S'_{vv} \end{bmatrix} \quad (4.24)$$

Equation (4.20) can be written as

$$\begin{bmatrix} V_h \\ V_v \end{bmatrix} = \mathbf{P}^T \mathbf{S}'_{BSA} \begin{bmatrix} \cos \phi M_1 \\ -\cos \theta \sin \phi M_1 + \sin \theta M_2 \end{bmatrix} \quad (4.25)$$

Denote

$$\begin{bmatrix} M_1^P \\ M_2^P \end{bmatrix} = \begin{bmatrix} \cos \phi M_1 \\ -\cos \theta \sin \phi M_1 + \sin \theta M_2 \end{bmatrix} \quad (4.26)$$

The voltage equation can be expressed as

$$\begin{aligned} \begin{bmatrix} V_h \\ V_v \end{bmatrix} &= \begin{bmatrix} \cos \phi S'_{hh} & -\cos \theta \sin \phi S'_{vv} \\ 0 & \sin \theta S'_{vv} \end{bmatrix} \begin{bmatrix} M_1^P \\ M_2^P \end{bmatrix} \\ &= \begin{bmatrix} \cos \phi M_1^P S'_{hh} - \cos \theta \sin \phi M_2^P S'_{vv} \\ \sin \theta M_2^P S'_{vv} \end{bmatrix} \end{aligned} \quad (4.27)$$

The variable S'_{vv} can be obtained directly from the second equation of the system (4.27). Substituting S'_{vv} into the first equation of (4.27) will produce S'_{hh} . The calculation is repeated for each pulse; therefore, it is termed a “pulse-to-pulse” correction method (Zrnic et al. 2011). Following this step, the signal parameters are estimated from S'_{ij} sequences using conventional methods such as the pulse-pair method. This approach is simple but computationally heavy because it needs to be done at each pulse. On the other hand, the mean of sample powers and correlations of the received voltages form a system of linear equations with unknowns that are the signal covariances,

$$\begin{aligned}\hat{P}_h &= \langle |V_h|^2 \rangle \\ &= \cos^2 \phi |M_1^p|^2 \langle |S'_{hh}|^2 \rangle - 2 \cos \theta \cos \phi \sin \phi \operatorname{Re} \left\{ S'_{hh}^* S'_{vv} \right\} (M_1^p)^* M_2^p \Big\} \\ &\quad + \cos^2 \theta \sin^2 \phi |M_2^p|^2 \langle |S'_{vv}|^2 \rangle\end{aligned}\tag{4.28a}$$

$$\begin{aligned}\hat{P}_v &= \langle |V_v|^2 \rangle \\ &= \sin^2 \theta |M_2^p|^2 \langle |S'_{vv}|^2 \rangle\end{aligned}\tag{4.28b}$$

$$\begin{aligned}\hat{R}_{v,h}(0) &= \langle V_v V_h^* \rangle \\ &= \cos \phi \sin \theta (M_1^p)^* M_2^p \langle S'_{hh}^* S'_{vv} \rangle - \sin \phi \cos \theta \sin \theta |M_2^p|^2 \langle |S'_{vv}|^2 \rangle\end{aligned}\tag{4.28c}$$

The covariances $\langle |S'_{hh}|^2 \rangle$, $\langle |S'_{vv}|^2 \rangle$ and $\langle S'_{hh}^* S'_{vv} \rangle$ are unknowns of a system of three linear equations (4.28). Solving this system of linear equations gives

$$\hat{P}_{co}^h = \langle |S'_{hh}|^2 \rangle = \frac{\hat{P}_h + 2\alpha \operatorname{Re} \{ \hat{R}_{v,h}(0) \} + \alpha^2 \hat{P}_v}{\cos^4 \phi |M_1|^2}\tag{4.29a}$$

$$\hat{P}_{co}^v = \langle |S'_{vv}|^2 \rangle = \frac{\hat{P}_v}{\sin^4 \theta (\alpha^2 |M_1|^2 - 2\alpha \operatorname{Re} \{ M_1^* M_2 \} + |M_2|^2)}\tag{4.29b}$$

$$\hat{R}_{vv,hh}(0) = \langle S'_{vv} S'^*_{hh} \rangle = \frac{\hat{R}_{v,h}(0) + \alpha \hat{P}_v}{\cos^2 \phi \sin^2 \theta (-\alpha M_1 + M_2)} \quad (4.29c)$$

where $\alpha = \sin \phi \tan^{-1} \theta$.

Clearly, the approach requires fewer computational operations than the pulse-to-pulse method; it is named the ‘‘power and correlations’’ method. Differential reflectivity (Z_{dr}), co-polar correlation coefficient ($|\rho_{co}|$), and differential phase (Φ_{dp}) can be obtained directly from (4.29).

In addition, velocity and spectrum width are estimated from the received signal at either the horizontal or vertical channel. For example, from the vertical channel,

$$V_v = (-\cos \theta \sin \theta \sin \phi M_1 + \sin^2 \theta M_2) S'_{vv} \quad (4.30)$$

The autocorrelation at lag 1 of the vertical channel signal is

$$\begin{aligned} \hat{R}_{v,v}(T_s) &= \langle V_{vv}^*(0) V_{vv}(T_s) \rangle \\ &= |-\cos \theta \sin \theta \sin \phi M_1 + \sin^2 \theta M_2|^2 \langle S_{vv}^*(0) S_{vv}(T_s) \rangle \end{aligned} \quad (4.31)$$

From (4.31), the mean velocity estimate based on the autocorrelation function at lag 1 is given as

$$\hat{v} = -\frac{\lambda}{4\pi T_s} \arg(\langle S_{vv}^*(0) S_{vv}(T_s) \rangle) = -\frac{\lambda}{4\pi T_s} \arg(\hat{R}_{v,v}(T_s)) \quad (4.32)$$

and the estimate of spectrum width is

$$\hat{\sigma}_p = \frac{\lambda}{2\sqrt{2}\pi T_s} \left[\ln \frac{\hat{P}_{co}^v}{|\hat{R}_{v,v}(T_s)|} \right]^{1/2} \quad (4.33)$$

In equation (4.28c), besides the requirement of a precise calibration for receiver gains, the differential phase between the two receivers needs to be calculated and accounted for.

4.4.2 Alternating mode

In this mode, an alternate polarization sequence of length $2N$ is transmitted and received. Without loss of generality, assume that the first pulse is horizontal polarization. The received voltages alternate as follows

at time $(2n-1)$, $n=1, \dots, N$ we have $[M_1 \ M_2] \propto [1 \ 0]$, then

$$\begin{bmatrix} M_1^p \\ M_2^p \end{bmatrix} = \begin{bmatrix} \cos \phi M_1 \\ -\cos \theta \sin \phi M_1 \end{bmatrix} \quad (4.34)$$

$$\begin{aligned} \begin{bmatrix} V_{hh}(2n-1) \\ V_{hv}(2n-1) \end{bmatrix} &= \mathbf{P}^T \mathbf{S}'_{BSA}|_{(2n-1)} \begin{bmatrix} \cos \phi M_1 \\ -\cos \theta \sin \phi M_1 \end{bmatrix} \\ &= M_1 \mathbf{P}^T \mathbf{S}'_{BSA}|_{(2n-1)} \begin{bmatrix} \cos \phi \\ -\cos \theta \sin \phi \end{bmatrix} \end{aligned} \quad (4.35)$$

$$V_{hh}(2n-1) = M_1 \left(\cos^2 \phi S'_{hh}(2n-1) - 2 \cos \theta \cos \phi \sin \phi S'_{hv}(2n-1) + \cos^2 \theta \sin^2 \phi S'_{vv}(2n-1) \right) \quad (4.36a)$$

$$V_{hv}(2n-1) = M_1 (\cos \phi \sin \theta S'_{hv}(2n-1) - \cos \theta \sin \theta \sin \phi S'_{vv}(2n-1)) \quad (4.36b)$$

at time $(2n)$, $n=1, \dots, N$ we have $[M_1 \ M_2] \propto [0 \ 1]$, then

$$\begin{bmatrix} M_1^p \\ M_2^p \end{bmatrix} = \begin{bmatrix} 0 \\ \sin \theta M_2 \end{bmatrix} \quad (4.37)$$

$$\begin{bmatrix} V_{vh}(2n) \\ V_{vv}(2n) \end{bmatrix} = \mathbf{P}^T \mathbf{S}'_{BSA}|_{(2n)} \begin{bmatrix} 0 \\ \sin \theta M_2 \end{bmatrix} = \sin \theta M_2 \mathbf{P}^T \begin{bmatrix} S'_{vh}(2n) \\ S'_{vv}(2n) \end{bmatrix} \quad (4.38)$$

$$V_{vh}(2n) = M_2 (\cos \phi \sin \theta S'_{hv}(2n) - \cos \theta \sin \theta \sin \phi S'_{vv}(2n)) \quad (4.39a)$$

$$V_{vv}(2n) = M_2 \sin^2 \theta S'_{vv}(2n) \quad (4.39b)$$

Figure 4.3 depict the alternating transmission mode for PAWR.

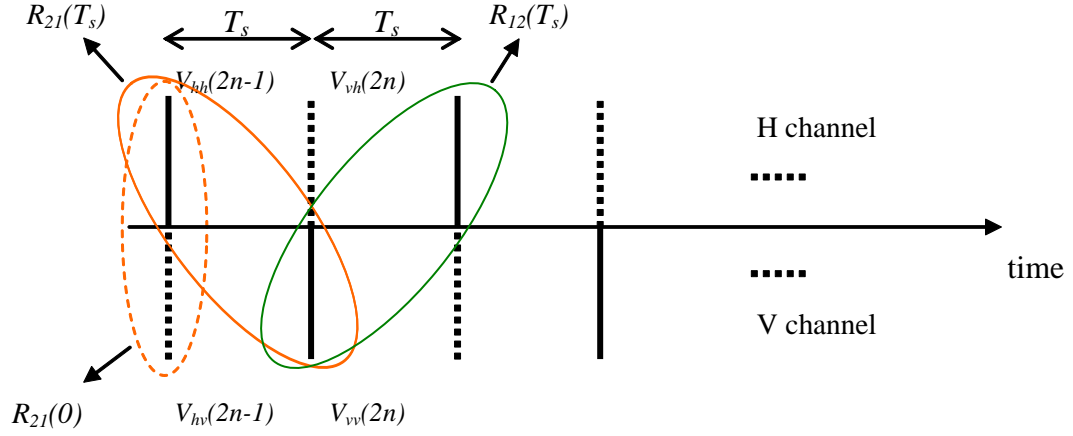


Figure 4.3: Alternating transmission mode for PAWR

Unlike the case of simultaneous mode, not all intrinsic scattering matrix elements can be simply obtained from odd and even sequences due to the different sampling time. Signal parameters are estimated from the estimated powers and correlations at lag 0 and 1. First, from the even sequence (4.39) the power and covariances $\langle |S'_{vv}|^2 \rangle$, $\langle |S'_{hv}|^2 \rangle$, and $\langle S'_{vv} S'_{hv} \rangle$ can be solved directly. The results are

$$\hat{P}_{co}^v = \langle |S'_{vv}|^2 \rangle = \frac{\langle |V_{vv}(2n)|^2 \rangle}{\sin^4 \theta |M_2|^2} \quad (4.40)$$

$$\hat{R}_{hv,vv}(0) = \langle S'_{hv} S'_{vv} \rangle = \frac{\langle V_{vh}(2n) V_{vv}^*(2n) \rangle + \alpha \langle |V_{vv}(2n)|^2 \rangle}{\sin^3 \theta \cos \phi |M_2|^2} \quad (4.41)$$

$$\hat{P}_{cx} = \langle |S'_{hv}|^2 \rangle = \frac{1}{\cos^2 \phi \sin^2 \theta |M_2|^2} \left(|V_{vh}(2n)|^2 + 2\alpha \operatorname{Re} \{ \langle V_{vh}(2n) V_{vv}^*(2n) \rangle \} + \alpha^2 \langle |V_{vv}(2n)|^2 \rangle \right) \quad (4.42)$$

with α as defined in the above section.

The estimations of other parameters are given below.

o *Estimation of velocity:*

$$\begin{aligned}
\hat{R}_{21}(T_s) &= \frac{1}{N} \sum_{n=1}^N V_{vv}(2n) V_{hh}^*(2n-1) \\
&= M_1^* M_2 \left(\cos^2 \phi \sin^2 \theta \langle S'_{hh}^*(2n-1) S'_{vv}(2n) \rangle - 2 \cos \theta \cos \phi \sin^2 \theta \sin \phi \langle S'_{hv}^*(2n-1) S'_{vv}(2n) \rangle + \right. \\
&\quad \left. + \cos^2 \theta \sin^2 \theta \sin^2 \phi \langle S'_{vv}^*(2n-1) S'_{vv}(2n) \rangle \right) \quad (4.43) \\
&= \cos^2 \phi \sin^2 \theta M_1^* M_2 \left(\hat{R}_{vv, hh}(T_s) - 2\beta \hat{R}_{vv, hv}(T_s) + \beta^2 \hat{R}_{vv, vv}(T_s) \right)
\end{aligned}$$

where

$$\hat{R}_{vv, hh}(T_s) = \langle S'_{hh}^*(2n-1) S'_{vv}(2n) \rangle \quad (4.44)$$

$$\hat{R}_{vv, hv}(T_s) = \langle S'_{hv}^*(2n-1) S'_{vv}(2n) \rangle \quad (4.45)$$

$$\hat{R}_{vv, vv}(T_s) = \langle S'_{vv}^*(2n-1) S'_{vv}(2n) \rangle \quad (4.46)$$

and $\beta = \cos \theta \tan \phi$

Similarly,

$$\begin{aligned}
\hat{R}_{12}(T_s) &= \frac{1}{N} \sum_{n=1}^N V_{vv}^*(2n) V_{hh}(2n+1) \\
&= \cos^2 \phi \sin^2 \theta M_1 M_2^* \left(\hat{R}_{hh, vv}(T_s) - 2\beta \hat{R}_{vv, hv}^*(T_s) + \beta^2 \hat{R}_{vv, vv}(T_s) \right) \quad (4.47)
\end{aligned}$$

where

$$\hat{R}_{hh, vv}(T_s) = \langle S'_{vv}(2n) S'_{hh}(2n+1) \rangle \quad (4.48)$$

Using the approximation of the co-polar/cross-polar correlation coefficient at lag 1 (Bringi and Chandrasekar, 2001),

$$R_{vv, hh}(T_s) = R_{vv, hh}(0) \rho(T_s) \quad (4.49)$$

$$R_{hh, vv}(T_s) = R_{hh, vv}(0) \rho(T_s) \quad (4.50)$$

$$R_{vv, hv}(T_s) = R_{vv, hv}(0) \rho(T_s) \quad (4.51)$$

$$R_{hv, vv}(T_s) = R_{hv, vv}(0) \rho(T_s) \quad (4.52)$$

with $\rho(T_s)$ the correlation coefficient between signal sample at T_s .

Then, equations (4.43) and (4.47) can be written as

$$\hat{R}_{21}(T_s) = \cos^2 \phi \sin^2 \theta \rho(T_s) M_1^* M_2 \left(\hat{R}_{vv,hh}(0) - 2\beta \hat{R}_{vv,hv}(0) + \beta^2 \hat{P}_{co}^v \right) \quad (4.53)$$

$$\hat{R}_{12}(T_s) = \cos^2 \phi \sin^2 \theta \rho(T_s) M_1 M_2^* \left(\hat{R}_{hh,vv}(0) - 2\beta \hat{R}_{hv,vv}(0) + \beta^2 \hat{P}_{co}^v \right) \quad (4.54)$$

Note that $R_{hh,vv}(0) = R_{vv,hh}^*(0)$ and $R_{vv,hv}(0) = R_{hv,vv}^*(0)$ it follows that the terms in the brackets of (4.53) and (4.54) are complex conjugate. Therefore, the phase of $\rho(T_s)$ can be estimated as,

$$\arg(\hat{\rho}(T_s)) = \frac{1}{2} (\arg(R_{21}(T_s)) + \arg(R_{12}(T_s))) \quad (4.55)$$

and

$$\hat{v} = -\frac{\lambda}{4\pi T_s} \frac{1}{2} (\arg(R_{21}(T_s)) + \arg(R_{12}(T_s))) \quad (4.56)$$

○ *Estimation of differential phase Φ_{dp} :*

Due to the coupling of co-polar and cross-polar signals in (4.53) and (4.54), an estimation of Φ_{dp} cannot be done in a similar manner as in the conventional method for alternating mode (i.e., from the difference between the phases of $R_{12}(T_s)$ and $R_{21}(T_s)$). Indeed, we have to estimate $R_{hh,vv}(0)$. To do that, we need to compute the correlation coefficient between co-polar samples at lag 1, $|\rho(T_s)|$. From (4.39b),

$$\hat{\rho}(2T_s) = \frac{\sum_{n=1}^{N-1} V_{vv}(2n+2) V_{vv}(2n)}{\sum_{n=1}^N |V_{vv}(2n)|^2} \quad (4.57)$$

and by equation 6.88 in Bringi and Chandrasekar (2001), we obtain

$$|\hat{\rho}(T_s)| = |\hat{\rho}(2T_s)|^{0.25} \quad (4.58)$$

From (4.53)

$$\hat{R}_{vv,hh}(0) - 2\beta\hat{R}_{vv,hv}(0) + \beta^2\hat{P}_{co}^v = \frac{\hat{R}_{21}(T_s)}{\cos^2\phi\sin^2\theta\rho(T_s)M_1^*M_2} \quad (4.59)$$

If we substitute \hat{P}_{co}^v from (4.40) and $\hat{R}_{vv,hv}(0)$ from (4.41) into (4.59) and simplify the result, we have

$$\hat{R}_{vv,hh}(0) = \frac{1}{\cos^2\phi\sin^2\theta|M_2|^2} \left(\begin{array}{l} \frac{M_2^*}{M_1^*} \langle V_{vv}(2n)V_{hh}^*(2n-1) \rangle / \hat{\rho}(T_s) \\ + 2\alpha \langle V_{vv}(2n)V_{vh}^*(2n) \rangle + \alpha^2 \langle |V_{vv}(2n)|^2 \rangle \end{array} \right) \quad (4.60)$$

By definition,

$$\hat{\Phi}_{dp} = \arg(\hat{R}_{hh,vv}(0)) \quad (4.61)$$

o *Estimation of horizontal signal power, Z_{dr} and $|\rho_{co}|$:*

Two power and covariance $\langle |S'_{hh}|^2 \rangle$ and $\langle S'_{hv}S'_{hh}^* \rangle$ are retained as unknowns. For these, we start with the odd sequence.

$$\begin{aligned} \hat{R}_{21}(0) &= \langle V_{hv}(2n-1)V_{hh}^*(2n-1) \rangle \\ &= M_1^*M_2\cos^3\phi\sin\theta \left(\begin{array}{l} \langle S'_{hv}S'_{hh}^* \rangle - 2\beta\hat{P}_{cx} + \beta^2\hat{R}_{hv,vv}(0) - \beta\hat{R}_{vv,hh}(0) \\ + 2\beta^2(\hat{R}_{hv,vv}(0))^* - \beta^3\hat{P}_{co}^v \end{array} \right) \end{aligned} \quad (4.62)$$

$$\begin{aligned} \hat{R}_{hv,hh}(0) &= \langle S'_{hv}S'_{hh}^* \rangle \\ &= \frac{\hat{R}_{21}(0)}{M_1^*M_2\cos^3\phi\sin\theta} + 2\beta\hat{P}_{cx} + \beta\hat{R}_{vv,hh}(0) - \beta^2\hat{R}_{hv,vv}(0) - 2\beta^2(\hat{R}_{hv,vv}(0))^* + \beta^3\hat{P}_{co}^v \end{aligned} \quad (4.63)$$

Insertion of \hat{P}_{co}^v , $\hat{R}_{hv,vv}(0)$, and \hat{P}_{cx} from (4.40), (4.41), (4.42) and $\hat{R}_{vv,hh}(0)$ from (4.60) into (4.63) gives the estimate of $\hat{R}_{hv,hh}(0)$.

The co-polar power of the received H signal contains the $\langle |S'_{hh}|^2 \rangle$ term, that is

$$\begin{aligned}\hat{P}_h &= \langle |V_{vv}|^2 \rangle \\ &= |M_1|^2 \cos^4 \phi \left(\begin{aligned} &\langle |S'_{hh}|^2 \rangle + 4\beta^2 \hat{P}_{cx} + \beta^4 \hat{P}_{co}^v - 4\beta \operatorname{Re}\{\hat{R}_{hv,hh}(0)\} \\ &- 4\beta^3 \operatorname{Re}\{\hat{R}_{hv,vv}(0)\} + 2\beta^2 \operatorname{Re}\{\hat{R}_{vv,hh}(0)\} \end{aligned} \right) \end{aligned} \quad (4.64)$$

$$\begin{aligned}\hat{P}_{co}^h &= \langle |S'_{hh}|^2 \rangle \\ &= \frac{\hat{P}_h}{|M_1|^2 \cos^4 \phi} - 4\beta^2 \hat{P}_{cx} - \beta^4 \hat{P}_{co}^v + 4\beta \operatorname{Re}\{\hat{R}_{hv,hh}(0)\} \\ &\quad + 4\beta^3 \operatorname{Re}\{\hat{R}_{hv,vv}(0)\} - 2\beta^2 \operatorname{Re}\{\hat{R}_{vv,hh}(0)\} \end{aligned} \quad (4.65)$$

Substitute \hat{P}_{co}^v , \hat{P}_{cx} , $\hat{R}_{hv,vv}(0)$, $\hat{R}_{hv,hh}(0)$, and $\hat{R}_{vv,hh}(0)$ in (4.64) and we obtain the estimate of \hat{P}_{co}^h

. Consequently, the differential reflectivity and co-polar correlation coefficient are given as

$$\hat{Z}_{dr} = 10 \log_{10} \left(\frac{\hat{P}_{co}^h}{\hat{P}_{co}^v} \right) \quad (4.66)$$

$$|\hat{\rho}_{co}| = \frac{|\hat{R}_{vv,hh}(0)|}{\sqrt{\hat{P}_{co}^h \hat{P}_{co}^v}} \quad (4.67)$$

○ *Estimation of spectrum width:*

Signal spectrum width can be estimated from the V channel signal of the even sequence (4.39b) with the corresponding period of $2T_s$.

4.5 Effect of noise

The analysis thus far was done in the absence of noise. In practice, the effect of receiver noise must be considered. First, let us analyze the case of the simultaneous mode. We assume

that the horizontal and vertical transmit moments are identical $M_1 \equiv M_2$. In the presence of additive noise, equation (4.27) is re-written as

$$\begin{bmatrix} V_h \\ V_v \end{bmatrix} = M_1 \begin{bmatrix} \cos^2 \phi & \cos^2 \theta \sin^2 \phi - \cos \theta \sin \theta \sin \phi \\ 0 & \sin^2 \theta - \cos \theta \sin \theta \sin \phi \end{bmatrix} \begin{bmatrix} S'_{hh} \\ S'_{vv} \end{bmatrix} + \begin{bmatrix} \eta_h \\ \eta_v \end{bmatrix} \quad (4.68)$$

where η_h and η_v are receiver noise at corresponding channels with variances σ_h^2 and σ_v^2 , respectively. When the received signals are adjusted to the same extent with a mechanically scanned weather radar, noise components are changed accordingly

$$\begin{aligned} \begin{bmatrix} V_h^c \\ V_v^c \end{bmatrix} &= M_1 \begin{bmatrix} S'_{hh} \\ S'_{vv} \end{bmatrix} + \begin{bmatrix} \cos^2 \phi & -\cos \theta \sin \phi (-\cos \theta \sin \phi + \sin \theta) \\ 0 & \sin \theta (-\cos \theta \sin \phi + \sin \theta) \end{bmatrix}^{-1} \begin{bmatrix} \eta_h \\ \eta_v \end{bmatrix} \\ &= M_1 \begin{bmatrix} S'_{hh} \\ S'_{vv} \end{bmatrix} + \begin{bmatrix} \frac{1}{\cos^2 \phi} & \frac{\cos \theta \sin \phi}{\cos^2 \phi \sin \theta} \\ 0 & \frac{1}{\sin^2 \theta - \cos \theta \sin \theta \sin \phi} \end{bmatrix} \begin{bmatrix} \eta_h \\ \eta_v \end{bmatrix} \\ &= M_1 \begin{bmatrix} S'_{hh} \\ S'_{vv} \end{bmatrix} + \begin{bmatrix} \eta_h^c \\ \eta_v^c \end{bmatrix} \end{aligned} \quad (4.69)$$

where the superscript c denotes bias *corrected*. The resulting noise powers are

$$\text{var}(\eta_h^c) = \frac{1}{\cos^4 \phi} \sigma_h^2 + \left(\frac{\cos \theta \sin \phi}{\cos^2 \phi \sin \theta} \right)^2 \sigma_v^2 \quad (4.70a)$$

$$\text{var}(\eta_v^c) = \frac{1}{(\sin^2 \theta - \cos \theta \sin \theta \sin \phi)^2} \sigma_v^2 \quad (4.70b)$$

One of the important inferences from (4.70) is that receiver noise powers are increased after bias correction. Correspondingly, the signal-to-noise ratio (SNR) decreases. Figure 4.4 shows the SNR loss as a function of beam direction angles. It can be seen that after bias correction, loss in SNRs can be over 20 dB when the radar scans at elevation angles larger than 45° . A similar analysis is done for an even sequence in alternating mode. The noise powers after bias correction are

$$\text{var}(\eta_{vh}^c) = \frac{1}{\cos^2 \phi \sin^2 \theta} \sigma_h^2 + \left(\frac{\cos \theta \sin \phi}{\cos \phi \sin^2 \theta} \right)^2 \sigma_v^2 \quad (4.71a)$$

$$\text{var}(\eta_{vv}^c) = \frac{1}{\sin^4 \theta} \sigma_v^2 \quad (4.71b)$$

Figure 4.5 demonstrates the effect given in equation (4.71). It shows a similar trend as in fig. 4.4: SNR drops drastically at high elevations. For the odd sequence in the alternating mode, the effect cannot be given in a closed-form expression. We will analyze it via radar simulation. Unquestionably, the problem of increasing noise leads to degradation in polarimetric data quality, especially at regions with weak signals. In order to maintain the accuracy of signal parameter estimation, this effect can be partly mitigated by subtracting noise powers from co-polar and cross-polar powers before applying a bias correction algorithm. Further analysis of this topic will be presented in the next section using radar simulation.

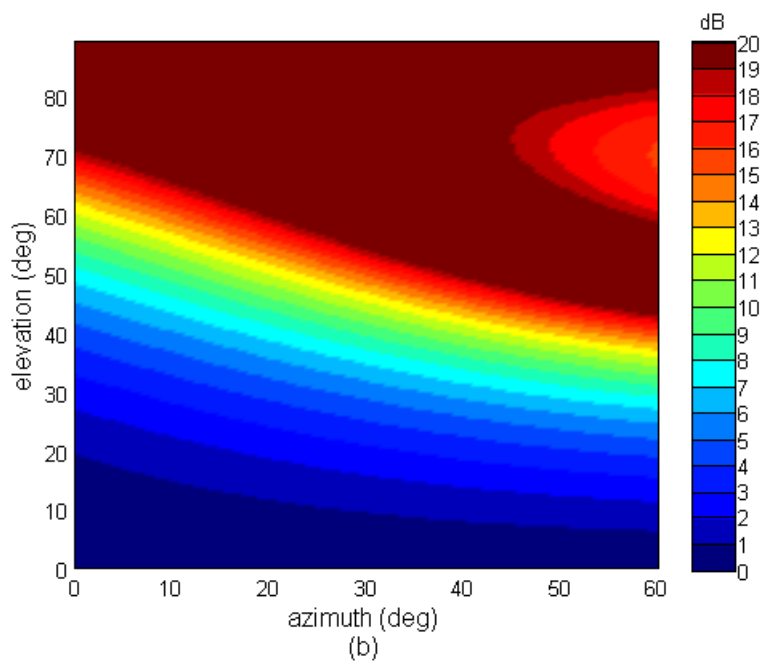
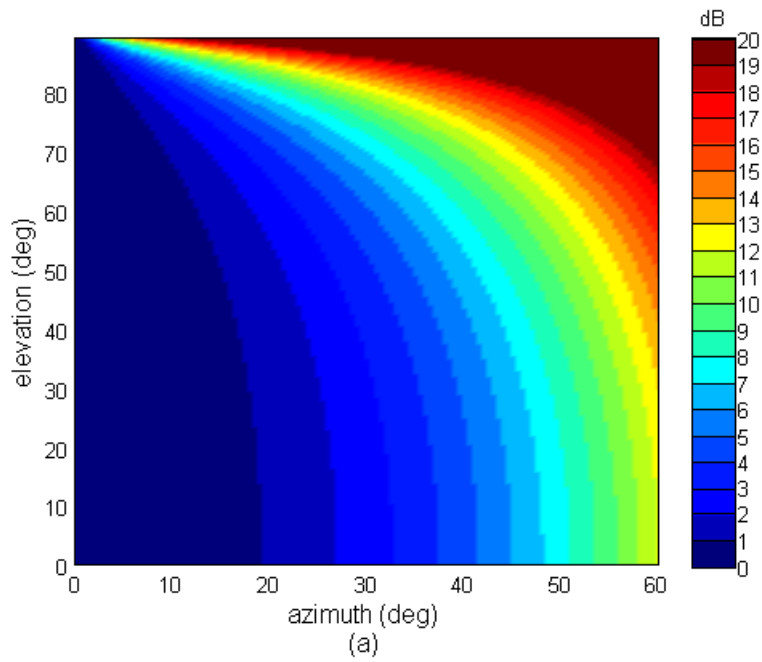


Figure 4.4: SNR loss in simultaneous mode after bias correction at the horizontal channel (a) and at the vertical channel (b).

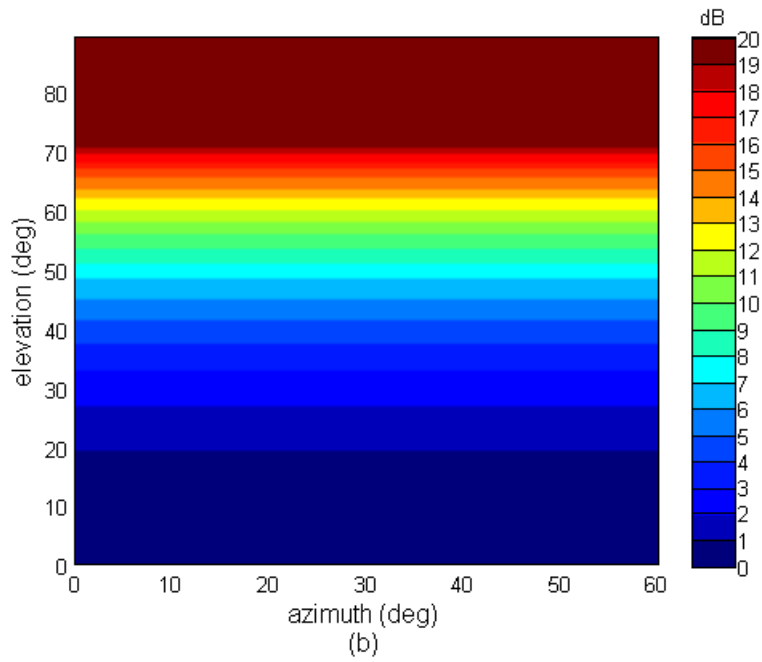
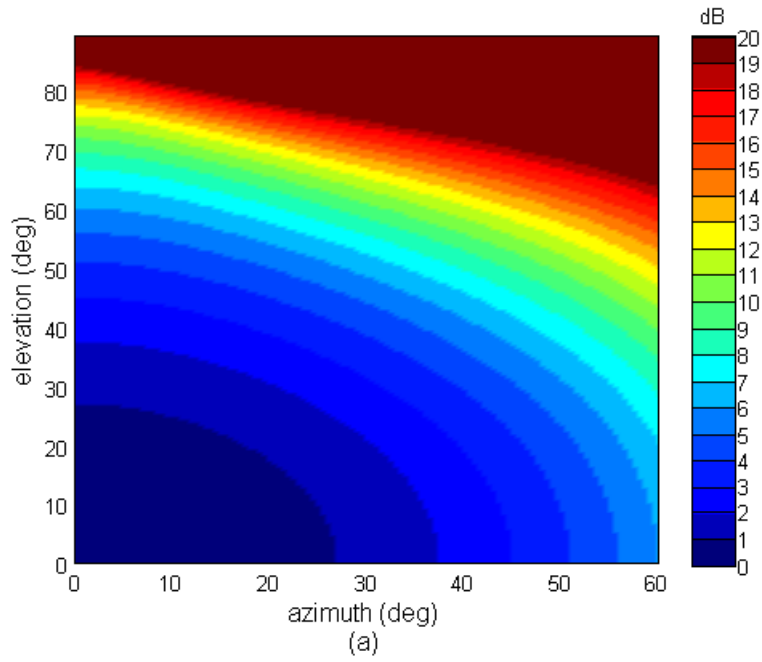


Figure 4.5: SNR loss in even sequence for alternating mode after bias correction at the horizontal channel (a) and at the vertical channel (b).

4.6 Evaluation of bias correction method using simulation

In the absence of noise, the bias correction methods described in the above section would provide unbiased estimates at any beam direction. In practice, receiver noise degrades data quality, especially polarimetric measurements. In this section, the question of how far off boresight the radar can scan without significant loss in data quality is addressed using radar simulation.

4.6.1 Signal simulation for polarimetric PAWR

The received signals of a polarimetric PAWR are simulated based on a procedure described in Chandrasekar et al. (1986). Two sets of dual-polarization signals are created. The first set is for the co-polar horizontal and vertical signals. The second set is for the cross-polar signals. We assume that

- Co-polar and cross-polar signals have the same Doppler mean velocity.
- Two co-polar (or cross-polar) signals have the same spectrum width.
- Spectrum width of cross-polar signals is slightly wider than that of co-polar signals (about 1.2 times larger).

In the alternating mode, sequences of simultaneous H and V co-polar, cross-polar signals are generated first, then appropriate pulses are dropped to construct alternate sequences. Effects of projection at direction (θ, ϕ) are implemented based on equation (4.27) for simultaneous mode and equations (4.36) and (4.39) for alternating mode. In addition, random white noise is added at each channel. In this work, the simulation is done for an S-band radar. Simulation inputs are given in table 4.1.

Table 4.1: Input for polarimetric PAWR signal simulation.

<i>Parameters</i>	<i>Values</i>
f , GHz	2.72
SNR, dB	20
LDR (V channel), dB	-30
σ_p , ms^{-1}	3
\bar{v} , ms^{-1}	$0.5v_{\max}$
$ \rho_{co} $	0.99
$ \rho_{cx} $	0.6
Φ_{dp} , deg	50
σ_N^2 , dB	14
m , samples	64
T_s , ms	1.0

4.6.2 Results for simultaneous mode

Two sets of results, one the estimates of the first three spectral moments (mean power, mean Doppler, and spectrum width) and the other the estimates of dual-polarimetric variables (differential reflectivity Z_{dr} , copolar correlation coefficient $|\rho_{co}|$, and differential phase Φ_{dp}), are shown in figs. 4.6 and 4.7, respectively. In this analysis, the azimuth angle spans from 0° to 60° and the elevation angle varies from 0° up to zenith. It is first noted that data quality degrades more rapidly in the elevation axis. Most of the measurement error plots follow a trend similar to that of the SNR loss functions, especially in the V channel (fig. 4.4). This is because V polarization is involved in the signals at both H and V channels (4.27) and its strength is proportional to the cosine of the elevation. However, in the range from -45° to 45° in both directions the bias correction method works fairly well. The estimates are unbiased and its standard deviations are acceptable for weather radar applications (ROC 2007). This observation is applied to the case where the SNR is equal to 20 dB. When the SNR is less, the effective range

for the bias correction method may be smaller. Therefore, in the design of polarimetric PAWR, the analysis needs to be done at various values of SNR.

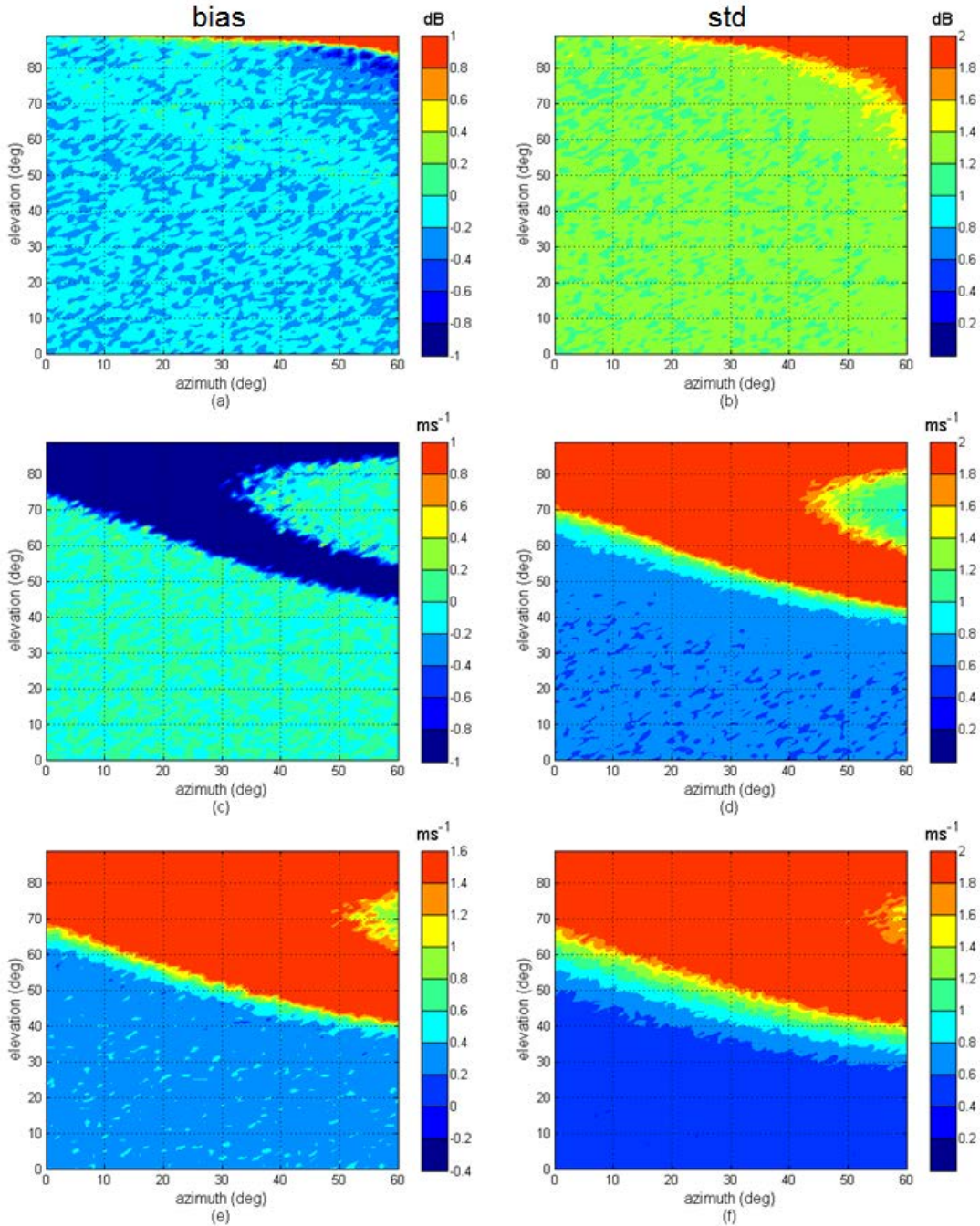


Figure 4.6: Bias and standard deviation of spectral moments estimates for polarimetric PAWR in simultaneous mode. The top row is for reflectivity, the middle row is for Doppler velocity, and the bottom one is for spectrum width.

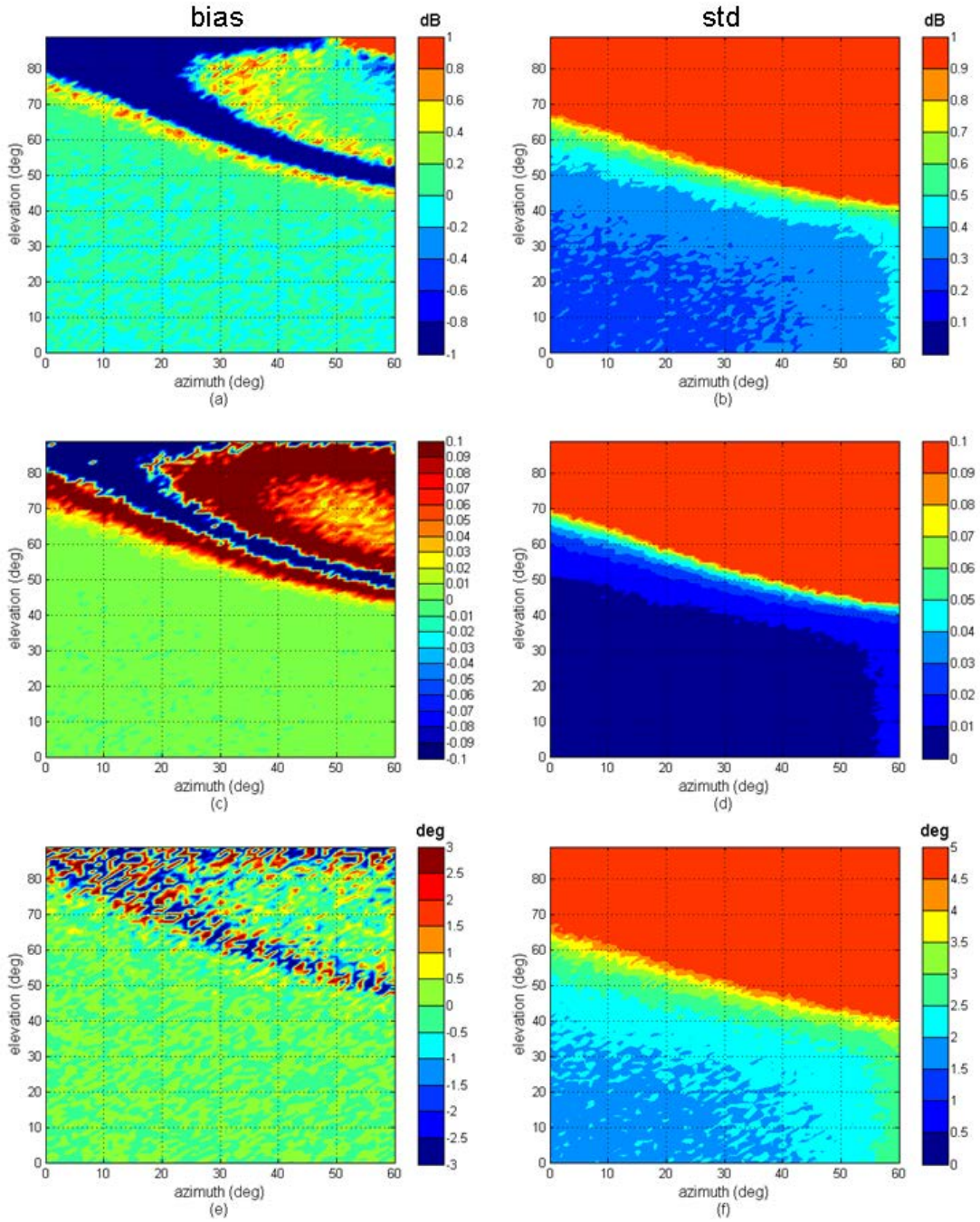


Figure 4.7: Bias and standard deviation of dual-polarization variables estimates for polarimetric PAWR in simultaneous mode. The top row is for differential reflectivity Z_{dr} , the middle row is for copolar correlation coefficient $|\rho_{co}|$, and the bottom one is for differential phase Φ_{dp} .

4.6.3 Results for alternating mode

In this mode, the azimuth and elevation ranges are set similarly to the case of the simultaneous mode. The performance of the spectral moment estimation for the alternating mode is shown in fig. 4.8. At the lower left corner of fig. 4.8a and 4.8b, the errors in power estimates are better than in the simultaneous mode. This is because the spacing between copolar samples is twice that of the simultaneous mode ($2T_s$ vs. T_s); therefore, the number of independent samples in the simultaneous mode is larger. However, due to the polarization coupling effect, the performance in power estimation degrades faster at higher azimuth and elevation angles. The velocity estimates, on the other hand, are surprisingly good. At all azimuths, unbiased velocity estimates can be achieved up to an elevation of 80° and the standard deviation is less than 0.6 ms^{-1} (figs. 4c and 4d). It is noticed that the tendency in these measurement error plots matches with that in the SNR loss plot shown in fig. 4.5b. That means the V signal in the even sequence governs the accuracy of the velocity estimates. While the velocity estimates are good, the spectrum width estimates show large biases just above 20° elevation. This may be because of the lag 0 and 1 estimator of the spectrum width at a sampling period of $2T_s$.

Results from the analysis for the dual-polarization variable retrieval are shown in fig. 4.9. In general, they are comparable to the performance in the simultaneous mode except for the standard deviation in copolar correlation coefficient estimates, which is slightly higher. This is expected in the alternating mode as the correlation of copolar signals is not available at lag 0. In this mode, the effective range for the bias correction method is also from -45° to 45° at the SNR=20 dB.

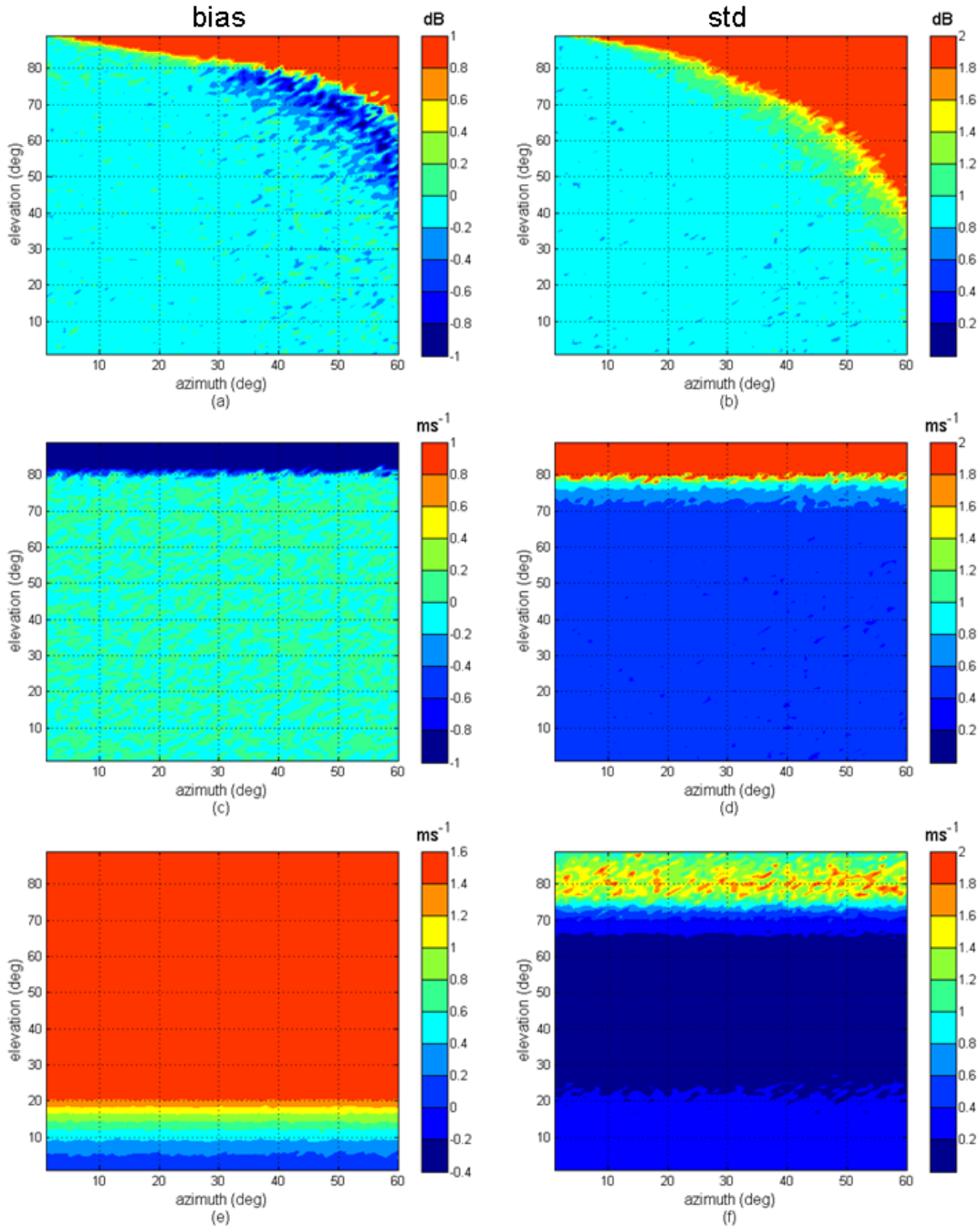


Figure 4.8: Bias and standard deviation of spectral moments estimates for polarimetric PAWR in alternating mode. The top row is for reflectivity, the middle row is for Doppler velocity, and the bottom one is for spectrum width.

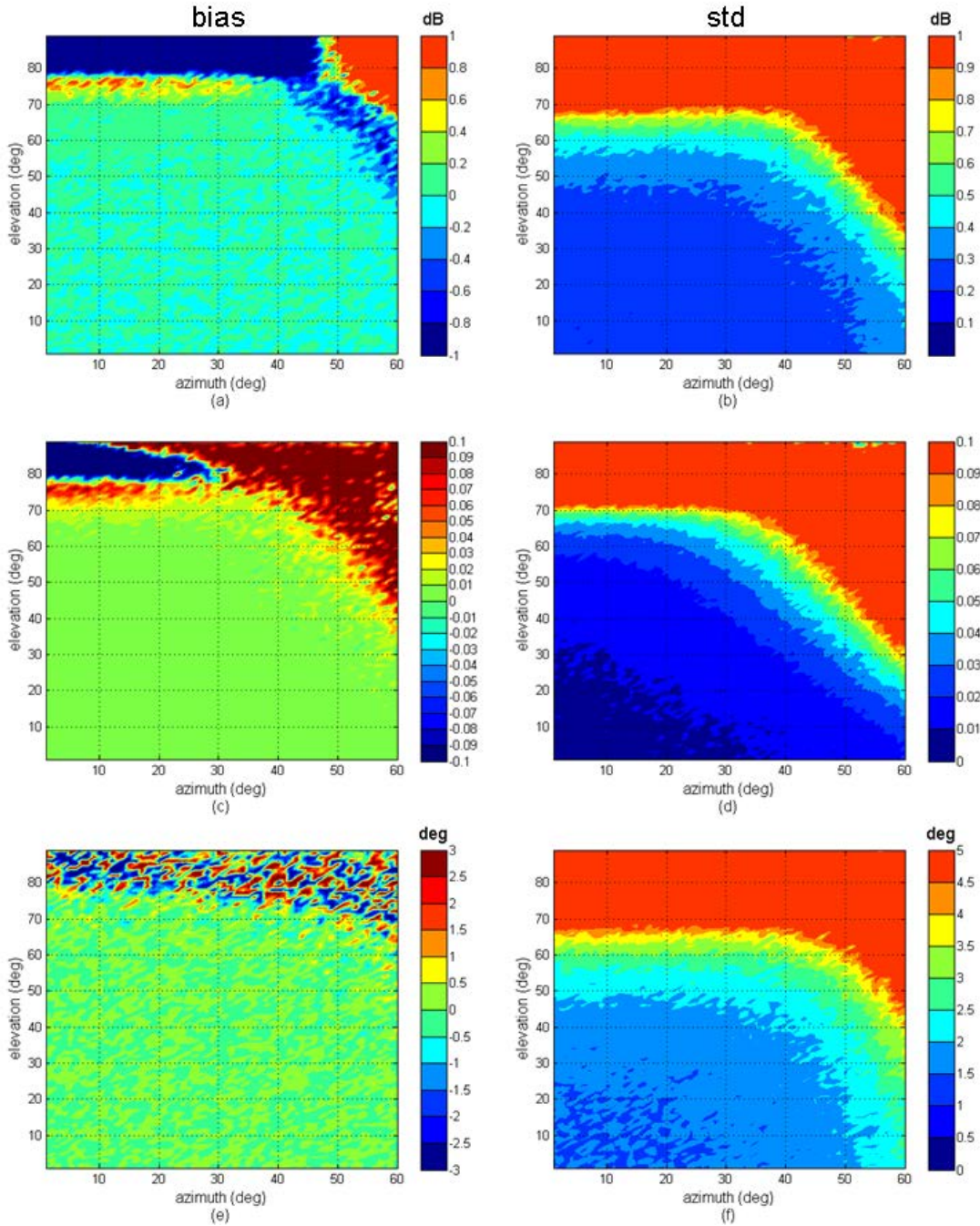


Figure 4.9: Bias and standard deviation of dual-polarization variables estimates for polarimetric PAWR in simultaneous mode. The first row is for differential reflectivity Z_{dr} , the middle row is for copolar correlation coefficient $|\rho_{co}|$, and the bottom one is for differential phase Φ_{dp} .

4.7 Summary

The polarimetric signals of an electronically scanned phased-array weather radar observing precipitation target have been studied. The array element is modeled by a pair of cross-dipoles, one for the horizontal polarization and the other for the vertical polarization. It is shown that the scattering matrix contains a complex cross-coupling between H and V polarizations due to the angular projection. As a result, the spectrum moment and dual-polarization estimates obtained by applying a standard method directly to the measured scattering matrix can produce large biases.

Methods to remove inherent biases associated with polarimetric PAWR are introduced for the simultaneous and alternating transmission modes. The correction procedures are based on the fact that the powers and correlations of the measured signals form a system of linear equations with the unknown signal covariances. In the simultaneous mode, only powers and correlations at lag 0 are used. Estimates of power, Z_{dr} , $|\rho_{co}|$, and Φ_{dp} can be directly obtained by solving systems of linear equations. Mean Doppler velocity and spectrum width are directly estimated from either the H or V signal. In the alternating mode, correlations between the odd and even sequence relate the signal covariances but they also include the effect of Doppler shift at lag 1. An approximation assumption for the correlation at lag 1 is needed. It turns out that the mean Doppler velocity can be achieved in a similar way as in the case of conventional weather radar. Then, the estimated velocity is used to de-couple the Doppler shift effects.

The bias correction procedure involves the amplitudes and phases of transmitting elements as well as those of the receivers. Therefore, precise calibration for polarimetric PAWR is mandatory to achieve unbiased polarimetric variables. In addition to the negative effect of beam broadening and increasing sidelobe levels at off-boresight directions, the quality of polarimetric estimates reduces considerably due to the loss in SNR. A signal simulation procedure for

polarimetric PAWR is developed to verify the performance of the proposed bias correction method. It is also used to investigate the effects of noise after bias correction. Using simulation, it is revealed that in the case of moderate SNR (SNR=20 dB), steering the beam by more than $\pm 45^\circ$ at both directions should be avoided to maintain acceptable data quality.

CHAPTER 5

CLUTTER FILTERING FOR BLOCK PULSING SCHEME

5.1 Introduction

Ground clutter suppression is critically important for improving the radar data quality of any weather radar system. If not removed, the clutter may produce strongly biased estimates of the fundamental spectral moments such as mean power, mean Doppler velocity, and spectrum width. For PAWR, the ground clutter issue is even more vital because the phased array antenna beamwidth and side lobe level performance are generally not as good as that of the parabolic antenna and it becomes even worse when the beam is directed off boresight. Therefore, PAWR demands a filter with a better clutter suppression ratio. Additionally, in the PAWR block pulsing transmission scheme (fig. 3.21), the received signal is not continuously sampled. In fact, it consists of many independent blocks with few samples so classical clutter filtering methods will not work on this type of data. Furthermore, to take full advantages of PAWR's capability for precipitation sensing, an adaptive waveform needs to be considered. For example, at further regions with very high radial velocity a non-uniform waveform can be used for range-velocity ambiguity problems. All these challenges require a new design of a ground clutter filter algorithm, which will be addressed in this chapter.

Conventionally, weather radar transmits and receives sequence of pulses with uniform spacing. Ground clutter can be filtered using infinite impulse response (IIR) or finite impulse response (FIR) filters. These are high-pass filters having sharp narrow notches characterized by their type, rejection depth, and the notch width. In many applications, these filters are sufficient.

However, when the signal and clutter overlap, as in the case of weather radar, the use of these filters removes clutter but also notches out a part of the signal and causes bias in the estimates. In order to mitigate this problem, advanced filtering methods have been developed. Gaussian Model Adaptive Processing (GMAP) (Siggia and Passarelli, 2004) is a frequency domain method that not only filters out clutter points but also attempts to recover precipitation components that have been removed. However, the limitation of this or any spectral filtering method is the effect of spectral leakage caused by finite data length on the estimates of signal spectral moments. In the GMAP algorithm, when clutter is strong, an aggressive window (Hamming or Blackman) is applied to isolate weather echo from clutter echo. The drawback of using data windows in spectral filtering techniques is that they effectively reduce the number of samples that are processed because samples at the beginning and end are weighted less than those in the center portion of the window (Siggia and Passarelli, 2004). This results in a higher standard deviation of the signal parameter estimates. Therefore, in practice, GMAP only works well with moderate clutter-to-signal ratios (CSR).

With the non-uniform pulsing techniques used for range-velocity ambiguity mitigation such as staggered pulse repetition time (PRT) (Skolnik, 2001), the clutter filtering problem becomes a challenge. Because of non-uniform sampling, standard clutter filters (IIR and FIR) cannot be applied directly to the staggered PRT sequences. Also, GMAP does not work directly with staggered PRT data since it requires a Fourier transform that cannot be used with a non-uniform sampling sequence. Cho and Chornoboy (2005) have defined a finite impulse response time-varying filter that can be applied to staggered PRT sequences. Torres et al. (1998) proposed a family of regression filters that operate by applying the regression polynomials to the time series. In 2000, a spectral deconvolution algorithm (Sachidananda and Zrnic 2000) was introduced to

solve the problem of clutter mitigation for staggered PRT sequences. However, those techniques suffer from large velocity errors in certain Doppler frequency bands. Moisseev et al. (2008) have extended PTDM (Nguyen et al. 2008) to the staggered PRT sampling case. It is shown that PTDM is able to mitigate ground clutter as well as accurately estimate signal spectrum moments, even in the case of a very high CSR. The results are as good as the case of uniform sampling since the covariance matrix model in PTDM adapts to the sampling scheme. Again, the drawback of PTDM is its computational load, which limits real-time implementation in today's general purpose processors.

In this chapter, we present the Gaussian model adaptive processing in the time domain (GMAP-TD) method for clutter mitigation for PAWR. The proposed algorithm addresses three important things. Firstly, it overcomes the disadvantages of spectral filter, as described above. Secondly, GMAP-TD can be applied to the staggered PRT technique used for range-velocity ambiguity mitigation. More importantly, GMAP-TD can work in the block-pulsing mode specially designed for PAWR. The computational requirement of GMAP-TD is reasonable and it can be implemented for real-time application using current general purpose processors.

5.2 Gaussian model adaptive processing – Time domain system

5.2.1 Signal model

For meteorological targets, the returned signal is the sum of the backscatter from individual hydrometeors in a radar pulse volume. Precipitation particles have widely different scattering amplitudes and move with different velocities relative to the radar. The distribution of the scatters' radial velocity can be approximated by a Gaussian distribution with a mean velocity and spectrum width. The ground clutter Doppler spectrum is also approximated by a Gaussian shape

(Doviak and Zrnic, 1993). Using those assumptions, one can write the Doppler spectrum of the radar signal of weather and clutter as follows,

$$\begin{aligned}
S(v) &= S_p(v) + S_c(v) + \eta \\
S_p(v) &= \frac{P_p}{\sigma_p \sqrt{2\pi}} \exp\left[-\frac{(v - \bar{v})^2}{2\sigma_p^2}\right] \\
S_c(v) &= \frac{P_c}{\sigma_c \sqrt{2\pi}} \exp\left[-\frac{v^2}{2\sigma_c^2}\right]
\end{aligned} \tag{5.1}$$

where $S(v)$, $S_p(v)$, $S_c(v)$ are Doppler spectra of the received signal, precipitation and clutter respectively; η is noise signal; P_p is the precipitation power, \bar{v} is the precipitation mean velocity, σ_p is the precipitation spectrum width, P_c is the clutter power, and σ_c is the clutter width. Here we assume that the radar signal includes signals coming from clutter, precipitation, and white Gaussian noise. Given the Doppler spectral representation (5.1), the auto-covariance functions for each component of the radar signal can be calculated using the inverse Fourier transform (Bringi and Chandrasekar, 2001) as

$$\begin{aligned}
R_c[\tau] &= P_c \exp\left(-\frac{8\pi^2 \sigma_c^2 \tau^2 T_s^2}{\lambda^2}\right) \\
R_p[\tau] &= P_p \exp\left(-\frac{8\pi^2 \sigma_p^2 \tau^2 T_s^2}{\lambda^2}\right) \exp\left(-j \frac{4\pi \bar{v} \tau T_s}{\lambda}\right) \\
R_N[\tau] &= \sigma_N^2 \delta(\tau)
\end{aligned} \tag{5.2}$$

where λ is wavelength, T_s is sampling period and σ_N^2 is the noise power. The subscripts p , c , N denote precipitation, clutter, and noise, respectively.

Let \mathbf{x} be the $m \times 1$ complex time sample data; its auto-covariance matrix, \mathbf{R}_x , can be written as

$$\mathbf{R}_x = \mathbf{R}_c + \mathbf{R}_p + \mathbf{R}_N \tag{5.3}$$

where \mathbf{R}_c , \mathbf{R}_p and \mathbf{R}_N are auto-covariance matrices of ground clutter, precipitation, and noise, respectively. In the case of uniform sampling with sampling rate T_s , the signal auto-covariance matrix is expressed (Bringi and Chandrasekar, 2001) as

$$\mathbf{R}_x = \begin{bmatrix} R(0) & R(T_s) & R(2T_s) & \cdots & R((m-1)T_s) \\ R(-T_s) & R(0) & R(T_s) & \cdots & R((m-2)T_s) \\ R(-2T_s) & R(-T_s) & R(0) & \cdots & R((m-3)T_s) \\ \vdots & \vdots & \vdots & \ddots & \vdots \\ R(-(m-1)T_s) & R(-(m-2)T_s) & R(-(m-3)T_s) & \cdots & R(0) \end{bmatrix} \quad (5.4)$$

For the staggered PRT transmission technique where the pulse repetition time alternates between two pulse spacings T_1 and T_2 , the signal auto-covariance matrix is given by

$$\mathbf{R}_x = \begin{bmatrix} R(0) & R(T_1) & R(T_1 + T_2) & R(2T_1 + T_2) & \cdots & R\left(\frac{m}{2}(T_1 + T_2)\right) \\ R(-T_1) & R(0) & R(T_2) & R(T_1 + T_2) & \cdots & R\left(\frac{m}{2}(T_1 + T_2) - T_2\right) \\ R(-T_1 - T_2) & R(-T_2) & R(0) & R(T_1) & \cdots & R\left(\frac{m-2}{2}(T_1 + T_2)\right) \\ R(-2T_1 - T_2) & R(-T_1 - T_2) & R(-T_1) & R(0) & \cdots & R\left(\frac{m-2}{2}(T_1 + T_2) - T_2\right) \\ \vdots & \vdots & \vdots & \vdots & \ddots & \vdots \\ R\left(-\frac{m}{2}(T_1 + T_2)\right) & R\left(-\frac{m}{2}(T_1 + T_2) + T_2\right) & R\left(-\frac{m-2}{2}(T_1 + T_2)\right) & R\left(-\frac{m-2}{2}(T_1 + T_2) + T_2\right) & \cdots & R(0) \end{bmatrix} \quad (5.5)$$

Here, the generic subscript x can be c (for clutter) or p (for precipitation).

Consider a filter \mathbf{A} of dimension $m \times m$; the auto-covariance matrix of the filter output $\mathbf{y} = \mathbf{A}\mathbf{x}$ can be written as

$$\begin{aligned} \mathbf{R}_y &= E\{\mathbf{y}\mathbf{y}^H\} = E\{(\mathbf{A}\mathbf{x})(\mathbf{A}\mathbf{x})^H\} \\ &= \mathbf{A}\mathbf{R}_x\mathbf{A}^H = \mathbf{A}(\mathbf{R}_c + \sigma_N^2\mathbf{I}_m)\mathbf{A}^H + \mathbf{A}\mathbf{R}_p\mathbf{A}^H \end{aligned} \quad (5.6)$$

where $E\{\bullet\}$ is the expectation operator and superscript H denotes a complex conjugate transpose.

The first term in the sum (5.6) is the response of the filter to signal from ground clutter and noise. In the case of no weather echo in the received signal (i.e., $\mathbf{R}_p = \mathbf{0}$) we want the output signal to have the auto-covariance matrix similar to that of a white noise process

$$\mathbf{R}_y = \mathbf{A}(\mathbf{R}_c + \sigma_N^2 \mathbf{I}_m) \mathbf{A}^H \approx \sigma_N^2 \mathbf{I}_m \quad (5.7)$$

In other words, the filter \mathbf{A} attenuates the clutter signal to a level comparable to the noise level, and does not whiten the clutter signal. The result is that the noise level of the output signal is the same as that of the input signal. It is an important property of this filtering process and therefore, we do not have to re-estimate the noise power and do not have to re-design the filter matrix \mathbf{A} for each step of the interpolation loop (see section 5.2.3). The equation (5.7) is termed the *filter equation*.

5.2.2 Clutter transformation matrix

Estimates of the first three signal spectral moments, i.e. the mean power, mean velocity, and spectrum width depend solely on the auto-covariance function of the filtered signal. It should also be noted that the auto-covariance function only depends on the signal power spectral density via the inverse Fourier transform. In other words, since the phase response of the filter is not involved in the transformation of the power spectral density of the signal, it has no effect on the auto-covariance function of the filter output and consequently, the phase response of the filter does not affect the signal spectral moment estimates. Therefore, in the design of the GMAP-TD filter, we can ignore the phase response of filter \mathbf{A} . It is relatively easy to prove that for any choice of matrix \mathbf{A} satisfying the filter equation (5.7), the power spectral density of the filter output is the same. For simplicity, in this work the clutter filter \mathbf{A} is chosen as

$$\mathbf{A} = (\mathbf{R}_c / \sigma_N^2 + \mathbf{I}_m)^{-1/2} \quad (5.8)$$

where, $(-1/2)$ power denotes the matrix square root. The solution (5.8) always exists since the auto-covariance matrix \mathbf{R}_c is a Hermitian positive semidefinite matrix as is the matrix $\mathbf{R}_c / \sigma_N^2 + \mathbf{I}_m$. It is straightforward to verify that filter \mathbf{A} satisfies the filter equation (5.7).

The clutter filter \mathbf{A} shown in (5.8) is an adaptive filter. It is a function of the clutter power, clutter spectrum width, and noise power at a given range gate that are generally unknown. In order to design filter \mathbf{A} , these parameters must be estimated from the time series data. Methods to estimate clutter power (P_c) and signal noise power (σ_N^2) for uniform sampling data are fairly straightforward and are described in the literature (e.g., Siggia and Passarelli, 2004). The clutter spectrum width σ_c can be chosen from predetermined values based on the antenna beamwidth and scan rate (Zrnic et al. 1993). For instance, for CSU-CHILL S-band radar, the ground clutter width is approximate 0.2 m s^{-1} at a scan rate of 8 deg s^{-1} .

The frequency response of a time-invariant filter can be defined by the Fourier transform of its impulse response. This definition cannot be applied to a general linear filter such as filter \mathbf{A} (5.8). However, a power frequency response at frequency w can be defined as the power of the output signal when a complex exponential signal $e^{jw\tau}$ is passed through the system. Figure 5.1 demonstrates the power frequency response of filter \mathbf{A} using (5.8) for the uniform sampling case. The depth of the notch at zero in fig. 5.1 depends on the relative ratio between the clutter power and noise power (in this case, 60 dB). Figure 5.2 shows an example of signal power spectrum before and after applying the clutter filter \mathbf{A} to the time series data. When applying matrix \mathbf{A} to the time series data, the ground clutter spectrum will be transformed to a “flat” spectrum. The width of this transformed spectrum depends on the clutter spectrum width (σ_c) and the clutter power (P_c) and is much narrower than the signal Doppler range. The amplitude of this

transformed spectrum depends on the ratio P_c / σ_N^2 (eqs. (5.2) and (5.8)), and if the clutter and noise power are estimated correctly, it equals the received signal noise power. In practice, the variance in clutter and noise power estimates may cause this level to vary within a few dBs. However, the width of the clutter-transformed spectrum is relatively small (a few tenths of ms^{-1}) and this error does not significantly affect the GMAP-TD performance.

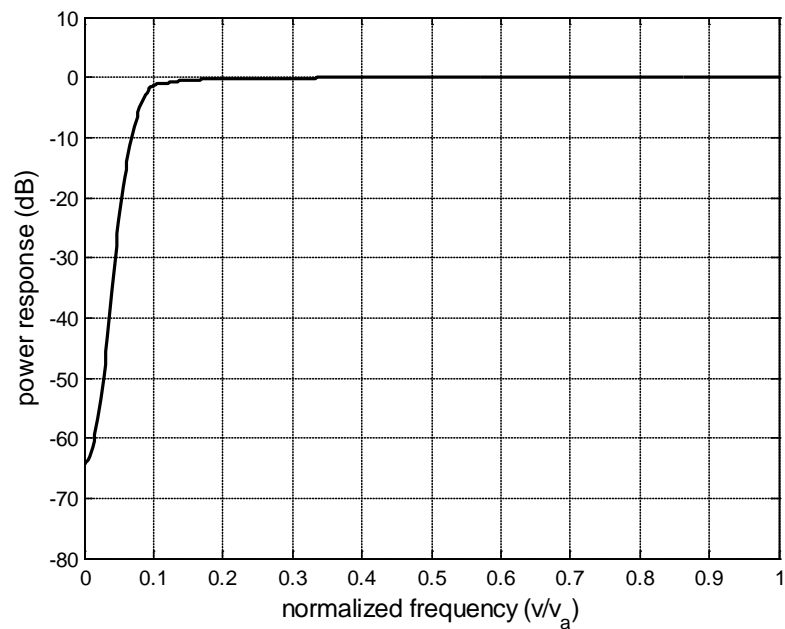


Figure 5.1: Power response of filter matrix A for the uniform sampling case with clutter-to-noise ratio $CNR = 50dB$, clutter spectrum width $\sigma_c = 0.3ms^{-1}$.

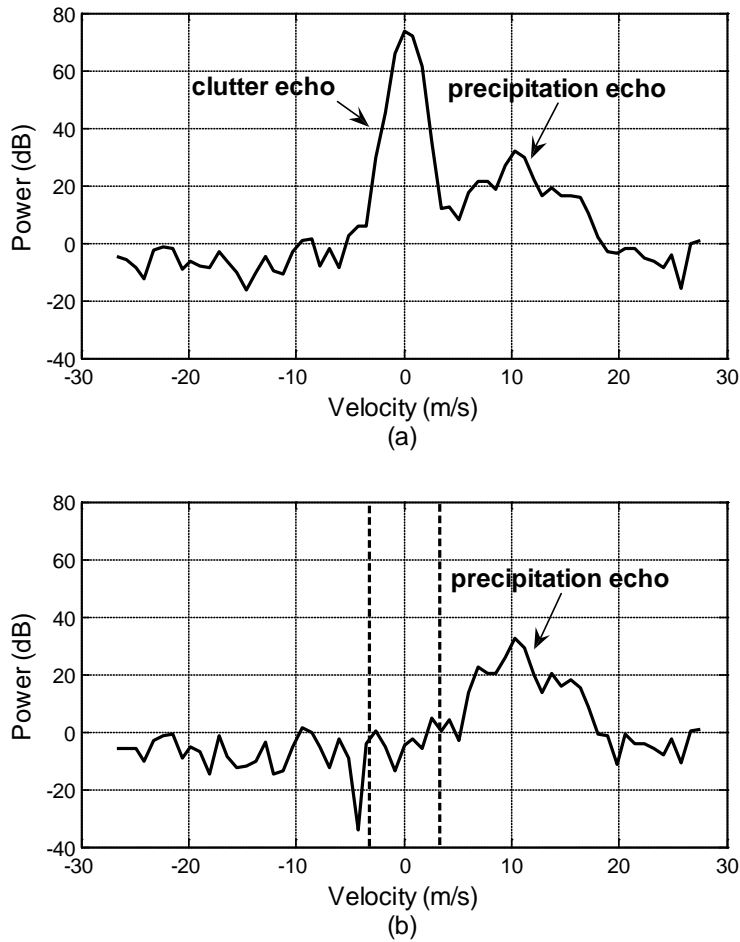


Figure 5.2: Example of signal spectrum before and after applying the filter matrix \mathbf{A} .

5.2.3 Signal interpolation procedure

In the second term of (5.6) one can see that the auto-covariance of the precipitation signal \mathbf{R}_p is modified. This is because part of the precipitation echo overlapping the clutter is also transformed to noise. To mitigate this problem, an interpolation procedure is developed to recover the transformed part of the weather echo. The main goal of this procedure is to ensure that the signal auto-covariance matrix has a Gaussian form (as assumed in section 2.1). After applying the clutter filter \mathbf{A} , this property may not hold. By finding the difference between a

Gaussian-fitted model before and after filtering, then compensating for the transformed part of the covariance function via a loop, it is possible to recover the lost portion of the signal. Figure 5.3 describes this concept. Firstly, the covariance matrix $\hat{\mathbf{R}}_y = \mathbf{A}\mathbf{x}\mathbf{x}^H \mathbf{A}^H$ is used as the initial input of the iteration, where $\hat{\mathbf{R}}_y$ is the sample auto-correlation matrix of the signal where clutter has been transformed to noise. It is similar to the spectral coefficients of weather echo after discarding clutter and noise coefficients in GMAP. Secondly, signal spectral moments (mean power (\hat{P}_p), mean velocity (\hat{v}) and spectrum width ($\hat{\sigma}_p$)) are estimated from the filtered covariance matrix $\hat{\mathbf{R}}_y$. It should be noted that the k th diagonal of the covariance matrix comes from samples of the auto-covariance function at lag k . As the signal parameters are estimated, a Gaussian model for precipitation is constructed using equations (5.2) and (5.4) (or (5) for the staggered PRT case). Next, the difference of the model before and after applying filter \mathbf{A} is computed and used to update the filtered covariance matrix $\hat{\mathbf{R}}_y$. This procedure is repeated until the power difference and/or the velocity difference between two consecutive iterations is/are less than certain predetermined thresholds. This can be considered as a cost function optimization. Tests conducted on radar data showed that thresholds of 0.1 dB and 0.5% of the Nyquist velocity provide good performance and the interpolation procedure will converge after a few steps. The final result will yield a signal after mitigating ground clutter.

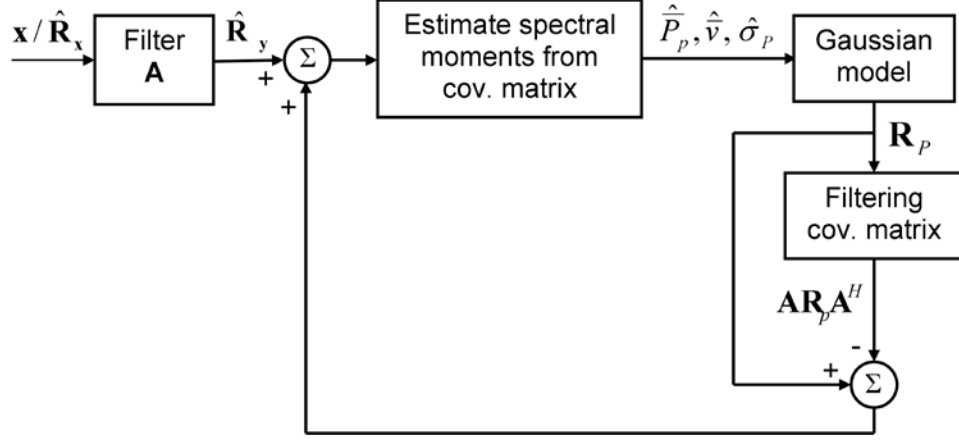


Figure 5.3: The architecture of the GMAP-TD system.

5.3 GMAP-TD filter for staggered PRT

The staggered PRT scheme (Skolnik, 2001) is used to resolve the range-velocity ambiguity problem and is described in fig. 5.3. For the fast-scanning strategy in PAWR, this scheme is preferred over other non-uniform sampling methods such as dual-PRF because it can achieve the same or better performance with a smaller dwell time (Nguyen et al. 2007). In the staggered PRT scheme, the pulse spacing alters between two pulse intervals, T_1 and T_2 , and the maximum unambiguous velocity is defined by $v_a = \lambda / [4 * (T_2 - T_1)]$ ($T_2 > T_1$) (Moisseev et al. 2008). Generally, T_1 and T_2 , are chosen as multiples of a certain unit time, T_u . It is shown that for the pulse pair estimator, the optimal PRT ratio T_1/T_2 is $2/3$ (Zrnic and Mahapatra, 1985). Theoretically, GMAP-TD can be directly applied to staggered PRT data. However, there are some practical considerations that need to be addressed to make GMAP-TD work well in this scheme. In this section, the application of GMAP-TD to a $2/3$ pulse ratio (staggered PRT $2/3$) is studied.

The first consideration is clutter and dynamic noise power estimates for staggered PRT. In the uniform sampling case, GMAP-TD uses the method described in Siggia and Passarelli (2004). This method estimates clutter power and dynamic noise power from signal spectrum points. However, in the case of staggered PRT, a signal spectrum is not available or at least cannot be obtained directly from the time series data. Here, the staggered PRT time series is zero-interpolated to form a uniform sequence with a sampling rate of T_u . The spectrum of this zero interpolated data includes some replicas of clutter and weather echoes at certain frequencies (Bringi and Chandrasekar, 2001). However, the clutter echo is still located at zero frequency and the method used by Siggia and Passarelli (2004) can be applied to this data to obtain clutter and noise power. It should be noted that GMAP-TD uses the signal power spectrum to calculate only clutter and dynamic noise powers.

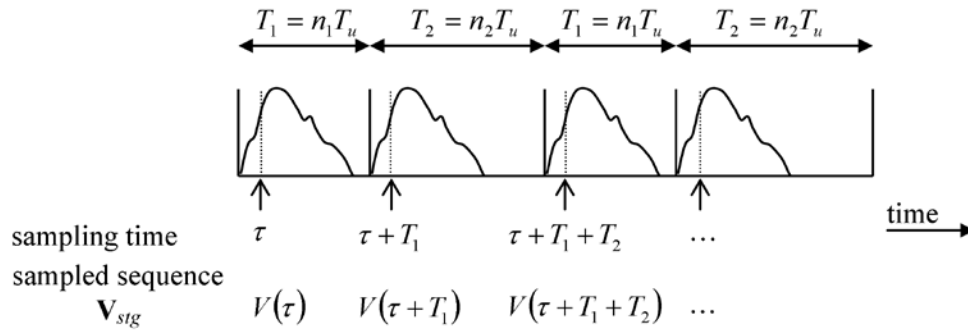


Figure 5.4: The staggered PRT transmission scheme.

The second consideration is estimation accuracy. Clutter filters that have been designed for staggered PRT sequences (Cho and Chornoboy 2005) suffer from unwanted notches in certain Doppler frequency bands. These unwanted notches introduce errors in signal estimates that limit the application of these algorithms in practice. The top panel in fig. 5.5 shows the power

response of the GMAP-TD filter for the staggered PRT 2/3 waveform. It can be seen that there are unwanted notches center at velocities $v = \pm 0.4v_a$ and $v = \pm 0.8v_a$. When the weather echo is present in the unwanted notches regions, part of the signal will be affected and estimation errors will occur. Because part of the signal is removed by the unwanted notch, its power will be underestimated. In section 5.2.c, we have explained how the GMAP-TD interpolation procedure (fig. 5.2) recovers portion of the signal removed by the main notch of the filter. Similar discussion can be applied to the unwanted notches of the filter. Hence, this bias error can be mitigated by the interpolation loop in GMAP-TD. In addition to the power bias, GMAP-TD velocity estimates show an increase in standard deviation that is similar to the analysis in Sachidananda et al. (2000). As we observe in the case of staggered PRT 2/3, at those specific cases, estimated velocities can be off by $\pm 0.4v_a$ or $\pm 0.8v_a$ which are equal to the spacings between unwanted notches. In general, it has the form of $\pm 2kv_a / (n_1 + n_2)$ where $k = 1, 2, \dots, \text{Int}((n_1 + n_2)/2)$ for staggered PRT n_1/n_2 . This error occurs because signal and its spectral replicas fall into unwanted notches with different depths and the estimator may pick up a replica signal instead of the correct one. To mitigate this problem, we modify filter \mathbf{A} to \mathbf{A}_{mod} such that filter \mathbf{A}_{mod} will have an equal notch depth at the frequencies $v = \pm 0.4v_a$ and $v = \pm 0.8v_a$. The modified filter \mathbf{A}_{mod} is shown as follows:

$$\mathbf{A}_{\text{mod}} = \mathbf{A} + \mathbf{A}_{0.4} + \mathbf{A}_{-0.4} + \mathbf{A}_{0.8} + \mathbf{A}_{-0.8} \quad (5.9)$$

where $\mathbf{A}_{\pm 0.4}$ and $\mathbf{A}_{\pm 0.8}$ are frequency-shifted versions of \mathbf{A} . That is, the frequency response of $\mathbf{A}_{\pm 0.4}$ has the main notch at $v = \pm 0.4v_a$ and the main notch of $\mathbf{A}_{\pm 0.8}$ is at $v = \pm 0.8v_a$.

$$\begin{aligned} \mathbf{A}_{\pm 0.4} &= \left(\mathbf{R}_{c, \pm 0.4} / \sigma_N^2 + \mathbf{I}_m \right)^{-1/2} \\ \mathbf{A}_{\pm 0.8} &= \left(\mathbf{R}_{c, \pm 0.8} / \sigma_N^2 + \mathbf{I}_m \right)^{-1/2} \end{aligned} \quad (5.10)$$

Matrices $\mathbf{R}_{c, \pm 0.4}$ and $\mathbf{R}_{c, \pm 0.8}$ are formed based on (5.5) and their elements are defined as,

$$\begin{aligned} R_{c, \pm 0.4}[\tau] &= P_c \exp\left(-\frac{8\pi^2 \sigma_c^2 \tau^2}{\lambda^2}\right) \exp\left(-j \frac{(\pm)0.4\pi\tau}{T_u}\right) \\ R_{c, \pm 0.8}[\tau] &= P_c \exp\left(-\frac{8\pi^2 \sigma_c^2 \tau^2}{\lambda^2}\right) \exp\left(-j \frac{(\pm)0.8\pi\tau}{T_u}\right) \end{aligned} \quad (5.11)$$

The power frequency response of the resulting filter \mathbf{A}_{mod} is shown in fig. 5.5b. It should be noted that the depth of the notches in the modified filter \mathbf{A}_{mod} are greater than that of the filter \mathbf{A} at zero frequency because placing additional notches has an impact on the notch at zero frequency. The modified filter \mathbf{A}_{mod} is only used to remove the potential offset in the estimated velocity, while the rest of the algorithm uses the original filter \mathbf{A} (eq. 5.8). The performance of this technique is shown in the next section using radar simulation. Beside these modifications, GMAP-TD processing for a staggered PRT sequence is similar to the case of uniform data and it would provide similar performance when applied to the uniform sample case.

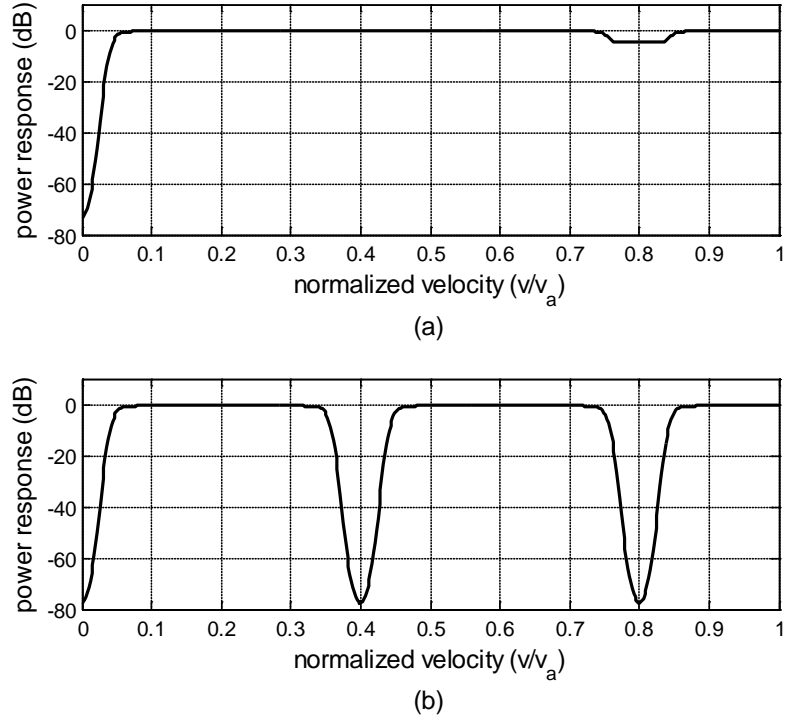


Figure 5.5: (a) The power response of filter matrix \mathbf{A} for staggered PRT 2/3 waveform with $CNR = 60dB$, $\sigma_c = 0.3ms^{-1}$. (b) The power response of modified filter matrix \mathbf{A}_{mod} for the velocity de-aliasing solution.

5.4 Performance of GMAP-TD using signal simulation

Extensive analysis of the performance of GMAP-TD has been carried out with radar signal simulation. The simulation procedure follows the work of Chandrasekar et al. (1986) with various input parameters. In order to evaluate GMAP-TD, results from a spectral filter (SF) that is implemented similarly to GMAP (Siggia and Passarelli 2004) are also presented for comparison. This SF is extensively tested and it is demonstrated that it can provide similar results to those reported in Ice et al. (2004). In the present work, where the clutter suppression performance is emphasized, attention is devoted to the cases of moderate CSR ($CSR = 40dB$)

and very high CSR ($CSR = 55dB$). In GMAP-TD and SF, dynamic noise power estimation is used. The simulation input parameters are given in Table 5.1.

Table 5.1: Simulation input parameters.

<i>Parameters</i>	<i>Values</i>
f , GHz	2.72
CSR, dB	40, 50, 55
SNR, dB	10, 20
σ_c , ms^{-1}	0.25
σ_p , ms^{-1}	2, 4
\bar{v} , ms^{-1}	$0, 0.05v_{\max}, 0.1v_{\max} \dots v_{\max}$
σ_N^2 , dB	14
m , samples	64
T_s , ms	1.0
T_u , ms	0.5
T_1/T_2	2/3

5.4.1 Uniform sampling case

For a uniform pulsing scheme with pulse repetition time T_s , the maximum unambiguous velocity is $v_a = \lambda/(4T_s)$ (Bringi and Chandrasekar, 2001). In this case, GMAP-TD performance will be directly compared to GMAP. In the first scenario, where the clutter is moderate, ($CSR = 40dB$), both GMAP-TD and GMAP perform well. It is noted that in GMAP a Blackman window is used (Siggia and Passarelli 2004). Figure 5.6 summarizes the performance of GMAP-TD and presents a comparison against GMAP. In fig. 5.6, GMAP-TD results are shown in solid lines while dashed lines represent GMAP. The first row in fig. 5 shows the errors for power estimates. For large velocity ($\bar{v}/v_a > 0.3$), GMAP-TD and GMAP perform equally in term of power biases. Both perform well as power biases are within 0.5 dB, even for this high CSR.

However, when the signal locates close to clutter ($\bar{v}/v_a < 0.3$), the difference in power bias is more obvious between the two methods. At small velocity, where clutter strongly overlaps precipitation echo in the GMAP method, the clutter spectrum was broadened due to the impact of the Blackman window used in GMAP; therefore, more signal will be removed compared to the GMAP-TD method. This explains why GMAP-TD has lower power biases compared to that of GMAP for small velocities. For velocity and spectrum width estimates, GMAP-TD biases are less than 0.5 ms^{-1} at all Doppler ranges for the case of $\text{CSR} = 40 \text{ dB}$.

The left column in fig. 5.6 shows a comparison in standard deviations of the three spectral moment estimates. Clearly, GMAP-TD shows an improvement over the GMAP in the standard deviation of the estimates in all parameters analyzed here. The higher standard deviation in the spectral-based method can be explained by the effect of the data window applied to the time series, in this case the Blackman window (Siggia and Passarelli 2004). On the other hand, GMAP-TD uses time domain processing and avoids the use of any data window. The standard deviations in power and velocity estimates of GMAP-TD are about 0.5 dB and 0.5 ms^{-1} less than that of GMAP, respectively.

For the second scenario, both the GMAP-TD and GMAP methods are tested with simulated data with very strong clutter contamination and fairly weak precipitation echo strength ($\text{CSR} = 55\text{dB}$ and $\text{SNR} = 10\text{dB}$). The results are summarized in fig. 5.7. In GMAP, a Blackman window was applied to the data. Because the peak side-lobe level of a Blackman window is -57 dB (Oppenheim, 2009), the clutter side lobe is only 2 dB below the clutter-to-signal level; thus, the spectral leakage from clutter is significantly strong when compared to the weather echo. Applying a Gaussian curve to fit three central components of clutter (step 3 in Siggia and Passarelli 2004) will not completely remove these leakage points because they are outside the

Gaussian curve. These clutter spectral leakage signals will add to the signal spectrum. This explains the overestimation in power estimate and the underestimation in velocity estimate by GMAP (fig. 5.7). The GMAP performance is compromised in such extreme scenarios. In contrast, GMAP-TD does not use a Blackman window; therefore, it does not suffer from its effect. The limitation of spectral filtering techniques caused by the effect of spectral leakage has been addressed with GMAP-TD.

In summary, for uniform sampling, GMAP-TD biases were shown to be as good as or better than that of GMAP. In addition, by avoiding the use of data windows, GMAP-TD provides lower standard deviations in all signal parameter estimates. It performs well even in cases of very strong clutter contamination (e.g., CSR is as high as 55 dB) where GMAP does not perform favorably.

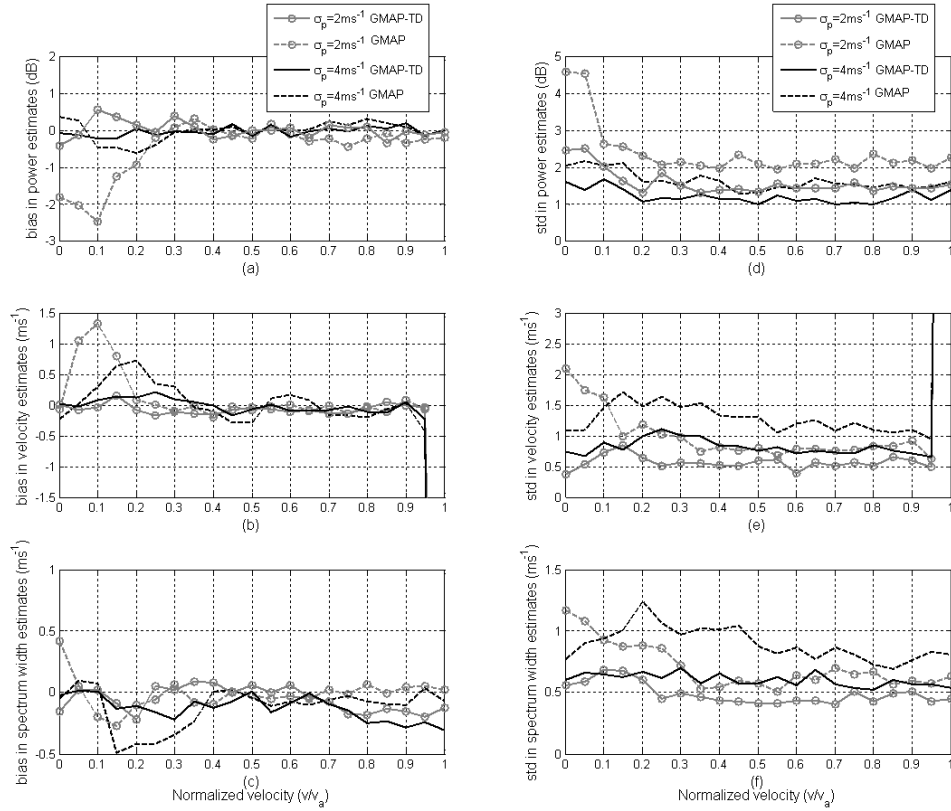


Figure 5.6: Error analysis for GMAP-TD filter and the GMAP filter in case of uniform sampling. Simulated data with $SNR = 10\text{dB}$, $CSR = 40\text{dB}$, signal spectrum width σ_p of 2 and 4 m/s and number of samples of 64. The left column is for bias and the right column is for standard deviation. Solid lines are for GMAP-TD results and dashed lines for GMAP.

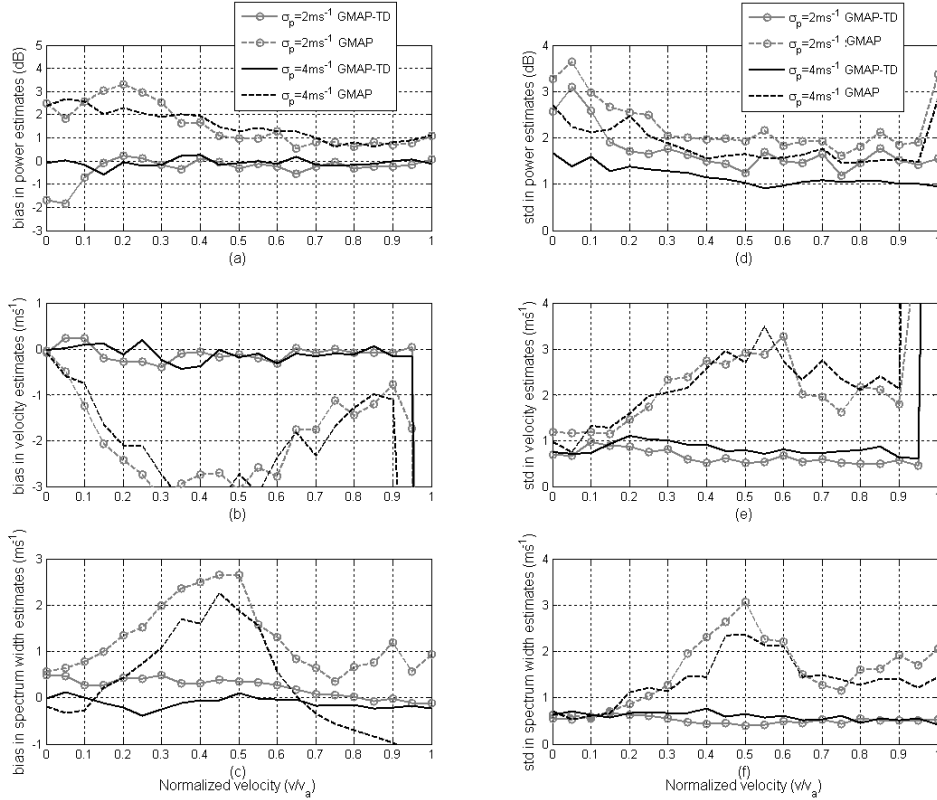


Figure 5.7: Same as in fig. 5 but $CSR = 55dB$. In this case, GMAP breaks in velocity and spectrum width estimates.

5.4.2 Staggered PRT 2/3 sampling case

The other major advantage of GMAP-TD over GMAP is that it can be directly extended to non-uniform sampling schemes such as the staggered PRT 2/3. For staggered PRT techniques, velocity estimate is the most challenging process (Sachidananda and Zrnic, 2000). For that reason, in this case simulation was carried on with a signal spectrum width of 4 m s^{-1} . The input parameters are $SNR = 20dB$, $CSR = 50dB$ and the staggered PRT sequence has a length of 64 samples. Figure 5.8 shows a scatter plot for velocity estimates using GMAP-TD. One hundred realizations comprise the simulations. It is shown that the estimated velocities are very close to the true values and there is almost no outlier. At the Doppler regions where the replicas of

ground clutter occur (Sachidananda and Zrnic, 2000), there is no increase in the estimation bias. More detailed analysis of GMAP-TD performance in this scenario is given in fig. 5.9. In addition to the GMAP-TD results, pulse pair (PP) estimates for simulated staggered PRT 2/3 data with the same input parameters but without clutter are also shown. These are considered to be the baselines and will be used to gauge GMAP-TD performance in this analysis. As shown in fig. 5.9, in most cases, GMAP-TD power and velocity biases are very close to pulse pair performance in the non-clutter environment. Moreover, the standard deviations of velocity and spectrum width estimates are better with GMAP-TD (figs. 5.9e and 5.9f). This can be explained by the use of the interpolation loop in GMAP-TD (fig 5.2). Basically, the loop updates the Gaussian model of the signal at each step and GMAP-TD outputs are obtained when the loop converges (after several iterations). The convergence helps reduce the variation in the estimated values. On the other hand, the PP method computes signal velocity and spectrum width directly from lag 1 and 2 of the signal auto-covariance function.

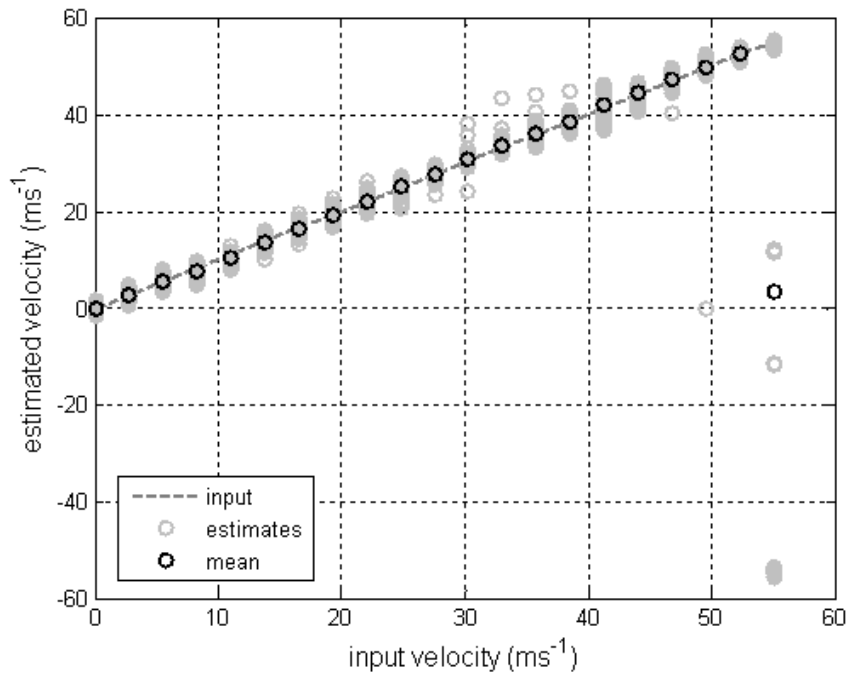


Figure 5.8: A scatter plot for velocity estimates for staggered PRT 2/3 with $CSR = 50\text{dB}$, $SNR = 20\text{dB}$ and $\sigma_p = 4\text{ms}^{-1}$ using GMAP-TD. The maximum unambiguous velocity in this case is 55ms^{-1} .

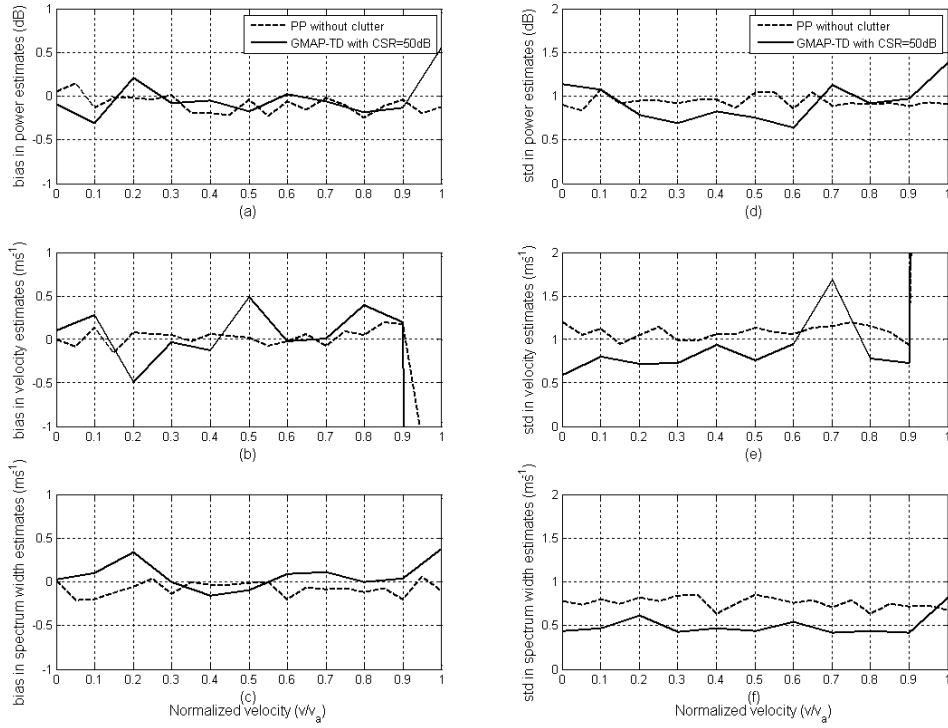


Figure 5.9: Bias and standard deviation of power, mean velocity and spectrum width estimates for staggered PRT 2/3 using GMAP-TD (solid lines) with $CSR = 50dB$, $SNR = 20dB$, $\sigma = 4ms^{-1}$ and 64 samples. For comparison, pulse pair (PP) estimator's results with the same parameters but without clutter are plotted (dashed lines).

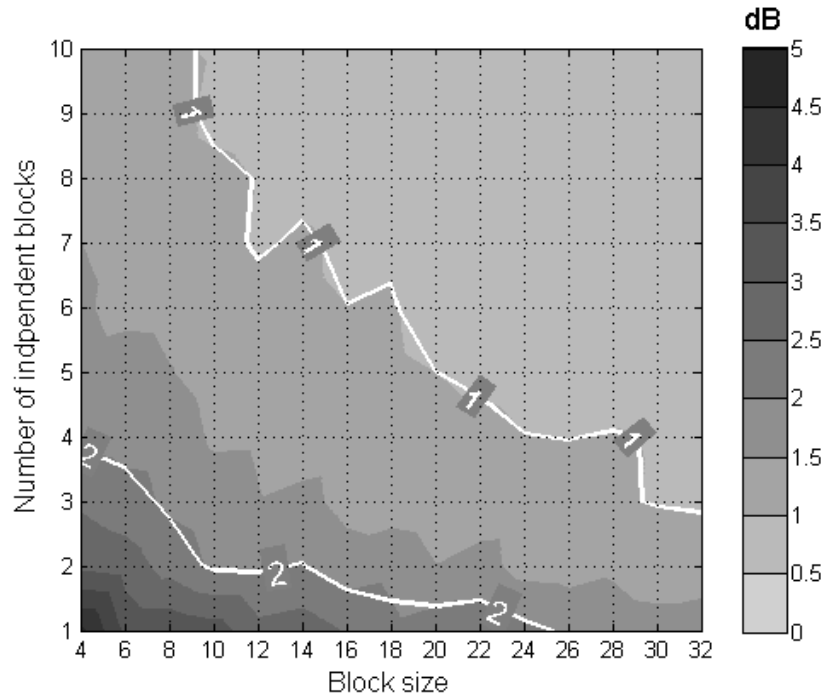
5.4.3 Application to block sampled data

In designing the GMAP-TD algorithm, the size of the covariance matrix (m) is configurable. This is very important feature of GMAP-TD because it allows GMAP-TD to work in PAWR block-pulsing mode. A signal covariance matrix is generated from each block of length m and then is averaged over all blocks. Block data are independent, as is the covariance matrix. This helps to reduce the variance of the average covariance matrix and, therefore, improves GMAP-TD performance. In fact, the three factors determining GMAP-TD performance are block size, number of independent blocks, and ground clutter level. For example, for a given CSR the same

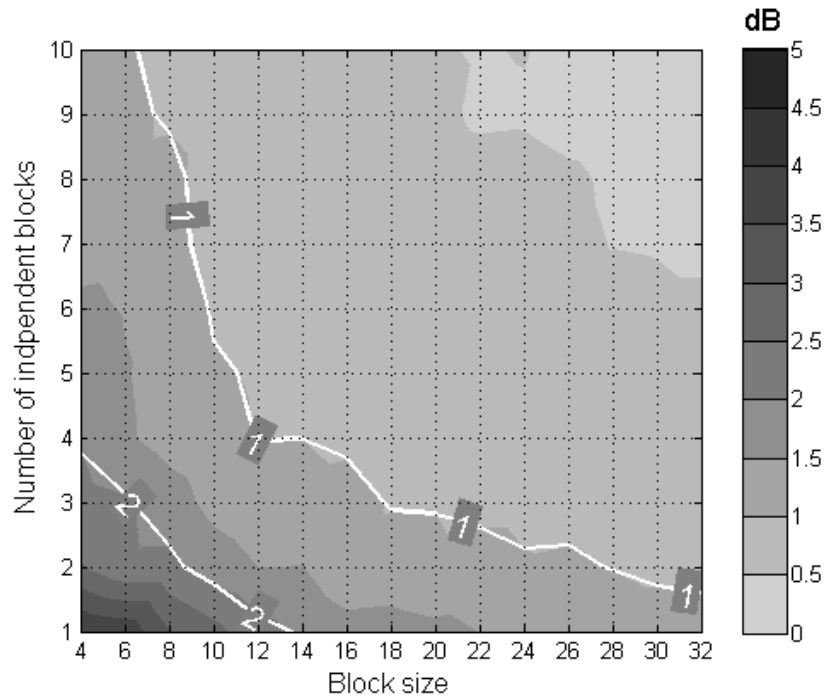
performance can be achieved by either using a larger block size or increasing the number of blocks. These factors are trade-offs and need to be taken into account when designing waveform for PAWR.

In this section, the performance of GMAP-TD is evaluated with different combinations of block size, number of blocks, and CSR. A uniform waveform is used within each block. A standard deviation of power estimate is used to gauge the GMAP-TD performance. The first analysis is done by fixing CSR and varying the other factors. Low CSR (20 dB) and moderate CSR (40 dB) are used and results are shown in fig. 5.10 and fig 5.11, respectively. White contour lines are superimposed at $std(P) = 1$ and $std(P) = 2$. It can be seen that GMAP-TD works pretty well even with a small block size. In most situations, 6 blocks of 8 samples would provide $std(P) \leq 1.5$ dB. In an extreme case, where CSR=40 dB and spectrum width is as small as $2ms^{-1}$, a block size of 10 can be used to obtain $std(P) \leq 1$ dB. This demonstrates that GMAP-TD is a very promising filtering algorithm for PAWR.

In the second analysis, we study the performance of GMAP-TD at various CSR levels (fig. 5.12). Block size is fixed at 8. Apparently, to retain the same performance, more blocks are required when CSR is increasing. If the accuracy requirement is $1.5 \leq std(P) \leq 2$ dB, the method needs a relatively small number of blocks (e.g., 8 blocks at $\sigma_p = 2ms^{-1}$ and 6 blocks at $\sigma_p = 4ms^{-1}$). If a highly accurate measurement ($std(P) = 1$) is required at CSR=40 dB and small spectrum width ($\sigma_p = 2ms^{-1}$), using a block size larger than 8 is recommended (fig. 5.12a).

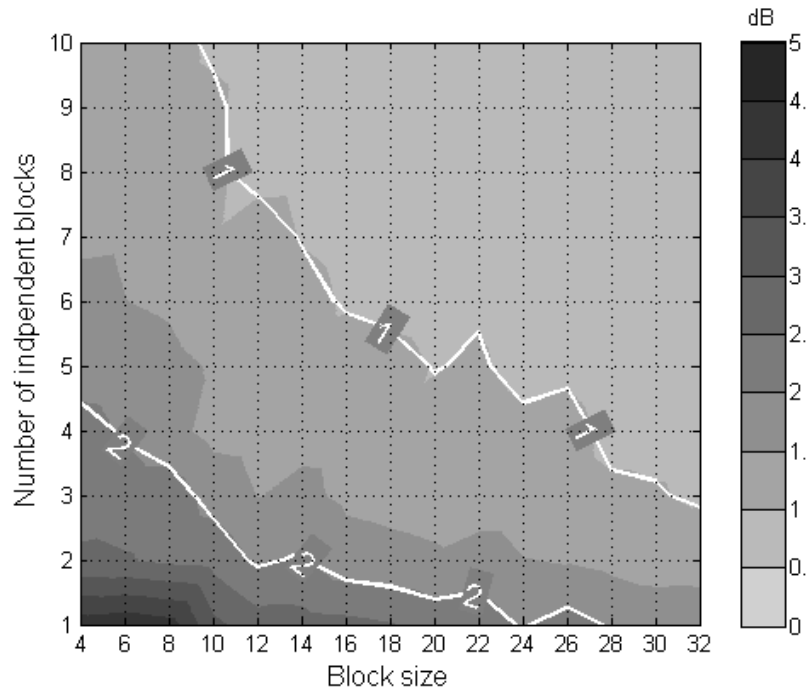


(a)

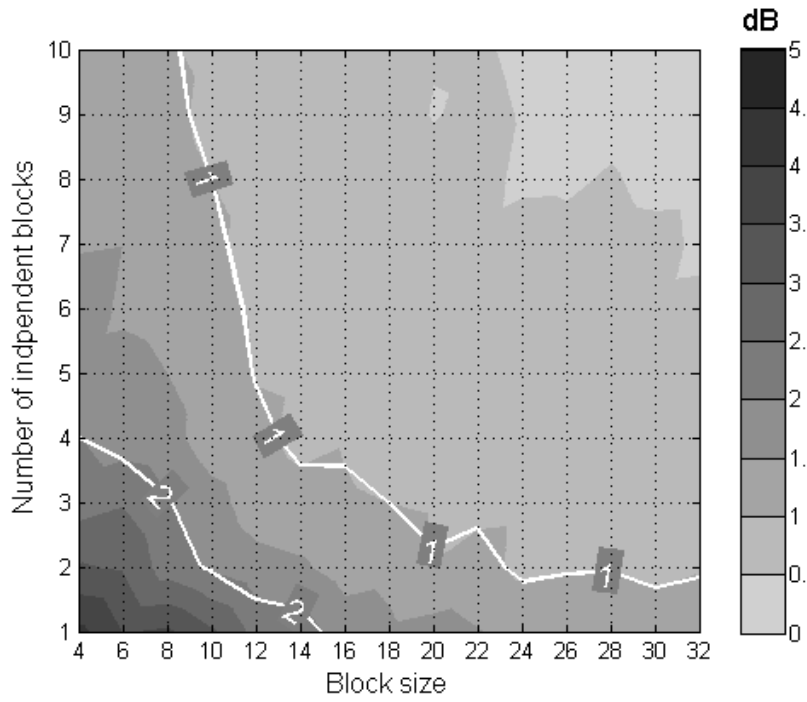


(b)

Figure 5.10: Standard deviation of power estimate as a function of data block size and number of blocks. CSR is 20 dB and (a) spectrum width $\sigma_p = 2ms^{-1}$; (b) spectrum width $\sigma_p = 4ms^{-1}$.

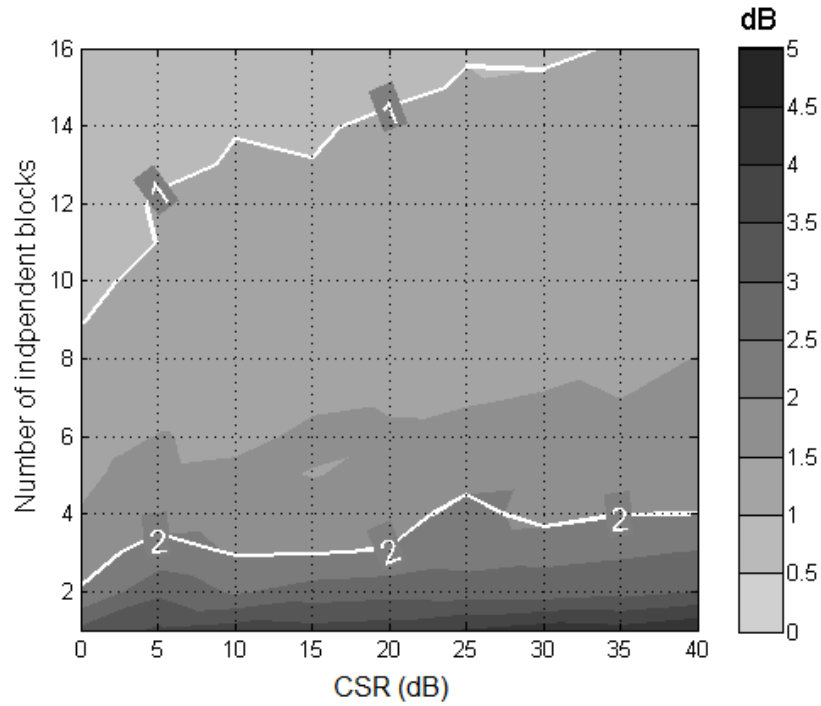


(a)

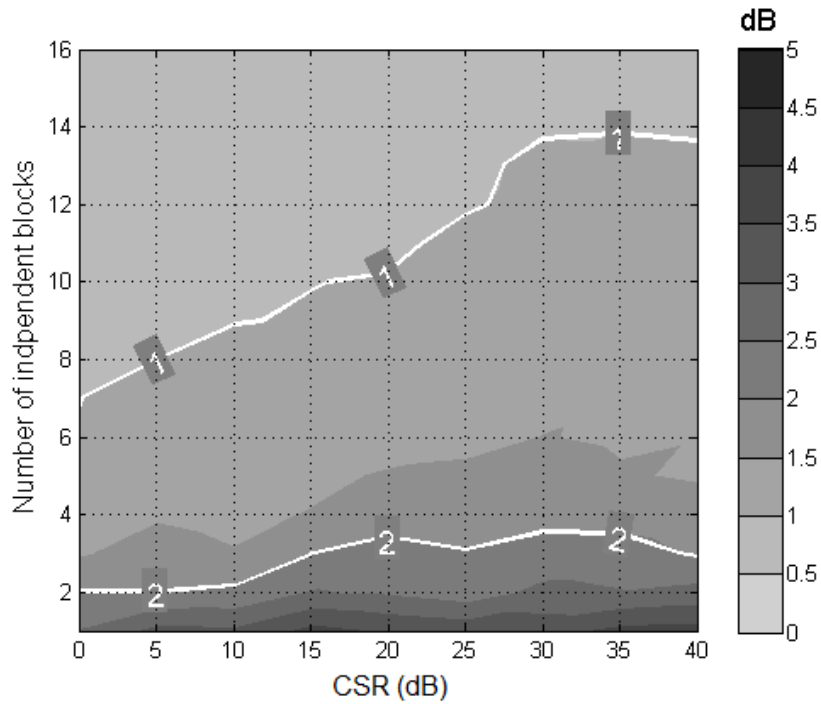


(b)

Figure 5.11: Same as figure 5.10 but for CSR=40 dB.



(a)



(b)

Figure 5.12: Standard deviation of power estimate at different values of CSR and number of blocks. Block size is 8 and (a) spectrum width $\sigma_p = 2ms^{-1}$; (b) spectrum width $\sigma_p = 4ms^{-1}$.

5.5 Test on CSU-CHILL radar data

At this time, observed block-sampled radar data are not available so we will verify the performance of GMAP-TD algorithm using CSU-CHILL radar measurements. Datasets with two sampling schemes were collected on December 20, 2006. The first dataset considered a staggered PRT 2/3 pulsing scheme taken at 23:58:19 UTC with $T_1 = 1 \text{ ms}$ and $T_2 = 1.5 \text{ ms}$. A minute later, a uniform sampling dataset was recorded at 23:59:20 UTC with $T_s = 1 \text{ ms}$. The small time difference between the two observations ensures a reasonable comparison of the results for the two schemes. With the data setup, the uniform sampling data has an unambiguous velocity of $\pm 27.5 \text{ ms}^{-1}$ while the staggered PRT 2/3 would attain double the range; i.e., from -55 ms^{-1} to 55 ms^{-1} . The data were collected during a snowstorm event where the signal-to-noise ratio is often less than 20 dB and spectrum widths larger than 4 ms^{-1} were observed in many regions. In addition, at 1.0 deg of elevation, observations came from the Rocky Mountain region west of the radar that showed a large amount of strong clutter. To gauge the GMAP-TD performance, GMAP was applied to the uniformly sampled dataset. Results are shown in fig. 5.13. One can observe that GMAP-TD removed ground clutter fairly well in both the uniform sampled and staggered PRT 2/3 data sets, especially at ranges less than 20 km and at the Rocky Mountain regions. Differentiating between original and filtered power plots shows a clutter suppression ratio up to 50 dB for staggered PRT 2/3 data from the CHILL radar. Reflectivity estimates from GMAP-TD and GMAP are comparable (first column in fig. 5.13). At a range of 60 km and an azimuth of 270° where strong clutter due to the mountains is present, GMAP-TD shows less variation in reflectivity estimates than does GMAP. At the ranges from 80 km to 100 km and the azimuth angles from 240° to 270° , reflectivity estimates from the staggered PRT 2/3 data by GMAP-TD show some clutter residues. This can be attributed to the power saturation of

the CHILL radar when working in staggered PRT 2/3 mode. The uniform pulsing data show velocity-folding at the northeastern quadrant (inside the highlighted ellipse). This means the precipitation mean velocity is over the maximum unambiguous velocity of the uniform sampling scheme (27.5 ms^{-1}). The color scale was selected from -32 ms^{-1} to 32 ms^{-1} for both uniform and staggered sampling data for comparison while still showing the velocity fields in full detail. The middle PPI plot in the last row (fig. 5.13) shows that the velocity folding problem was solved by applying GMAP-TD to the staggered PRT 2/3 observations. In this case, GMAP-TD provides correct velocity estimates without any folded velocity points.

The third column in fig. 5.13 shows the estimated signal spectrum width from uniform and staggered PRT modes. One can see that the results from uniform sampling data using GMAP and GMAP-TD and from staggered PRT 2/3 data using GMAP-TD are comparable. In this dataset, the signal spectrum width varied from 1 to 7 ms^{-1} . Good results from GMAP-TD for both uniform and staggered PRT 2/3 data validate the performance of the GMAP-TD method.

Although the estimated fields from uniform PRT observations obtained using GMAP-TD and GMAP appear to be similar, there are differences that can be shown by a quantitative comparison. In fig. 5.14, reflectivity and velocity profiles at the azimuth angles of 120° and 280° from fig. 5.9b and 5.9c are plotted. Figure 5.14 shows that GMAP-TD performs better than GMAP. The main improvement we expect is the smaller variance in the estimates of reflectivity and velocity. One way to see this is by observing the fluctuation of the profiles. At the azimuth angle of 120° (fig. 5.14b and 5.14d) where no ground clutter is present, GMAP-TD and GMAP results are almost the same. At the azimuth angle of 280° (fig. 5.14a and 5.14c) for the ranges from 40 km to 60 km, where strong ground clutter due to the mountains is present, GMAP-TD

estimates (gray lines) show less variation than GMAP estimates (black lines). It is consistent with the inference from simulation (fig. 5.6).

5.6 Summary

In this chapter, a new method for ground clutter filtering for beam-agile phased-array weather radar, GMAP-TD, was presented. GMAP-TD assumes that the radar signal consists of ground clutter and weather echoes whose spectral shapes are approximately Gaussian. GMAP-TD adopts many advanced techniques used in the state-of-the-art spectral filter (GMAP) such as adaptive clutter and noise power estimates and interpolation procedure. With the adaptive clutter estimates, GMAP-TD does very little or nothing to the signal in cases of no clutter. This eliminates the requirement of applying a clutter map, which often requires regular updates. When the signal and clutter overlap, the interpolation loop enables GMAP-TD to recover the part of the signal that was filtered out.

The most important feature of GMAP-TD is that it works with a signal covariance matrix in the time domain. It has several advantages over the current state-of-the-art spectral filtering method. Firstly, some limitations due to spectral leakage and data window effects present in GMAP are eliminated. Because there is no need for any data window in GMAP-TD, lower standard deviations in signal parameter estimates are observed. In addition to that, because GMAP-TD does not use the signal spectrum, it is not affected by spectral leakage due to ground clutter. GMAP-TD was shown to perform well for the cases where signal and clutter strongly overlap. This property allows GMAP-TD to work well in scenarios of very high clutter contamination ($CSR > 55dB$) and weak signal, where GMAP does not. Furthermore, GMAP-TD can be directly applied to staggered PRT data with some very simple modifications. GMAP-TD

performance for staggered PRT case was shown to be as good as in the case of uniform sampling.

Secondly, by varying the size of the covariance matrix, GMAP-TD can adapt to block-sampled data that are proposed for use in PAWR. For PAWR, the covariance matrix size is chosen to be equal to the block length and is averaged from all independent blocks. Although no actual PAWR block-sampled data are available, GMAP-TD performance for this type of data has been assessed intensively with various sets of parameters using means of simulation. Results show GMAP-TD algorithm to be stable and a promising performer.

Based on the experience with CSU-CHILL implementation, GMAP-TD computational complexity is similar to that of GMAP. Normally, it converges after a few iteration loops. Our first attempt at implementing GMAP-TD for weather radars shows that we process a ray of 300 range gates within a dwell time of 40 ms. The processing was split into many parallel threads and run in a server with two Intel Xeon Quad Core E5530 (2.4 GHz) processors and 16 GB RAM.

In summary, GMAP-TD is shown to be a promising method for ground clutter filtering for PAWR. It can be adapted for uniform sampling as well as staggered PRT observations. Additionally, GMAP-TD is able to retrieve weak signal in severe clutter contamination.

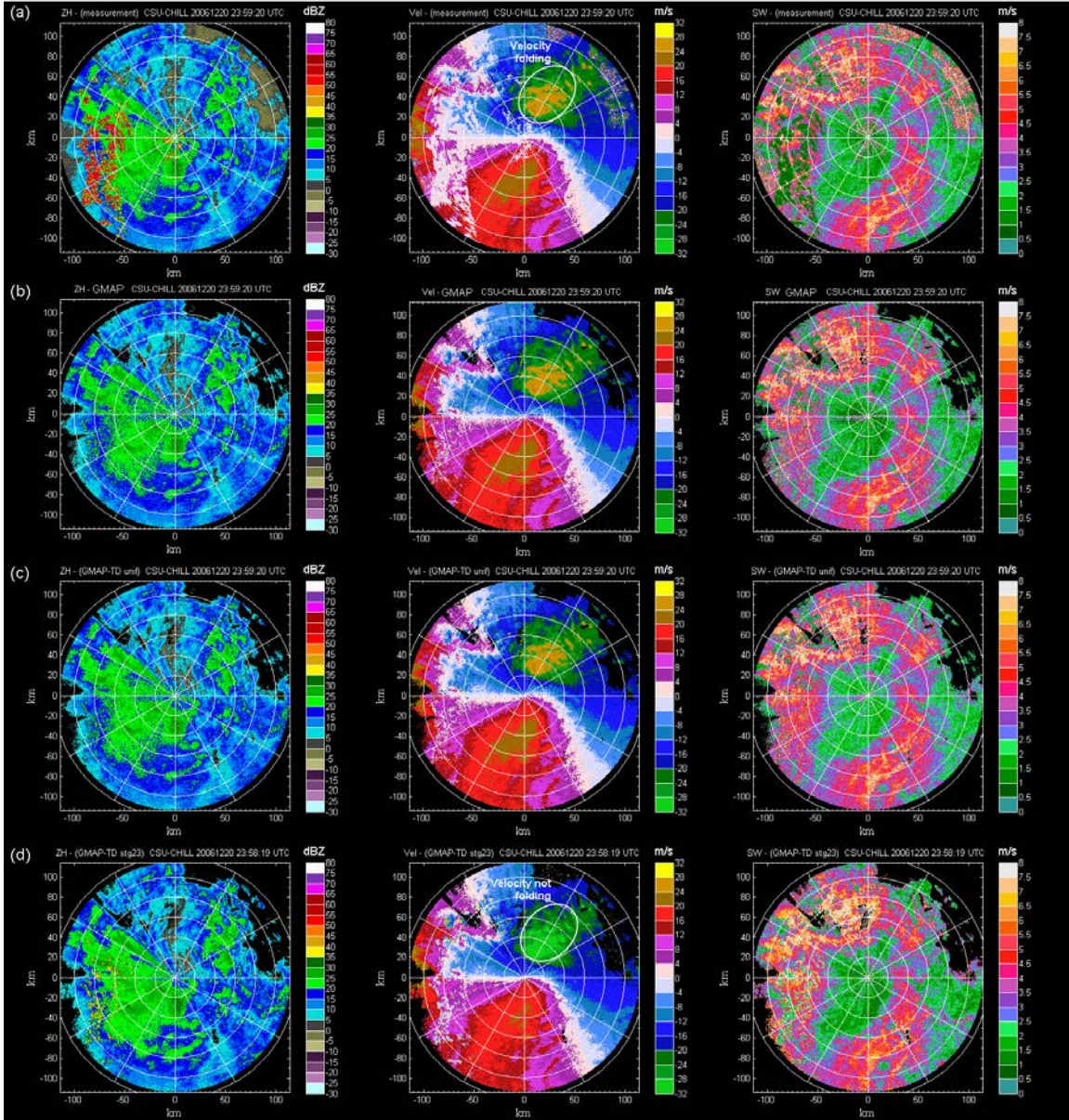


Figure 5.10: PPI plots show performance of GMAP-TD filter and GMAP filter on CSU-CHILL measurements. The first column is for reflectivity, the middle column is for velocity and the third column is for spectrum width. First row is for PP method (no clutter filtering) applied to uniform data set collected at 23:59:20 UTC. The second and third rows are for GMAP and GMAP-TD applied to the same uniform data set. Figures in the last row are GMAP-TD results on staggered PRT 2/3 data collected at 23:58:19 UTC. The unambiguity velocity is 27.5 ms^{-1} for uniform case and 55 ms^{-1} for staggered PRT 2/3. Except for the unfiltered data, others are threshold using $SNR > 3 \text{ dB}$.

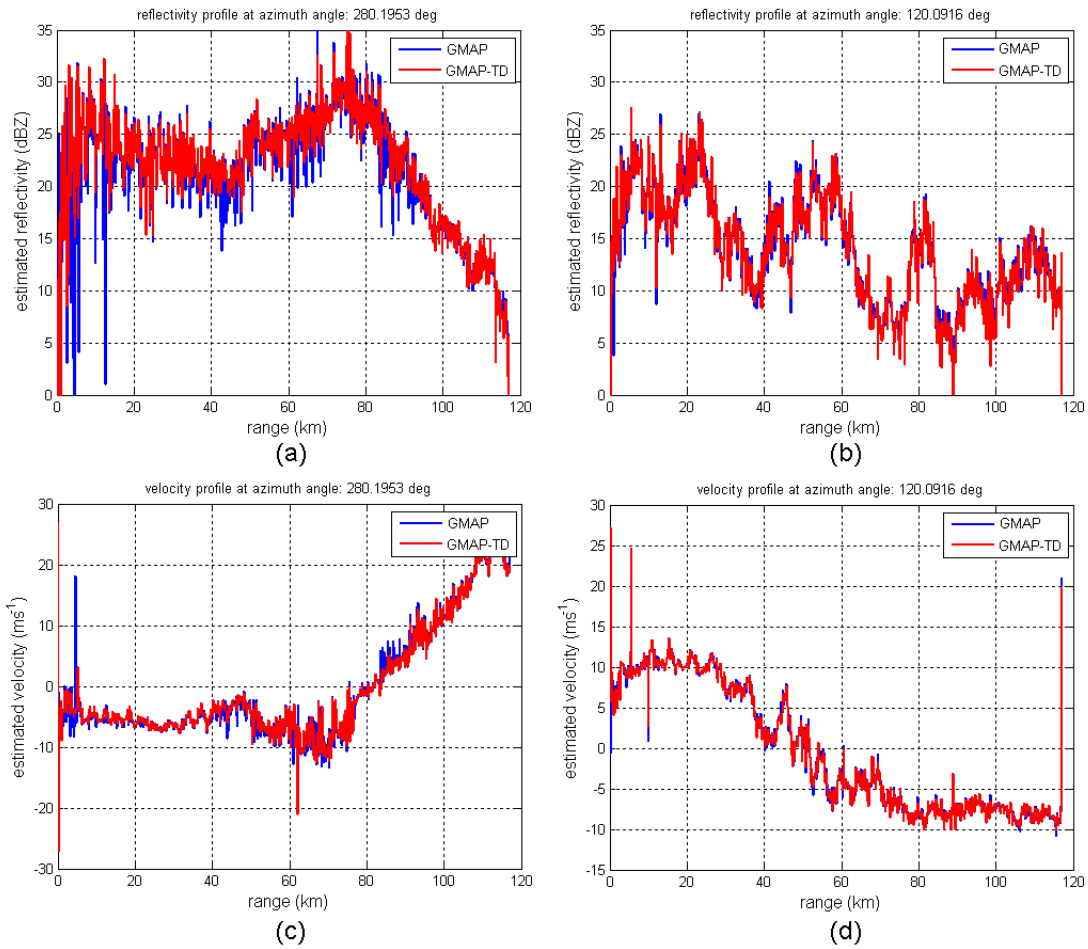


Figure 5.14: Comparison of reflectivity and radial velocity profiles at azimuths of 120° ((b) and (d)) and 280° ((a) and (c)). Top panels are reflectivity profiles and bottom panels are corresponding velocity profiles.

CHAPTER 6

POLARIMETRIC VARIABLES RETRIEVAL WITH CLUTTER SUPPRESSION FOR STAGGERED PRT SEQUENCES

6.1 Introduction

The polarimetric PAWR signal model (see chapter 4) highlights bias issues inherent in electronic steered beam planar phased array radar. The biases are significant and can be as large as the parameters themselves. However, these biases can be removed to produce unbiased estimates. Methods to mitigate the biases are introduced in chapter 4 and they open the possibility of using planar polarimetric PAWR for weather sensing. In chapter 5, a new clutter filtering method (GMAP-TD) for PAWR has been developed. The filter is designed to work with block-sampled data and to adapt to both uniform and non-uniform waveforms. It has been demonstrated to provide very good results on the spectral moment estimates. In this chapter, GMAP-TD is extended for polarimetric variables retrieval in the case of clutter contamination. We will focus on the case of the staggered PRT waveform because this is one of the most important waveforms for PAWR and it is always more challenging to perform clutter filtering on non-uniformly sampled data than on uniformly sampled data.

In polarimetric PAWR, besides the first three conventional spectral moments (mean power, mean Doppler velocity, and spectrum width), there are parameters generated from dual-polarized radar signals. Polarimetric variables provide valuable information for hydrological and meteorological studies such as improved rainfall estimation, retrieval of drop size distribution (DSD) parameters, and hydrometeor classification (Bringi and Chandrasekar 2001, Gorgucci et

al. 2002). Among polarimetric variables, differential reflectivity (Z_{dr}), differential propagation phase (Φ_{dp}), and co-polar correlation coefficient ($|\rho_{co}|$) are highly significant. They play a key role in most dual-polarization radar applications (Bringi and Chandrasekar, 2001). Several studies have proposed different estimators and investigated various factors that affect these parameters estimates from the simple uniformly sampled radar data (Liu et al. 1993, Illingworth and Caylor 1991, Doviak and Zrnic 1984). Golestani et al. (1995) presented an analysis of the accuracies of parameters estimates from dual-polarized staggered PRT measurements. However, all these studies have conducted analyses with radar signals that are free of ground clutter contamination. In reality, weather radars have difficulties in their ability to process data contaminated by ground clutter; especially with non-uniform pulsing schemes. Recently, Sachidananda et al. (2005) have proposed a method to tackle one of the most challenging tasks - clutter suppression for dual-polarized, staggered PRT sequences. The procedure processes complex spectra of the interpolated H and V staggered PRT sequences to remove clutter components and recover both the magnitude and phase of weather signals. However, that method is limited to staggered PRT dual-polarized data in simultaneous transmission and simultaneous reception mode (or hybrid mode; Bringi and Chandrasekar 2001). Besides, it requires further work to reduce the impact of the remaining clutter residues on dual-polarization parameter estimates after clutter filtering (Sachidananda et al. 2005).

While many clutter-filtering methods for uniform sampling radar data have been reported in the literature, there is no effective filtering method for dual-polarized staggered PRT sequences, especially in alternating mode. In this work, a GMAP-TD algorithm for polarimetric variables retrieval is designed to work on both simultaneous and alternating dual-polarized transmission modes. The algorithm is also based on covariance processing in the time domain so it retains the

capability to work with PAWR block-sampled data. We will focus on analyzing the accuracies of the parameters estimates with clutter suppression in both transmission modes. Based on radar simulation, the error analysis is carried out for different scenarios, concentrating on the cases of received signals contaminated by large ground clutter. The method's performance is also demonstrated with actual CSU-CHILL dual-polarized staggered PRT data.

6.2 Dual-polarized staggered PRT scheme in simultaneous mode

In simultaneous mode, horizontal and vertical signals are transmitted and received simultaneously. Dual-polarized staggered PRT sequences are shown in fig. 6.1. In this mode, both H and V channel signals follow identical staggered waveform PRT T_1/T_2 . Dual-polarized variables are estimated in a similar way as the case of uniform simultaneous mode (Bringi and Chandrasekar, 2001).

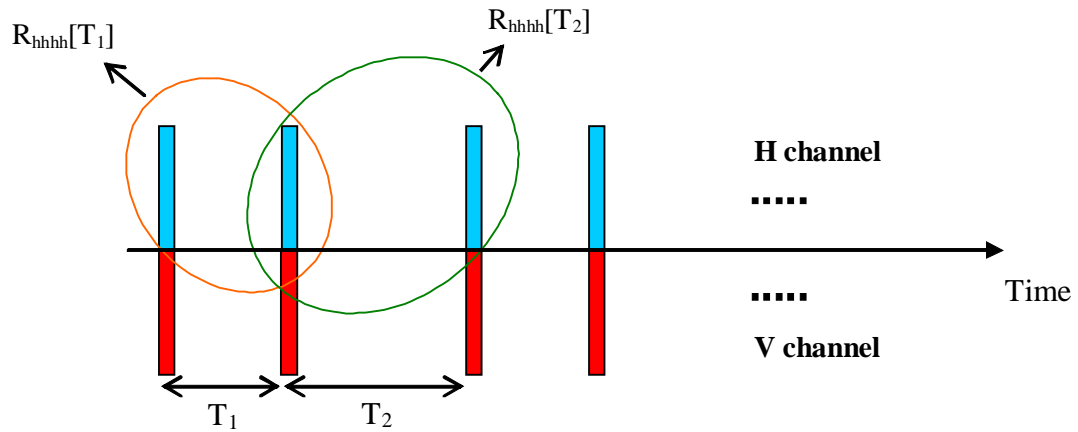


Figure 6.1: Dual-polarized staggered PRT pulsing scheme in simultaneous mode.

6.3 Dual-polarized staggered PRT scheme in alternating mode

In conventional alternating mode, polarizations are transmitted in sequence ... *hvhv*... with equal spacing between alternating H and V pulses. Figure 6.24 (page 364 from Bringi and Chandrasekar (2001)) shows the sequence of the received signal in this waveform. Velocity can be estimated from pairs of alternating polarization pulses that are spaced T_s in time after correcting for the differential phase (Φ_{dp}) between polarizations. In the staggered PRT alternating mode, the transmitted signal at one of the polarizations is a staggered waveform and the signal at the other polarization is transmitted in a uniform pattern, as shown in fig. 6.2. Similarly to the simultaneous mode, the stagger ratio T_1/T_2 defines the structure of this pulsing scheme.

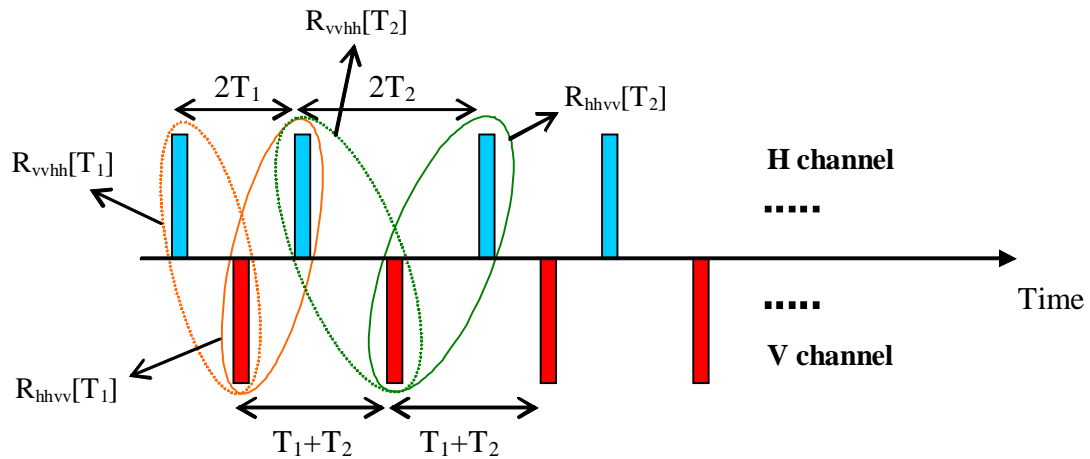


Figure 6.2: Dual-polarized staggered PRT pulsing scheme in alternating mode.

With no loss of generality, it can be assumed that the H polarization pulse is transmitted first. Let $V_{hh}[2n-1], V_{vh}[2n-1], V_{vv}[2n], V_{hv}[2n], \dots n = 1, \dots, N$ be the samples of the received signals. N

is the total number of samples in H or V channel. The correlation estimates of adjacent co-polar samples can be computed by

$$\begin{aligned}
R_{vvh} [T_1] &= \frac{2}{N} \sum_{n=1}^{N/2} (V_{hh} [4n-3])^* V_{vv} [4n-2] \\
R_{hvv} [T_1] &= \frac{2}{N} \sum_{n=1}^{N/2} V_{hh} [4n-1] (V_{vv} [4n-2])^* \\
R_{vvh} [T_2] &= \frac{2}{N} \sum_{n=1}^{N/2} (V_{hh} [4n-1])^* V_{vv} [4n] \\
R_{hvv} [T_2] &= \frac{2}{N} \sum_{n=1}^{N/2} V_{hh} [4n+1] (V_{vv} [4n])^*
\end{aligned} \tag{6.1}$$

In this mode, direct estimation of the co-polar correlation ($R_{hvv} [0]$) is not possible. However, the following approximation can be used (Sachidananda and Zrnic, 1985)

$$\begin{aligned}
\rho_{hvv} [T_1] &= \rho_{hvv} [0] \rho_{hhh} [T_1] = \rho_{hvv} [0] \rho [T_1] \\
\rho_{vvh} [T_1] &= \rho_{vvh} [0] \rho_{vvv} [T_1] = \rho_{vvh} [0] \rho [T_1]
\end{aligned} \tag{6.2a}$$

and,

$$\begin{aligned}
\rho_{hvv} [T_2] &= \rho_{hvv} [0] \rho_{hhh} [T_2] = \rho_{hvv} [0] \rho [T_2] \\
\rho_{vvh} [T_2] &= \rho_{vvh} [0] \rho_{vvv} [T_2] = \rho_{vvh} [0] \rho [T_2]
\end{aligned} \tag{6.2b}$$

Note that $\rho_{vvh} = (\rho_{hvv})^*$. In this work, we assume that there is no instrument bias in phase shifts introduced in the hv and vh pairs at different time lags of the staggered PRT scheme (Golestani et al. 1995). It follows that the phase of ρ_{hvv} and ρ_{vvh} can be computed as

$$\begin{aligned}
\arg(\rho_{hvv} [T_1]) &= \Psi_1^{T_1} = -\Psi_{dp} + \arg(\rho [T_1]) \\
\arg(\rho_{vvh} [T_1]) &= \Psi_2^{T_1} = \Psi_{dp} + \arg(\rho [T_1])
\end{aligned} \tag{6.3a}$$

and,

$$\begin{aligned}
\arg(\rho_{hvv} [T_2]) &= \Psi_3^{T_2} = -\Psi_{dp} + \arg(\rho [T_2]) \\
\arg(\rho_{vvh} [T_2]) &= \Psi_4^{T_2} = \Psi_{dp} + \arg(\rho [T_2])
\end{aligned} \tag{6.3b}$$

where Ψ_{dp} is the phase of $R_{vvh}[0]$. Bringi and Chandrasekar (2001) show that $\Psi_{dp} = \Phi_{dp} + \delta_{co}$,

where Φ_{dp} is the differential propagation phase and δ_{co} is the differential phase upon scattering.

If Rayleigh scattering is assumed, then $\delta_{co} = 0$ and $\Psi_{sp} = \Phi_{dp}$. The Ψ_{dp} can be estimated from

(6.3) as

$$\widehat{\Psi}_{dp}^{T_1} = \frac{1}{2}(\Psi_1^{T_1} - \Psi_2^{T_2}) \quad (6.4a)$$

$$\widehat{\Psi}_{dp}^{T_2} = \frac{1}{2}(\Psi_3^{T_2} - \Psi_4^{T_2}) \quad (6.4b)$$

The two estimates can be combined to reduce the estimation errors

$$\widehat{\Psi}_{dp} = \frac{1}{2}(\widehat{\Psi}_{dp}^{T_1} + \widehat{\Psi}_{dp}^{T_2}) \quad (6.5)$$

Also, from (6.2), the $|\rho_{co}|$ can be written as

$$|\rho_{co}^{T_1}| = \frac{|\rho_{vvh}[T_1]|}{|\rho[T_1]|} \quad (6.6a)$$

$$|\rho_{co}^{T_2}| = \frac{|\rho_{vvh}[T_2]|}{|\rho[T_2]|} \quad (6.6b)$$

and by averaging

$$|\rho_{co}| = \frac{1}{2}(|\rho_{co}^{T_1}| + |\rho_{co}^{T_2}|) \quad (6.7)$$

6.4 GMAP-TD implementation

The estimation of differential reflectivity, Z_{dr} , is straightforward. It is given by

$$\widehat{Z}_{dr} = \widehat{P}_h - \widehat{P}_v \quad (6.8)$$

where \hat{P}_h and \hat{P}_v are the estimated signal powers in the H and V channels using the GMAP-TD algorithm (chapter 5). When the ground clutter and weather spectra are located apart, the signal power is not affected by the clutter-filtering process. In the case where the ground clutter and the signal spectra overlap, the interpolation procedure in GMAP-TD efficiently recovers the portion of the signal that is filtered out (fig. 5.9). Hence, in most situations, GMAP-TD is able to provide an unbiased estimation of Z_{dr} . This will be demonstrated in the following sections.

On the other hand, the use of an interpolation procedure does not always retain the correlation between the H and V polarization signals. In fact, it may create artificial biases in the $|\rho_{co}|$ and Φ_{dp} estimates. For these parameters, the estimates should be obtained directly from a clutter-transformed time series without the interpolation loop. This approach is similar to the conventional methods implemented in dual-polarized weather radar systems using IIR or FIR filters. In the following sections, we describe the implementation of the GMAP-TD filter to estimate $|\rho_{co}|$ and Φ_{dp} from dual-polarized staggered PRT radar time series with the two different transmission modes.

6.4.1 Simultaneous mode

In the simultaneous mode, both horizontal and vertical polarization states are simultaneously transmitted and received; therefore, their waveforms are identical. Note that the GMAP-TD clutter-filtering matrix (equation (5.8)) is designed for a single-polarization signal. Generally, ground clutter contaminates H and V signals at different levels; therefore, the clutter filter matrices for the H and V signals are not always identical. Applying two different filters to the strongly correlated received signals may introduce bias in their correlation coefficient estimate. To avoid this situation, we modify the GMAP-TD filter implementation so that a unique filter

can be used for both channels. Equations (5.7) and (5.8) show that the filter depth depends on the ratio between the clutter power and the noise power, while the pre-set clutter spectrum width will determine the filter width. It is simple to verify that if the clutter filter's parameters are chosen as

$$\begin{aligned} P_{dual-pol}^c &= \max(P_h^c, P_v^c) \\ \sigma_{N,dual-pol}^2 &= \min(\sigma_{N,h}^2, \sigma_{N,v}^2) \\ w_{dual-pol}^c &= \max(w_h^c, w_v^c) \end{aligned} \quad (6.9)$$

then the resultant filter is able to efficiently remove ground clutter in both channels. With this modification, the filter equation is now written as

$$\mathbf{A}_{dual-pol} = \left(\mathbf{R}_{dual-pol}^c / \sigma_{N,dual-pol}^2 + \mathbf{I}_m \right)^{-1/2} \quad (6.10)$$

where $\mathbf{R}_{dual-pol}^c$ is constructed from (5.4) and its elements are defined as

$$R_{dual-pol}^c[\tau] = P_{dual-pol}^c \exp\left(-\frac{8\pi^2 w_{dual-pol}^2 \tau^2 T_s^2}{\lambda^2}\right) \quad (6.11)$$

The signals after applying clutter filtering are

$$\mathbf{V}_h^f = \mathbf{A}_{dual-pol} \mathbf{V}_h \quad (6.12a)$$

$$\mathbf{V}_v^f = \mathbf{A}_{dual-pol} \mathbf{V}_v \quad (6.12b)$$

where the superscript f indicates filtered data. Then, $|\rho_{co}|$ and Φ_{dp} can be estimated from the filtered time series (6.12) using the standard method (Bringi and Chandrasekar, 2001).

6.4.2 Alternating mode

In the alternating mode (fig. 6.2), the signal at the H channel follows a staggered PRT waveform with two time spacings, $2T_1$ and $2T_2$, while the signal at the V channel is a uniform

waveform with the period of $(T_1 + T_2)$. As discussed in chapter 5, we focus on the case of the staggered PRT waveform 2/3. We denote T_u to be the unit time, then $T_1 = 2T_u$ and $T_2 = 3T_u$.

Similar to the simultaneous mode, in order to obtain accurate estimates of $|\rho_{co}|$ and Φ_{dp} we use a common clutter filter for both the H and V channels. Note that the GMAP-TD filter for the H channel (staggered PRT waveform) is derived from equations (5.5) and (5.8) in chapter 5 while the filter for the V channel (uniform waveform) is derived from equations (5.4) and (5.8). In addition to the difference in clutter rejection levels, the two filters have different structures. The issue with different filter depths can be sorted out easily using the same technique described in section 6.4.1, while the difference in filters structures is more challenging to overcome.

In the H channel, the Nyquist velocity obtained from the staggered PRT scheme is $v_a^H = \lambda / 4(2T_2 - 2T_1) = \lambda / (8T_u)$ and the GMAP-TD filter's power response has additional notches at $\pm 0.4v_a^H = \pm \lambda / (20T_u)$ and $\pm 0.8v_a^H = \pm 2\lambda / (20T_u)$ besides the main notch at zero frequency (fig. 5.5a). The uniform waveform of the V channel provides a Nyquist velocity of $v_a^V = \lambda / 4(T_1 + T_2) = \lambda / (20T_u)$, which is equal to 2/5 of v_a^H , and the corresponding filter has no additional notch. Figure 6.3 shows an example of the power frequency responses of the GMAP-TD filters for the two channels with $v_a^H = 27.5ms^{-1}$ and $v_a^V = 11ms^{-1}$.

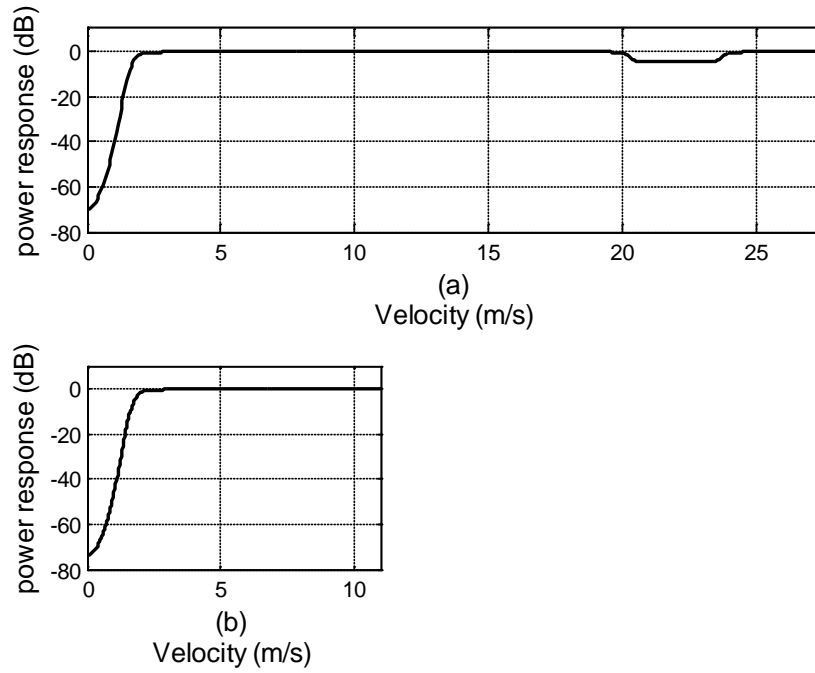


Figure 6.3: The power frequency response of GMAP-TD filter for H channel (a) and V channel (b).

In section 6.3, we have shown that when the phase shift between alternating polarization pulses is used, the alternating staggered PRT scheme provides a maximum unambiguous velocity of $v_a = \lambda / (4T_u)$ that is much higher than that from the signal at each individual channel. When the signal velocity exceeds the maximum unambiguous velocity of either channel, velocity aliasing occurs. Therefore, the filter responses of the two channels with respect to Doppler range v_a include the replicas of the responses with respect to Doppler ranges v_a^H and v_a^V , respectively. Figures 6.4a and 6.4b illustrate those responses.

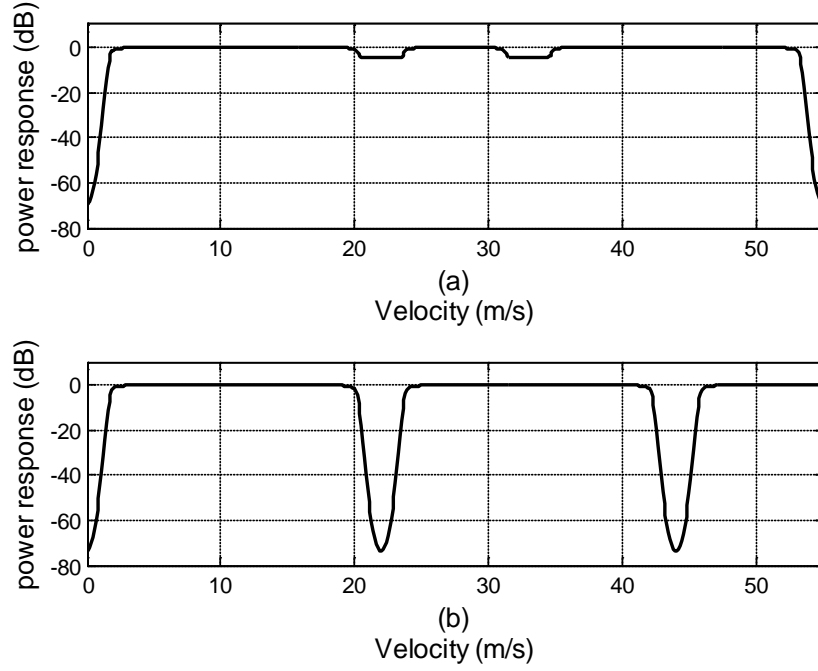


Figure 6.4: The power frequency response of GMAP-TD filter with respect to Doppler range $v_a = 55 \text{ms}^{-1}$ for the case presented in figure 6.3 for H channel (a) and V channel (b).

It is noticed that the response in fig. 6.4b is similar to that of the modified filter A_{mod} introduced in chapter 5 (fig. 5.5b). This observation suggests a solution based on the technique to create filter A_{mod} . In detail, we modify GMAP-TD filters for H and V channels for polarimetric variables retrieval as follows:

For H channel,

$$\mathbf{A}_{h, \text{dual-pol}} = \mathbf{A}_{\text{dual-pol}} + \mathbf{A}_{0.4, \text{dual-pol}} + \mathbf{A}_{-0.4, \text{dual-pol}} + \mathbf{A}_{0.8, \text{dual-pol}} + \mathbf{A}_{-0.8, \text{dual-pol}} \quad (6.13)$$

where subscript h stands for horizontal polarization. $\mathbf{A}_{\text{dual-pol}}$ is as in (6.9) and $\mathbf{A}_{\pm 0.4, \text{dual-pol}}$ and $\mathbf{A}_{\pm 0.8, \text{dual-pol}}$ are computed as in equation (5.10) but with $\mathbf{R}_{\text{dual-pol}}^c$ instead of \mathbf{R}_c (± 0.4 and ± 0.8 in the superscripts are dropped).

For V channel,

$$\mathbf{A}_{v,dual-pol} = \mathbf{A}_v + \mathbf{A}_{1.0,v} \quad (6.14)$$

where,

$$\mathbf{A}_{1.0,v} = \left(\mathbf{R}_{1.0,dual-pol} / \sigma_{N,dual-pol}^2 + \mathbf{I}_m \right)^{-1/2} \text{ and elements of the clutter covariance matrix for V}$$

channel $\mathbf{R}_{dual-pol}^c$ are

$$R_{1.0,dual-pol}[\tau] = P_{dual-pol}^c \exp\left(-\frac{8\pi^2\sigma_c^2\tau^2T_s^2}{\lambda^2}\right) \exp(-j\pi\tau) \quad (6.15)$$

The power responses of these filters are shown in fig. 6.5. When expanded to the entire Doppler range v_a , they will be identical (fig. 6.6). The filtered time series from the two channels are given as

$$\mathbf{V}_h^f = \mathbf{A}_{h,dual-pol} \mathbf{V}_h \quad (6.16a)$$

$$\mathbf{V}_v^f = \mathbf{A}_{v,dual-pol} \mathbf{V}_v \quad (6.16b)$$

From filtered data, $|\rho_{co}|$ and Φ_{dp} can be obtained using the standard method (Bringi and Chandrasekar, 2001).

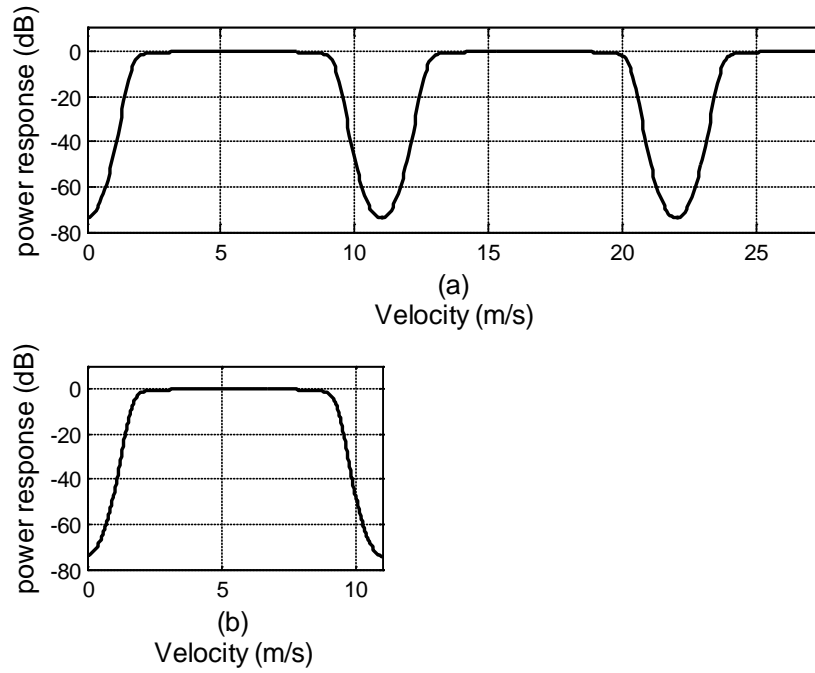


Figure 6.5: The power frequency response of the modified GMAP-TD filter for polarimetric variables retrievals for H channel (a) and for V channel (b).

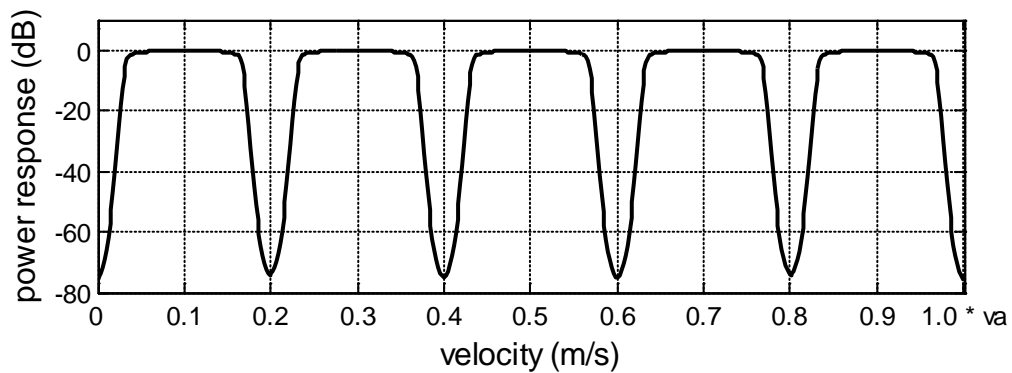


Figure 6.6: The power frequency responses of the modified GMAP-TD filters with respect to the Doppler range $v_a = 55 \text{ m/s}$ are identical for both channels.

The modified GMAP-TD filter for dual-polarization variables retrieval presents additional notches along the Doppler range (fig. 6.6). When the signal velocity is near those notches, a portion of the signal is removed by the filter and it reduces the SNR. The result is that the standard deviation in the $|\rho_{co}|$ and Φ_{dp} estimates increase at those Doppler ranges due to a lower SNR. The algorithm is evaluated in the next section using radar simulation.

6.5 Method evaluation using signal simulation

With the presence of ground clutter, the error analysis of the dual-polarization parameter estimation algorithm for staggered PRT waveforms is challenging. We approach this problem by means of simulations. In this section, simulated radar data with different sets of parameters are used to demonstrate the performance of GMAP-TD for dual-polarization parameter estimation. Dual-polarized uniform data with a PRT of T_u is created first (Chandrasekar, 1986) and appropriate samples are removed to generate the staggered PRT sequences. Two time series are created, one for the weather echo plus noise and the other for the ground clutter only. The signal with ground clutter data are obtained from the sum of the two time series. In this experiment, to evaluate the performance of the GMAP-TD method, we compare the statistical errors of two set of Z_{dr} , $|\rho_{co}|$ and Φ_{dp} estimates. A reference set of parameters estimates is obtained from the weather-plus-noise time series (clutter-free time series) using a standard pulse pair method (section 6.3). The second set of parameter estimates is achieved by passing the clutter-contaminated signal through the GMAP-TD filter.

In every simulation case, a large ground clutter signal ($CSR = 40 \text{ dB}$) is used. Signal velocity is varied in the Doppler range v_a with an increment of one-tenth of Nyquist velocity to examine the effect of additional notches on Z_{dr} , $|\rho_{co}|$ and Φ_{dp} estimates. The signal spectrum width is

chosen between two values representing narrow and wide signal spectra. Inputs of the simulation are summarized in table 6.1.

Table 6.1: Simulation input parameters.

<i>Parameters</i>	<i>Values</i>
f , GHz	2.72
CSR, dB	40
SNR, dB	30
σ_c , ms^{-1}	0.25
σ_p , ms^{-1}	1, 4
\bar{v} , ms^{-1}	$0, 0.05v_{\max}, 0.1v_{\max} \dots v_{\max}$
σ_N^2 , dB	14
m , samples	64
T_u , ms	0.5
T_1 / T_2	2/3

6.5.1 Results for simultaneous mode

With the waveform parameters given in table 6.1, the Nyquist velocity of the scheme is 55 ms^{-1} . Figure 6.7 shows the bias and standard deviation in the parameter estimates as a function of the mean velocity of the signal for a very narrow signal spectrum width ($\sigma_p = 1 \text{ m s}^{-1}$). Dashed lines present results from a clutter-free time series using pulse-pair processing and solid lines present results from clutter-contaminated data using a GMAP-TD filter. The performance of the clutter filter is remarkable even for a CSR of 40 dB. At most velocity values, the performance of the GMAP-TD method matches the pulse pair processing for signals without ground clutter. Only in the extremely overlapping situation where the weather echo velocity is near zero (say less than $0.1v_a$) do the estimates by GMAP-TD show slightly higher biases and deviations. This is explained by the significant reduction in the SNR after applying the clutter filter. The co-polar

correlation coefficient ρ_{HV} is more sensitive to the SNR (Bringi and Chandrasekar, 2001), and therefore shows the most obvious error in these cases. However, estimation biases and standard deviations are still within acceptable limits for weather radar applications.

A similar analysis is shown in fig. 6.8 but for a wider spectrum signal ($\sigma_p = 4 \text{ m s}^{-1}$). The results are better than those with a narrower spectrum width. Even in the strong overlapping situation, the estimates are as good as the case without clutter. With a wide spectrum signal, the portion of the signal filtered out in the overlapping situation is smaller compared to the case of the narrow signal. Hence, after the applying clutter filter the SNR is not greatly affected. The matching results demonstrate the effectiveness of the GMAP-TD algorithm.

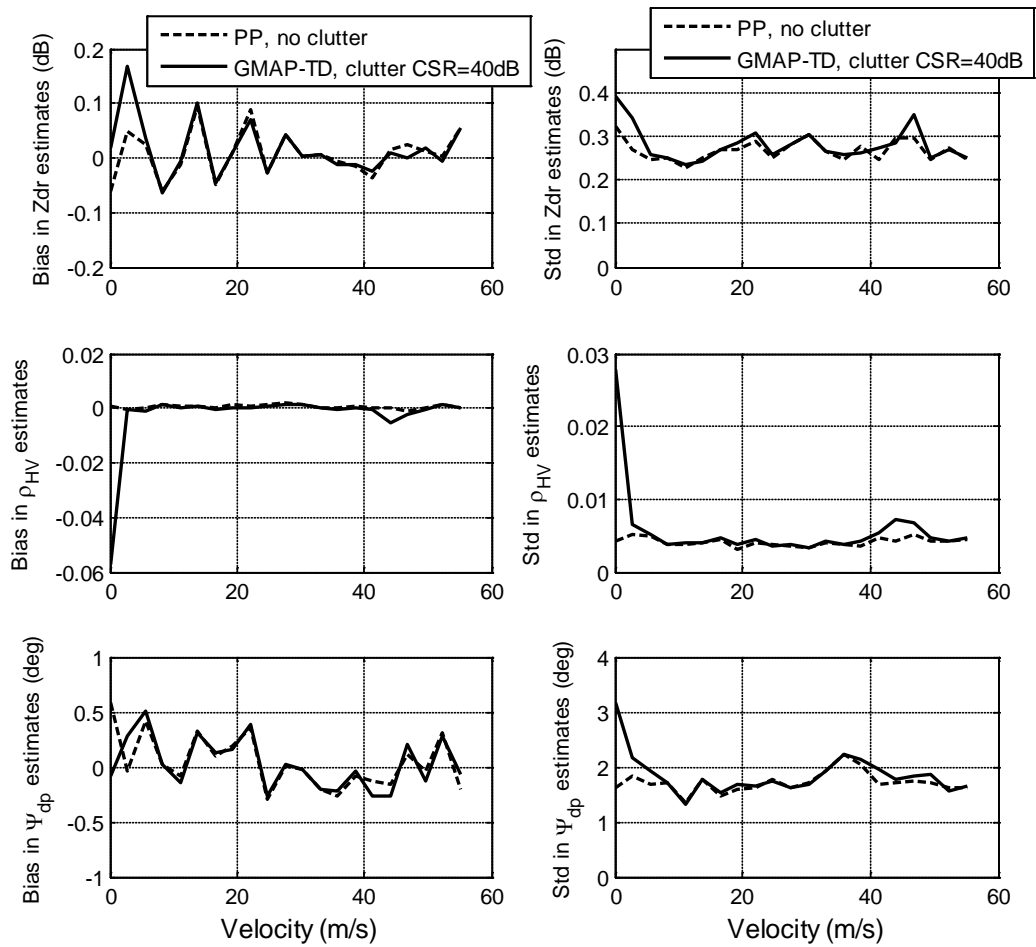


Figure 6.7: Biases and standard deviations in the dual-polarization parameters estimates using the GMAP-TD method for staggered PRT sequences in simultaneous mode. Inputs parameters for the simulation program are $CSR = 40 \text{ dB}$, $\sigma_p = 1 \text{ m s}^{-1}$.

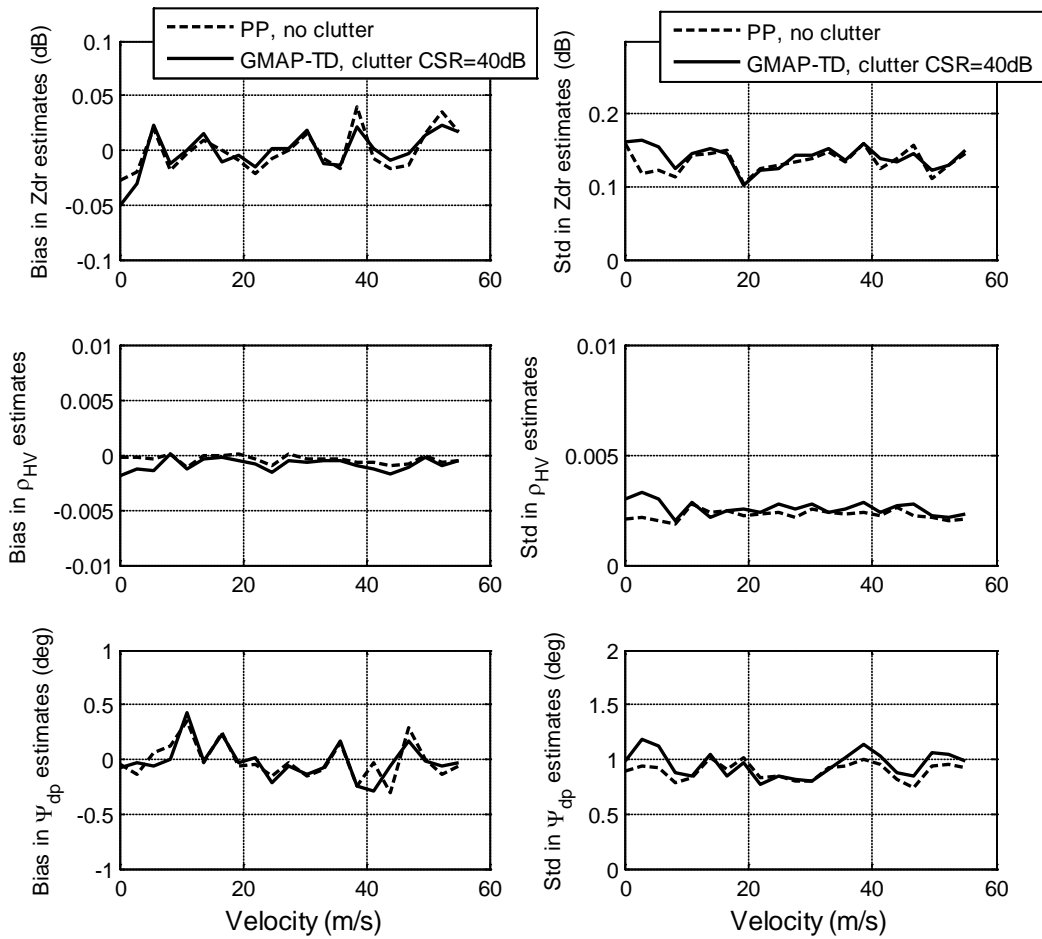


Figure 6.8: Same as figure 6.7, but for $\sigma_p = 4 \text{ m s}^{-1}$.

6.5.2 Results for alternating mode

It is noticed that in this pulsing technique, the maximum unambiguous velocity obtained from the combination of the two polarizations is much larger than that of each individual channel. Given the pulse spacing T_1 and T_2 in table 6.1, by combining the H and V samples, this pulsing scheme has a maximum unambiguous velocity of 55 ms^{-1} , while the maximum unambiguous velocity of the H channel (staggered PRT) is 27.5 ms^{-1} and that of the V channel (uniform) is only 11 ms^{-1} . When the Nyquist velocity is small, the signal spectrum becomes

relatively “wider.” Consequently, in these scenarios, the likelihood of signal overlapping clutter increases.

Again, evaluation of the GMAP-TD filter for polarimetric estimation with respect to the mean velocity is carried out. Figure 6.9 shows the biases and standard deviations of Z_{dr} , $|\rho_{co}|$ and Φ_{dp} estimates with a signal spectrum width of 1 ms^{-1} . It can be seen that there is an increase in the estimation errors at Doppler regions corresponding to the notches’ locations in the filter response (fig. 6.6). The reduction in SNR after filtering explains this effect. It is an inevitable situation because in this case, the signal spectrum is narrow and falls into the notch region of the filter. The increase in standard deviation is more obvious in the $|\rho_{co}|$ estimate than in the other two estimates. In fact, the Z_{dr} and Φ_{dp} standard deviation increment is less than about 0.1 dB and 0.5 deg, respectively, at those regions while the biases are still close to the reference data.

The biases and standard deviations in the estimates of Z_{dr} , $|\rho_{co}|$, and Φ_{dp} for a signal with a spectrum width of 4 ms^{-1} are shown in fig. 6.10. It can be seen that the difference in bias between the GMAP-TD results and the reference data is negligible. The increases in standard deviation of Z_{dr} estimate (less than 0.1 dB) and Φ_{dp} estimate (less than 0.5°) with GMAP-TD filter are tolerable when considering the complexity of the waveform and strong clutter contamination situation. Similar to the case of the simultaneous mode, the GMAP-TD filter appears to perform better with wide spectrum signals.

From this simulation-based study, we can conclude that the GMAP-TD filter can be extended for parameter retrieval from dual-polarized staggered PRT sequences in the presence of ground clutter. Different implementations are made for each transmission mode. The method performance is remarkable in the simultaneous mode, where the two polarization waveforms are

identical. Most of the time, there is no difference in performance when comparing results from data with and without ground clutter. In the alternating mode, where polarizations waveforms are very different, estimation statistical errors increase. However, in extreme scenarios when clutter is strong and the signal spectrum is very narrow, large errors appear only at certain Doppler bands. Otherwise, the errors are only slightly higher than those with clutter-free data.

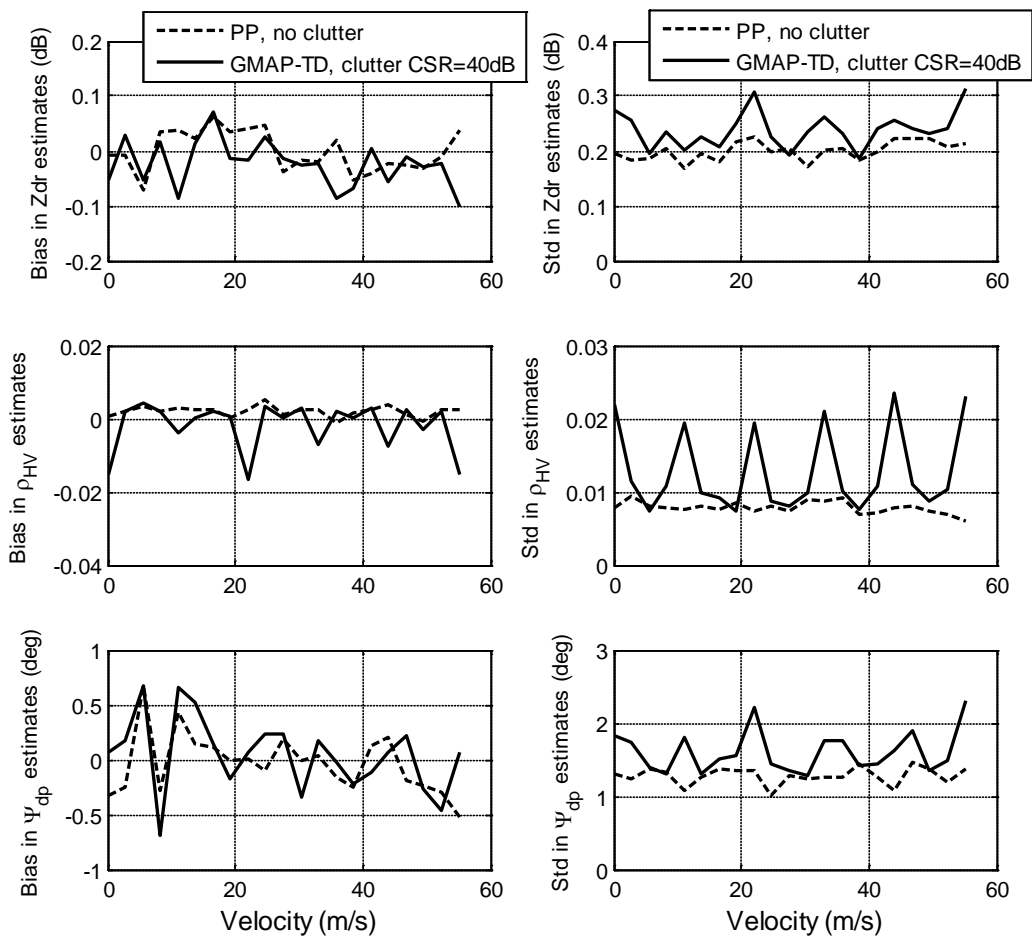


Figure 6.9: Biases and standard deviations in the dual-polarization parameter estimates using the GMAP-TD method for staggered PRT sequences in alternating mode. Inputs parameters for the simulation program are $CSR = 40 \text{ dB}$, $\sigma_p = 1 \text{ m s}^{-1}$.

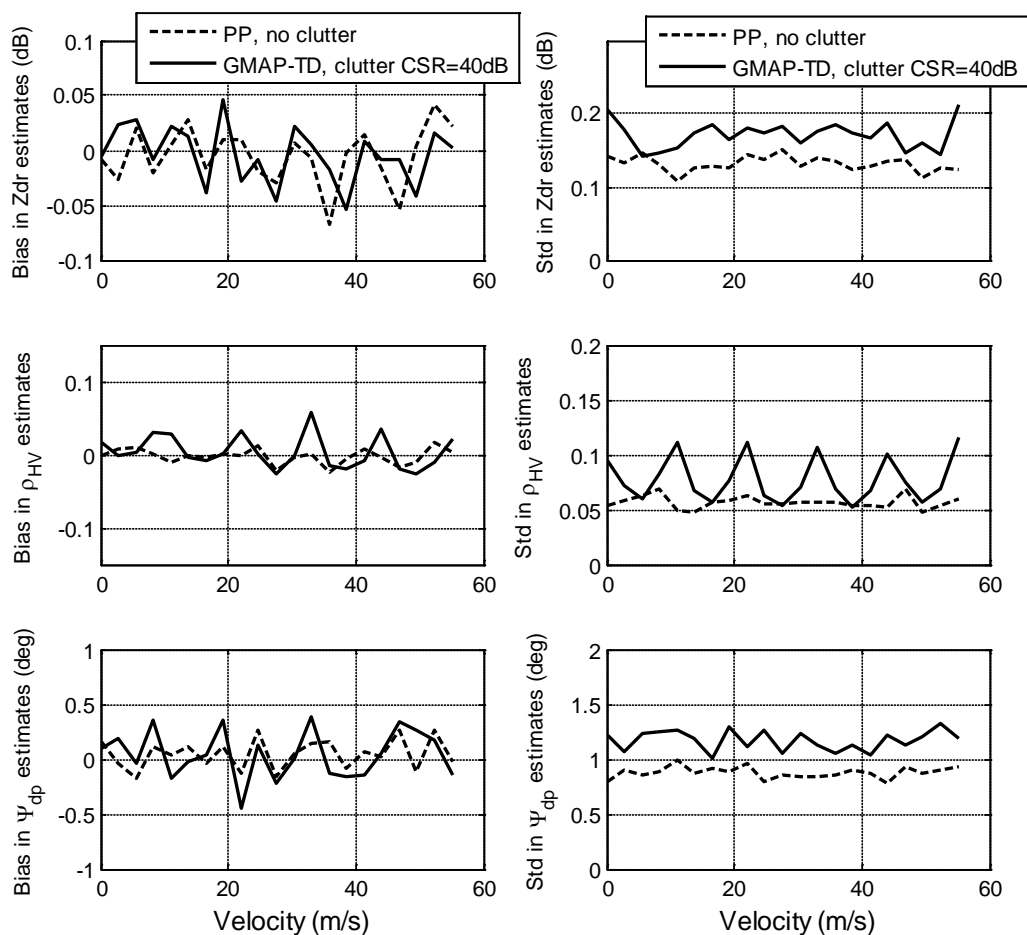


Figure 6.10: Same as figure 6.9, but for $\sigma_p = 4 \text{ m s}^{-1}$.

6.6 Test on CSU-CHILL radar data

In this section, the clutter filter for dual-polarization variables is validated using actual radar data. Staggered PRT ($T_1 = 1 \text{ ms}$ and $T_2 = 1.5 \text{ ms}$) observations of a large snowstorm were recorded at 23:58:19 UTC on December 20, 2006, by the CSU-CHILL radar. Due to the setup of the radar at that time, only data in the simultaneous mode are available. Detailed data collection is described in section 5.5, chapter 5.

Results for polarimetric retrievals are shown in fig. 6.11. The top row are PPI plots of measured Z_{dr} , $|\rho_{co}|$, and Φ_{dp} fields. The ellipses indicate large ground clutter present in the areas near the radar (within 20 km range) and the Rocky Mountain regions that severely contaminates the polarimetric measurement. At those regions, Z_{dr} biases can be as high as -2 dB; $|\rho_{co}|$ values drop from 0.99 to 0.94, and Φ_{dp} profiles are intermittent. Panels in the second row depict the estimates after applying the dual-polarization GMAP-TD algorithm to the data. A comparison between plots in the top and bottom rows shows a significant improvement: Z_{dr} and $|\rho_{co}|$ biases are removed and Φ_{dp} profile discontinuity is mitigated. Over all, the data quality after filtering is much better than that of the original measurement, except we lose data at some points around the mountainous regions where the clutter signal is very strong. Again, this can be a problem of the power saturation of the CSU-CHILL radar when working in staggered PRT 2/3 mode.

6.7 Summary

The main difficulty associated with the staggered PRT pulsing technique has been clutter filtering. In a transmission mode where staggered PRT combines with PAWR block pulsing, this task is even more challenging. In chapter 5, we have proposed a time domain method, GMAP-TD, that allows effective filtering of ground clutter for spectral moments estimation. In this chapter, the GMAP-TD filter is implemented for polarimetric retrievals. Implementations for simultaneous and alternating modes are proposed. Both employ the same principle of using one filter for two channels to maintain the signal correlation after filtering. The GMAP-TD polarimetric filter is modified from the GMAP-TD filter. In the simultaneous mode, where the H and V polarization waveforms are identical, filter modification is minimal. In the alternating

mode, waveforms and Doppler intervals of the two polarizations are different and the procedure involves more advanced techniques.

The radar simulation study described above indicates that the procedure is very effective in retrieving polarimetric variables even in cases of strong clutter contamination ($CSR = 40dB$). For the simultaneous transmission mode, the performance of the method is as good as in the case of signals without clutter. For the alternating mode, statistical errors in the estimates slightly increase due to the mismatch in polarization waveforms and the complexity of the filter. This can be considered as a trade-off in this mode: a technique that utilizes the depolarization characteristics of precipitation targets to suppress second-trip echoes and staggered PRT waveforms to increase unfolding velocity. However, the noticeable increment in errors occurs in rare situations where the signal spectrum width is narrow and located at certain Doppler bands. The effectiveness of the clutter-filtering process is also successfully demonstrated with actual CSU-CHILL dual-polarized staggered PRT time series.

The GMAP-TD procedure for polarimetric retrievals does not include an interpolation loop so the computational load is not demanding. Thus, it is suitable for PAWR where the use of radar resources is critical.

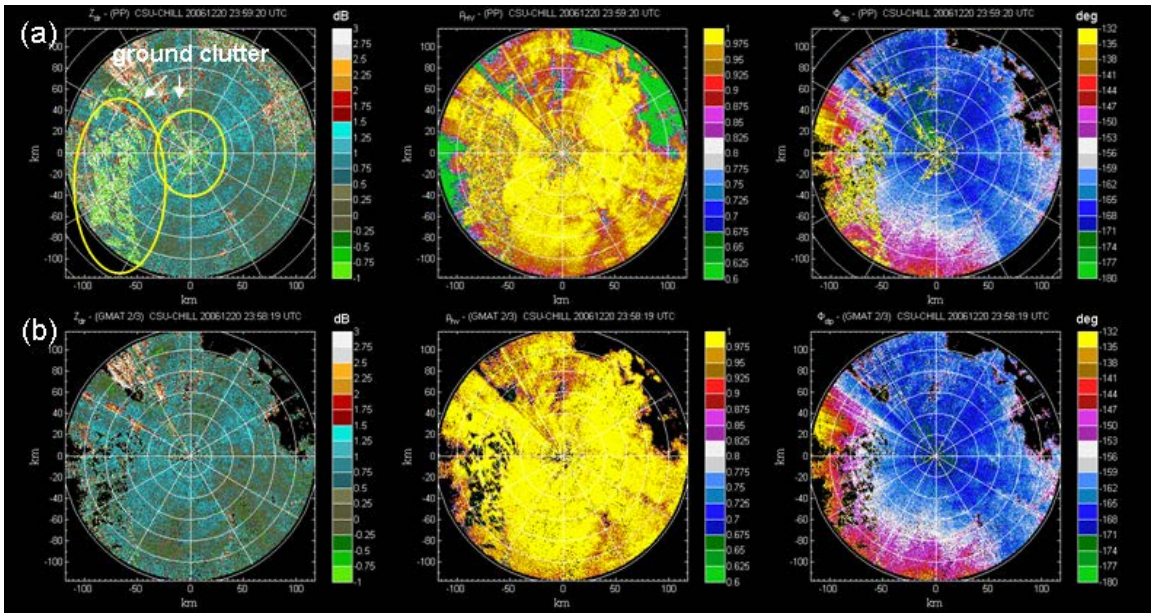


Figure 6.11: PPI plots show performance of GMAP-TD for dual-polarized variable retrieval on CSU-CHILL measurements. Panels in the top row (a) are differential reflectivity (Z_{dr}), co-polar correlation coefficient ($|\rho_{co}|$) and differential phased (Φ_{dp}) before clutter filtering. Panels in the bottom row (b) are the corresponding estimates with GMAP-TD.

CHAPTER 7

SENSITIVITY ENHANCEMENT SYSTEM FOR PULSE COMPRESSION WEATHER RADAR

7.1 Introduction

Sensitivity is a critical aspect of any radar system. It is especially critical for weather radar because the system is supposed to detect patterns as well as precisely measure relatively weak precipitation echoes. This aspect is even more imperative for PAWR because the system sensitivity decreases significantly at off-boresight directions (chapter 4). Modern active phased-array antennas include many elements in which each has its own transmit and receive modules. To keep costs down, low-power, solid-state transmitters are used at each element. The primary drawback of these transmitters is low peak power. This is because the weather radar sensitivity is inversely proportional to the product of pulse width and peak power (Bringi and Chandrasekar, 2001). However, solid-state transmitters have relaxed restrictions on the duty cycle that allow implementation of pulse compression techniques in order to obtain acceptable sensitivity for weather observations.

Pulse compression is a technique that allows a radar system to transmit a long coded waveform and compress the received echo to obtain a narrow pulse. The primary objective of the pulse compression technique is to improve range resolution and sensitivity while avoiding transmission of higher peak power. This technology has been widely used in military and air-traffic control radar systems since early the 1950s and is reviewed in the literature (Skolnik, 2001). However, the use of pulse compression in ground-based weather radar to study

precipitation targets is very limited. In the early 1970s, Fletter demonstrated a 7-bit Barker phase-coded pulse on the coherent FPS-18 radar at McGill University (Fetter, 1970). Bucci and Urkowitz (1993), Keeler (1995), and Mudukutore et al. (1998) have presented technical and engineering aspects of this application. Recently, frequency-diversity pulse compression waveforms have been implemented and demonstrated in the Ku-Ka band NASA Dual-Frequency Dual-Polarized Doppler Radar (D3R) (Chandrasekar et al. 2011). In this work, system sensitivity, a critical aspect of pulse compression technique for weather targets, has been studied.

In a pulse compression weather radar, the transmitted pulse has a long duration and wide bandwidth. A long pulse width is needed to increase measurement sensitivity. For example, with the same peak/average transmitted power, a system using a 40 μs pulsewidth is nearly 15 dB more sensitive than one transmitting a pulse of 1 μs width. In order to get improved range resolution, the wideband signal is vital; however, it is accompanied by a major drawback. Because the receiver noise is proportional to the bandwidth, a wider band receiver would introduce more noise into the system, thereby decreasing system sensitivity. For instance, an operational system using a Taylor mismatch filter designed for a peak sidelobe level (PSL) of 38.5 dB would require a time-bandwidth product (BT) of 400. Thus, if 40 μs pulses are used, the transmitted signal bandwidth has to be at least 10 MHz. When compared to a system using uncoded pulses of 1 MHz bandwidth, the system noise increases by 10dB. Consequently, the system sensitivity is held back by 10 dB. To overcome this problem, one might think of using a low-pass filter (LPF) to remove the noise at the receiver. However, due to inherent properties of the wideband signal and the white noise, employing any LPF at the receiver to reduce noise will also increase the filter loss. Hence, improving the system sensitivity using such standard techniques is not recommended.

In this chapter, a sensitivity enhancement system (SES) for pulse-compression weather radars is introduced. SES utilizes a transmission scheme with two different waveforms that is implemented to make sure that both waveforms will measure the same precipitation volume. At the receiver, an adaptive filter is designed based on the self-consistency between signals from the waveforms. The signal from the second waveform is estimated at each range gate using prior knowledge of the medium obtained from the first waveform. The SES processing is more complex than the conventional pulse compression techniques but it is able to improve the system sensitivity significantly and provide very good Doppler tolerance and PSL performance.

7.2 Signal model

Consider a pulse compression radar system with a chirp frequency of F_s . The corresponding sampling time is $T_s = 1/F_s$. The range resolution corresponding to the sub-pulse is $r = cT_s/2$, where c is the velocity of light in a vacuum. For example, a system with a 10 MHz chirp gives a sub-pulse range resolution of 15 m. Figure 7.1 shows a signal transmission model where both precipitation range profile and transmitted waveform are sampled at frequency F_s . The range profile is represented by a vector of contiguous samples $\mathbf{x} = [x_0, x_1, \dots, x_M, \dots]$ where x_i is the signal from the i^{th} range gate.

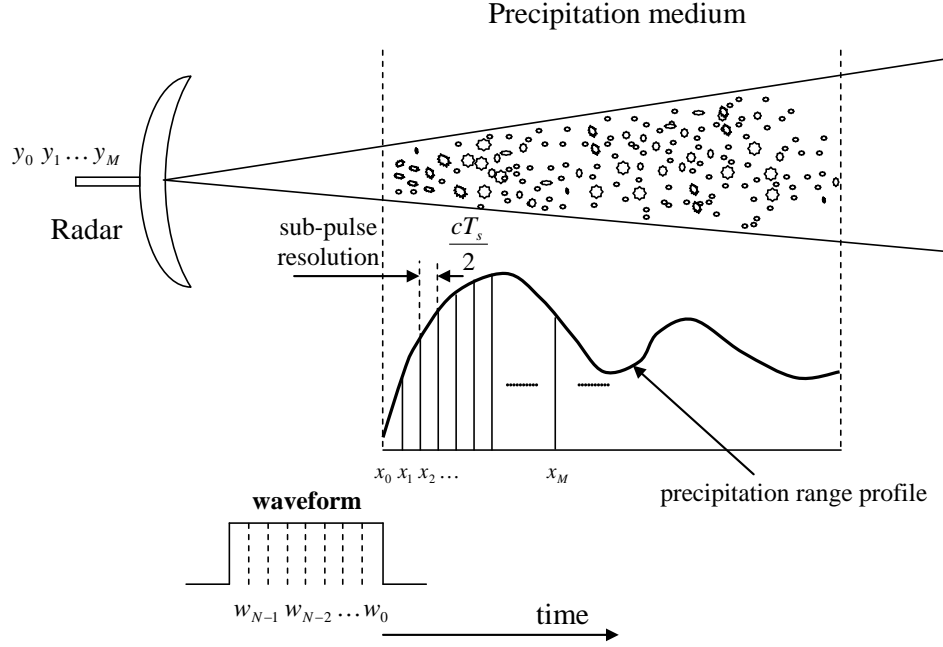


Figure 7.1: Discrete signal model.

According to Bringi and Chandrasekar (2001), the received signal is a convolution of the medium and transmitted waveform. Denoting a N -length vector $\mathbf{w} = [w_0, w_1, \dots, w_{N-1}]^T$ as a transmit waveform, the received signal at the antenna port is expressed by

$$\mathbf{y} = \mathbf{x} * \mathbf{w} + \boldsymbol{\eta} \quad (7.1)$$

where $(*)$ denotes the convolution operator; $\boldsymbol{\eta}$ is noise vector.

The convolution (7.1) can be expressed in a matrix form,

$$\begin{bmatrix} y_0 \\ y_1 \\ y_2 \\ \vdots \\ y_{M-1} \\ y_M \end{bmatrix} = \begin{bmatrix} x_0 & 0 & \cdots & 0 \\ x_1 & x_0 & \cdots & 0 \\ x_2 & x_1 & \cdots & 0 \\ \vdots & \vdots & & \vdots \\ x_{M-1} & x_{M-2} & \cdots & x_{M-N} \\ x_M & x_{M-1} & \cdots & x_{M-N+1} \end{bmatrix} \begin{bmatrix} w_0 \\ w_1 \\ w_3 \\ \vdots \\ w_{N-1} \end{bmatrix} + \begin{bmatrix} \eta_0 \\ \eta_1 \\ \eta_2 \\ \vdots \\ \eta_{M-1} \\ \eta_M \end{bmatrix} \quad (7.2)$$

For $n \geq N - 1$ we define a processing window $[n-N+1, n+N-1]$ as

$$\begin{bmatrix} y_n \\ y_{n+1} \\ \vdots \\ y_{n+N-1} \end{bmatrix} = \begin{bmatrix} x_n & x_{n-1} & \cdots & x_{n-N+1} \\ x_{n+1} & x_n & \cdots & x_{n-N+2} \\ \vdots & \vdots & \ddots & \vdots \\ x_{n+N-1} & x_{n+N-2} & \cdots & x_n \end{bmatrix} \begin{bmatrix} w_0 \\ w_1 \\ \vdots \\ w_{N-1} \end{bmatrix} + \begin{bmatrix} \eta_n \\ \eta_{n+1} \\ \vdots \\ \eta_{n+N-1} \end{bmatrix} \quad (7.3)$$

or in a short notation

$$\mathbf{y}_n = \mathbf{X}_n \mathbf{w} + \boldsymbol{\eta}_n \quad (7.4)$$

where $\boldsymbol{\eta}_n$ is an additive white noise vector within the processing window, $\boldsymbol{\eta}_n \sim N(0, \sigma_N^2 \mathbf{I}_N)$,

σ_N^2 is noise power, and \mathbf{I}_N is an identity matrix.

7.3 Sensitivity enhancement system (SES)

7.4.1 Sensitivity of pulse compression weather radar

The reflectivity is estimated from the received power at the shifted reference plane (fig. 7.2).

The reflectivity is given by

$$Z_e = C' R^2 \bar{P}_{ref} \quad (7.5)$$

In equation (7.5), \bar{P}_{ref} is the received power at the reference port, R is the radar range, and C' is a constant given by

$$C' = \frac{1}{\pi^5 |K_w|^2} \left(\frac{2}{c\tau} \right) \left[\frac{(4\pi^3 l_{wg}^2)}{P_t G_0^2} \right] \left(\frac{8 \ln 2}{\pi \theta_B \phi_B} \right) \lambda^2 \quad (7.6)$$

The power at the reference plane is related to the power at the output of the receiver by

$\bar{P}_{ref} = \left(\frac{l_r}{G_r} \right) \bar{P}_0$, where l_r is the filter loss and G_r is the receiver gain (Bringi and Chandrasekar,

2001). Hence, the equivalent reflectivity can be computed from the receiver output power,

$$Z_e = CR^2 \bar{P}_0 \quad (7.7)$$

where

$$C = \frac{1}{\pi^5 |K_w|^2} \left(\frac{2}{c\tau} \right) \left(\frac{l_r}{G_r} \right) \left[\frac{(4\pi^3 l_{wg}^2)}{P_t G_0^2} \right] \left(\frac{8 \ln 2}{\pi \theta_B \phi_B} \right) \lambda \quad (7.8)$$

The unit of Z_e is $mm^2 m^{-1}$. In practice, this is expressed in decibel scale (dBZ). The radar equation can now be written as

$$Z_e [dBZ] = \bar{P}_0 [dBm] + C [dB] + 20 \log(R [km]) \quad (7.9)$$

The notations used in the above equations are explained in Bringi and Chandrasekar (2001).

It is customary to define the minimum detectable reflectivity Z_e at a given range R when the signal-to-noise ratio is unity; i.e., $\bar{P}_0 = P_N = kTB$, where B is the receiver-equivalent noise bandwidth. Equation (7.9) can be rewritten as

$$\min(Z_e) [dBZ] = 10 \log_{10}(kTB) + C [dB] + 20 \log(R [km]) \quad (7.10)$$

The radar sensitivity is studied in terms of the minimum reflectivity (Bringi and Chandrasekar, 2001).

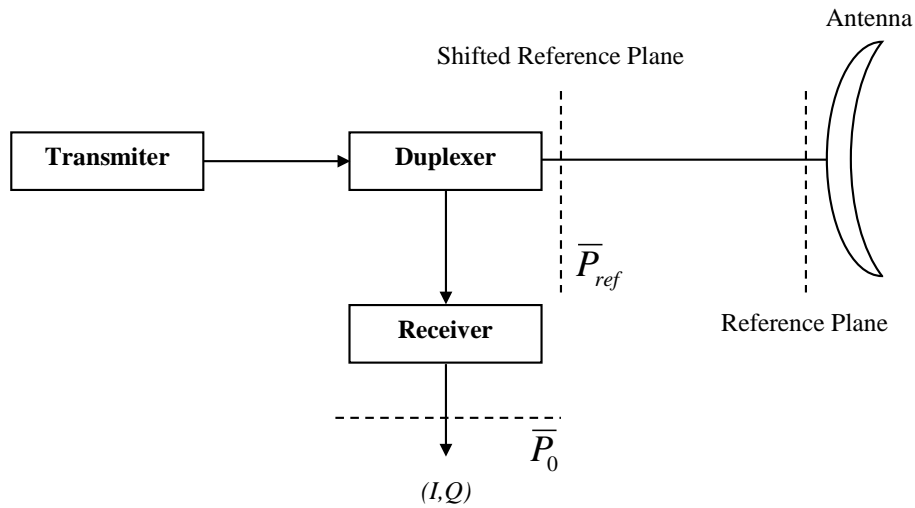


Figure 7.2: Illustrating the shifted reference plane for reflectivity calculation (Bringi and Chandrasekar, 2001).

Equations (7.8) and (7.10) suggest several ways to improve system sensitivity. While the option of increasing the transmit peak power is limited by the use of low-power solid-state transmitters in PAWR, designing a better pulse compression filter for sensitivity enhancement is a potential solution. An intuitive way to do this is to narrow the receiver filter bandwidth to reduce the product kTB in (7.10). However, given the fact that a pulse compression waveform is a wideband signal, reducing filter bandwidth results in increasing the filter loss l_r (Bringi and Chandrasekar, 2001) and therefore, it degrades the system sensitivity performance. In addition, a narrower filter bandwidth will lead to a larger output's range resolution, which may be unacceptable for many meteorology applications. Hence, improving the system sensitivity using this approach is not recommended.

It is known that the received radar returns (\mathbf{y}_n) include convolutional components involving samples of \mathbf{X}_n prior to and after the n^{th} gate. Conventional pulse compression filters such as matched filter or ISL filter do not account for this characterization. As a result, when a significantly large signal is present within the $(N-1)$ range gates prior to or after sample x_n , the performance of those filters can be deleteriously affected. In addition, a conventional pulse-compression matched filter may not always provide an optimal SNR. Those shortcomings suggest that it is necessary to obtain an adaptive filter for the received signals of a pulse-compression weather radar. The filter's coefficients should be able to adapt to the distribution of signal density over the measurement range and also be able to account for the Doppler shift effect. The remainder of this chapter develops a novel system called a sensitivity enhancement system (SES) for pulse-compression weather radar that significantly improves system sensitivity while maintaining robust estimates of signal parameters.

7.4.2 Signal covariance matrix

For precipitation targets, signals from different range gates are zero-mean and uncorrelated.

The covariance matrix of the measured signal can be represented as

$$\begin{aligned}
\mathbf{R}_{yy} &= E\{\mathbf{y}_n \mathbf{y}_n^H\} = E\{(\mathbf{X}_n \mathbf{w} + \boldsymbol{\eta}_n)(\mathbf{X}_n \mathbf{w} + \boldsymbol{\eta}_n)^H\} \\
&= E\{\mathbf{X}_n (\mathbf{w} \mathbf{w}^H) \mathbf{X}_n^H\} + E\{\boldsymbol{\eta}_n \boldsymbol{\eta}_n^H\} \\
&= E\{\mathbf{X}_n \mathbf{W} \mathbf{X}_n^H\} + \sigma_N^2 \mathbf{I}_n \\
&= \sum_{k=-(N-1)}^{N-1} p_{n+k} \mathbf{W}_k + \sigma_N^2 \mathbf{I}_n
\end{aligned} \tag{7.11}$$

where the superscript H denotes Hermitian transpose and p_{n+k} is signal power at gate $(n+k)^{th}$.

$\mathbf{W} = \mathbf{w} \mathbf{w}^H$ and \mathbf{W}_k is a shifted version of \mathbf{W} by k elements and the remainder is zero-padded.

We denote $\mathbf{W}_k = \text{circ}(\mathbf{W}, k)$. If k is positive, the values of \mathbf{W} are shifted down and right. If k is

negative, the values of \mathbf{W} are shifted up and left. For example,

$$\mathbf{W}_1 = \text{circ}(\mathbf{W}, 1) = \begin{bmatrix} 0 & 0 & \cdots & 0 \\ 0 & w_{1,1} & \cdots & w_{1,N-1} \\ \vdots & \vdots & \ddots & \vdots \\ 0 & w_{N-1,1} & \cdots & w_{N-1,N-1} \end{bmatrix} \tag{7.12a}$$

$$\mathbf{W}_{-1} = \text{circ}(\mathbf{W}, -1) = \begin{bmatrix} w_{2,2} & \cdots & w_{2,N} & 0 \\ \vdots & \ddots & \vdots & \vdots \\ w_{N,2} & \cdots & w_{N,N} & 0 \\ 0 & \cdots & 0 & 0 \end{bmatrix} \tag{7.12b}$$

For $m \leq N-1$, denote $\mathbf{x}_m = [x_{n-m}, x_{n-m+1}, \dots, x_{n+m-1}, x_{n+m}]^T$ and its covariance matrix is expressed

as

$$\mathbf{R}_{xx} = E\{\mathbf{x}_m \mathbf{x}_m^H\} = \begin{bmatrix} p_{n-m} & 0 & \cdots & 0 \\ 0 & p_{n-m+1} & \cdots & 0 \\ \vdots & \vdots & \ddots & \vdots \\ 0 & 0 & \cdots & p_{n+m} \end{bmatrix} \tag{7.13}$$

Note the signal covariance matrix is only defined by power samples of the medium.

7.4.3 SES processing

In this section, we derive the estimator of the unobserved vector \mathbf{x}_m on the basis of observed vector \mathbf{y}_n . By definition,

$$\hat{\mathbf{x}}_m = \arg \max_{\mathbf{x}_m} f_{\mathbf{y}|\mathbf{x}}(\mathbf{y}_n | \mathbf{x}_m) f_{\mathbf{x}}(\mathbf{x}_m) \quad (7.14)$$

where $f_{\mathbf{y}|\mathbf{x}}$ is the probability distribution of \mathbf{y}_n given \mathbf{x}_m and $f_{\mathbf{x}}$ is the prior distribution of \mathbf{x}_m .

The distributions of the weather radar signals are multivariate normal (Bringi and Chandrasekar, 2001), and therefore

$$f_{\mathbf{x}}(\mathbf{x}_m) = \frac{1}{(2\pi)^{(2m+1)/2} \det(\mathbf{R}_{\mathbf{xx}})} \exp\left\{-\frac{1}{2} \mathbf{x}_m^H \mathbf{R}_{\mathbf{xx}}^{-1} \mathbf{x}_m\right\} \quad (7.15a)$$

$$f_{\mathbf{y}|\mathbf{x}}(\mathbf{y}_n | \mathbf{x}_m) = \frac{1}{(2\pi)^{N/2} \det(\mathbf{R}_{\mathbf{zz}})} \exp\left\{-\frac{1}{2} (\mathbf{y}_n - \mathbf{S}_m \mathbf{x}_m)^H \mathbf{R}_{\mathbf{zz}}^{-1} (\mathbf{y}_n - \mathbf{S}_m \mathbf{x}_m)\right\} \quad (7.15b)$$

where $\mathbf{R}_{\mathbf{xx}}$ is described in (7.13) and $\mathbf{R}_{\mathbf{zz}}$ is the covariance matrix of $\mathbf{z} = \mathbf{y}_n - \mathbf{S}_m \mathbf{x}_m$,

$$\mathbf{R}_{\mathbf{zz}} = \sum_{\substack{k=-(N-1) \\ |k|>m}}^{N-1} p_{n+k} \mathbf{W}_k + \sigma_N^2 \mathbf{I}_N \quad (7.16)$$

$$\mathbf{S}_m = \begin{bmatrix} w_m & w_{m-1} & \cdots & w_0 & 0 & \cdots & 0 \\ w_{m+1} & w_m & \cdots & w_1 & w_0 & \cdots & 0 \\ \vdots & \vdots & \ddots & \vdots & \vdots & \ddots & \vdots \\ 0 & 0 & \cdots & w_{N-1} & w_{N-2} & \cdots & w_{N-m-1} \end{bmatrix} \quad (7.17)$$

Substituting equations (7.15), (7.16), and (7.17) in (7.14), taking the derivative with respect to \mathbf{x}_m and solving for minima, we obtain the estimator for \mathbf{x}_m in a closed-form expression,

$$\hat{\mathbf{x}}_m = (\mathbf{S}_m^H \mathbf{R}_{\mathbf{zz}}^{-1} \mathbf{S}_m + \mathbf{R}_{\mathbf{xx}}^{-1})^{-1} \mathbf{S}_m^H \mathbf{R}_{\mathbf{zz}}^{-1} \mathbf{y}_n \quad (7.18)$$

The solution (18) has a form $\hat{\mathbf{x}}_m = \mathbf{F}\mathbf{y}_n$ where

$$\mathbf{F} = \left(\mathbf{S}_m^H \mathbf{R}_{zz}^{-1} \mathbf{S}_m + \mathbf{R}_{xx}^{-1} \right)^{-1} \mathbf{S}_m^H \mathbf{R}_{zz}^{-1} \quad (7.19)$$

is termed the adaptive filter for SES.

7.4.4 Doppler compensation

The analysis described in the above section does not include the Doppler shift effects. It simply assumes that the Doppler shifts of the samples \mathbf{x}_m are equal to zero. Although the gradient in radial Doppler shifts of weather targets is not as high as that in the case of military targets, it may still affect the filter performance, especially where a weather radar system is required to measure weather signals accurately. For example, a strong and fast-moving storm may heavily contaminate nearby weak cells due to the sidelobe problem. Therefore, in designing a pulse-compression filter for weather radar, the Doppler effect needs to be taken into account.

Let f_i be the Doppler frequency corresponding to a signal at sub-pulse gate i^{th} , the Doppler phase shift over a period of T_s is $\theta_i = -2\pi T_s f_i$. At the receiver, the transmit waveform is modified to include this Doppler shift

$$\mathbf{w}^i = [w_0, w_1 e^{j\theta_i}, \dots, w_{N-1} e^{j(N-1)\theta_i}]; \quad j = \sqrt{-1} \quad (7.20)$$

and

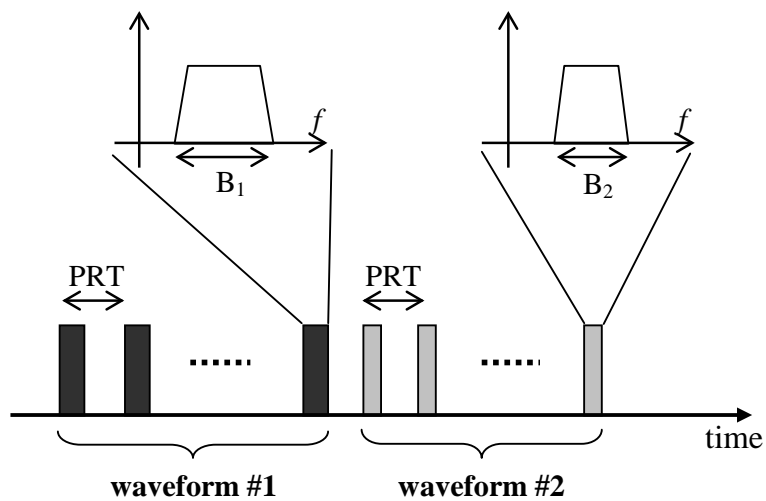
$$\mathbf{W}^i = (\mathbf{w}^i)(\mathbf{w}^i)^H \quad (7.21)$$

Accordingly, \mathbf{W}_k needs to be replaced by its Doppler-modulated version,

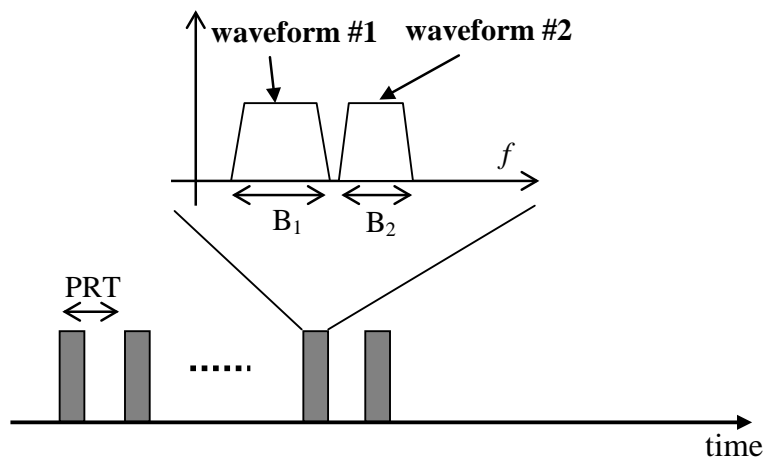
$$\mathbf{W}_k \rightarrow \mathbf{W}_k^D = circ(\mathbf{W}^{(n+k)}, k) \quad (7.22)$$

7.4 SES dual-waveform scheme

SES processing requires a prior knowledge of the signal power and Doppler shifts, which are unknown. To tackle this problem, SES proposes a transmission scheme that utilizes two different waveforms. The two waveforms are transmitted separately either in time or in frequency but they both measure the same precipitation volume. Figure 7.3 depicts that scheme.



(a) In time domain



(b) In frequency domain

Figure 7.3: The SES transmission waveform scheme.

In the scenario where the two waveforms can be transmitted simultaneously at different frequencies, observed volume is perfectly matched. If the two waveforms are transmitted at different times, the time difference selected should be small enough to ensure that the precipitation volume can be assumed to be statistically stationary. For instance, the two waveforms can be transmitted in a sequence (fig. 7.3b); the difference in transmission time between the two waveforms is equal to the dwell time for the first waveform, which is normally on the order of ms. With the different time periods, precipitation targets can be assumed to be unchanged.

The main idea of SES is that the first waveform is used to obtain initiative knowledge of the medium and the second waveform uses this information to deploy SES processing. In detail, the first waveform provides the density distribution and Doppler shift profile of the medium. Using power samples and Doppler samples from these profiles, we generate the adaptive filter (7.19) for the second waveform. The filter is specified at each range gate. It is noticed that the power samples from the first waveform are independent if the range spacing between them is equal to or greater than the range resolution. Therefore, in designing the second waveform, it is suggested to constraint the second waveform bandwidth to be equal to or smaller than the bandwidth of a rectangular pulse with the pulse width equal to the range resolution of the first waveform.

7.4.1 Waveform design procedure

Depending on system resources, the SES waveforms can be designed to be time diverse or frequency diverse. For a system with limited bandwidth, the two waveforms can be transmitted consecutively. In that way, both waveforms can use the entire system's available bandwidth. In this scheme, the hardware requirement is minimal. Figure 7.3a illustrates this transmission technique. The major drawback of this method is that it requires a larger dwell time. Therefore, it

is not the best choice for fast-scanning systems like PAWR but is very useful for systems such as cloud radars where the targets do not move or evolve quickly while the sensitivity is more critical. In a system whose bandwidth is large enough, the two waveforms can be designed so that their bandwidths are fitted within that band (e.g., the NASA D3R system (Chandrasekar et al., 2011)). Volume-matching in this case is perfect and dwell time is reduced by half compared to the previous scheme. Apparently, this scheme is more suitable for PAWR. However, the cost is that the system needs more hardware components and computation power. Each scheme has its own advantages and disadvantages, but SES implementation is flexible enough to fit the design space of most radar pulse compression systems. In general, SES waveform design includes the following steps:

1. Assign the first waveform frequency and bandwidth given the available resources of the system.
2. Determine the waveforms' durations. The first waveform duration is chosen so that it is able to provide adequate PSL performance for weather targets (for example, -50 dB). Again, the selection depends on the system specifications (e.g., transmitter duty cycle), the design domain (time or frequency domain) and other factors such as the system's blind range requirement. Note that the blind ranges of the waveforms will determine the region where SES processing can be applied.
3. Design the first waveform and its pulse compression filter. At this step, the objective is to acquire a decent PSL and range resolution performance at the output of the first waveform.
4. Compute the range resolution of the compressed pulse of the first waveform.

5. Determine the second waveform's bandwidth. This depends on the desired range resolution of the final output. If possible, this bandwidth is chosen to be equal to or smaller the inverse of the range resolution of the first waveform.
6. Design the second waveform with parameters specified in steps 2 and 5.

7.4.2 Result combination

In SES processing, there are products available from the two waveforms. Output from the second waveform has better sensitivity and it is able to measure weak signals more accurately. However, at regions with strong returns, both waveforms should be able to provide comparable measurements. The products are independent because they come from two different waveforms; therefore, they can be arithmetically averaged to generate final results that have lower standard deviations.

7.5 Method evaluation using simulation

7.5.1 Pulse compression weather radar data simulation

To validate the performance of the sensitivity enhancement system developed in this chapter, pulse compression radar signals are simulated for a variety of observation scenarios. Input profiles for the simulation are either synthesized profiles or actual measurements by the Collaborative Adaptive Sensing of the Atmosphere Integrative Project 1 (CASA IP1) radars. The simulation method is done similarly to the procedure described in Mudukutore et al. (1998) except that the effect of the Doppler shift (section 7.4.4) is added. In order to evaluate the sensitivity improvement, we chose that the two waveforms have the same width, which is 40 μ s. The first waveform's bandwidth is set at 4 MHz to provide an acceptable peak sidelobe level

when using a conventional mismatched filter. The second waveform is computed using the procedure described in the above section. Input parameters for the simulation are given in table 7.1.

Table 7.1: Pulse compression simulation input parameters.

<i>Parameters</i>	<i>Values</i>
peak transmit power, W	200
sampling frequency (F_s), MHz	5
waveform 1 pulse width, μs	40
waveform 2 pulse width, μs	40
waveform 1 bandwidth, MHz	4
waveform 2 bandwidth, MHz	0.83
noise figure, dB	4.5
spectrum width, ms^{-1}	2
m , samples	64

7.5.2 Minimum ISL filter

The minimization of integrated sidelobe level (ISL) (Ackroyd and Ghani, 1973) is an efficient technique for designing a mismatched pulse compression filter. The ISL filter has been shown to be excellent for weather radar applications (Bharadwaj et al. 2012). In this work, an ISL filter (also called L_p -norm filter) is used for the first SES waveform.

This technique is based on the observation that if the input signal is an impulse, then the compressed pulse is the convolution of the transmit waveform and the pulse compression filter. If the compressed pulse's peaks are pre-defined and are removed from the output, the remainder coefficients are considered as sidelobe components. An optimization procedure is formed where the cost function is the integrated sidelobe. Solving the optimization problem provides the ISL filter's coefficients. The solution has a closed-form expression; therefore, the design of the filter is very fast and effective.

7.5.3 SES range-sidelobe performance

When SES is primarily designed to improve the system sensitivity of a pulse compression weather radar, it needs to perform well in other aspects. First, SES should provide a good range sidelobe performance because this property is very important for a pulse-compression weather radar system. Radar measurements often show strong and steep gradients in range-power profile. Strong echoes may contaminate the nearby range gates via their sidelobes, resulting in large measurement biases. In this experiment, the analysis is done with simulated radar range profiles that allow us to control the power gradient level. Along with SES, a standard system using matched filters (MF) for the two waveforms is also implemented for comparison. Estimates from the first waveform will be averaged in range and be downsampled to have a comparable range resolution to that from the second waveform. In fig. 7.4, a range profile of radar reflectivity is synthesized as the summation of two Gaussian-shaped echoes. The narrow echo with high power mimics the return signals from ground clutter and the other simulates a weather echo. The two echoes are located close together to study the sidelobe effect of the filtering process. In addition, Doppler velocity is set to 25 ms^{-1} at all range gates.

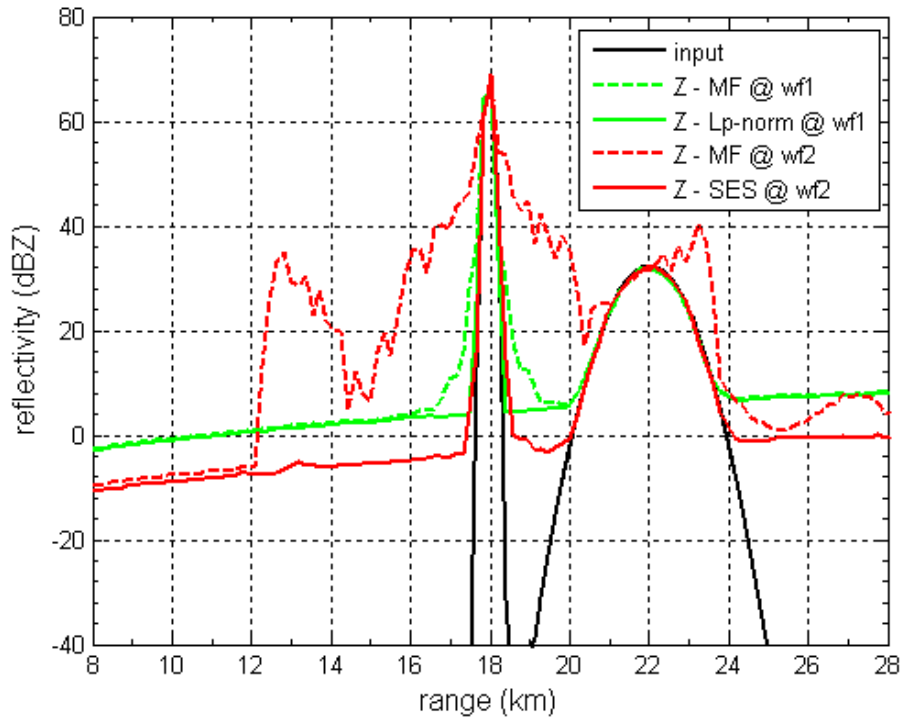


Figure 7.4: Simulated input profile (solid black line) and results from different pulse compression filters.

In figure 7.4, the L_p -norm filter for the first waveform (solid green line) performs pretty well. Its sensitivity is matched to that of the matched filter (dashed green line) while its PSL performance is significantly improved. In this case, the PSL level of the L_p -norm filter for the first waveform approximates -60 dB. Among those conventional filters, the matched filter for the second waveform (red dashed line) has a better sensitivity. This is explained by its smaller bandwidth. In contrast, its PSL performance is by far the worst, which is expected for a waveform with a time bandwidth product (BT) of only 33. As can be seen in fig. 7.4, the simulated weather echo is heavily contaminated by the sidelobes from the ground clutter and cannot be detected by this filter. The MF system for the second waveform does not meet the requirements for pulse-compression weather radar and cannot be used in practice. On the other

hand, the SES output (solid red line) for the second waveform shows the best performance in term of PSL. Even at high Doppler velocity (25 ms^{-1}), SES can provide -70 dB PSL. This level of range sidelobe suppression exceeds the sidelobe level of a typical two-way antenna pattern and, therefore, is adequate for most weather radar measurement scenarios.

7.5.4 SES power measurement accuracy

The second consideration is power measurement accuracy. In this section, a qualitative analysis of bias and standard deviation of SES power estimates is presented. Instead of using a Gaussian-shaped echo profile, a trapezoid profile with a specific gradient of 40 dB/km is used. The power ratio between the signals on either side of the gradient is 50 dB. Within a distance equal to a pulse's length, from 12 km to 18 km, the power level changes from -112 dBm to -62 dBm. Estimating a weak signal will be very challenging because of the strong signal involved in the de-convolution process. This is an extreme case and is used to test the power estimation performance of any pulse compression filters. The simulation runs many realizations to generate statistical plots. Figure 7.5a shows the input (solid blue line) and SES estimates. It can be seen that the estimates match pretty well with the input. Details of the measurement errors are depicted in fig. 7.5b. The solid line is for biases and the dashed line is for standard deviations. At most locations, the SES power bias is less than 1 dB. A slightly degraded performance occurs at the low region before the leading edge of the trapezoid, where SES underestimates the signal power by -2 to -1 dB and the corresponding standard deviations are a bit over 2 dB. However, at other ranges, the standard deviation is less than 2 dB. Results from a preliminary study demonstrate that, in the case of a moderate power gradient, SES provides unbiased estimates.

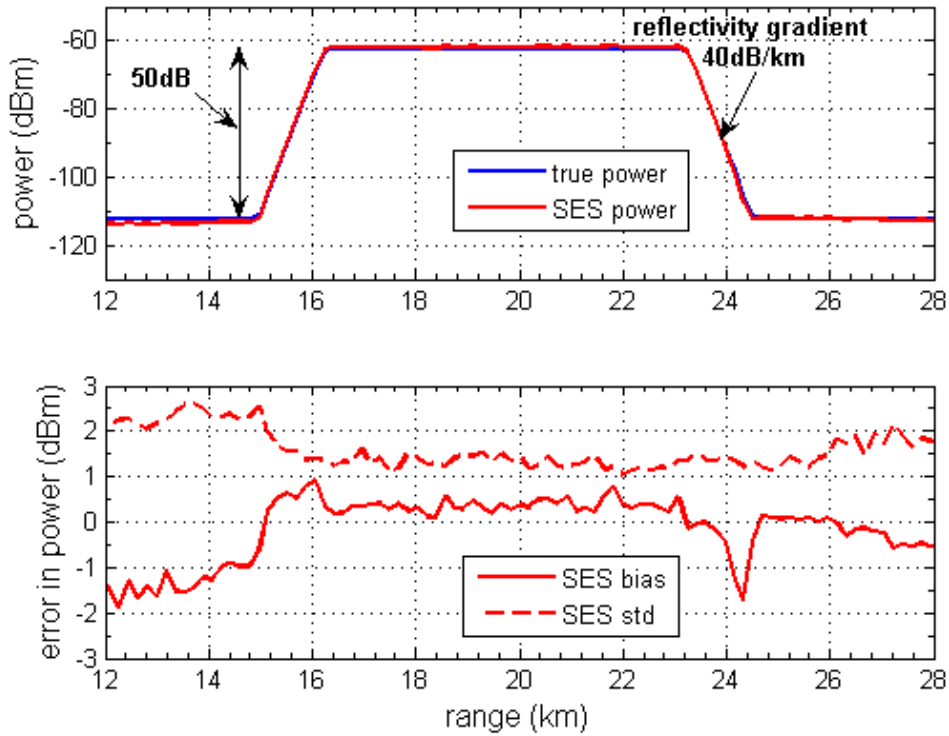


Figure 7.5: A trapezoid-shaped profile with a specific gradient of 40 dB/km. (a) Range profiles of input powers and estimated powers; (b) bias and standard deviation of the power estimates.

7.5.5 SES Doppler velocity measurement accuracy

Another important aspect that needs to be considered is the accuracy of Doppler velocity estimates. As mentioned above, a high gradient in Doppler shifts would degrade the performance of a pulse-compression filter system. On the other hand, the filter itself needs to estimate these Doppler shifts correctly. To test this capability of SES, a step-function velocity profile is used. The simulated velocity jumps from -13 ms^{-1} to 13 ms^{-1} at a range of 22 km and spectrum widths at all range gates are set at 2 ms^{-1} . The power range profile is created in a similar way as in fig. 7.4. Figure 7.6a shows the range profiles of the true power (black line), estimated power from first waveform of SES (blue line), and from SES (red line). Input Doppler velocity profile

and output of the SES filter (red line) are plotted in fig. 7.6b. Within the precipitation region (located between the two dashed black lines), the estimated velocity profile closely matches the input profile.

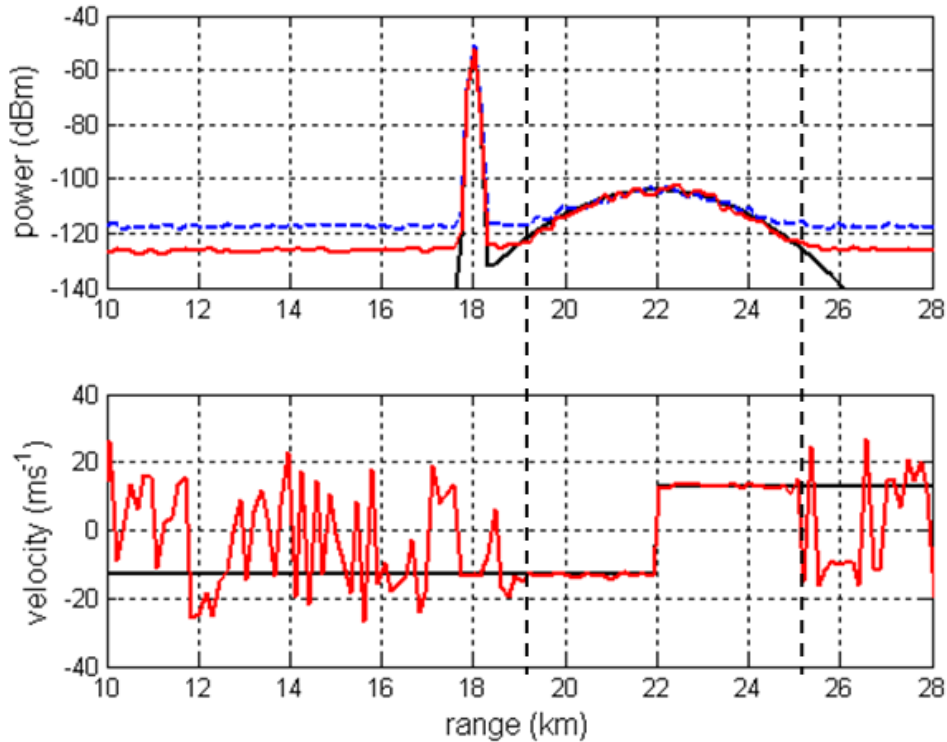


Figure 7.6: Step-function Doppler velocity profile with a 26 ms^{-1} step. Range profiles of signal power (a) and Doppler velocity (b).

7.5.6 SES sensitivity gain

The main contribution of SES is to provide a better sensitivity performance than conventional filter systems. In this section, an extensive analysis is performed to evaluate SES in this aspect. To assess the improvement in sensitivity, we define the SES sensitivity gain as the difference in sensitivity between the outputs of SES and a matched filter for the first waveform.

Minimum detectable reflectivity of the system using a matched filter for the first waveform is computed based on equation 7.10. For SES, since the filter coefficients change at each range gate, we cannot apply equation 7.10 directly. Thus, the sensitivity curve is obtained by means of simulation. To do that, a profile containing only receiver noise signal is used as the input for SES. The output profile is the sensitivity curve for SES.

The first experiment in fig. 7.4 clearly shows that SES achieves the best sensitivity performance. Besides the excellent PSL performance, the sensitivity curves of the filters for the first waveform (solid red) and the SES filter for the second waveform (green lines) implies an improvement of 8.9 dB in sensitivity for SES.

The analysis of the performance of SES thus far was done using synthetic profiles for reflectivity, velocity, SNR, etc. These profiles show the performance of SES in extreme conditions and provide a worst-case analysis. It is interesting to observe the behavior of SES with real weather profiles. To do that we ran SES on pulse-compression simulated data where inputs were generated from data collected by CASA IP1 Cyril radar during a tornado event in Oklahoma on February 10, 2009. The only modification here is that the power profiles are lowered for the purpose of studying sensitivity. All another moment profiles were retained as in the original data. The profiles were sampled at azimuth 330°. In fig. 7.7, powers are 20 dB less compared to the measurements. The top panel shows input reflectivity profile (solid black line), results from SES (red line) and MF for the first waveform (green line). The bottom panel depicts statistical plots. At regions with strong echoes (for example, a range from 16 to 19 km), SES and MF performance are comparable. Both systems are capable of providing accurate measurements. However, when the signal strength decreases (e.g., at a range from 23 to 25 km), the matched filter starts showing large power biases due to its lower sensitivity while SES still performs well.

The minimum sensitivity curves for both systems are generated and superimposed in the plot for comparison. With the radar specifications given in table 7.1, the SES sensitivity gain is 8.9 dB.

In the next experiment, we reduce the input powers further (by 30 dB) so that the input reflectivity profile is completely below the sensitivity curve of the MF system for the first waveform (fig. 7.8a). The result is that the MF system for the first waveform fails to estimate the signal. Its power estimates show large biases (from 3.5 to 15 dB) at all range gates. In contrast, SES still works fairly well (fig. 7.8b). Due to the lower SNR, the biases and standard deviations in the SES power estimates are slightly worse compared to those in fig. 7.7. However, at the regions where the signal is above the minimum reflectivity curve, SES is able to provide measurements with adequate data quality for weather radar. It is recalled that SES deploys information about the medium extracted from the first waveform outputs which, in this case, is off by a large margin. Therefore, this test demonstrates that SES is a very stable and robust method.

The advantage in sensitivity leads to more accurate estimates for SES compared to the conventional matched filters. One may think about improving the SES performance further by introducing an additional iterative procedure. In the first iteration, the reference profiles are extracted from the first waveform, as is normal. In the second iteration, they are replaced by the SES outputs at the first iteration. Using this strategy, the system sensitivity may be improved further. However, that technique is beyond the scope of this work and is not discussed here.

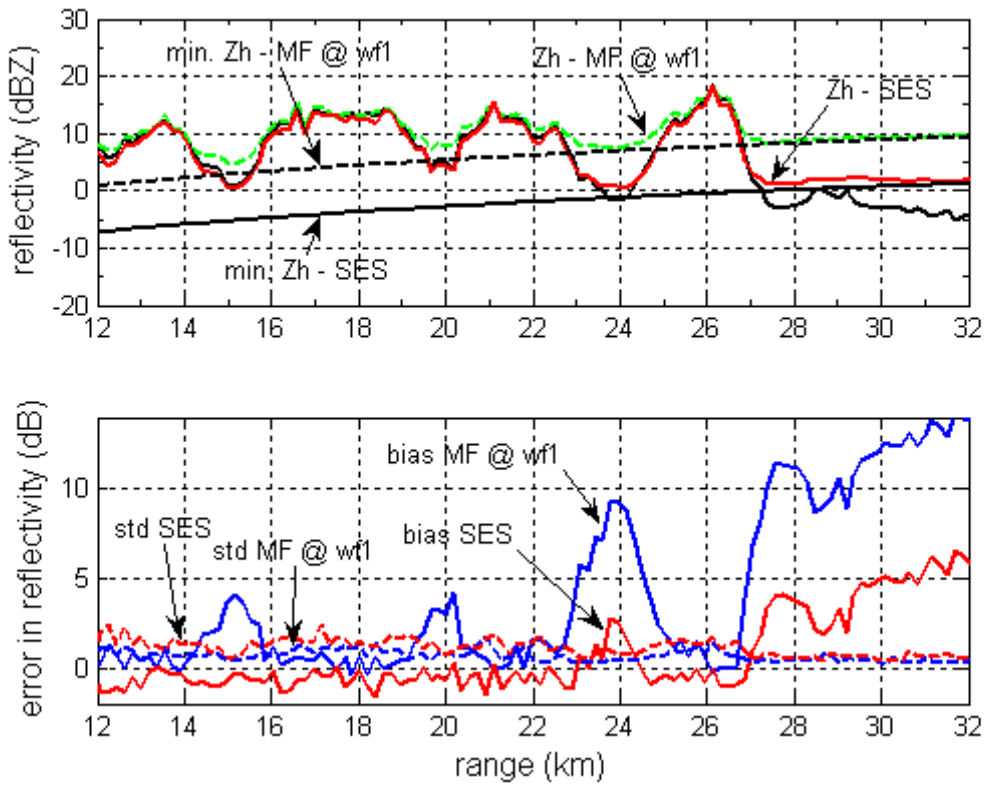


Figure 7.7: Cyril radar reflectivity profile at azimuth 330° (lowered by 20 dB for sensitivity analysis). (a) Estimated reflectivity profiles for MF and SES; (b) bias and standard deviation of reflectivity estimates.

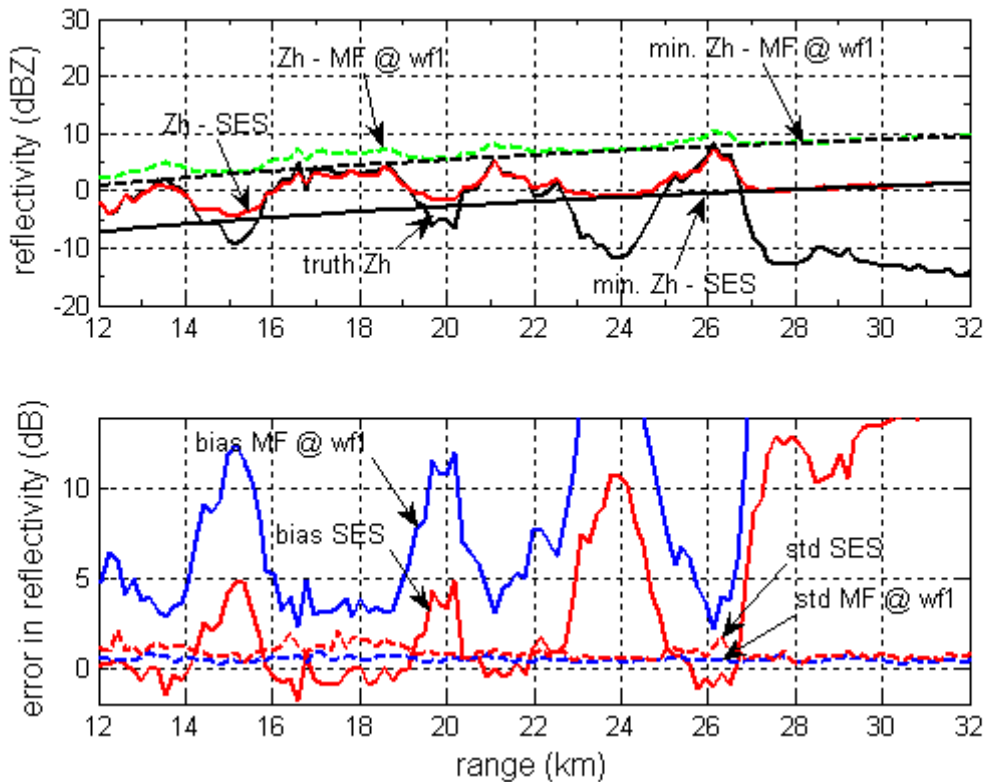


Figure 7.8: Same as in fig. 7 but the input reflectivity profile was lowered by 30 dB.

7.6 Illustration with D3R Ku-Ka system observations

The objective of the D3R system is to provide ground-based measurements for cross-validation with the precipitation observations of the GPM (Global Precipitation Measurement) program (Chandrasekar et al. 2010). To enable measurements for light rain and snow, the radar employs frequencies in the Ku and Ka bands. For both of these highly attenuating frequencies, the required sensitivity of the D3R is pegged at -10 dBZ at 15 km for a single pulse measurement in clear air. The radar also has a requirement of measuring Doppler velocity up to 25 ms^{-1} , to enable this it operates in the staggered PRT 2/3 mode. With such a premium placed on its

sensitivity, the D3R system is an appropriate platform for testing the efficacy of the SES waveform.

In its normal operational mode, the D3R employs a novel frequency-diversity waveform (Bharadwaj et. al., 2009) consisting of three subpulses of durations 40 μ s (long), 20 μ s (medium), and 1 μ s (short). The long and medium pulses are each coded with the signal bandwidth of 3.6 MHz. For transmission, this waveform is upconverted from a baseband sample rate of 50MHz. The digital receiver subsamples the received waveform at 200 MHz and then processes the downconverted data through a pulse compression filter that has an output sample rate of 10 MHz (Mishra et. al., 2011). The in-phase (I) and quadrature-phase (Q) outputs are finally made available at a downsampled rate of 1 MHz.

For the SES experiment on the D3R system, the waveform scheme consisted of only the long and medium subpulses. The pulse durations for the two-pulse SES waveform were kept identical to those of the long and medium pulses of the normal three-pulse D3R waveform (fig. 7.9). Further, the measurements obtained by the medium pulse in the SES waveform were used as a reference (the first waveform in the SES scheme). Therefore, the signal bandwidth (= 3.6 MHz) of the SES medium pulse was also identical to that of the medium pulse in the regular three-pulse waveform. However, the SES long pulse was designed for 1 MHz bandwidth, which is different than that of the regular long pulse. This is because even though the medium pulse is processed in the 10 MHz compression filter, these data are only available at a downsampled rate of 1 MHz in the current radar configuration. This setup enables a fair comparison between the data corresponding to the two waveforms and maximum compatibility with the normal processing mode of the radar. The SES experiment on the D3R system was carried out on

October 17, 2011, during a light rain event. The D3R radar was deployed at the CSU-CHILL radar facility at Greeley, Colorado, at the time of the experiment.

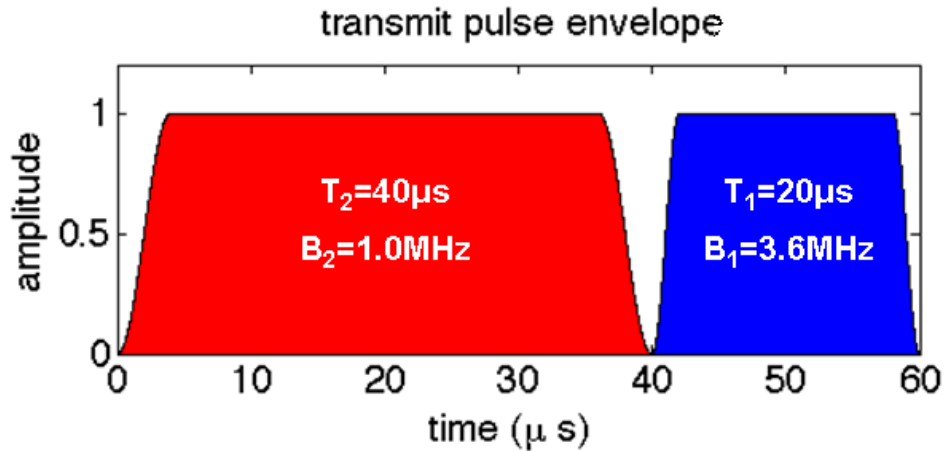


Figure 7.9: Waveform scheme for SES experiment on D3R system.

Figure 7.10 shows the Ku-band measurements obtained by the two waveforms during a sector PPI scan. It should also be noted that the total blind range for the long pulse is approximately 9 km when operated in multi-pulse mode. The first row in fig. 7.10 shows the estimates of the signal's first three spectral moments (reflectivity, mean velocity, and spectrum width) from a matched filter for the medium pulse in the SES scheme. The second row shows the outputs of the SES processing. In the weak echo regions such as the 330-360° sector, it is obvious that the SES processing provides enhanced sensitivity when compared to the medium pulse. Further, the observations made by the SES long and medium pulses show a remarkable agreement in the reflectivity as well as the velocity for the stronger echo regions (region between azimuth of 300-345° and range of 10-20 km).

Figure 7.11 shows in detail the reflectivity and velocity profiles at an azimuth of 279° as observed for the processing modes depicted in fig. 7.10. For the range gates with stronger echoes (such as those present from 10-18 km), the outputs of the MF for the medium pulse and the SES algorithm closely agree. At the range gates where weaker signals are exhibited (from 19 to 25 km range), SES performance is superior over the MF system. SES is able to pick up lower reflectivity and significantly improves velocity estimates in those range gates.

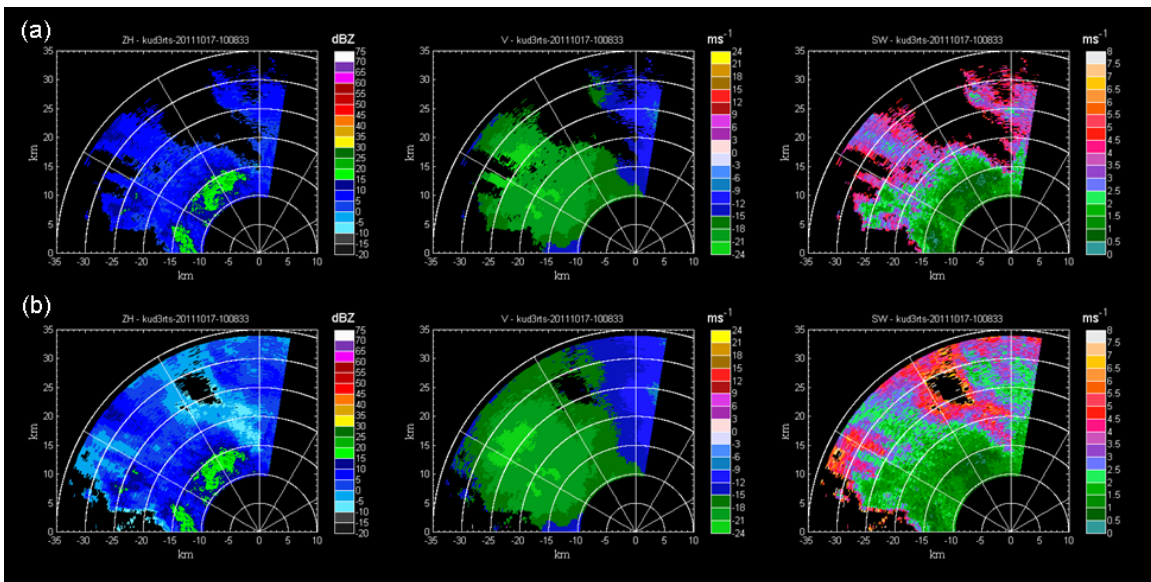


Figure 7.10: Sector PPI images of reflectivity (H-polarization) (left column), velocity (middle column), and spectrum width (right column) during a light rain event observed by the D3R system. Data are masked using a threshold of SNR>0 dB. (a) Top row: 3.6 MHz bandwidth medium pulse output processed with a matched filter. (b) Bottom row: Output of the SES system - a 3.6 MHz bandwidth medium pulse processed with an ISL filter as the reference signal for 1 MHz bandwidth long pulse, coded and processed using SES algorithm.

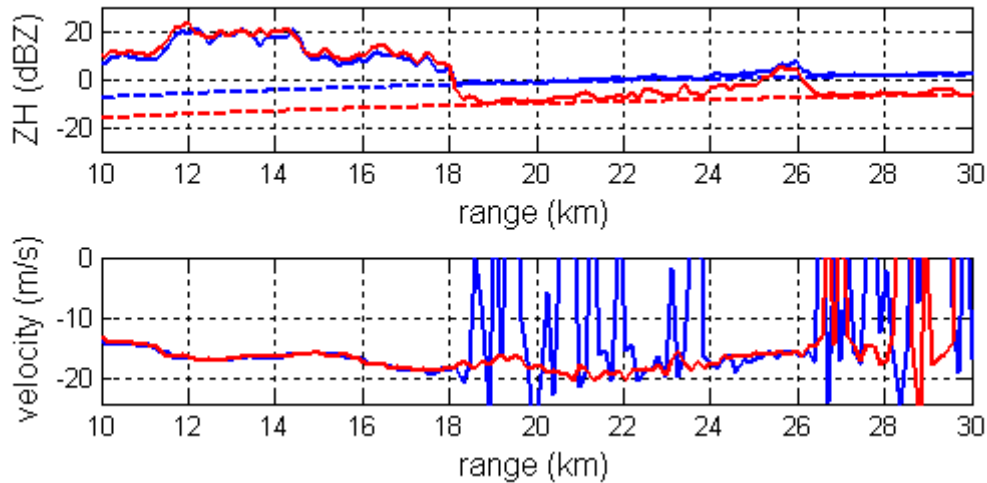


Figure 7.11: Sample profile at azimuth of 279° to show the reflectivity and velocity measurements from SES (red lines) and from second waveform of D3R (blue lines).

7.7 Summary

It is likely that final goal for phased-array weather radar technology will include the use of low-power solid-state transmitters at each element of an active array. To meet the requirement of sensitivity for weather observations, a pulse compression technique is required. The conventional matched or mismatched filters have some limitations that partly downgrade the sensitivity. The work in this chapter addresses this problem.

A new pulse compression system, SES, is developed here to achieve a better sensitivity than the traditional matched filter system. SES deploys a dual-waveform scheme. The two waveforms are related and can be transmitted simultaneously in the frequency domain or consecutively in the time domain. Time spacing between the two waveforms transmission is kept small to ensure that the precipitation is statistically stationary. Using the knowledge of the medium extracted from the first waveform, an adaptive filter for the second waveform is designed. The new filter is capable of achieving better sensitivity than the conventional matched filter. As demonstrated by

radar simulation and actual observations from the D3R Ka/Ku radar, SES is able to enhance the system's sensitivity by 8 to 10 dB. SES also provides better range sidelobe performance and Doppler tolerance. Additionally, in regions with strong echoes, the results from the two SES waveforms can be combined to reduce the measurement standard deviations. The solid performance and flexibility in waveform design of SES are very useful for any pulse compression weather radar. In particular, the use of SES compensates for the loss of sensitivity in planar phased array weather radar at off-boresight directions.

CHAPTER 8

SUMMARY AND FUTURE WORK

8.1 Introduction

The motivation for this research is the need for adaptive scan strategies and advanced signal processing techniques for phased-array weather radars (PAWR). For any phased-array radar, the scan strategy is considered as one of the most important components of the system. It is designed to command the radar to scan, to track, and to perform surveillance. It makes sure the system is working at its best capability. A scan strategy of a phased-array radar is designed based on the features and properties of the radar target and the goal of the sensing. The target of PAWR is weather, a volume target, which is very different from a point target in many aspects. Scan strategies for point targets have been developed extensively (e.g., in military applications) but research on this topic for volume targets is limited. This research work focuses on developing an electronic scan principle for PAWR with the objective of increasing scan speed without giving up measurement quality. To achieve a significant increase in scan speed, advanced signal designs and processing are required.

The space-time variability feature of a weather system is the key to developing a scan scheduler for PAWR. Observations of storms show that the temporal scale of weather phenomena is proportional to their spatial scale. A space-time characterization model was introduced to verify this hypothesis and to provide scanning conditions for the scheduler. The model assumes that a storm system is a combination of motion and evolution processes. A procedure was developed to separate the two processes and to estimate the spatial scales present

in the storm. By applying the characterization model to a sequence of radar observations, a storm can be segmented into different scanning regions corresponding to each estimated spatial scale. Next, evolution times (or temporal scales) of these regions can be derived from their 2D correlation function. Tests on simulated and actual radar data confirm that large-scale regions evolve more quickly than regions with smaller spatial scales. The adaptive scan strategy is based on the principle that quickly evolving regions are scanned more often and spatial sampling must be matched to the spatial scale. Other considerations such as nowcasting and adaptive waveforms are also addressed to improve radar observations. In order to make the best use of radar resources, a block-pulsing scheme is employed. The block size should be kept as small as possible but must be large enough for efficiently implementing a clutter-filtering algorithm. Along with the pulsing scheme, a measurement error model is introduced to provide information on the estimate's accuracy. The final but most important component of the scan strategy is a task-scheduling algorithm. In this work, the scheduling algorithm was designed based on a time balance concept. The scheduler works on a ray-by-ray basis. It also includes a procedure optimizing revisit times to obtain the fastest scan. Simulation-based analysis shows that the proposed scan strategy can reduce the scan time by a large factor.

Due to the electronic scanning mechanism of PAWR, the coupling of H and V polarizations is more complicated than that of mechanically scanned weather radar. If not removed, this coupling results in large biases in the polarimetric variables retrieval. The bias issue has been addressed by using a signal model for polarimetric PAWR. Based on the signal model, methods for bias correction are suggested. The model is also used as a framework for developing a simulation procedure for polarimetric PAWR. Preliminary results indicate that if the radar is well calibrated, inherent biases associated with polarimetric PAWR can be mitigated effectively.

However, noise effects after bias correction degrade the measurements' accuracy at off-boresight directions. The degradation level depends on how far off boresight the beam is directed and how strong the signal is. Given all these conditions, the simulation turns out to be an important tool in designing a polarimetric PAWR.

A PAWR scans different parts of the storm in a sequence and revisits them. While this strategy allows PAWR to precisely capture a storm's evolution and reduces scan time significantly, it generates non-continuously sampled data. The received signal samples are grouped into blocks that are temporally separated by the revisit times. This characteristic of PAWR received signals brings difficulties to signal processing techniques, especially in handling ground clutter. To overcome this problem, a new clutter-filtering method based on the signal covariance matrix was developed. The size of the covariance matrix can be varied to meet the requirement of the clutter suppression ratio. In the case of PAWR, the covariance matrix size is set to be equal to the block size. Since the filter works in the time domain, it avoids the limitations associated with any spectral-based processing methods such as the spectral leakage problem. In addition, the new algorithm can take advantage of the absence of beam smearing due to non-rotating antenna in PAWR, thus resulting in a better performance. It has been demonstrated that the new filter performs equal to or better than that of the current state-of-the-art filtering method. Moreover, it can be directly extended to staggered PRT waveforms, which is critical for waveform selection in PAWR.

In order to design a PAWR with dual-polarization capability, additional techniques are developed to allow the clutter filter to perform polarimetric variable retrieval. Solutions for staggered PRT waveforms in the simultaneous mode and the alternating mode are presented. A unique filter is used for both horizontal and vertical channels in order to maintain the signal's

correlation. In the simultaneous mode, filter modification is minimal because the waveforms used at the two channels are identical. In the alternating mode, a more complex modification is required due to the difference between the transmit waveforms. The result is that the final filter has additional notches besides the main notch at zero Doppler frequency. However, extensive analyses show that the method's performance in the alternating mode is comparable to that in the simultaneous mode except for some slight increase in the standard deviation of the estimates in specific cases where the signal's spectrum is narrow and overlaps the notches. The algorithm was successfully tested on both radar-simulated data and experimental observations from CSU-CHILL radar.

The system sensitivity of a PAWR is limited by the use of low-power solid-state transmitters at the array element. Further, the performance degrades significantly at off-axis directions. On the other hand, PAWR requires a large SNR to increase the scanning speed. Therefore, the quest for improving PAWR sensitivity is high. The solid-state transmitter has a high duty cycle that allows the use of a pulse-compression technique to improve sensitivity. However, in order to obtain acceptable range resolution for weather observations, the signal's bandwidth must be increased such that it partly degrades system sensitivity. To mitigate this issue, we developed a sensitivity enhancement system (SES). The system uses a dual-waveform transmission scheme. The waveforms are transmitted diversely in the time or frequency domain. They are related and can be obtained via a unique design procedure. At the receiver, an adaptive filter is determined based on the self-consistency between the signals from the waveforms. The SES filter employs the information of the precipitation medium; therefore, it can achieve a better SNR than a conventional matched filter. By using appropriate waveforms, SES can improve the sensitivity by 8 to 10 dB. Radar simulations have been carried out for different scenarios to evaluate the

performance of the method. Further, a set of waveforms was designed and implemented on the NASA D3R system. Observed data were analyzed and the results are consistent with the simulation analysis.

8.2 Future work

The following items are suggested for future work in this area of research:

Scan strategy

- Perform more extensive studies on space-time variability on radar observations
- Extend the space-time characterization model to three-dimensional data
- Update the task scheduler to sample the atmosphere in three dimensions
- Study the question of how to match spatial sampling resolution to spatial scale

Signal processing

- Study the effect of calibration errors on the bias correction methods
- Study the possibility of the second-trip echoes suppression and recovery methods on PAWR

Implementation

- Implement the advanced principles on a prototype phased array radar

BIBLIOGRAPHY

- Ackroyd, M. and F. Ghani, 1973: Optimum mismatched filters for sidelobe suppression. *Aerospace and Electronic System, IEEE Transaction on AES*, **9**, 214-218.
- Banjanin, Z. B., and D. S. Zrnic, 1991: Clutter rejection for Doppler weather radars which use staggered pulses. *IEEE Trans. Geosci. Remote Sens.*, **29**, 610- 620.
- Bharadwaj, N, K. V. Mishra and V. Chandrasekar, 2009: Waveform Considerations for Dual-Polarization Doppler Weather Radar with Solid-State Transmitters. *IEEE International Geoscience and Remote Sensing Symposium*, Cape Town, South Africa.
- Bharadwaj, N., and V. Chandrasekar, 2007: Phase Coding for Range Ambiguity Mitigation in Dual-Polarized Doppler Weather Radars. *J. Atmos. Oceanic Technol.*, **24**, 1351- 1363.
- Boyer, E., P. Larzabal, C. Adnet, and M. Petitdidier, 2003: Parametric spectral moments estimation for wind profiling radar. *IEEE Trans. Geosci. Remote Sens.*, **41**, 1859- 1868.
- Bringi, V. N. and V. Chandrasekar, 2001: *Polarimetric Doppler Weather Radar: Principles and Applications*. Cambridge University Press, 636 pp.
- Brown, R. A., V. T. Wood, and D. Sirmans, 2002: Improved tornado detection using simulated and actual WSR-88D data with enhanced resolution. *J. Atmos. Oceanic Technol.*, **19**, 1759-1771.
- Bucci N. J., and H. Urkowitz, 1993: Testing of Doppler tolerant range sidelobe suppression in pulse compression meteorological radar. *Proceedings of the IEEE National Radar Conference*, Lynnfield, MA, USA, 206-211.
- Casella, G., and R. L. Berger, 2002: *Statistical Inference*. Duxbury Press, Pacific Grove, CA, 2nd edition.
- Chandrasekar, V., V. Bringi, and P. Brockwell, 1986: Statistical properties of dual-polarized radar signals. *Preprints 23rd Conf. Radar Met.*, AMS, Snowmass, 193-196.

Chandrasekar, V., M. Schwaller, M. Vega, J. Carswell, K. V. Mishra, R. Meneghini and C. Nguyen, 2010: Scientific and Engineering Overview of the NASA Dual-Frequency Dual-Polarized Doppler Radar (D3R) System for GPM Ground Validation. *IEEE International Geoscience and Remote Sensing Symposium*, Honolulu, Hawaii.

Cheng, D. K., 1989: *Field and Wave electromagnetics*. Addison-Wesley, 2nd edition.

Cho, J. Y. N., and Chornoboy E.S., 2005: Multi-PRI signal processing for the Terminal Doppler Weather Radar. Part I: Clutter filtering. *J. Atmos. Oceanic Technol.*, **22**, 575-582.

Doviak, R. J., and D. S. Zrnic, 1993: *Doppler Radar and Weather Observations*. Academic Press, London.

Fetter R. W., 1970: Radar weather performance enhanced by compression. *Proceedings of the 14th Conference in Radar Meteorology*, AMS, Tucson, AZ, 413-418.

Golestani Y., V. Chandrasekar, and R. J. Keeler, 1995: Dual polarized staggered PRT scheme for weather radars: analysis and applications. *IEEE Trans. Geosci. Remote Sens.*, Vol.33, No. **2**, pp 239-246.

Groginsky, H. L., and K. M. Glover, 1980: Weather radar canceller design. *Proceedings Of 19th Radar Meteorol. Conf.*, 192-198.

Hildebrand, P. H., and R. S. Sekhon, 1974: Objective Determination of the noise Level in Doppler Spectra, *Journal of Applied Meteorology*, **13**, 808-811.

Hoeks, .A.P, J.J. Van de Vorst, A. Dabekaussen, P.J. Brands, and R.S. Reneman, 1995: An efficient algorithm to remove low frequency Doppler signals in digital Doppler systems. *IEEE Transactions on Ultrasonics, Ferroelectrics, and Frequency Control*, **42**, 927-937.

Ice, R. L., D. A. Warde, D. Sirmans, and D. Rachel, 2004: Report on open RDA-RVP8 signal processing. Part I: Simulation study, including Gaussian model adaptive processing clutter filter evaluation. *WSR-88D Radar Operations Center Engineering Branch Tech. Rep.*, 87 pp.

Keeler, R. J. 1995: Pulse Compression waveform analysis for weather radar. *Proceedings of the COST 75 International Semiconductor Advanced Weather Radar Systems*, European Commission, Luxemburg, Belgium, 603–614.

Kumar, V. M., V. Chandrasekar, C. M. Nguyen, and M. Vega, 2011: Waveform Design and Implementation for the Solid-State NASA Dual-Frequency Dual-Polarized Doppler Radar. *IEEE International Geoscience and Remote Sensing Symposium*, Vancouver, Canada.

Lagarias, J. C., J. A. Reeds, M. H. Wright, and P. E. Wright, 1998: Convergence properties of the Nelder-Mead algorithm in low dimensions. *SIAM J. Optim.*, **9**, 112–147.

Lawson, C. L., and R. J. Hanson, 1987: Solving Least Squares Problem. *Society for Industrial Mathematics*, 158-173.

Liu, L., V. N. Bringi, V. Chandrasekar, E. A. Mueller, and A. Mudukutore, 1993: Analysis of the copolar correlation coefficient between horizontal and vertical polarizations, *J. Atmos. Oceanic Technol.*, **11**, 950-963.

May, T. Peter, and Richard G. Strauch, 1998: Reducing the Effect of Ground Clutter on Wind Profiler Velocity Measurements, *J. Atmos. Oceanic Technol.*, **15**, 579-586

Meymaris, G., J. Hubbert, and M. Dixon, 2009: An alternative approach to staggered PRT clutter filtering. *34th Conference on Radar Meteorology*, AMS, Williamsburg, VA.

Moisseev, D. N., C. M. Nguyen, and V. Chandrasekar, 2008: Clutter suppression for staggered PRT waveforms. *J. Atmos. Oceanic Technol.*, **25**, 2209-2218.

Mudukutore, A. S., V. Chandrasekar, and R. J. Keeler, 1998: Pulse compression for weather radars, *IEEE Transaction on Geoscience and Remote Sensing*, Vol. 36, No 1, 125-142.

Nelder, J. A., and R. Mead, 1965: A simplex method for function minimization. *Comput. J.*, **7**, 308–313.

Nguyen, C. M., D. N. Moisseev, and V. Chandrasekar, 2006: Precipitation spectral moments estimation and clutter mitigation using parametric time domain model. *Proceedings of IGARSS, IEEE*, Denver, CO.

_____, 2008: A parametric time domain method for spectral moment estimation and clutter mitigation for weather radars. *J. Atmos. Oceanic Technol.*, **25**, 83-92.

Oppenheim, V. A., and R. W. Schafer, 2009: *Discrete-time signal processing*. 3rd Edition, Prentice Hall.

Reinoso-Rondinel, R., T. Y. Yu, and S. Torres, 2010: Multifunction Phased-Array Radar: Time Balance Scheduler for Adaptive Weather Sensing. *J. Atmos. Oceanic Technol.*, **27**, 1854–1867.

ROC, 2007: WSR-88D system specification. WSR-88D Radar Operations Center Rep. OWY55, 164 pp.

Rood R. B., 1987: Numerical advection algorithms and their role in atmospheric transport and chemistry models. *Reviews of Geophysics*, Vol. 25, Issue 1, 71-100.

Rust, B. W., 2002. Fitting nature's basic function part I: polynomials and linear least squares, *Computing in Science and Eng.*, **4**, 84-89.

Sachidananda, M., and D.S. Zrnic, 1999a: Systematic phase codes for resolving range overlaid signals in Doppler weather radar, *J. Atmos. Oceanic Technol.*, **16**, 1351-1363.

_____, 2000: Clutter filtering and spectral moment estimation for Doppler weather radars using staggered pulse repetition time (PRT). *J. Atmos. Oceanic Technol.*, **17**, 323–331.

_____, 2002: An improved clutter filtering and spectral moment estimation algorithm for staggered PRT sequences. *J. Atmos. Oceanic Technol.*, **20**, 672-684.

Sato, T. and R. F. Woodman, 1982: Spectral parameter-estimation of CAT radar echoes in the presence of fading clutter. *Radio Sci.*, **17**, 817-826.

Siggia, A. D., and R. E. Passarelli, 2004: Gaussian model adaptive processing (GMAP) for improved ground clutter cancellation and moment calculation. *Proceedings of Third European Conf. on Radar Meteorology*, Visby, Sweden, ERAD, 67-73.

Skolnik, M. I., 2001: *An Introduction to Radar Systems*. McGraw-Hill.

Stafford, W. K., 1990: Real time control of multifunction electronically scanned adaptive radar (MESAR). Preprints, *IEE Colloquium on Real Time Management of Adaptive Radar Systems*, London, UK, Siemens Plessey Radar, 1-5.

Torp, H., 1997: Clutter rejection filters in color flow imaging: a theoretical approach. *IEEE Trans. Ultrasonics, Ferroelectrics and Frequency Control*, **44**, 417-424.

Torres, S. M., and D. Zrnić, 2003: Whitening in range to improve weather radar spectral moment estimates. Part I: Formulation and simulation. *J. Atmos. Oceanic Technol.*, **20**, 1433–1448.

Torres, S., D. S. Zrnic, and D. J. Doviak, 1998: Ground clutter canceling with a regression filter, *National Severe Storms Laboratory Interim Report*, Norman, Oklahoma

Tripoli, G. J., and M. L. Buker, 2012: Numerical simulation of three-dimensional vortical interactions within an idealized tornado. *Conference on Severe Local Storms*, 26th, Nashville, TN, AMS, 5-8.

Wikle C. K., 2002: A kernel-based spectral model for non-Gaussian spatio-temporal processes. *Stastical Modelling*, Vol. 2, 299-314.

- Wooding, R. A., 1956: The multivariate distribution of complex normal variables, *Biometrical*, **43**, 212-215.
- Xu, G., and V. Chandrasekar, 2005: Radar storm motion estimation and beyond: a spectral algorithm and radar observation based dynamic model. *The World Weather Research Programme's symposium on nowcasting and very short range forecasting (WSN05)*, Toulouse, France, paper 2.41.
- Yu, T-Y., M. B. Orescanin, C. D. Curtis, D. S. Zrnić, and D. E. Forsyth, 2007: Beam multiplexing using the phased-array weather radar. *J. Atmos. Oceanic Technol.*, **24**, 616-626.
- Zhang, G., R. J. Doviak, D. S. Zrnic, J. Crain, D. Stainman, and Y. Al-rashid, 2009: Phased array radar polarimetry for weather sensing: a theoretical formulation for bias corrections. *IEEE Trans. Geosci. Remote Sens.*, Vol.47, No. **11**, 3679-3689.
- Zrnic, D. S., 1979: Estimation of spectral moments for weather echoes. *IEEE Trans. Geosci. Remote Sens.*, **17**, 113-128.
- Zrnić, D. S., and Coauthors, 2007: Agile beam phased-array radar for weather observations. *Bull. Amer. Meteor. Soc.*, **88**, 1753–1766.
- Zrnic, D. S., G. Zhang, and R. J. Doviak, 2011: Bias correction and Doppler measurement for polarimetric phased-array radar. *IEEE Trans. Geosci. Remote Sens.*, Vol. 49, No. **2**, 843-853.
- Zrnic, D. S., and P. R. Mahapatra, 1985: Two methods of ambiguity resolution in pulsed Doppler weather radars. *IEEE Trans. Aerospace Electron. Syst.*, **21**, 470–483.